INDUSTRIAL WASTEWATER TREATMENT USING ELECTROCHEMICALLY GENERATED OZONE

Submitted by:

KHALID ZAKARIA

Supervised by:
Prof. P. A. Christensen & Prof. T. P. Curtis

Submitted in partial fulfilment of the requirements for the degree of Doctor of Philosophy (PhD) in Environmental Engineering in the Faculty of Science Agriculture and Engineering.

School of Civil Engineering and Geosciences
Newcastle University
Newcastle Upon Tyne
NE1 7RU UK

Submission Date: September 2013

Declaration

I hereby declare that the work embodies in this thesis entitled "Industrial Wastewater Treatment Using Electrochemically Generated Ozone" is the result of investigations carried out in the School of Civil Engineering and Geosciences and the school of Chemical Engineering and Advanced Materials, University of Newcastle, United Kingdom between January 2010 and December 2012 under the supervision of Professor Tom P. Curtis and Professor Paul A. Christensen.

Extracts from this work has been accepted for publication in the following journals:

1. Christensen, P. A., **K. Zakaria** and T. P. Curtis, "Structure and Activity of Ni – and Sb – Doped SnO_2 Ozone Anodes", *Ozone Science and Engineering*, 34: 49 – 56 (2012).

2. Christensen, P. A., T. Yonar and **K. Zakaria**, "The Electrochemical Generation od Ozone: A Review", *Ozone Science and Engineering*, 35: 149 – 167 (2013).

3. Christensen, P. A., **K. Zakaria**, H. Christensen and T. Yonar, "The Effect of Ni and Sb Oxide Precursors, and of Ni Composition, Synthesis Conditions and Operating Parameters on the Activity, Selectivity and Durability of Sb – Doped SnO_2 Anodes Modified with Ni", Journal of The Electrochemical Society, 160: H405 – H413 (2013).

1. Zakaria, K. and P. A. Christensen, "The The Use of Ni/Sb–SnO2-based Membrane Electrode Assembly for Electrochemical Generation of Ozone and the Decolourisation of Reactive Blue 50 Dye Solutions", Electrochimica Acta, 135: 11-18 (2014).

2. **Zakaria, K**. "Highly Efficient, Low Cost Electrochemical Ozone Generation Using Membrane Electrode Assemblies (MEA's) with Ni/Sb – SnO_2 Anodea and Air Breathing Cathodes", Submitted to Indian Journal of Chemical Technology.

3. **Zakaria, K**., and R. Ariffin , "Electrochemical Decolourisation of Reactive Blue

50 Dye on Ni/Sb – SnO_2 Anodes", Submitted to Journal of Environmental Chemical Engineering.

Poster Presentations

1. The 2010 Civil Engineering and Geosciences postgraduate conference, "Industrial Wastewater Treatment Using Electrochemically Generated Ozone", 22 – 23 June 2010, School of Civil Engineering and Geosciences, University of Newcastle, Newcastle, UK

2. The September 2010 Science Agriculture and Engineering faculty public engagement presentation, "Electrochemically Generated Ozone", 23 September 2010, Hershel Building, University of Newcastle, Newcastle, UK

Oral Presentations

The 2011 Civil Engineering and Geosciences postgraduate conference, "Industrial Wastewater Treatment Using Electrochemically Generated Ozone", 23 – 24 June 2011, School of Civil Engineering and Geosciences, University of Newcastle, Newcastle, UK

Acknowledgement

First and foremost is to thank Almighty Allah (SWT) for giving me the opportunity and the ability to carry out this research, without his mercy, blessings and guidance I would not have completed this work successfully. He (SWT) blessed me with uncountable gifts that does not start with the project and the supervision and does not end with health and patience throughout the work reported in this thesis. Asking Him (SWT) to make it sincere for his face, accept it and accept all of the efforts behind it.

Unlimited and endless thanks and gratitude to my parents: Mr. Abdunnaser Zakaria and Mrs. Samira Zakaria for everything. Thank you and my Allah grant you with his mercy.

I would like to express my sincere gratitude to Prof. P. A. Christensen for his supervision of this research. I deeply thank him for everything he did for me and my research. It has been a privilege to work with him. I also would like to thank Prof. T. P. Curtis for his help throughout my presence in Newcastle University. Thank you Paul and Tom.

Many thanks to Clarizon Ltd, Dr Henriette Christensen, for the collaboration, supporting and assistance. I would like to thank Langholm Dyeing Co and all people working there for their help and providing me with dye needed for this project. Many thanks for Dr. T. Yonar for his help. Thanks Taner.

I would like to thank everyone, the staff and students in the School of Civil Engineering and Geosciences and the school of Chemical Engineering and Advanced Materials and in Newcastle University for all their help and assistance. Thanks also to technicians in Cassie building teaching lab, the mechanical and glass blowing workshops for building and maintaining the equipment used in my work. I would also like to thank Robin Ingleton, store supervisor at school of Chemistry, Pauline Carrick at Advanced Chemical and Material Analysis (ACMA) in Newcastle University, and I also thank Dr. Adrain Boatwright at Centre for Surface Chemical Analysis (CSCA), Dr. David Scurr at Laboratory of Biophysics and Surface Analysis (LBSA) at Nottingham University.

Unlimited thanks go to the Syrian People, who I belong to, for providing me with the scholarship to do this research. Thanks to my local supervisor Dr. Basam Al Aji for his help. Thanks Basam.

Many thanks to all my friends, classmates and colleagues for their support and help. Thank you everyone I knew and affected my life in Newcastle.

Finally, millions of thanks to my wife Mrs. Najed Alkadoor who was with me and provided me with all my needs and made the life in this country much easier, to my son Abdunnaser and daughter Aseel who made my life full of happiness. Thank you Najed, Abode and Aseel.

To my parents, wife, children and to the Syrian Martyrs

Khalid Zakaria , Sep. 2013

Abstract

The remediation of industrial wastewater is highly challenging, difficult task, and demands highly efficient technologies. Electrochemical and ozonation technologies are among the most efficient methods in treating the industrial wastewater. The electrochemical generation of ozone can provide very high concentrations of the reagent in both the gas phase and solution.

The aim of the research reported in this thesis was to develop durable and highly efficient Ni/Sb – SnO_2 anodes to generate ozone and to investigate their efficiency in treating industrial wastewater. Different anode sizes were studied: 0.64 cm^2, 6.25 cm^2 and 24 cm^2 using Ti mesh as substrate.

With respect to the 0.64 cm^2 anodes, replacing Sb and Ni chlorides with their respective oxides and adding Au or Pb had little or no effect upon the anodes electrochemical properties. The research showed that all 0.64 cm^2 anodes were porous with dimensionalities < 2. However, the presence of the Au in the precursors reduced the ozone current efficiency. The 0.64 cm^2 anodes achieved ozone current efficiencies of ca. 30% at cell voltages of 2.7 V routinely.

Using 6.25 cm^2 anodes prepared with the Sb and Ni oxides in the precursor solution and annealed at 550 ^oC gave electrodes which were durable for more than 200 h operation at a current density of 100 mA cm^{-2} (corresponding to cell voltages of ca. 3 V) in 1 M $HClO_4$. These current densities and service life are the highest reported for Ni/Sb – SnO_2 anodes. A service life of more than 600 h was achieved in a later investigation. The 6.25 cm^2 anodes achieved current efficiencies up to 38%, with 25 -30% routinely achievable. The presence of Ni is crucial for ozone generation with optimum Ni content (in the precursor solution) of ca. 1.04 at % Ni. The optimum annealing temperature was 460 ^oC.

In terms of the 24 cm^2 anodes, they were employed to prepare membrane electrode assemblies (MEA's) for ozone generation from deionised (Millipore) water. MEA's with air breathing cathodes suffered from flooding of the cathode pores, resulting in limited current densities. MEA's with hydrogen – evolving cathodes did not suffer from flooding or low current densities. Overall, current efficiency of ca. 36 % at cell voltage of 1.6 V (40 mA cm^{-2}) with Millipore water as anolyte was obtained using MEA's with air breathing

cathodes; corresponding to a power consumption of 16.7 kWh (kg O_3)$^{-1}$ which is the lowest reported for electrochemical ozone generation of any description, MEA's with H_2 cathodes achieved a current efficiency of 33% at ca. 25 mA cm^{-2} and a cell voltage of 2.5 V, corresponding to ca. 25 kWh (kg O_3)$^{-1}$.

The 0.64 cm^2 anodes were used to decolourise solutions containing : Reactive Blue 50 (RB50), Naphthol Green B (NGB) and Congo Red (CR) dyes. The operational conditions of the decolourisation process were investigated and the optimum conditions were: 3 g dm^{-3} Na_2CO_3 as electrolyte, 50 mA cm^{-2} and 200 mg dm^{-3} dye in Millipore water. RB50 solutions could be decolourised completely within 20 min, with 90% of the COD removal after 60 min, NGB and CR proved more refractory. Indirect oxidation mediated by OH radicals was the main decolourisation mechanism at the Ni/Sb – SnO_2 anodes.

Ozonation, UV_{254} irradiation and O_3/UV were used to decolourise the dye solutions for comparison with electrochemical decolourisation at the Ni/Sb – SnO_2 anodes. Ozone was generated by MEA – based electrochemical cells and ozonation occurred in a bubble column reactor (BCR). The O_3/UV combination was the most efficient, achieving 100 % decolourisation of RB50 and NGB solutions within 20 and 35 min, respectively, with 33% and 64% COD removal after 60 min.

Preface

Contents

List of Tables

Chapter One: Introduction

Chapter Two: Experimental

Chapter Three: Structure and Activity of Small Scale (0.8 cm × 0.8 cm) Ozone Anodes

Chapter Five: Ozone Generation Using Membrane Electrode Assembly (MEA)

Chapter Six: Chapter Six: Electrochemical Dye Decolourisation on NATO Anodes

Chapter Seven: Dye Decolourisation by Ozone, UV irradiation and O_3/UV Combination

List of Schemes

Chapter One: Introduction

Chapter Two: Experimental

Chapter Three: Structure and Activity of Small Scale (0.8 cm × 0.8 cm) Ozone Anodes

Chapter Four: Activity, Selectivity and Durability of 6.25 cm^2 NATO Anodes

Chapter Five: Ozone Generation Using Membrane Electrode Assembly (MEA)

Chapter Six: Electrochemical Dye Decolourisation on NATO Anodes

Chapter Seven: Dye Decolourisation by Ozone, UV irradiation and O_3/UV Combination

Appendices

Index of Nomenclature, Greek symbols and Acronyms

Nomenclature	Name	Unit
A	Absorbance	
A	Electrode area	cm^2
b	Pathlength	cm
C	Concentration	mol dm^{-3}
d_f	Dimensionality	
ΔE	Anodic and cathodic peak separation	V
E^0	Standard reduction potential	V
F	Faraday constant/96485	C mol^{-1}
I	Current	A
I_p	Current of the peak	A
I_{cap}	Capacitance current	A
j	Current density	A cm^{-2}
j_{lim}	Limiting current density	A cm^{-2}
k_a	Rate constant of decolourisation of RB50	min^{-1}
k_b	Rate constant of benzene ring destruction of RB50	min^{-1}
MW	Molecular weight	g mol^{-1}
P	Power consumption	kWh kg^{-1} O_3
Q	Electric charge	C
R	Gas constant (8.3145)	J mol^{-1} K^{-1}
R	Electric resistance	Ω cm^2
t	Time	min
T	Temperature	^oC
V	Volume of solutions	cm^3, dm^3
V	Cell voltage	V
W	Energy	W
z	Number of electrons	

Greek Symbol	Name	Unit
α	Dimensionality related parameter = $(d_f - 1)/2$	
β	Asymmetry parameter	
λ	Wavelength	nm
Ω	Unit of resistance	Ω cm^2
f	Flow rate	cm^3 min^{-1}
ℓ	Pathlength	cm
n	Mole of substance	mol
η	Current efficiency	%
ε	Extinction coefficient	M^{-1} cm^{-1}

Acronyms	Name
Abs or ABS	Absorbance
BCR	Bubble Column Reactor
BDD	Boron Doped Diamond
COD	Chemical Oxygen Demand / mg O_2 dm^{-3}

CR	Congo Red Dye
DC	Direct Current
ED	Electrodeposition
EDIL	Electro Deposition Inter Layer
EDX	Energy Dispersive X – ray analysis
Fig.	Figure
g	Gram
h	Hour
MEA	Membrane Electrode Assembly
MEA – OGS	MEA – based Ozone Generation System
min	Minute
NGB	Naphthol Green B
NHE	Natural Hydrogen Electrode
OPR	Ozone Production Rate
PEM	Polymer Electrolyte Membrane
PSU	Power Supply Unit
PTFE	Poly Tetra Fuoro Ethylene
RB50	Reactive Blue 50 Dye
s	Second
SCE	Saturated Calomel Electrode
SEM	Scanning Electron Microscopy
SHE	Standard Hydrogen Electrode
Tof – SMS	Time – of – flight Secondary Ion Mass Spectrometry
UV – Vis	Ultraviolet – Visible
XPS	X – ray Photoelectron Spectrometry

CHAPTER ONE

1 Introduction

1.1 An Overview of Electrochemical Ozone Generation

Ozone was first identified as a distinct chemical compound by Schönbein in work that commenced with his observation that the electrolysis of water produced an odour at the anode identical to that from an electric arc[1]. Schönbein's acquisition of a Grove cell, which was able to deliver a much higher current than his previous apparatus, led to his proposal that the odour was due to a distinct chemical[2], which he named "ozone"[3]. There is a nice circularity in the acquisition of the Grove cell by Schönbein in the mid-19th century being so critical to the discovery of ozone and the use of air cathodes in electrochemical ozone cells in the 21st century (see, for example[4]). For an in-depth review of Schönbein's work see[5]. The molecular formula of ozone was determined by Andrews and Tait[6], only after which could the compound be determined quantitatively.

The electrolysis of water is generally believed to produce ozone *via* a 6-electron process [7, 8]:

$$3H_2O \rightarrow O_3 + 6H^+ + 6e^- \qquad E^0 = +1.51\ V \qquad (1.1)$$

As E^0 for the oxidation of water to oxygen is somewhat lower, +1.23 V [9]:

$$2H_2O \rightarrow O_2 + 4H^+ + 4e^- \qquad E^0 = +1.23\ V \qquad (1.2)$$

oxygen is always produced simultaneously with ozone ([7] and references therein), and the current efficiency for ozone generation is the percentage of the observed current that is generating ozone.

Ozone is not always observed as soon as Faradaic current (ie. electrons cross the electrode/electrolyte interface) flows: at PbO_2 anodes (the most commonly employed electrodes for ozone generation), Kötz and Stucki[10] report that ozone was only observed at current densities > 50 mA cm^{-2} whilst Feng and co-workers[11] did observe ozone as soon as Faradaic current flowed. At Si/TiO_x/Pt/TaO_x anodes, Kaneda et al.[12] observe the onset of ozone evolution at current densities > 30 mA cm^{-2}.

The solubility of ozone in acidic solutions is generally accepted as being up to *ca.* 10 times that of O_2 [13-15] *i.e.* the saturation solubility at 0 °C and 1 atm is 22 mM.

Ozone is commonly measured in the gas phase and solution by UV spectroscopy and iodometric titration[16]. The UV approach employs the ozone peak near 254 nm (gas phase) or 258 nm (solution phase)[17]. The majority of papers in the literature quote a value of 3000 ± 125 mol^{-1} dm^3 cm^{-1} for both the gas and aqueous phase extinction coefficients (see, for example,[18-20]) with a typical gas phase value of 3024 mol^{-1} dm^3 cm^{-1} at 254 nm and aqueous phase value of 2900 mol^{-1} dm^3 cm^{-1} at 258 nm[17]. The International Ozone Association[18], recommends a value of 3000 mol^{-1} dm^3 cm^{-1}, and this was employed throughout. It is worth mentioning that some concerns have been expressed with respect to the adverse effect of water vapour on the UV analysis of low concentrations of gas phase ozone[21].

Iodometric titration is the standard method recommended by the International Ozone Association [22]. Briefly, the iodometric method relies on the oxidation of I^- by O_3 followed by the determination of the amount of iodine so formed by titration with sodium thiosulfate using starch indicator.

1.1.1 The mechanism of electrochemical ozone generation

With any chemical or electrochemical reaction, a good place to start is to identify the intermediates. Wabner and Grambow[23] employed various methods to detect hydroxyl radicals, singlet oxygen and peroxo species (H_2O_2 and $HOO^{\cdot}$) during the electrolysis of pH 7 phosphate buffer at Pt and PbO_2 anodes[23]. The spin trap p-nitrosodimethyl aniline (NDMA) was employed to detect OH radicals, *via* the bleaching of the NDMA absorption at λ_{max} = 440 nm; singlet oxygen was monitored via its reaction with histidine and the bleaching of the 440 nm absorption of NDMA by the endoperoxides so formed. Peroxo species were detected via their conversion to OH radicals by Fe^{2+} and reaction with NDMA. Pt was used for comparison with PbO_2 as the former did not produce ozone at the low current densities employed (5 mA cm^{-2}). As well as O_2, Pt and PbO_2 both produced singlet oxygen; however, Pt produced peroxo species and only traces of OH radicals, whilst OH radicals were clearly produced at the PbO_2. On the basis of their results, the authors concluded that OH radicals were intermediates in the production of ozone according to:

$$H_2O \rightarrow OH_{ads} + H^+ + e^- \qquad (1.3)$$

$$OH_{ads} + O_{2ads} \rightarrow HO_{3ads} \qquad (1.4)$$

$$HO_{3ads} \rightarrow HO_3^+ + e^- \quad (1.5)$$

$$HO_3^+ \rightarrow O_3 + H^+ \quad (1.6)$$

Kim and Korshin[24] also detected OH radicals during the electrolysis of aqueous Na_2SO_4 at PbO_2 and postulated that these species were intermediates in electrochemical O_3 generation, and this remains a common postulate[7, 8, 11, 25-27], with the first step (1.3), the primary water discharge, being the rate determining step (rds).

The gas phase reaction:

$$(O^{\cdot})_{(g)} + O_2 \rightarrow O_3 \quad (1.7)$$

is well known to proceed with low activation energy[28], and the role of atomic oxygen as a key intermediate to O_3 has hence also long been postulated in electrochemistry (see, for example,[29]). Initially, dissolved O_2 was believed to be the other reactant[17, 30]. Stucki and co-workers employed a pressured Membrel electrolyzer[31] to investigate the possible role of dissolved O_2, but found that pressure had no effect upon current efficiency, an observation they rationalised in terms of the reactions:

$$(O)_{ads} + O_{2(g)} \xrightarrow{k_1} O_{3(g)} \quad (1.8)$$

$$(O)_{ads} + O_{3(g)} \xrightarrow{k_2} 2O_{2(g)} \quad (1.9)$$

Increasing the pressure increases O_3 and O_2 but decreases $(O)_{ads}$, hence the ratio of the two reaction rates (1.8) and (1.9) remains unchanged. Reactions (1.8) and (1.9) show another commonly held view, that $(O^{\cdot})_{ads}$ is common to both O_2 and O_3 formation, and it is now generally accepted that adsorbed O_2 is the active intermediate, along with $(OH^{\cdot})_{ads}$ and $(O^{\cdot})_{ads}$[11, 30, 32], and (as stated above) that the discharge of water is the rate determining step.

Mechanistic studies on electrochemical ozone evolution have primarily focused on the interpretation of overpotential vs log(current density), or Tafel, plots (see Appendix I for a critical description of the Tafel approach). Broadly speaking, in terms of the first two postulated steps in electrochemical ozone evolution:

$$(H_2O)_{ads} \rightarrow (OH^{\cdot})_{ads} + H^+ + e^- \text{ (rate determining step)} \quad (1.10)$$

$$(OH^{\cdot})_{ads} \rightarrow (O^{\cdot})_{ads} + H^{+} + e^{-} \qquad (1.11)$$

if all the species in (1.10) and (1.11) were in solution, *ie*. (1.10) and (1.11) are outer sphere processes, the slope of the Tafel plot would be expected to be 118 mV at 298K, if (1.10) was rate limiting, or 39 mV at 298K if (1.11) was the rate determine step (rds)[33, 34]. In the latter case, at high enough overpotentials, there should be a switch of the rds to (1.10) with a concomitant increase in the slope to 118 mV. If any adsorbed species are involved (as is the case with (1.10) and (1.11)), the analysis becomes significantly more complicated and a range of Tafel slopes are possible. The above analysis requires that the mass transport of reactants to the electrode, and of products away from the electrode, is controlled; in most papers reporting Tafel analyses, this is not the case.

The work of Kötz and Stucki may be considered as seminal in the Tafel-based analysis of the ozone evolution reaction for several reasons[10]. The authors studied the electrolysis of 3M H_2SO_4 at (static) 1 cm^2 PbO_2 anodes at 0 °C, measuring current density as a function of the electrode potential, and the data so obtained are shown in fig. 1.1. The authors drew attention to the important fact that the method of IR compensation (to take into account the resistance of the electrolyte as well as any insulating film that may form on the electrode, *etc*) is crucial, as different methods can give rise to markedly different results, as may be seen in fig. 1.1, see curve (I). The authors employed the current interruption method (solid line) and the positive feedback approach (dashed line). As may be seen from the figure, at low overpotentials/current densities, there is no difference in the data obtained via the two approaches; however, at high current densities the two methods diverge quite markedly. The correct choice of IR compensation remains a major concern in such experiments[7, 25]. Kötz and Stucki decided that the current interruption method was appropriate, and interpreted the switch from a Tafel slope of 120 mV at low overpotentials (< 50 mA cm^{-2}) to 70 mV at high overpotentials (the axes are reversed with respect to conventional Tafel plots) to the formation of OH_{ads} or O_{ads} becoming the rds, as ozone formation was only observed in the region of the lower Tafel slope. The current leading to ozone formation was calculated by the authors *via* the UV analysis of the gas evolved from the anode, employing an extinction coefficient of 3024 mol^{-1} dm^3 cm^{-1} for the λ_{max} of O_3 at 254 nm, and is shown as curve (II) in fig. 1.1. The slope of the "ozone Tafel plot" so obtained was found to be 70 mV and this was interpreted in terms of a reaction common to O_2 and O_3 generation that becomes rds at higher current densities; overall the authors postulated the

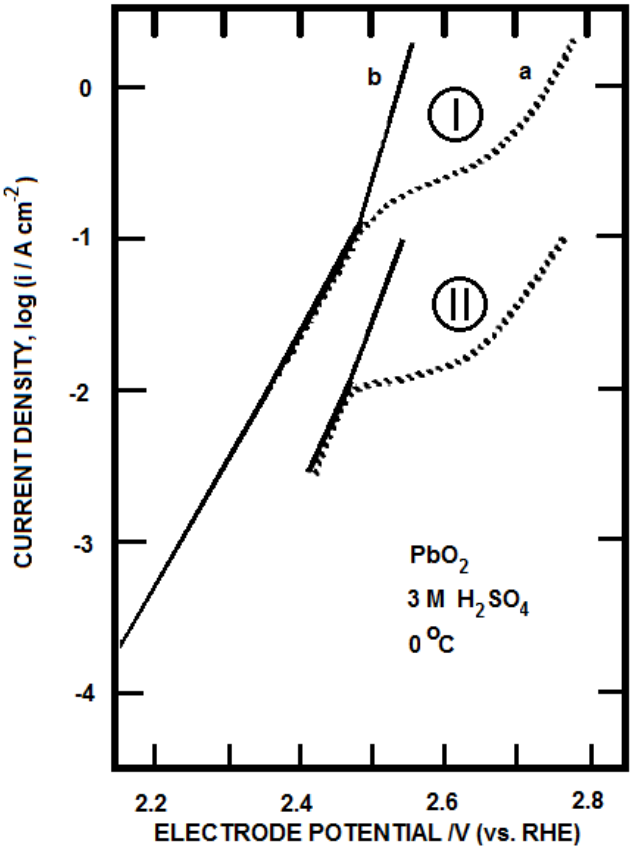

Figure 1. 1. Current-potential curves for PbO_2 in 3M H_2SO_4 at 0°C. Curve (I) is the total current & curve (II) the partial current for O_3 evolution calculated from the measured values of the O_3 concentration in the anode product gas. IR correction carried out via (—) current interruption or (...) positive feedback. Reproduced from [10].

mechanism shown in fig. 1.2. The mechanism shown in fig. 1.2 is referred to as the 'oxide path' mechanism, and was postulated by Bockris and Reddy[35] and concerned the evolution of oxygen at Pt electrodes and postulates that the first step, the primary water discharge, is the rds based on the ratio of the number of electrons transferred (n = 4) to the forward and backward asymmetry parameters (both taken as 0.5).

The model proposed by Kötz and Stucki[10] is the most commonly accepted, general mechanism for electrochemical ozone generation essentially irrespective of anode material, and has remained at the core of the mechanisms proposed for electrochemical ozone evolution since, and is typified by the model postulated by Da Silva and co-workers [8, 25]:

$$(H_2O)_{ads} \rightarrow (OH^{\cdot})_{ads} + H^+ + e^- \quad \text{(rds)} \qquad (1.10)$$

$$(OH^{\cdot})_{ads} \rightarrow (O^{\cdot})_{ads} + H^+ + e^- \qquad (1.11)$$

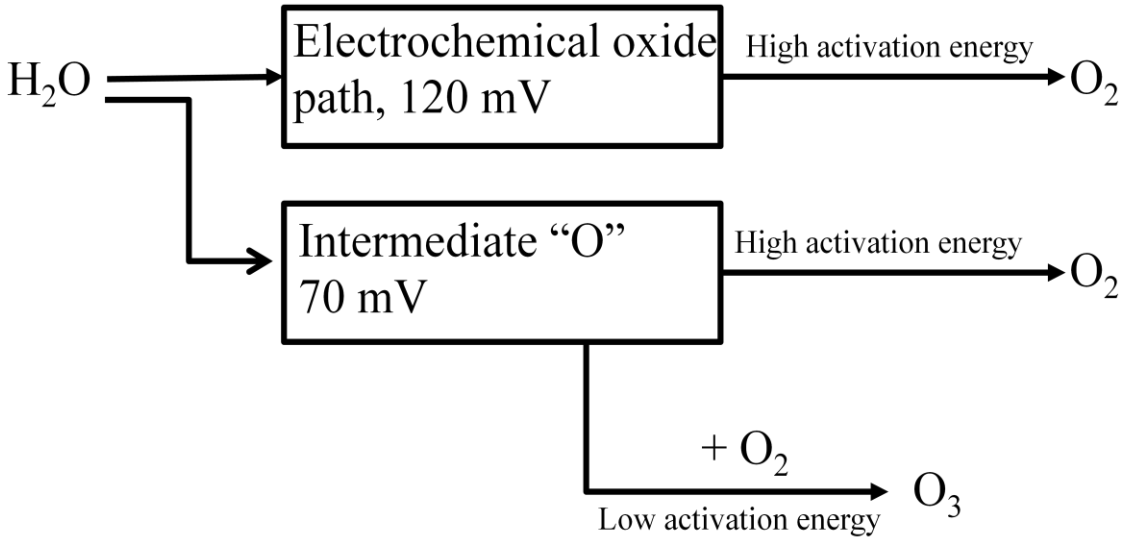

Figure 1. 2. The mechanism for the electrochemical generation of ozone proposed by Kötz and Stucki. Redrawn from[10].

$$(O^{\cdot})_{ads} \rightarrow [1-\theta](O^{\cdot})_{ads} + \theta(O^{\cdot})^*_{ads} \quad (0 < \theta < 1) \qquad (1.12)$$

$$[1-\theta](2O^{\cdot})_{ads} \rightarrow [1-\theta](O_2)_{ads} \qquad (1.13)$$

$$[1-\theta](O_2)_{ads} \rightarrow [1-\beta].[1-\theta](O_2)_{ads} + \beta[1-\theta](O_2)^*_{ads} \quad (0 < \beta < 1) \qquad (1.14)$$

$$[1-\beta].[1-\theta](O_2)_{ads} \rightarrow O_2\uparrow \qquad (1.15)$$

$$\theta(O^{\cdot})^*_{ads} + \beta[1-\theta](O_2)^*_{ads} \rightarrow [\theta + \beta(1-\theta)](O_3)_{ads} \qquad (1.16)$$

$$[\theta + \beta(1-\theta)](O_3)_{ads} \rightarrow O_3\uparrow \qquad (1.17)$$

"θ" and "β" represent the surface coverage by oxygen species while "*" represent the fractional surface coverages of intermediates leading to O_3.

The majority of papers concerning the kinetics of electrochemical ozone evolution interpret data in terms of the principles detailed above. In general, and after suitable IR correction, Tafel plots are found to exhibit two linear regions (as observed by Kotz and Stucki[10]) corresponding to O_2 evolution at low current densities and $O_2 + O_3$ at high current densities[7]. The change in slope is taken as showing a transition in the rds and/or of the asymmetry parameter β see, for example[25, 36] (PbO_2) and[27, 37] (IrO_2+Nb_2O_5). Based on the Tafel equation (see Appendix I), the Tafel slope should be linearly dependent upon temperature; however, such a simple dependence is not observed [8], and this was interpreted in terms of the effect of bubble adherence (especially at high current densities) and/or

anion adsorption, both of which will have significant effect upon the observed Tafel slope, illustrating again that Tafel measurements have to be interpreted with great care. It is also clear from the literature that anions can have a very significant effect upon ozone efficiency, and this is dealt with in a separate section below.

1.1.2 The electrochemical cell

The types of cell employed in the electrochemical generation of O_3 reflect those generally employed in electrolysis.

In the simplest cell configuration, the electrodes are immersed directly in the electrolyte[38] and the gases evolved at anode and cathode are allowed to mix, see fig. 1.3. Separated cells employ an inert separator such as glass [8, 38, 39], wetted Teflon [39, 40] or Nafion[24, 41] and the anode and cathode gases are vented separately, see figs. 1.4(a) and (b).

Zero gap, filter-press and Membrane Electrolyte Assembly (MEA) - based cells employ a solid polymer electrolyte (SPE) membrane (typically Nafion) as the electrolyte, with the anode and cathode being pressed tightly against the membrane. Protons can move through pores in the membrane and hence maintain the essential, *ionic* conductivity between the

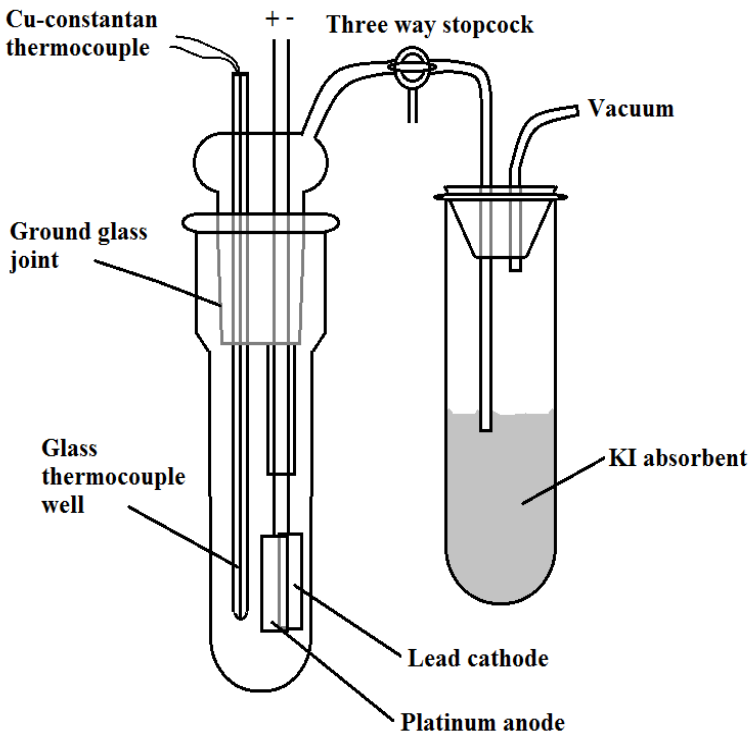

Figure 1. 3. Single compartment electrochemical cell; anode and cathode gases mix. Redrawn from [38].

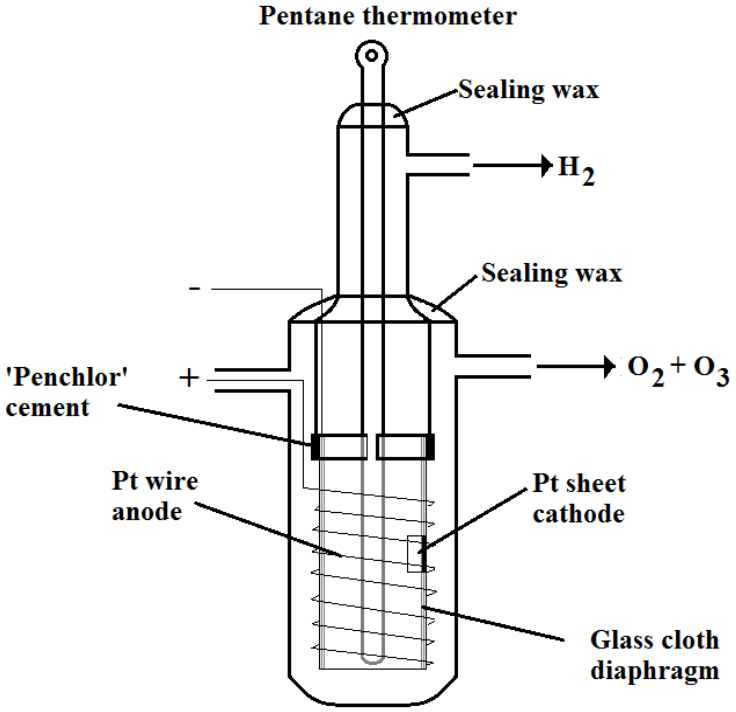

(a)

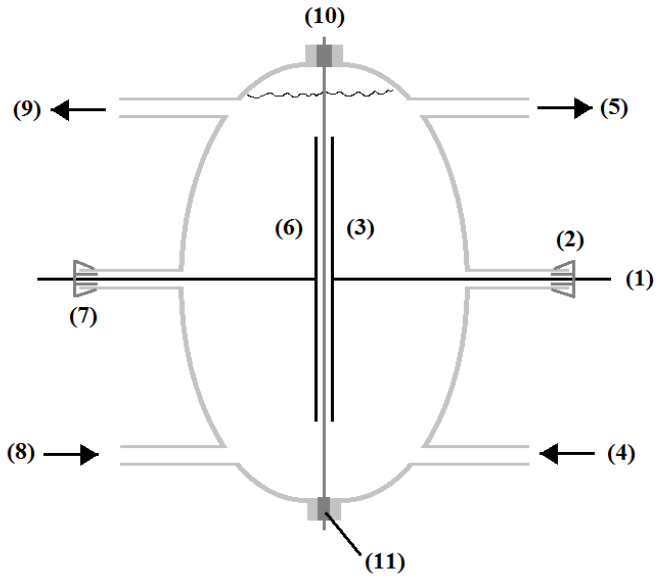

(b)

Figure 1. 4. Cells where the anode and cathode gases are kept separated. (a) The Diaphragm laboratory cell employed by Putnam et al.; the anolyte and catholyte are separated by a glass cloth diaphragm. Redrawn from [38]. (b) The separated (glass) cell employed by Christensen and co-workers [42]; the anolyte and catholyte are separated by a Nafion membrane and the two hemispherical glass sections of the cell are clamped either side of the membrane with silicone seals. (1) Ti wire, (2) rubber seal, (3) Pt/Ti mesh cathode , (4) catholyte inlet, (5) catholyte outlet, (6) Ni/Sb-SnO_2 coated Ti mesh anode, (7) rubber seal, (8) anolyte inlet, (9) anolyte outlet, (10) Nafion membrane and (11) silicone rubber "O" ring seals.

electrodes[43]. In MEA-based cells, the membrane is hot-pressed between the anode and cathode to form a free-standing MEA prior to inclusion in the cell [4, 44]; otherwise the electrodes are pressed tightly either side of the membrane mechanically[45].

If water is fed to a Pt-based cathode (*e.g.* Pt or Pt/Ti mesh), hydrogen is evolved as the cathode reaction [30, 31, 45-49], see fig. 1.5. In contrast, if an air breathing cathode is employed (*i.e.* Pt particles deposited upon porous carbon in a gas diffusion electrode), oxygen is reduced to water at the cathode [4, 35, 50], which is a safer system, especially for domestic applications, as hydrogen is not evolved. In principle, there is an additional advantage in using such a cathode. Given that cell voltage is the difference between the two individual electrode potentials (anode and cathode), the potential of a hydrogen evolving cathode should be 0V *vs* the Reversible Hydrogen Electrode (RHE, a standard reference electrode, see[33], p. 93 *ff*) based (only) on thermodynamic considerations (ie. ignoring kinetic effects, see below), whilst oxygen reduction should occur at 1.23 V *vs* RHE. Hence, the cell voltage required to drive ozone evolution at a particular rate should be less when employing an air cathode compared to a hydrogen evolving cathode. Thus, Katoh and co-workers monitored the anode and cathode potentials during electrolysis of water in a zero gap cell employing a β-PbO_2 anode and air breathing cathode fed with pure

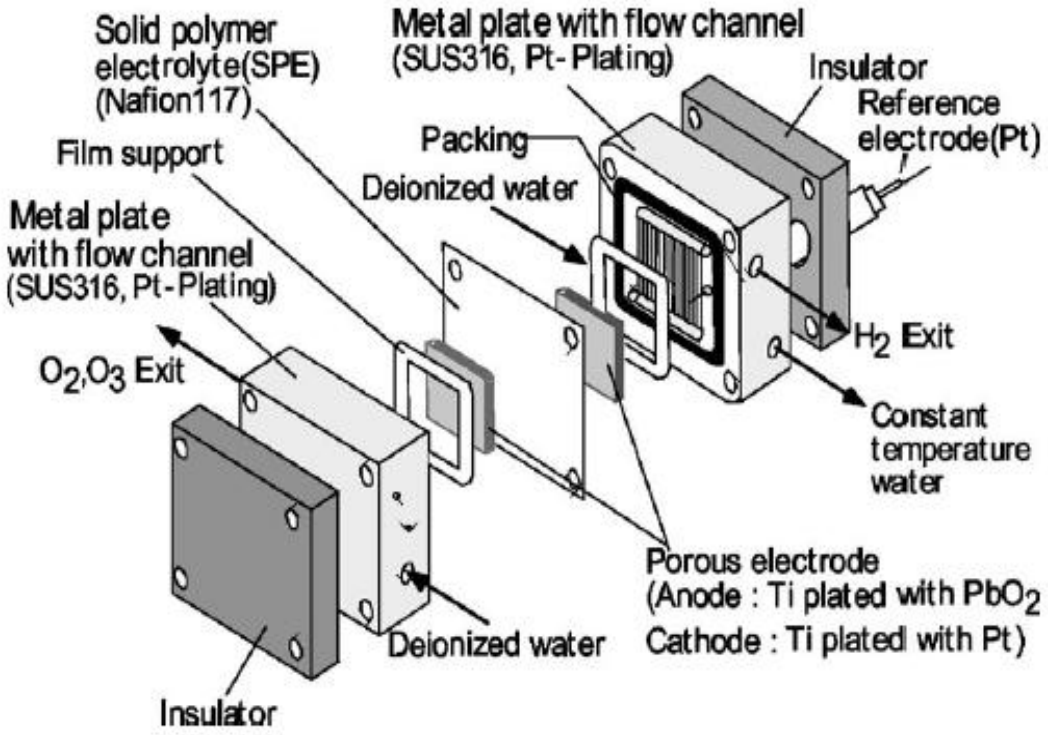

Figure 1. 5. Schematic of the solid polymer electrolyte membrane cell employed by Onda and co-workers [48].

oxygen or with no oxygen and so allowed to generate hydrogen; the authors found that the cell voltage observed at 1 A cm^{-2} using the oxygen cathode was 0.85V lower than when hydrogen was evolved[44]. There are a number of reports on variations of the zero gap cell, *e.g.* feeding humidified O_2 to a gas diffusion cathode to generate H_2O_2 [51] using an air breathing cathode/Nafion "half MEA" separated from the anode by acidic electrolyte [40] and a spiral wound MEA-based cell[52].

Foller and Kelsall [40] reported a variation of the zero gap cell. This is a remarkable study for several reasons: (1) it was one of the first to employ an air breathing cathode (air depolarized) as in a fuel cell; (2) the maximum current efficiency obtained was 45% using a glassy carbon anode, albeit in highly concentrated (corrosive and expensive) HBF_4 at -5 °C; (3) the paper presents a thoroughgoing analysis of the engineering aspects of the electrochemical reactors employed. One of the two reactors employed in the study utilized two air breathing cathodes between which were cooled, tubular glassy carbon electrodes immersed in the aqueous HBF_4 electrolyte. The authors employed an air cathode following the work of the Permelec Electrode Corporation who incorporated such an air cathode into Membrel-type cell[53] and obtained current efficiencies of *ca.* 16% at a cell voltage of *ca.* 2.3 V. Other variations of the zero gap configuration include the work by Okada and Naya[54] who employed a polyethylene terephthalate felt separator between the Nafion membrane and Pt mesh cathode in order to prevent degradation of the Nafion on the cathode side of the cell due to transport of Pt particles from the Pt mesh anode to the cathode. As the cathode was no longer in contact with the Nafion membrane, dilute NaCl or Na_2SO_4 was employed as the catholyte. The authors reported a current efficiency of 20% at room temperature; a remarkably high value for Pt.

Unfortunately, there are a number of challenges to be addressed when employing zero gap cells with air-breathing cathodes.

In terms of the decreased cell voltage, in practice, kinetic realities mean that the overpotentials (the extra driving force required over and above the potentials predicted on the basis of thermodynamics) at anode and cathode can reduce this advantage. For example, any practical electrolysis cell will operate with air, rather than pure oxygen, at the cathode hence decreasing the maximum rate of the cathode reaction and increasing its overpotential.

Katoh et al.[44] highlight another problem associated with air breathing cathodes, which is that of flooding. Water balance in such electrodes is crucial[55] since water is produced at the cathode *via* the reverse of reaction (1.2); in addition, every proton drags between 1 and 5 water molecules with it as it passes through the polymer electrolyte membrane from anode to cathode (electro-osmotic drag[55, 56]). As a result, the pores of the cathode may become flooded with water, which blocks access to the oxygen gas and hence increases cell voltage (under constant current operation) or decreases current (under constant voltage operation). By employing a "water permeable, high performance gas diffusion" cathode, Katoh et al., reported that no flooding was observed, and the electrolyser operated at a current density of 1.0 A cm^{-2} and current efficiency of 16 – 17% for 85 days. However, this is the only such report in the literature.

Less obvious from the electrochemical ozone literature is the very serious problem of calcification[52, 57]: multiply charged ions such as Ca^{2+} and Mg^{2+}, which are present in hardwater, precipitate inside Nafion (probably near the cathode) as hydroxides and/or carbonates[58] causing a significant increase in membrane resistance and precluding the use of MEA-based cells to inject ozone directly into tapwater. Whilst the problem is mentioned explicitly by Nishiki et al.[52], and Valdes and Moussy[57], (the latter with respect to the use of Nafion in sensors for biological applications), and the use of "imitation" tapwater is reported by Kaneda et al.[59], and Awad et al.[60], the only indication that this is a serious problem is that all the other publications on MEA-based electrochemical ozone generation employ very low conductivity, de-ionised water and avoid using multiply charged cations where electrolyte is employed rather than electrolyte-free water.

Finally, the solubility of ozone in water depends upon pH[13-15], decreasing as pH increases. This can present additional problems when employing neutral anolytes as increased bubble formation at the electrode/Nafion interface has been postulated as having an adverse affect upon proton transfer into the Nafion membrane [50], increasing membrane resistance.

Presumably as a result of the challenges detailed above, by far most reports concern pure water and H_2 cathodes [17, 26, 30, 46-49, 60-62], with only Katoh et al.[44], and the Chan group[4, 50] reporting work on electrochemical ozone generation in zero gap cells using air cathodes, the latter operating at significantly lower current densities ($\leq$ 60 mA cm^{-2}) than the former due to limitations imposed by flooding[63].

In general, electrochemical ozone generation is carried out either in single pass/flow operation[50], or in batch recycle mode [17] in which the ozonated anolyte is returned to the electrochemical cell. In the former case, ozone is generated in both gas and liquid phases continuously; in the latter, once saturation of the anode solution has taken place, all the ozone produced is released into the gas phase. Under batch recycle operation, Stucki and co-workers employing PbO_2 in an MEA-based, zero gap cell found that inlet ozone concentrations of 5 – 25 ppm in de-ionised water had no effect on current efficiency [17]. In contrast, Christensen et al.[42], have reported that the current efficiencies observed during operation under flow conditions were consistently higher (> 30%) than those observed during batch recycle operation (3 – 8%). The authors employed Ni/Sb-SnO_2 anodes in a standard acid/acid cell, see fig. 1.4(b), and postulated that the presence of high concentrations of O_3 in aqueous sulphuric acid inhibits the O_3 evolution process at Ni/Sb-SnO_2 anodes, possibly by replacing key adsorbed intermediates by adsorbed O_3 [64].

1.1.3 The effect of temperature on the electrochemical generation of ozone

It was realised very early in the research on electrochemical ozone generation that low temperatures favoured higher ozone current efficiencies at Pt and Pt-based electrodes [38, 39, 65-67], an observation later confirmed using other anode materials; *e.g.* PbO_2 [25, 29, 68] and carbon [40]. However, some authors have reported that ozone efficiency at PbO_2 decreases with decreasing temperature,[46, 69]. Early workers took great care to cool the anode as it was generally believed that the anode temperature, rather than that of the electrolyte, was critical [29, 38, 39, 65], and that gas bubbles could adversely affect heat transfer[29, 39, 70-72]. Putnam and co-workers[38], Lash and co-worker [65], and Feng and co-workers[11] have reported that the real effect of current density on O_3 evolution is hidden by the secondary heating effect at higher current densities. Lash and co-workers[65] deconvoluted the two effects by effective (internal) cooling of their PtIr tubular anode and were able to show a linear relationship between log(current density) and current efficiency.

Briner et al.[66], electrolysed a 5.0 M H_2SO_4 solution using a Pt anode, obtaining a maximum current efficiency of 8.5% at -67 °C. Putnam et al.[38], obtained a maximum current efficiency of 19.4% by electrolysing a 30% $HClO_4$ solution at -50 °C using a Pt anode; however, they found significantly lower efficiencies using H_2SO_4 at temperatures down to -62 °C, in contrast to the results reported by Briner and co-workers. Interestingly, Putnam et al.[38], analysed the ozone evolved from their cells by liquefaction and measurement of the

boiling point; an interesting risk assessment to perform under current health and safety strictures.

In general, ozone efficiency falls dramatically as the temperature approaches room temperature when Pt anodes are employed[38, 39, 73], and the primary effect of increasing temperature on electrochemical ozone generation is generally accepted to be to increase the decomposition of O_3, at least at Pt anodes; this was first postulated by Fisher and co-workers in 1907 [70, 72]. In more recent papers and reviews of electrochemical ozone generation at a variety of anodes, this theory has remained unchallenged [7, 8, 11, 24-26, 29, 31, 32, 36].

1.1.4 The anode material

The anodes employed for electrochemical generation fall into two time periods: ≤ 1982 and > 1982. Up to 1982, the only anode materials that had been investigated were Pt and PbO_2 ([29] and references therein), and then only in aqueous acid electrolytes. After 1982, Pt ceased to be of interest (with one exception, see[54]) presumably due to the poor current efficiencies observed near room temperature when compared with, for example, PbO_2. Whilst β-PbO_2 continues to be researched with respect to electrochemical ozone generation (see, for example,[46, 74]) alternative materials have been investigated, including glassy carbon [40], Ni/Sb-SnO_2 [42, 75-77] , IrO_2-Nb_2O_5 [27, 37], tantalum oxide[12, 59], TiO_2 [78-80] and Boron Doped Diamond (BDD) [41, 45, 52, 61, 62, 81].

It is generally accepted that the most active of the α and β forms of PbO_2 is the latter[25]. A comparison of ozone evolution at 0 °C at PbO_2 anodes gives a fairly accurate view of the general activity of this material. In the absence of added F^- or fluoride-containing electrolytes, the current efficiencies observed at PbO_2 are ca. 3 - 10% at current densities of ca. 1.0 A cm^{-2} in aqueous H_2SO_4 or $HClO_4$ [7, 10, 29, 36]. Addition of NaF increased current efficiency to 21% [10] or 10% [8], and in 7.3 M HPF_6, an efficiency of ca. 50% was observed at -65 ºC by Foller and Tobias [29],

IrO_2-Nb_2O_5 shows a very low ozone current efficiency at 0 °C in 3.0 M H_2SO_4, *ca.* 1%, rising to *ca.* 12% at 800 mA cm^{-2} in the presence of 0.03 M KPF_6 [37]. Using a layered anode formed on Si and exposing TiO_2 to the 0.01 M $HClO_4$ solution, Kitsuka et al. [79] have reported a current efficiency of *ca.* 9% at 50 mA cm^{-2} and 15 °C. Tantalum oxide-based anodes have shown a current efficiency of *ca.* 12% at room temperature and 200 mA cm^{-2}

using model tap water at neutral pH.

Boron doped diamond electrodes remain something of an enigma in the field of electrochemical ozone generation in that it is not entirely clear that they can be expected to generate ozone routinely. Typically, BDD electrodes are grown on suitable substrates (Ti, Ta, Mo, glassy carbon and, most generally, Si) by chemical vapour deposition, doping with boron decreases the resistivity of the semiconducting diamond, with *ca*. $10^{20} – 10^{21}$ B atoms cm^{-3} giving a resistivity of ca. 10^{-3} Ω cm [82]. BDD anodes show high anodic stability and a wide potential window for water discharge (high overpotentials for water reduction and oxidation); they are regarded as essentially inert and with poor adsorptive qualities such that electron transfer takes place *via* outer sphere reactions[82]. In terms of water treatment, rather than as ozone-generating anodes, BDD electrodes are generally regarded as oxidizing organic molecules by direct electron transfer at potentials below oxygen evolution and indirectly *via* OH radicals at higher potentials [82, 83], produced *via* the primary water discharge reaction[10, 84, 85]. The number of papers reporting O_3 generation is relatively few (see, for example, [41, 45, 52, 61, 62, 81]) compared to the very large number of papers on direct/indirect combustion (see, for example,[73], and the extensive work by Ch. Comninellis and co-workers[83] and references therein). Michaud and co-workers[41, 86] reported that the main product of water electrolysis in H_2SO_4 is peroxydisulfate ($S_2O_8^{2-}$), and in $HClO_4$ it is oxygen. Both Katsuki et al.[81] and Michaud et al.[41] report ozone current efficiencies of a "few percent" electrolyzing aqueous acid in divided cells. In contrast, Kraft et al.[62] and Arihara et al. [45, 61] electrolyzed de-ionized water (< 1 µS cm^{-1}) using zero gap cells with Nafion membranes and obtained maximum current efficiencies of 24% and 47%, respectively. Given the small number of papers to consider, the drawing of detailed conclusions is of questionable validity, but it may be that anion adsorption disfavours the production of ozone at BDD anodes, eg. by inhibiting reactions (1.11) and/or (1.16) above via interference of anions in the encounters between active oxygen species[61]. The exception to this postulate is the work reported by Nishiki et al.[52], who observed a relatively low current efficiency in "pure" (source unspecified by the authors) water (13%) as well as in tapwater containing calcium and magnesium salts (6%); however, this work is unusual for several reasons and hence is dealt with in detail below.

Kraft et al.[62], employed BDD-coated niobium expanded metal electrodes (29 mm x 45 mm) as anode and cathode, pressed either side of a Nafion membrane positioned in a pipe flow-

through reactor, with only the solution ozone being monitored by the indigo method[87]. Higher flow rates gave higher current efficiencies, the maximum efficiency of 24% being observed at a flow rate of 40 dm^3 hr^{-1} and 115 mA cm^{-2}; this was attributed to more ozone being entrained at higher flow rates, as well as cooling effects reducing the thermal decay of O_3 (as usual with BDD electrodes, high cell voltages were required, *eg*. 23V at 383 mA cm^{-2}, leading to the very real possibility of local heating effects). Increasing the conductivity of the anolyte feed was found to cause a marked drop in ozone current efficiency, *eg*. at a flow rate of 10 dm^3 hr^{-1} and 77 mA cm^{-2}, the current efficiency dropped to ca. 2% when the conductivity was increased from 1 to 2000 µS cm^{-1}, *ie* comparable to the efficiencies observed by Michaud et al.[41] and Katsuki et al.[81], in their studies employing acid electrolytes. This was attributed by the authors to more of the BDD surface becoming electrochemically active as the conductivity of the anolyte increased, and hence the real current density decreasing.

Arihara and co-workers [45, 61] have reported the generation of ozone at 50 mm x 15 mm x 2 mm free-standing, perforated BDD plate anodes, see fig. 1.6. The BDD anode and Pt mesh cathode were pressed either side of a Nafion membrane. Deionised water (< 1 µS cm^{-1}) was employed as the catholyte and anolyte, with the ozone being monitored only in the solution phase by spectrophotometry. At an anolyte flow rate of 2 dm^3 min^{-1}, anolyte temperature of 12 °C and 530 mA cm^{-2}, the authors reported an optimum current efficiency of 47%, a very significant achievement. However, the cost in terms of energy usage was high since cell voltages of 22 – 24 V were required, equating to 175 kWh per kg O_3 at 530 mA cm^{-2}; this does not compare well with the standard method of generating ozone, cold corona discharge, the optimum energy consumption of such systems is often quoted as being between 13 and 29 kWh kg^{-1} [13], or even as low as 8 kWh kg^{-1} [88], a fact the authors themselves highlight. At higher current densities, the efficiency was found to decrease; the authors interpreted this in terms of more partition of ozone into the gas phase, increased autolysis due to the increased solution concentration and an increase in side reactions such as the production of hydrogen peroxide. The latter has been reported as increasing the decay of ozone, catalysed by glass reactor walls [89], due to reactions such as:

$$H_2O_2 + O_3 \rightarrow HO^{\cdot} + HO_2^{\cdot} + O_2 \qquad (1.18)$$

Nishiki and colleagues employed a 40 mm long, 2 mm diameter BDD rod anode, wrapped in Nafion strips over which was coiled a stainless steel wire cathode, see fig. 1.7; this

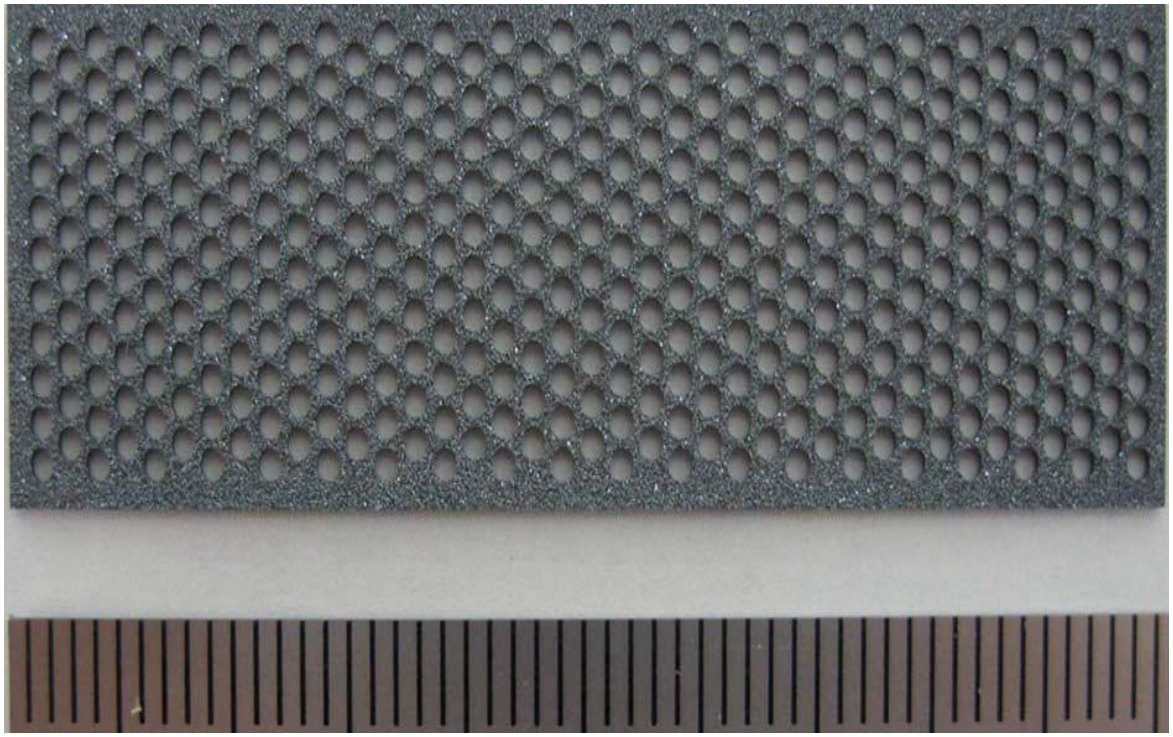

Figure 1. 6. Photograph of an example of the free-standing, perforated Boron Doped Diamond electrodes employed by Arihara and co-workers [45, 61].

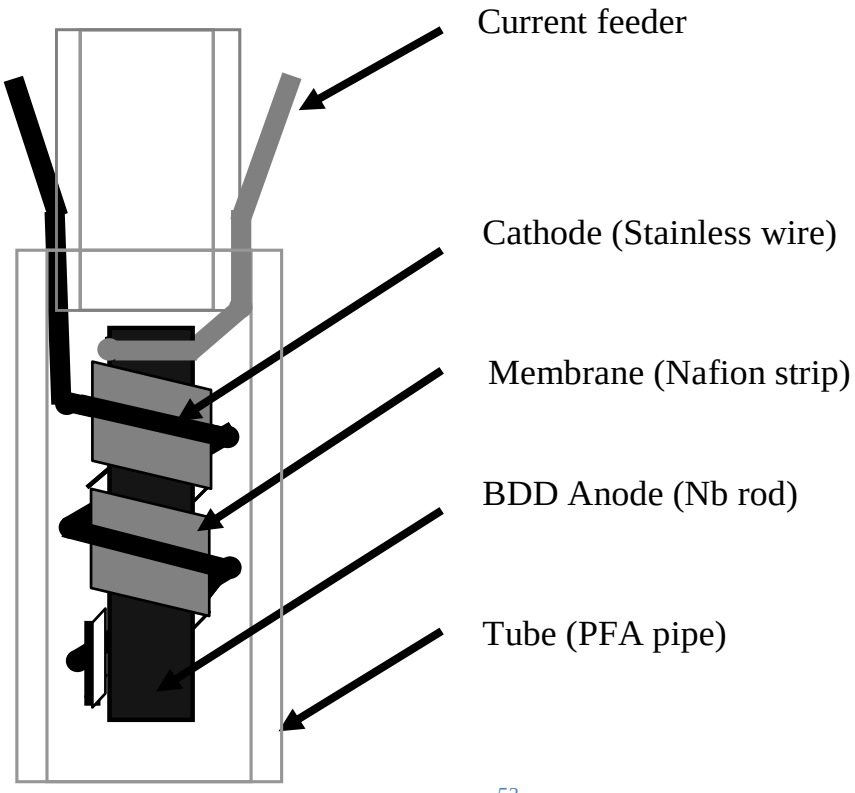

Figure 1. 7. The cell employed by Nishiki et al [52].

was mounted inside a 4 mm inside diameter tube to form a flow cell[52]. Presumably, the anolyte contacts the BDD/Nafion water interface at the edges of the strips (which are not presented as wound so as to completely cover the BDD rod) or the ozone is generated at the BDD/Nafion interface directly below the wire counter electrode (as would be expected on the basis of electric field considerations) then diffuses through the Nafion to the Nafion/water interface. However, the latter process would enhance the expected dehydration of the BDD/Nafion interface due to water discharge and the electro-osmotic effect[55, 56].

In any case, the actual active area of the anode was unclear. It appeared that the ozone + oxygen generated at the anode and hydrogen generated at the cathode were allowed to mix; again, this was not explicitly stated. The authors employed tapwater (Fujisawa City, total hardness 70 mg dm^3, chloride concentration 10 mg dm^3), and tapwater with added Ca^{2+} (as $CaCl_2$, to assess the effect of hardness) or Cl^- (as NaCl); they also used 'pure' water, but the source and composition of this was not specified. The calcification of the membrane was assessed by the mass change after 2 hours electrolysis, with no mass change being observed in the case of pure water. In tap water, at a constant current of 0.8A and cell voltage of 16 V, the authors observed a current efficiency of 2.5%; under the same conditions, "pure" water gave 8% current efficiency at 10 V. The cell voltage increased from ca. 3 V at 0.2 A to 16 V at 0.8 A.

The authors found that the current efficiency was lower in the more conducting tapwater than in pure water, see table 1.1, which shows data obtained as a function of flow rate at 0.75 A. This was attributed to two primary effects: (1) more of the BDD electrode becoming electroactive and hence a decrease in current density, as was postulated by Arihara et al.[45, 61], and (2) competition from the generation of chlorine-containing products *via* the oxidation of chloride ions. The latter was supported by UV Vis data.

Source	Flow rate/ cm^3 min^{-1}	Current efficiency/ %	O_3 concentration/ mg dm^{-3}
Pure water	40	7	6
	250	10	2.5
	400	13	1
Tap water	40	2.5	2
	150	4.5	1
	400	6	0.5

Table 1. 1. Typical performance of the BDD cell employed by Nishiki and co-workers [52].

Figure 1.8 shows the variation in cell voltage and solution ozone concentration observed by Nishiki et al.[52], as a function of hardness (as added $CaCl_2$, although the exact definition of hardness as mg dm^3 was not specified by the authors, nor was the flow rate specified). The cell voltage increased very little with hardness (albeit already high at 12 – 15 V); however, the membrane was found to increase in mass following 2 hours electrolysis at 1 A, see fig. 1.9. The mass gain, due to calcification, was found to decrease as flow rate increased, attributed by the authors to physical removal of the deposit. Interestingly, when the cell was operated with the current on for 8 minutes and off for 2 minutes, a marked decrease in calcification was observed, see fig. 1.9; the authors postulated that this was due to the cathode pH decreasing back to neutral during the 'off' periods and facilitating dissolution of the scale.

Durability studies over 250 hours electrolysis under constant and interrupted current conditions supported the benefits of on/off operation, with the ozone current efficiency remaining constant at around 3% under current interrupt operation, whereas it fell steadily to < 1% at constant current.

The high cell voltage and low current results in a very high energy cost, *eg*. 1675 kWh kg^{-1} O_3 under current interrupt operation. Nevertheless, the authors believe the system to have

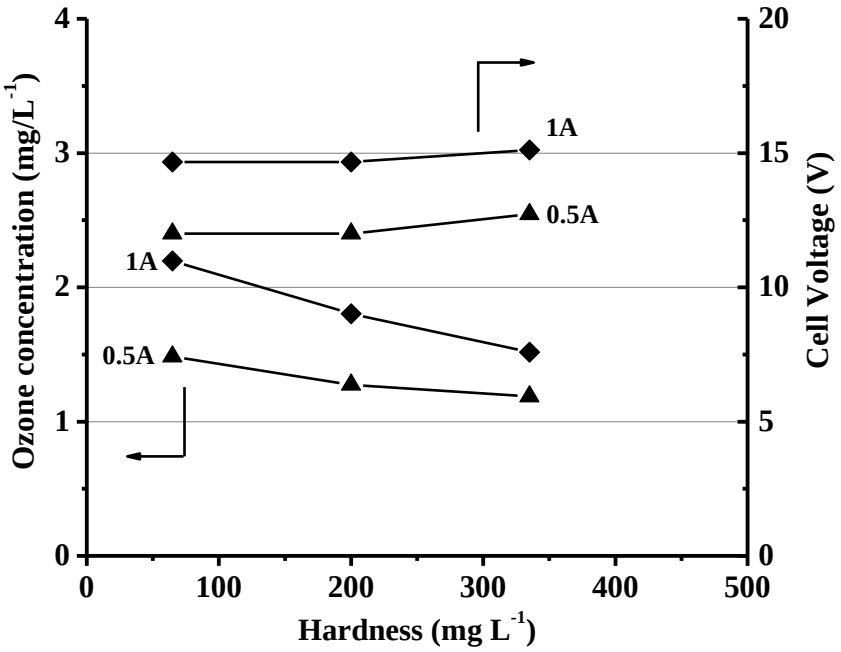

Figure 1. 8. The dependence of ozone concentration and cell voltage on hardness observed by Nishiki et al [52].

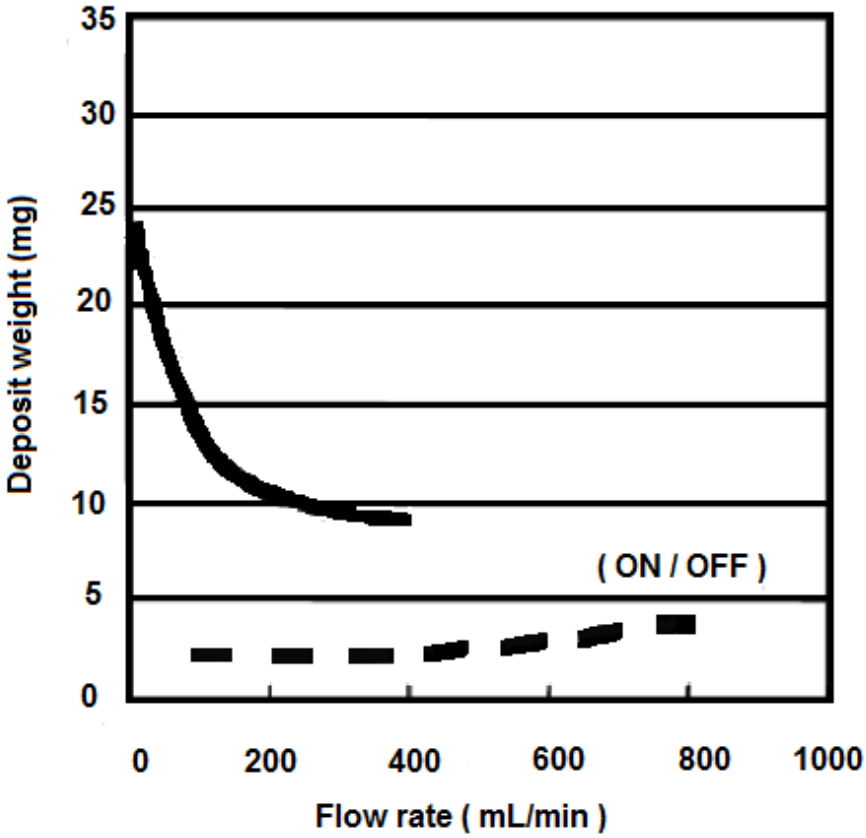

Figure 1. 9. The increase in mass of the Nafion membrane employed by Nishiki and co-workers [52] following 2 hours electrolysis at 1 A under constant current operation, and with current on for 8 minutes and off for 2 minutes.

real application, and reported data on the disinfection of water inoculated with *Pseudomonas aeruginosa*, *Escherichia coli*, and *Staphylococcus epidermidis*. They also employed the cell to treat 43 dogs and 10 cats suffering from Superficial Pyoderma and Seborrhea.

To date, there are only two anode materials that have been reported as generating ozone at current efficiencies > 20%, temperatures > 0 °C and in water, or water with non-fluoride electrolyte; the first is BDD [41, 45, 52, 61, 62, 81] and the second is Ni/Sb-SnO_2 [4, 42, 50, 64, 75-77, 90-93]. In 2004, Prof. K. Y. Chan of Hong Kong University [93] reported (incorrectly) that his group had generated ozone from 0.64 cm^2 Sb-SnO_2 Ti foil electrode in 0.1 M $HClO_4$ in a UV-Vis cuvette electrochemical cell, see fig. 1.10, with a maximum current efficiency of 15% at cell voltages < 3 V. In a second paper[75], it was reported that the activity of the anodes reported in the first publication was due to adventitious Ni. This latter paper detailed the preparation of Ni/Sb-SnO_2 electrodes and reported a maximum current efficiency of 35%, again using the UV-Vis cuvette cell. There had been one previous report of ozone

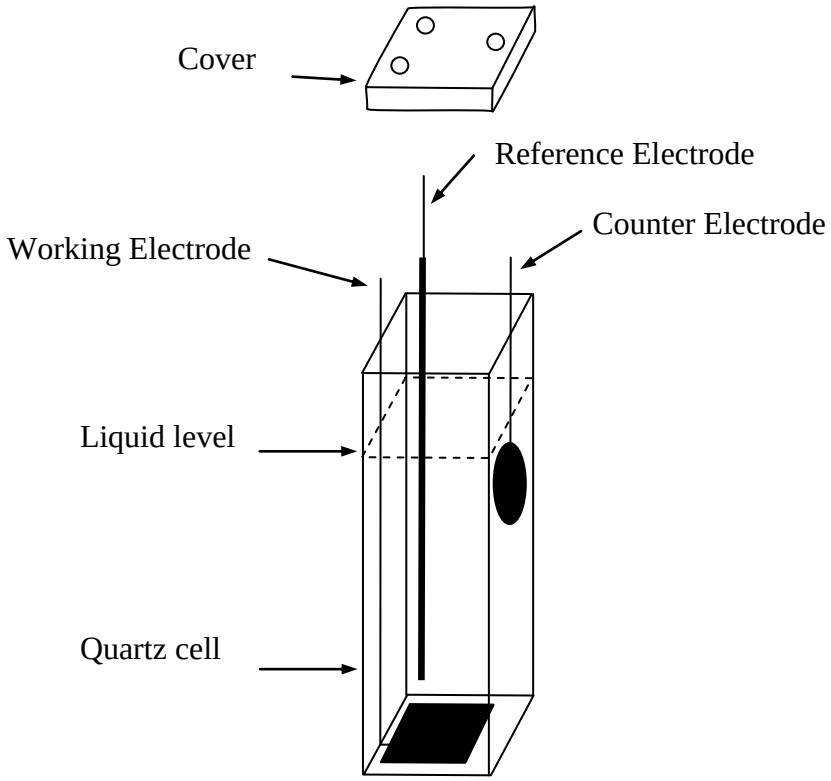

Figure 1. 10. Schematic of the electrolysis UV cell employed by Wang et al. showing the arrangement of the working electrode, reference electrode, and the counter electrode. From [75].

generation at Sb-SnO_2/Ti mesh by Foller and Tobias[29]; the authors reported a maximum current efficiency of *ca.* 4% in 5.0 M H_2SO_4 at 0 ºC, which was short lived, due to dissolution of the electrode. Otherwise, Sb-SnO_2 electrodes are generally considered not to be ozone active. In general, Sb-SnO_2 anodes supported on Ti are associated with the direct, electrochemical oxidation of organics[85]. Hence, the production of very high O_3 activity at low cell voltages under ambient conditions and in a simple electrolyte through the addition of small amounts of Ni to Sb-SnO_2 is truly remarkable, and could not have been predicted. In a later paper, Christensen et al.[42], reported current efficiencies up to 50% (equivalent to 18 kWh kg^{-1} O_3) employing Ni/Sb-SnO_2 anodes with platinised Ti mesh cathodes in a divided glass cell utilizing a Nafion membrane separator and 0.5 M H_2SO_4 as the electrolyte. More recently, Parsa and Abbasi[90] reported a maximum ozone current efficiency of 53.7% using 6.3 cm^2 Ni/Sb-SnO_2 Ti mesh anodes in acid solution, no current density data were provided. However, the cell employed was an open beaker, and no experimental details were given as to precisely how the ozone measurements were made. Further, on the basis of the data presented in the paper, the extinction coefficient employed by the authors for the absorption of ozone at 258 nm was 4700 M^{-1} cm^{-1}, significantly

higher than the values typically employed in the literature of 3100 ± 200 M^{-1} cm^{-1} [18, 19, 22, 61, 62, 89, 94, 95] and that recommended by the International Ozone Association of 3000 M^{-1} cm^{-1} [18]. Parsa and Abbasi appear to have employed the erroneous value of the extinction coefficient used by Wang et al.[75]; this group later employed a value of 2900 M^{-1} cm^{-1} [50]. In addition to the incorrect extinction coefficient, the ozone absorption peaks observed by Parsa and Abbasi[90] deviated from Gaussian shape at higher ozone concentrations. Finally, the maximum of 53.7% current efficiency was seen only as a single data point, with the efficiencies tending toward steady state values < 20%. Hence, the claim by the authors of such a high efficiency is somewhat suspect.

In 2006, the Hong Kong group reported the electrochemical generation of ozone in deionised water and the cathode was operated in 'passive' mode, *ie*. without pumping air past it. A maximum current efficiency of 15% was observed at a cell voltage of 2.0V, whilst the lowest energy consumption was 48 kWh kg^{-1}, also at 2.0V, and 17 mA cm^{-2}. The current density being limited principally by cathode flooding.

In a later paper [50], the Hong Kong group reported data on a scaled up cell and 4 cell stack. The anodes were Ni/Sb-SnO_2 coated Ti mesh (8 cm x 13 cm), and the cell & stack operated in both passive and forced airflow (10 dm^3 min^{-1}). The single cell, 4 cell stack and balance of plant are shown in figs. 1.11(a) – (c), respectively. Deionised water (18.2 MΩ cm) was fed to the anode(s) at flow rates from 0.2 to 4.0 dm^3 min^{-1} (linear velocities from 0.52 to 10.42 cm s^{-1}).

Ozone was monitored using a flow cell linked by fibre optic cables to a spectrophotometer. Typical spectra so obtained are shown in fig. 1.12; as may be seen, the peak due to ozone (λ_{max} = 258 nm) was superimposed upon a significant baseline offset and an underlying absorption having a peak < 250 nm. The baseline offset was attributed to bubbles scattering the incident light; Arihara et al.[45] observed the same problem and employed a reservoir before the UV Vis cell in order to allow gas release. The authors did not discuss the underlying absorption, and it is not possible from the data presented in the paper to identify if the absorption showed a maximum. However, as stated above, H_2O_2 is an expected side product of electrochemical ozone generation, and has an absorption below *ca*. 350 nm with no maximum above 200 nm [64, 96, 97].

The current densities employed by the authors (< 60 mA cm^{-2}) were again limited by

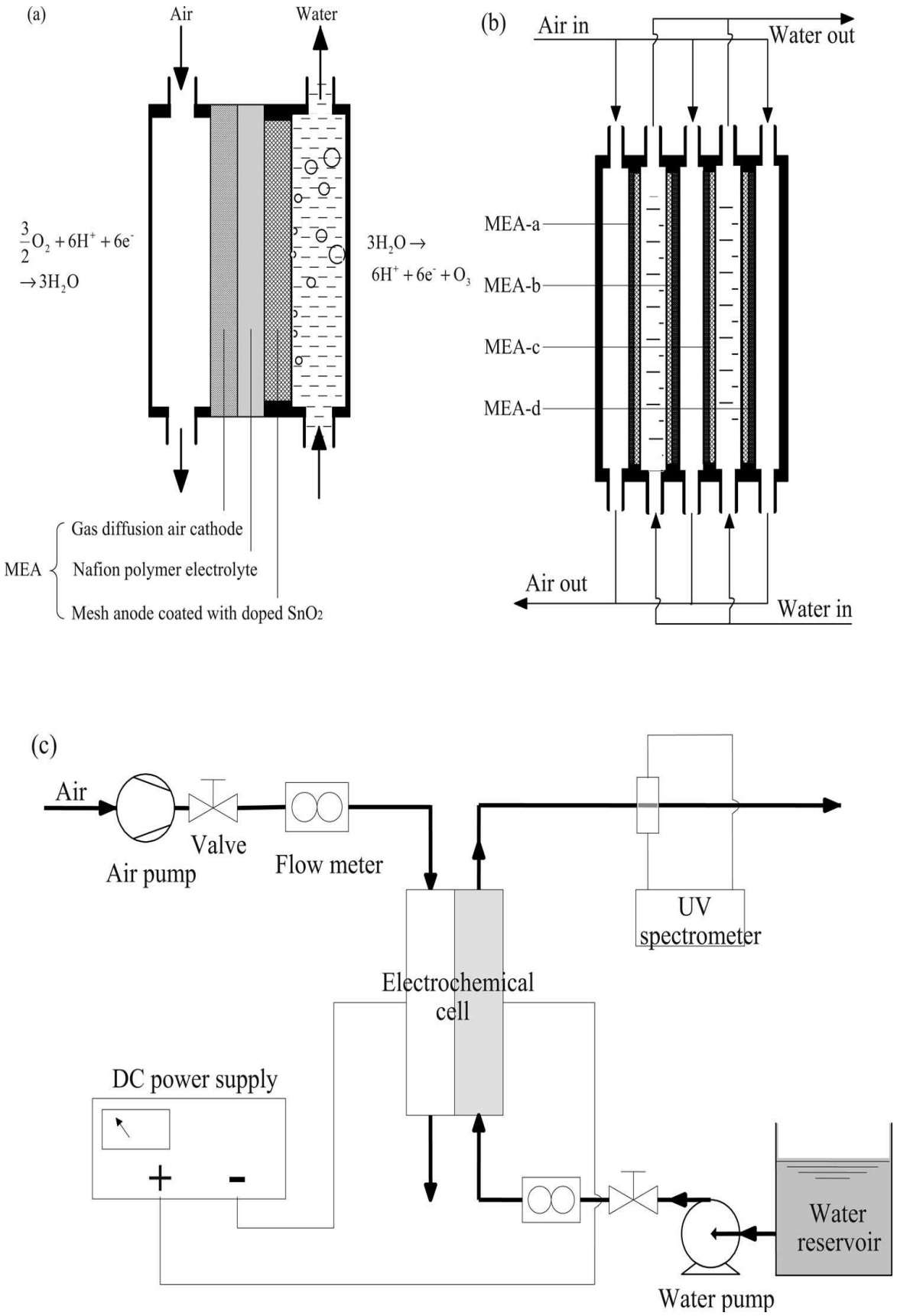

Figure 1. 11. (a) The single cell, (b) 4-cell stack and (c) balance of plant employed by Cui et al[50].

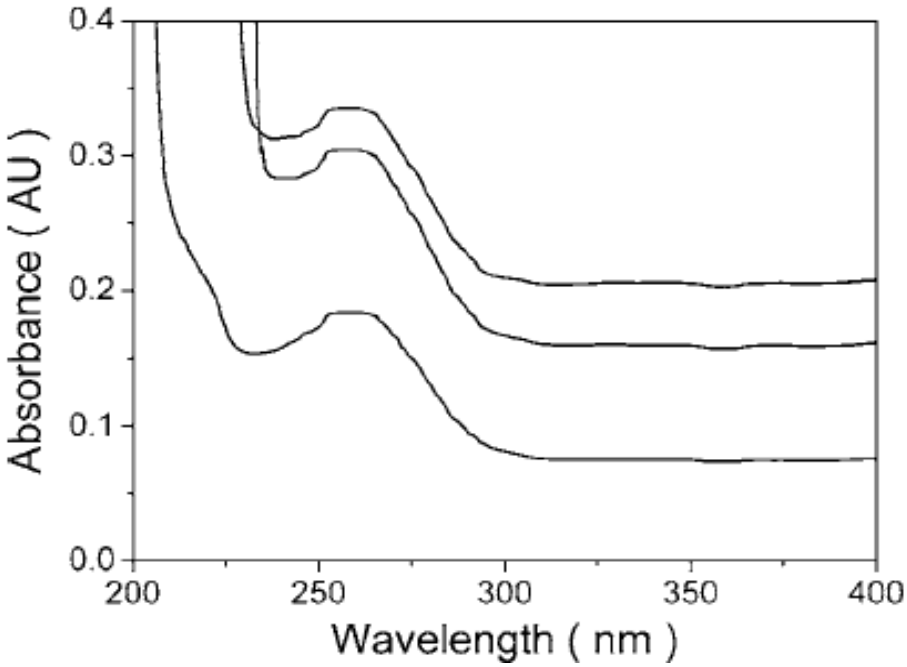

Figure 1. 12. Typical spectra obtained during the operation of the flow cell. (from Cui et al. [50])

flooding [63], with cell voltages between 3 V and 6 V for the single cell. The four cell stack gave a maximum current efficiency of *ca*. 22% at an anolyte flow rate of 5.9 dm^3 min^{-1}, 29.8 mA cm^{-2} and 3.0V; the lowest energy consumption was 42 kWh kg^{-1} O_3 at 24.3 mA cm^{-2} and 5.4 dm^3 min^{-1}. The energy requirement is the lowest of MEA-based cells (injecting ozone directly into water and either air breathing or hydrogen evolving), thus: Katoh and co- workers[44] (maximum current efficiency 19%, PbO_2 anode) obtained an energy requirement of 40 – 50 kWh kg^{-1} O_3 (pure oxygen feed) or 60 – 80 kWh kg^{-1} O_3 (hydrogen evolved), Stucki and co-workers using a commercial Membrel electrolyser (20% maximum current efficiency, PbO_2 anode, commercial since the early 1980's, hydrogen evolving;[31]) obtained an energy requirement of 65 kWh kg^{-1} O_3; more recently, Da Silva and co-workers[46], reported an energy requirement of 70 kWh kg^{-1} O_3 (13% efficiency, PbO_2 anode, H_2 evolving cathode). In contrast, Arihara and co-workers[45] obtained an energy cost of 140 kWh kg^{-1} O_3 at the maximum current efficiency of 47%, reflecting the significantly higher cell voltages required when using BDD anodes. In general, PbO_2 and BDD systems operate at current densities of *ca*. 1 A cm^{-2}; in contrast, Ni/Sb-SnO_2 –based systems operate at < 100 mA cm^{-2}; hence the latter generate less O_3 per cm^2 than the former two.

The Hong Kong university group used an Electro Deposited Inter Layer (EDIL) with the aim of improving the service life (durability) of their ozone anodes. The "service life" of

Sb-SnO_2/Ti anodes is typically defined as the time taken for the anode potential to rise to 5.0 V vs. the reference electrode, where Ding et al.[98] reported a service live of less than an hour. Montilla et al.[99] attributed this short durability to the oxidation of the Ti substrate to TiO_2. Chan and co-workers[100] employed 8 dip-coats as this suggesting the Ti substrate was fully covered. However, the work by Montilla et al.[99] discovered that durable anodes cannot be achieved by thick catalyst coatings alone.

Correa-Lozano et al.[101] reported an increase of the durability of Sb –SnO_2 anodes by ca. 2 orders of magnitude when an IrO_2 interlayer was deposited by thermal decomposition. In addition, Chen and Nigro[102] postulated that the 12-fold increase in electrode life was due to protection of the Ti substrate by the Au interlayer (a sputtered, nanoscale gold film).

The interlayer must adhere to both catalyst and Ti substrate, be electronically conductive and non-porous, and preferably have a high oxygen overpotential. The Hong Kong group used electrodeposited interlayer (EDIL) from a solution of $SnCl_4.5H_2O$ + $SbCl_3$ + HCl in ethanol based on the work of Li et al.[103].

1.1.5 The effect of current density

In general, at PbO_2 anodes, current efficiency increases essentially linearly with current density [11] before levelling out and becoming independent [29-31, 46, 47, 49]; typically, the current density at which this change occurs is *ca.* 1.0 A cm^{-2}, but this value depends upon the electrolyte composition[29]. Exceptions to this observation are Onda and co-workers [48] and Awad and co-workers[74], both groups observe current efficiency to go through a maximum, at around 1.0 A cm^{-2} and 1.5 - 2.0 mA cm^{-2} (respectively), before decreasing.

Boron doped diamond anodes show similar behaviour to PbO_2, with current efficiency becoming independent of current density [45] or showing a clear maximum[62]. TiO_2 [78, 79], Pt [39], C [40] and TaO_x [12, 59] show increasing current efficiency with current density; however, this may simply reflect the fact that, should the current density have been increased beyond the maximum employed by these workers, a levelling out or decrease in current efficiency may have been observed. IrO_2-Nb_2O_5 shows an onset current density for ozone evolution that varies with IrO_2 content [37]. Ni/Sb-SnO_2 electrodes show a clear maximum [4, 75].

When employing zero gap cells with low conductivity (*eg*. de-ionised) water as the anolyte, the active area of the anode is significantly less than its geometric area, since the former will be only that region of the anode at the boundary with water and the Nafion membrane.

Hence, the actual current density will be higher than that calculated on the basis of the geometric area[62]; one consequence of this is that, if the conductivity of the anolyte is increased, current efficiency decreases due to the decrease in current density as more of the anode becomes active [40, 61, 62].

To date, there are no reports in the literature in which current efficiency vs current density data are modelled on the basis of a detailed, mechanistic framework.

1.1.6 The effect of electrolyte

As it is generally believed that ozone efficiency increases with decreasing pH[7, 13, 75], most of the papers in the electrochemical ozone literature concern ozone generation using either aqueous acid electrolytes or, to a lesser extent, using Nafion as an (acidic) polymer electrolyte membrane, (Nafion is also commonly employed as the cell separator in the studies using acidic electrolytes). There are a few studies on the effect of the anion on ozone efficiency in acid solution. By far the most comprehensive work on this was reported by Foller and Tobias in 1982 [29]. The authors found a linear relationship between ozone current efficiency in 2.0 M acid at 0 °C using β–PbO_2 anode and the "composite electronegativity" of the anions. The composite electronegativity was obtained by summing the tabulated electronegativities of the individual atoms of the anion. The data were rationalised essentially in terms of a model similar to that elucidated above (see equations (1.10) – (1.17)), in which one of the active intermediates in the formation of O_3 is the adsorbed oxygen atom. Quite simply, anion and oxygen coverage are competitive, with the former determined by the electronegativity of the anion: the more electronegative the less adsorption takes place. Thus, at high anion coverage, the free energy of adsorption of $O^{\cdot}$ is too low and the activation energy for $O^{\cdot}_a + O^{\cdot}_a \rightarrow O_2$ is so low that O_3 does not have time to form. Conversely, too little anion adsorption causes the O atoms to be bound too tightly. However, the authors also commented that, due to the evolution of gas, the free energy of adsorption of the O atom would actually assume a broad range of values. An ideal anion coverage, specific for a particular electrolyte and anode material, would then produce the maximum possible ozone efficiency for that combination. Anions such as F^- that are non-adsorbing may never show such a maximum in efficiency as 'optimum' surface coverage is never reached. The authors also postulated that F^- could inhibit the discharge of water (to O_2) by hydrogen bonding to the H atoms of water in the Inner Helmholtz Layer.

There does not appear to be any detailed later studies on the general effect of anion adsorption on electrochemical ozone generation in acid solution; studies in acid electrolyte focus primarily on the effect of F^- or F-containing electrolytes *e.g.* [8, 10, 25, 36, 37]. Da Silva and co-workers [8, 29] re-iterate the postulate of Foller and Tobias that F^- stabilises the coverage of adsorbed oxygen atoms as well as inhibiting the oxygen evolution reaction.

With respect to the effect of common acid electrolytes on ozone current efficiency, this appears, as expected, to depend upon the anode material, thus Franco et al.[104] found that the ozone current efficiency at a β–PbO_2 anode was 3.5% in 6.0 M $HClO_4$ compared to 2.9% in 3.0 M H_2SO_4. Wang et al.[75] observed a current efficiency of *ca.* 35% in 0.1 M H_2SO_4 and *ca.* 32% in 0.1 M $HClO_4$ at a Ni/Sb-SnO_2 anode. At -50 °C at a Pt anode[38], the current efficiency was *ca.* 20% in 30% $HClO_4$ and *ca.* 6% in 28% H_2SO_4. However, Kötz and Stucki[10] observed a complex dependence of ozone efficiency at 1 A cm^{-2} when using 3.0 M $HClO_4$, H_2SO_4 and H_3PO_4 as a function of temperature. Ozone efficiency at fixed current density generally goes through a maximum as the concentration of the acid electrolyte is increased[29, 75].

A number of studies have been reported using aqueous electrolytes at near neutral pH [11, 50, 51, 86-88] with ozone current efficiencies of 5-12%, including work using imitation tap water, aimed at the potential application of electrochemical ozone generation in water treatment [59, 61]. Feng et al.[11] obtained ozone current efficiencies of 6% and *ca.* 14% using β-PbO_2 anodes without and with Fe doping, respectively, in pH 7.5 phosphate buffer at 10 °C . El-Shall et al. [105] observed a maximum current efficiency of 7% at PbO_2 in pH 7 phosphate buffer. Kaneda and co-workers[59] have studied anodes based on tantalum oxide in imitation tap water, *i.e.* Millipore water containing added Na^+, Ca^{2+}, K^+ and Mg^{2+} salts to a conductivity of 160 μs cm^{-1}. The authors observed a maximum ozone current efficiency of *ca.* 12%, comparable to that observed by Feng et al. [11] using Fe-doped β-PbO_2. To date, there have been no attempts to discuss the implications of such high ozone efficiencies obtained in neutral solution.

Low temperatures are often employed in conjunction with fluorine-containing anions to obtain high ozone current efficiencies[10, 27, 29, 32]; as was stated above, this is generally believed to be due to the ability of small amounts of F^- to raise the oxygen overpotential[29] and was first reported in 1950 by A. Hickling and S. Hill[106], although it has also been

postulated that F^- stabilises the coverage of singlet oxygen at PbO_2, enhancing the production of O_3 [8]. Thus, PbO_2 at 0 ºC typically exhibits current efficiencies of 10-12% in the absence of specialist anions, this increases up to *ca.* 20% in the presence of PF_6^- at the same temperature[29]. Foller and Kelsall [40] reported a current efficiency of 45% using glassy carbon electrodes at -5 ºC in 62 wt% HBF_4; however, the very high concentration of HBF_4 employed required that it was especially synthesised and also resulted in intermittent passivation of the electrode which could only be reversed by periodic switching to open circuit potential. F^--doping of PbO_2 anodes to inhibit O_2 evolution and hence improve ozone current efficiency has also been employed see, for example, the work by Amadelli et al.[107] who obtained a maximum current efficiency of *ca.* 8% at 25 ºC in 1 M H_2SO_4, using PbO_2 anodes formed by electrodeposition from solutions containing 0.01 M NaF. Higher F^- concentrations in the electrodepostion solution caused the ozone efficiency to decrease, reaching 1% at 40 mM NaF. The latter observation was interpreted by the authors as higher F^--doping of PbO_2 facilitating the formation of persulfate ions at the expense of O_3.

1.2 Commercial Technology for Ozone Generation

Ozone production by the electrolysis of water has a number of advantages including: simple and robust system design and low voltage operation. However, despite the advantages of electrochemical synthesis, the current, dominant commercial technology for ozone generation is Cold Corona Discharge (CCD) first reported by Siemens in 1857 [108]. This technology has a number of disadvantages, including: (i) low concentration of ozone in the output, in the range of 2% to 12% by volume; (ii) CCD generators require cold, dry and pure O_2, if air is employed the O_3 concentration and production efficiency are significantly reduced and nitrous oxides produced[13]; (iii) CCD generates only gas phase O_3, which is difficult to dissolve for aqueous applications[13] and (iv) CCD requires high voltage (kV range) power supplies.

1.3 Dye Wastewater Decolourisation

1.3.1 Dye wastewater

Dyes find extensive use in a wide range of applications, from tanning to hair colouring, and the annual production of these materials is estimated at over 7×10^5 tons per annum [85, 109-112].

The main characteristic of dyes is the chromophore group which includes: azo (– N = N –), anthraquinone, indigoide, triphenylmethyl, xanthene, sulphur and phthalocyanine

derivatives[113]. A polyaromatic structure, high molecular weight and atoms of nitrogen, sulphur and metals are characteristics of most dye molecules[114]. Dyes can be reactive, direct, etc according to the method by which they are fixed on fibres[115]. In addition, reactive dyes (which include azo, anthraquinone dyes) are designed to improve colour fastness as they have functional groups in their structure which form a covalent bonds with fibres[116, 117].

Synthetic dyes can cause considerable non-aesthetic pollution and public concern and are serious health-risk factors due to their large-scale production and extensive application as well as their release into the environment [85, 109, 112, 113, 118]. Over 20-25 % of reactive dyes are lost from the dyeing process and leave with the wastewater[117].

Conventional wastewater treatment plants are not able (in most cases) to decolourise dye – containing wastewaters due to the high stability of dyes under sunlight and resistance to microbial attack and temperature[85, 111, 112, 114]. Hence, the search for powerful and practical methods and technologies for the decolourising and degradation of dye – containing wastewaters has become the focus of increasing interest. Some of the methods of interest include physico-chemical and chemical methods, advanced oxidation processes (AOPs), biological techniques, membranes (nanofiltration, reverse osmosis etc) and electrochemical technologies [85, 110-112, 119].

1.3.2 Electrochemical decolourisation

To date, electrochemical technologies have developed such that they are more efficient and more compact than other technologies, but cost is still an issue [112, 117]. Highly efficient chemical oxidants such as ozone, hydroxyl radicals or hydrogen peroxide can be generated electrochemically [120]. For some industrial wastewaters, electrochemical technologies may be the indispensable step in the treatment of refractory pollutants [121]. The main advantage of electrochemical methods is that added chemicals are not required and sludge is not produced [111].

Electrochemical oxidation is the most popular electrochemical procedure for removing organic pollutants from industrial wastewaters[85], and it has recently been used for decolorizing and degrading dyes in aqueous solution[85, 122]. The electrochemical oxidation of pollutants can be either direct or indirect[85, 122]. During indirect oxidation, which take place near the anode surface, two main processes occur: (i) electrochemical conversion, in

which organics are oxidised selectively to biodegradable compounds, usually carboxylic acids and (ii) electrochemical combustion (or electrochemical incineration), where organics are completely mineralized, i.e. oxidized to CO_2, H_2O and inorganic ions[123, 124]. In direct electro-oxidation, organics are attacked at the anode surface by chemisorbed, active oxygen which causes incomplete degradation of the organics[124, 125].

The OH radical, a highly efficient, non – selective oxidising agent with oxidation potential of 2.8 V vs NHE[85], can undergo side reactions including the generation of oxygen, ozone and hydrogen peroxide, etc which will consume the OH radicals and reduce the organic oxidation current efficiency[85].

It has been found that the nature of the anode material influences strongly both the selectivity and efficiency of the electrochemical oxidation process. Comninellis[125] explained the different behaviour of electrodes in electrochemical oxidation dividing the elcectrode in to two types: active and inactive. Typical examples for the former are Pt, IrO_2 and RuO_2 [85, 119, 126]and PbO_2, SnO_2 and BDD for the latter[85, 119, 126]. The inactive electrode does not participate in organic oxidation and does not provide any catalytic active site for organic adsorption from the aqueous medium[85, 119, 126]. It only acts as an inert substrate and as a sink for the removal of electrons, whereas the active anodes do participate in organic oxidation and the oxidation byproducts adsorb on the anode surface[85, 119, 126].

1.3.3 Decolourisation by ozone

Ozone is well known as a highly efficient oxidant that is used in treating water and wastewater[127] which reacts with a large number of organic compounds either by direct oxidation as molecular ozone (in acidic solutions) or by indirect reaction through formation of secondary oxidants like hydroxyl radicals (in alkaline solutions)[114, 128, 129]. To achieve as high as 90 % transfer efficiency of the ozone to the water, a conventional fine bubble contactor (column reactor) is the most widely ozonation reactor used[130].

As the water quality standards are increasing, the use of ozonation in the treatment of dye – containing wastewater is increasing, where ozone attacks the dye molecules and destroys the carbon-carbon double bonds and other functional groups of the molecules[114, 129], and causes the decolourisation[129].

The main parameters that affect colour removal by ozonation are dye concentration (greater dye concentration results in more ozone consumption which in turn enhances mass

transfer that causes more ozone to dissolve in liquid phase or more destruction intermediates to react with ozone and increases colour removal)[127, 129], temperature (colour removal efficiency increases with increasing temperature from 25°C to 50°C[127, 131] and pH (alkaline conditions facilitate the decomposition of O_3 to OH radicals, hence higher colour removal occurs[127, 129, 132].

1.3.4 Decolourisation by O_3 / $UV_{254\ nm}$ combination

The mechanism involves the photolysis of ozone to release an oxygen atom and O_2, the O atom then reacts with water to produce OH radicals[109, 133-135]:

$$O_3 + hv \rightarrow O_2 + O \qquad (1.19)$$

$$O + H_2O \rightarrow 2OH^{\cdot} \qquad (1.20)$$

Where hv is the UV light.

H_2O_2 can also be generated[133-135]:

$$O_3 + H_2O + hv \rightarrow H_2O_2 + O_2 \qquad (1.21)$$

Hydrogen peroxide can undergo either photolysis (1.22) or react with O_3 (1.23) to generate OH radicals[133-135]:

$$H_2O_2 + hv \rightarrow 2OH^{\cdot} \qquad (1.22)$$

$$H_2O_2 + O_3 \rightarrow 2OH^{\cdot} + 3/2O_2 \qquad (1.23)$$

1.4 Conclusions

Whilst there is a generally-accepted mechanism for electrochemical ozone generation, it is generic and does not take into account the wide variation in behaviour observed across the range of ozone active anodes reported in the literature in terms of required current density, the requirement for a minimum current density or not, etc. In particular, the fact that the addition of a minute quantity of Ni to (essentially) ozone-inactive Sb-SnO_2 renders the latter significantly active and selective towards the electrochemical generation of ozone at low current densities strongly suggests that all ozone-active anodes are not the same. Furthermore, the 'generic' mechanism remains largely unproven; not surprising given the obvious challenges associated with obtaining kinetic (or indeed any) information from electrodes vigorously evolving gas.

The early studies of electrochemical ozone generation were carried out at very low temperatures in corrosive and, in some cases, expensive electrolytes and primarily using Pt anodes. Later, and to date, the favoured anode material was PbO_2 in more conventional, acidic electrolytes, at temperatures around 0 ºC. These materials require high current densities for high current efficiencies, typically ca. 1 A cm^{-2}.

It is clear that very high ozone current efficiencies (around 20 – 50%) can be routinely obtained at certain anodes; for example, the activities and selectivities of BDD anodes can be very high indeed, albeit at a very high energy cost. Ni/Sb-SnO_2 anodes also show such high activities and selectivities but at much lower currents and cell voltages; the former is a disadvantage in terms of the amount of ozone generated per unit area of electrode, although the development of synthetic routes to particulate electrocatalysts that can be deposited directly onto Nafion (as is commonly employed in MEA's utilizing PbO_2) may well ameliorate this problem.

The Ni/Sb – SnO_2 ozone anodes thus offer great promise for the electrochemical approach, and the advantages of the electrochemical generation of ozone have been well-rehearsed in the literature (see, for example,[42] and references therein). However, the ability to exploit probably the most useful advantage of electrochemical ozone generation, of direct injection into water as opposed to dissolving gas phase O_3, remains elusive for two reasons. To inject ozone directly into water requires the use of MEA-based, zero gap cells; these naturally utilize either hydrogen-evolving or air breathing cathodes, and all currently employ Nafion as the polymer electrolyte membrane. The latter essentially precludes the application of such cells in the treatment of 'real' or softened waters; Ca^{2+} and Mg^{2+} in the former essentially block the membrane, and Na^{+} ions in the latter replace protons as the mobile species in the Nafion, move more slowly and increase resistance across the cell. This may be overcome by the development of membranes that can reject multiply-charged cations; for example Trogadas et al.[136], have reported that incorporating SiO_2 into Nafion slows down the crossover of V^{3+} and V^{4+} ions. However, the flooding of air-breathing cathodes appears to limit the current densities accessible to commercially non-viable values, whilst hydrogen-evolving cathodes will only be applicable for larger applications where the hydrogen can be utilized and is not a safety issue.

The stability of anodes such as PbO_2 was regarded as a problem[137], as was that of BDD anodes[82] but the plethora of available commercial electrochemical ozone generation

systems based on these materials seems to mitigate against this; however, the toxicity of lead continues to be a barrier to its application in potable water treatment. The stability of Ni/Sb-SnO_2 remains to be clarified.

1.5 Aim and Objectives

The aim of the work reported in this thesis was to design, commission and employ an electrochemical ozone system capable of treating water contaminated with organic pollutants including dyes.

To achieve this aim, the following objectives were set:

- To investigate the structure and activity of the small (0.8 cm × 0.8 cm) Ni/Sb – SnO_2 ozone anodes,
- To investigate the activity, selectivity and durability of (2.5 cm × 2.5 cm) Ni/Sb – SnO_2 ozone anodes,
- To investigate ozone generation using Membrane – Electrode Assemblies (MEA's) with (5 cm × 7 cm) ozone anodes,
- To determine if, and to what extent, water contaminated with dye – containing wastewater could be decolourised using Ni/Sb – SnO_2 ozone anodes,
- To compare the efficiency of electrochemical decolourisation to that of electrochemically generated ozone.

This thesis consists of nine chapters; including: Introduction, Experimental, five results chapters, Conclusions and Future Work. In the first three results chapters, the structure, activity, selectivity and durability of different sizes (0.64, 6.25 and 24 cm^2) Ni/Sb – SnO_2 anodes were investigated. The efficiency of these anodes in terms of applications in industrial wastewater (dye containing) treatment was also studied in the last two chapters of the results ones.

CHAPTER TWO

2 Experimental

2.1 Chemicals and Materials

Tables 2.1 and 2.2 list the chemicals, materials and equipment used during the work reported in this thesis, along with purity and suppliers. All the chemicals were used as received unless otherwise stated.

Reagents / Materials	**Formula**	**Analysis**	**Supplier**
Tin (IV) chloride pentahydrate	$SnCl_4.5H_2O$	Puriss min 98%	Riedel-de Haën
Antimony (III) chloride	$SbCl_3$	A.C.S. reagent 99%	Sigma-Aldrich
Antimony Oxide	Sb_2O_3	A.C.S. reagent 99.9 +%	Aldrich
Nickel (II) chloride hexahydrate	$NiCl_2.6H_2O$	A.C.S. reagent	Sigma-Aldrich
Nickel (II) Oxide	NiO	A.C.S. reagent 99.8 %	Aldrich
Oxalic acid	$(COOH)_2$	98%	Sigma-Aldrich
Gold (III) chloride hydrate	$HAuCl_4.xH_2O$	99.99% metal	Sigma-Aldrich
Dihydrogen hexachloroplatinate (IV) hexahydrate	$H_2PtCl_6.6H_2O$	99.9 %	Alfa Aesar, A John Matthey
Potassium chloride	KCl	> 99.5%	Fluka
Potassium Ferrocyanide	$K_4Fe(CN)_6.3H_2O$	Analytical, 99%	Hopkin and Williams
Sodium Hydroxide	NaOH	Puriss	Riedel-de Haën
Reactive Blue 50 Dye	$C_{26}H_{23}Br_2N_3O_9S_2Na_2$	Dye content>50%	Langholm Dyeing
Naphthol Green B Dye	$C_{30}H_{15}FeN_3Na_3O_{15}S_3$	Dye content, 50%	Sigma – Aldrich
Congo Red Dye	$C_{32}H_{22}N_6Na_2O_6S_2$	Dye content, ≥35%	Sigma – Aldrich
Millipore water	H_2O	18.2 MΩ.cm	Millipore
Hydrochloric acid	HCl	Puriss min 37%	Riedel-de Haën
Sulfuric acid	H_2SO_4	Puriss 95-97%	Fluka
Perchloric Acid	$HClO_4$	Puriss 96%	Fluka
Hydrogen peroxide	H_2O_2	Puriss, 35%	Riedel-de Haën
Ethanol	C_2H_5OH	Puriss	Fluka
Acetone	CH_3COCH_3	Puriss	Fluka
Nafion 117 Membrane	$C_7HF_{13}O_5S\ .C_2F_4$	Not available	(DuPont Corp., USA)
Platinum mesh, 0.25 mm, 20 x 20 mm	Pt	99.9%	Goodfellow
Titanium mesh	Ti	20%	Dexmet, USA
Titanium wire (0.5 mm)	Ti	99.8 %	Advent
Titanium wire (1.0 mm)	Ti	99.6%	Advent
Platinised titanium mesh of all sizes	Pt/Ti	0.8 cm × 0.8 cm, 5 cm × 5 cm and 7 cm × 5 cm	NRK Electrochem
UV lamp	$UV_{254\ nm}$	TUV 16W 4P SE UNP	Philips, UK

Table 2. 1. List of chemicals and materials employed in the work reported in this thesis.

Equipment	Supplier
Spot-Welding machine	HIRST Electric Industries Ltd
UV/VIS 200 nm FF Concave Holographic Spectrometer EEP 2000C	Stellar Net Inc.
Xenon Flash Lamp Module, 11-28 V DC(1 A)	Hamamatsu
UV/VIS Spectrometer and software, Astranet Systems	Astranet Systems Limited, Cambridge, UK
MasterFlex Digital Standard Pump L/STM Console Drive, model 7519-06 cartridge pump	Cole-Palmer
Flow meter system, WU series	Cole-Palmer
Hameg HM 7044 Power supply	Hameg Instrument
Air admiral air pump	Cole-Palmer
Potentiostat/Galvanostat version 4.9 and General Purpose Electrochemical System Program (GPES)	Windsor Scientific
Precision DC Power supply, TS3022S, 30V-2A	Thandar
Hot surface heating press	Chauffante Elcometer
Ultrasonic bath, 2510	Branson
Oven, model N6C	Genlab Ltd. Thermal Engineers
Furnace, Carbolite Type 301, MC16-GB-C-1, Eurotherm 301 controller	Barlword Scientific
Stirrer Bar, PC-351	Corning
Magnetic Stirrer CB 162	Stuart
Ceramic Boat	Shenzhen Jinghui Electronics Co. Ltd.
Thermometer76 mm immersion,	Fisherbrand
Analytical balance, model R 20	Oertling

Table 2. 2. List of equipment employed in the work reported in this thesis.

2.2 Anode Preparation

The anodes were prepared according to methodology similar to that employed by Wang et al.[75] and Christensen et al.[42].

Titanium as a support for SnO_2-based anodes is well documented in the literature, see for example: [75, 93, 101, 138]; therefore, it was chosen as a substrate for the anodes reported in this thesis. Ti mesh substrates of dimensions 0.8 cm × 0.8 cm, 2.5 cm × 2.5 cm and 7.0 cm × 5.0 cm were employed.

2.2.1 Small scale anodes (0.8 cm × 0.8 cm)

This included three main steps, Ti mesh preparation, formation of electrodeposited interlayer (EDIL) and catalyst deposition on the EDIL – coated Ti mesh, unless otherwise stated.

Ti Mesh Preparation

Each Ti mesh was cut to produce a 0.8 cm × 0.8 cm section which was then pressed in a Chauffante Elcometer press at room temperature and 1000 N for 5 minutes to flatten out

any protrusions. A 0.5 mm diameter Ti wire was cut to ca. 6.0 cm. One edge of the Ti wire was flattened with a hammer and spot-welded onto the mesh such that the wire ran along the middle of the mesh in firm contact with its entire length.

The meshes were then degreased by immersing in beaker containing acetone, followed by thorough washing with Millipore Milli-Q water (18 MΩ cm). The immersion in acetone and then in Millipore water was repeated 6 times.

The Ti meshes were etched by boiling in 10 wt.% oxalic acid (20 g in 200 cm^3 Millipore Milli-Q water) for at least 30 minutes, *i.e*. until the solution took on a brownish tinge. The solution was allowed to cool to room temperature after which the meshes were washed with copious amounts of Millipore Milli-Q water. They were then placed in fresh Millipore Milli-Q water in a beaker immersed in an ultrasonic bath for 10 minutes, the water replaced and the procedure repeated three times until no oil/grease was observed on the surface of the water. The meshes were then dried in a 60 ^{O}C oven for 1 hour by placing in a beaker with the meshes uppermost, in the oven. The meshes were then weighed and their masses recorded.

Formation of the Electrodeposited Interlayer (EDIL)
The electrodeposition solution consisted of 0.5 M $SnCl_4.5H_2O$ and 0.05 M $SbCl_3$ in 500 cm^3 ethanol, *i.e.* to give a Sn: Sb molar ratio of 10:1. A Pt/Ti double mesh as anode and Ti mesh as cathode were both immersed in the electrodeposition solution (see fig. 2.1). The Ti mesh was clamped *via* its connecting wire, and held vertically in 200 cm^3 of the electrodeposition solution, co-facial to and between two Pt-coated Ti meshes, see fig. 2.1. The Ti mesh was then connected to the (-) pole of a TTi TSX 1820P programmable DC power supply and the two Pt/Ti meshes to the (+) pole. Deposition was initiated at a current density of 5 mA cm^{-2} for 1 min, then at 2.5 mA cm^{-2} for 20 minutes according to the method reported by Cui et al.[50].

Following electrodeposition, each Ti mesh was washed thoroughly with Millipore Milli-Q water and placed in a beaker with the meshes uppermost, and allowed to dry at room temperature for 1 hour. The meshes were then weighed and the masses recorded.

The Ti mesh electrodes were placed in a beaker in an oven, with the meshes uppermost, at 100 ºC for 15 minutes. The meshes were then removed and immediately laid horizontally in a silica boat and placed in a furnace pre-heated to 390 ^{O}C for 1 hour. The furnace was

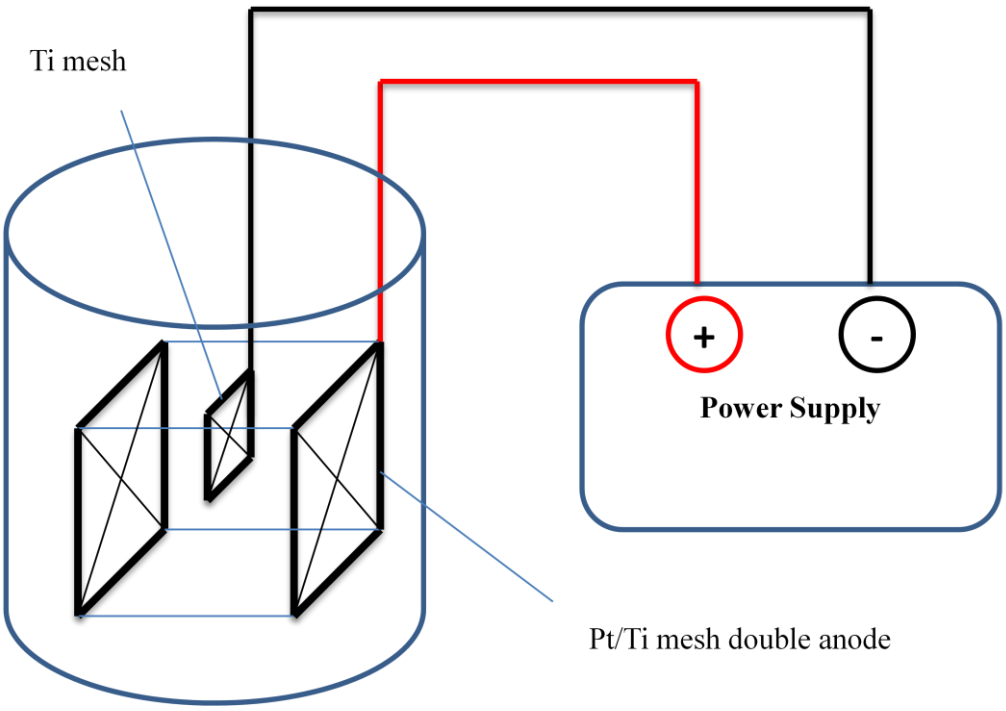

Figure 2. 1. The inter layer electrodeposition procedure.

switched off, the meshes removed and allowed to cool for 1 minute before commencing dip-coating.

Thermal Deposition of the Catalyst (Dip - Coating)

The catalyst coating solution consisted of $SnCl_4.5H_2O$, $SbCl_3$ and $NiCl_2.6H_2O$ in the molar ratio 500: 8: x where x = 1 in the Wang et al. recipe [75] (see section 1.1.4); for the latter, 35.0 g, 0.365 g and 0.0475 g, respectively, of the reactants were placed in 100 cm^3 ethanol in a 100 cm^3 volumetric flask and shaken thoroughly to dissolve. Gold or lead were used in the coating solution for some anodes (see fig. 2.2). The solution was poured into a beaker. Each mesh electrode was dip-coated with catalyst solution. The electrodes were then placed in a beaker (mesh uppermost) and transferred to an oven at 110 ^OC for 5 minutes after which they were removed, laid horizontally in a furnace boat and placed in a furnace pre-heated to 460 ^OC. The furnace was switched off before admitting the meshes. It was then turned on and allowed to attain 460 ^OC again (*ca.* 2 minutes) and the meshes heated for 10 minutes. The boat + mesh electrodes were then removed, the meshes allowed to cool for 1 minute and the coating repeated (see fig. 2.2). The coating, oven and furnace steps were then repeated 18 times. The final (20^{th}) coating was heated in the furnace for 60 minutes at 460 ^OC. After every 5 coats, the cool mesh electrodes were then weighed and the masses recorded. Some exceptions to the small scale anodes preparation were applied. Some small scale anodes were prepared without EDIL, and others were prepared without

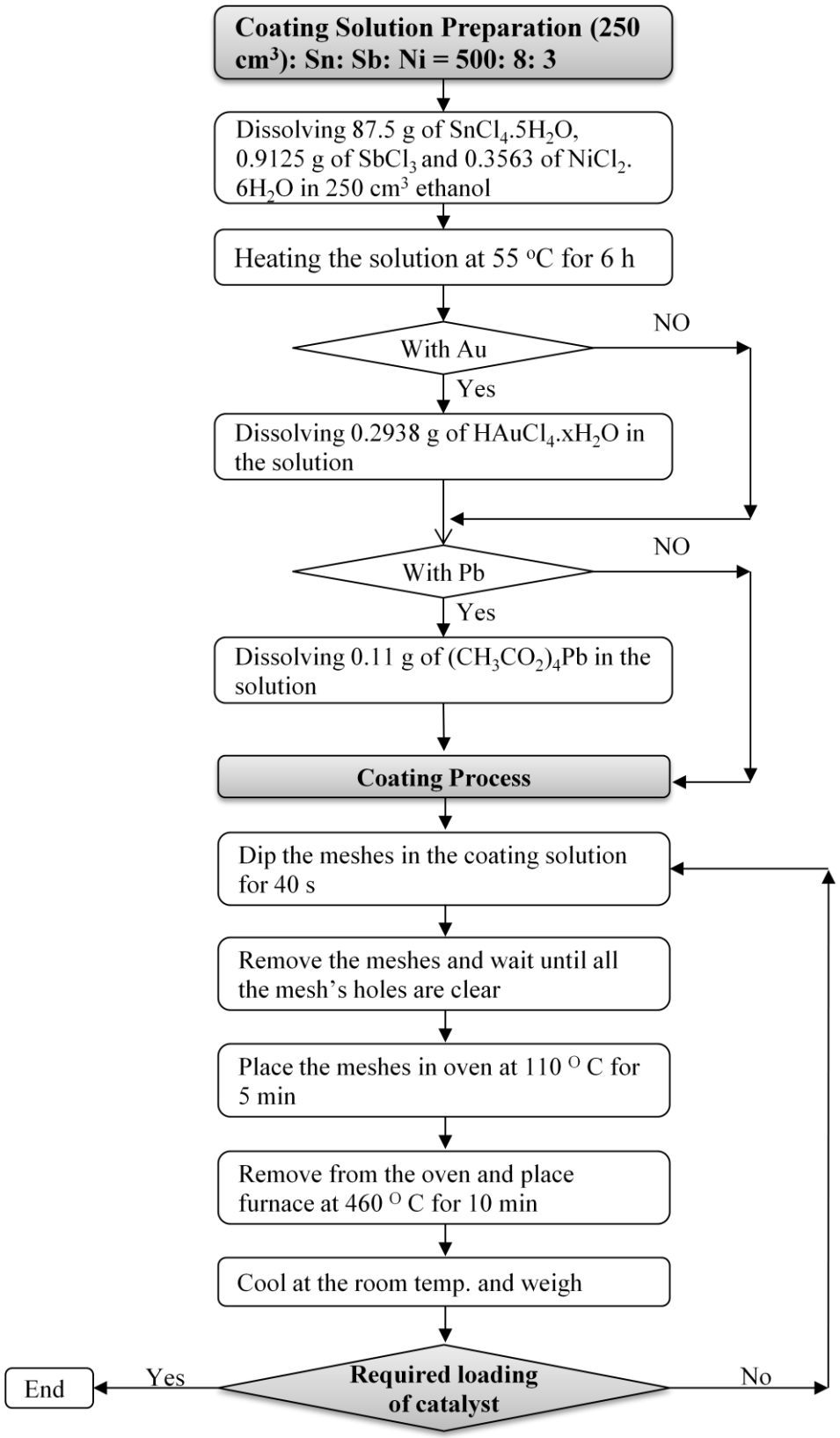

Figure 2. 2. The procedures of catalyst thermal deposition on the small anodes (0.8 cm × 0.8 cm).

EDIL and using new precursors similar to that described in section 2.2.2.

2.2.2 Larger scale anodes (2.5 cm × 2.5 cm and 7 cm × 5 cm)

The main aspects of fabrication of these anodes were: Ti mesh preparation and the dip-coating process. The same procedure was followed as in section 2.2.1 with respect to the Ti mesh preparation. However, the differences between the preparation of these anodes and the small scale ones were: (i) the application of an EDIL was stopped for reasons that will be discussed in section 3.9 and (ii) the composition and chemicals of the precursor in the coating solutions were different, in that Sb_2O_3 and NiO were employed instead of the chlorides, and the furnace temperature was 550 ^{o}C, unless otherwise stated (for more details see fig. 2.3). The Sn: Sb: Ni ratio was 67: 4.3: ×, and × was varied between 0.1 and 2.

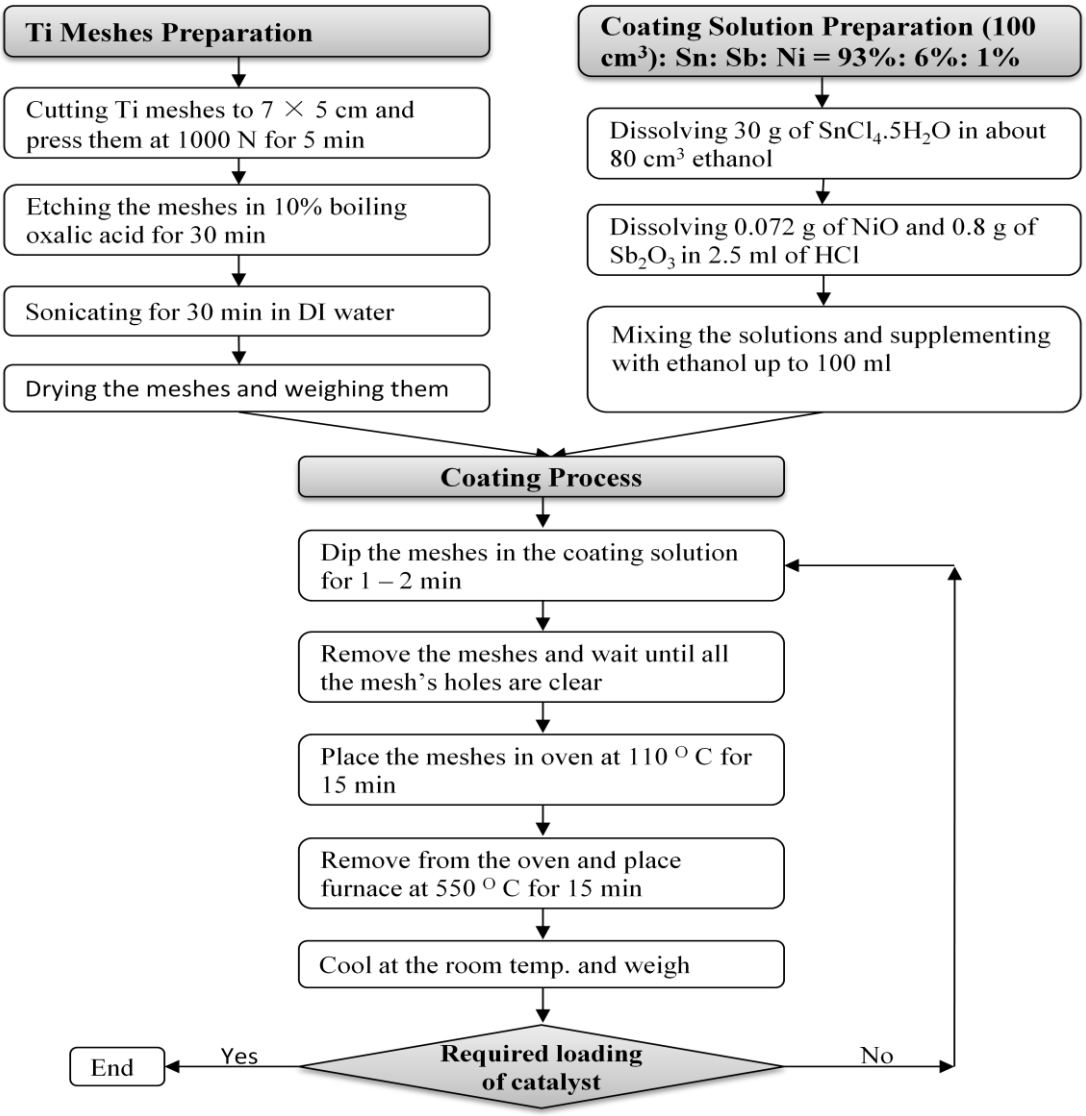

Figure 2. 3. The method employed to make the larger scale anodes (2.5 cm × 2.5 cm and 7 cm × 5 cm).

The 7.0 cm × 5.0 cm anodes were made for use in the polycarbonate cells (see sections 2.9) and were spot welded into a titanium frame once the mesh was coated with catalyst, giving an active area of 6 cm × 4 cm.

2.3 Anode Nomenclature

Table 2.3 summarises the details of the anodes discussed in this thesis. It may be seen from the table that 18 electrode series were investigated. As discussed above, these include series of anodes of different sizes: 0.8 cm × 0.8 cm, 2.5 cm × 2.5 cm and 7 cm × 5 cm, and prepared using different precursor solution compositions. These solutions fall into two main categories: with Sb and Ni chlorides or with Sb and Ni oxides. In addition, some series included anodes that were with or without added Au or Pb, and with or without EDIL. The anodes with Sb and Ni chlorides will be called standard Ni/Sb – SnO_2 (SNATO) anodes in the discussion below, the anodes using Sb and Ni oxides will be called Ni/Sb – SnO_2 (NATO) anodes. The standard anodes with Au or Pb will be called AuSNATO or PbSNATO, respectively. The anode names are extended to take into account variations in composition and series number and this exemplified by table 2.4 for anode series KZ01. The remaining anode series details (similar to what shown in table 2.4) are included in Appendix II.

2.4 The Fabrication of Membrane Electrode Assemblies

Membrane Electrode Assemblies (MEA's) were fabricated by hot-pressing (Elcometer, heated press / 250 ^{O}C / 30000 N Digit) the Ni/Sb-SnO_2 mesh anode, Nafion 117 membrane (DuPont Corp., USA) and Pt/Ti mesh or air breathing (Johnson Matthy, or Clarizon) cathode at 150 ºC and 800 N for 3 minutes, after which the MEA was turned through 180º and the pressing repeated. Figure 2.4 shows a schematic diagram of an MEA with Pt/Ti mesh cathode. The MEA was mounted between the cathodic and anodic compartments (ca. 10 cm^3 volume) of the polycarbonate cell, with sealing maintained using silicon "O" rings. The cell was assembled via 10 stainless steel bolts passed through holes on the periphery of the polycarbonate cell (see section 2.9).

2.5 Power Supplies and Pumps

The DC power supplies employed in the work reported in this thesis was Hameg HM 7044 power supply unit (PSU), see fig. 2.5.

The pump most commonly employed was a Masterflex L/S with an "Easyload II" 77200-

Series name	N° of electrodes	Sb and Ni chlorides	Sb and Ni oxides	Size cm × cm	EDIL	The series contains:
KZ01	8	√	-	0.8×0.8	√	AuSNATO
KZ02	8	√	-	0.8×0.8	√	SNATO and AuSNATO
KZ03	20	√	-	0.8×0.8 & 5 × 7	√	SNATO, AuSNATO and PbSNATO
KZ04	17	√	-	0.8×0.8	√	SNATO, AuSNATO and PbSNATO
KZ05	26	√	-	0.8×0.8	√	SNATO, AuSNATO and PbSNATO
KZ06	12	-	√	0.8×0.8	-	NATO and PbNATO
KZ07	11	-	√	2.5×2.5	-	NATO
KZ08	8	-	√	2.5×2.5	-	NATO
KZ09	8	-	√	2.5×2.5	-	NATO
KZ10	6	-	√	2.5×2.5	-	NATO
KZ11	16	-	√	2.5×2.5 & 0.8×0.8	-	NATO
KZ12	16	-	√	2.5×2.5 & 0.8×0.8	-	NATO
KZ13	16	-	√	2.5×2.5 & 0.8×0.8	-	NATO
KZ14	16	-	√	2.5×2.5	-	NATO
KZ15	6	-	√	2.5×2.5	-	NATO
KZ16	3	-	√	2.5×2.5 & 5×7	-	NATO
KZ17	10	-	√	2.5×2.5 & 5×7	-	NATO
KZ18	23	-	√	2.5×2.5	-	NATO

Table 2. 3. Summary of the anode series reported in this thesis.

Series name	Anode name	Composition: Sn:Sb:Ni:Au:Pb	Size cm × cm	EDIL / mg	N° of coats	Catalyst loading / mg	Furnace temp. °C
KZ01	AuSNATO01A	500:8:3:1.5:0	0.8 × 0.8	0.28	18	3.2	460
	AuSNATO01B	500:8:3:1.5:0	0.8 × 0.8	0.3	18	3.5	
	AuSNATO01C	500:8:3:1.5:0	0.8 × 0.8	0.31	18	3.3	
	AuSNATO01D	500:8:3:1.5:0	0.8 × 0.8	0.29	18	3.6	
	AuSNATO01E	500:8:3:1.5:0	0.8 × 0.8	0.32	18	3.6	
	AuSNATO01F	500:8:3:1.5:0	0.8 × 0.8	0.2	18	3.4	
	AuSNATO01G	500:8:3:1.5:0	0.8 × 0.8	0.35	18	3.4	
	AuSNATO01H	500:8:3:1.5:0	0.8 × 0.8	0.22	18	4.0	

Table 2. 4. The names of anode series KZ01.

60 tubing cassette, see fig. 2.6.

2.6 The Spectrophotometer

The spectrophotometer employed throughout the work reported in this thesis was an Astranet UV-Vis fibre optic spectrometer utilizing 1.0 cm path length flow cells, see fig. 2.7.

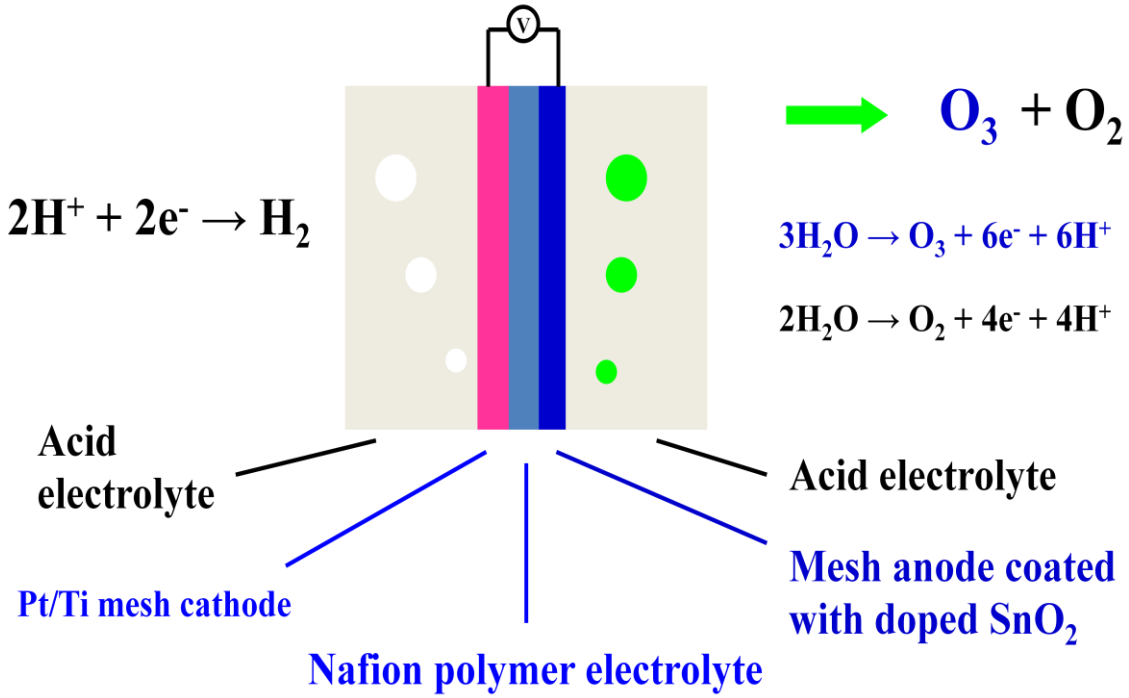

Figure 2. 4. Schematic diagram of a membrane electrode assembly.

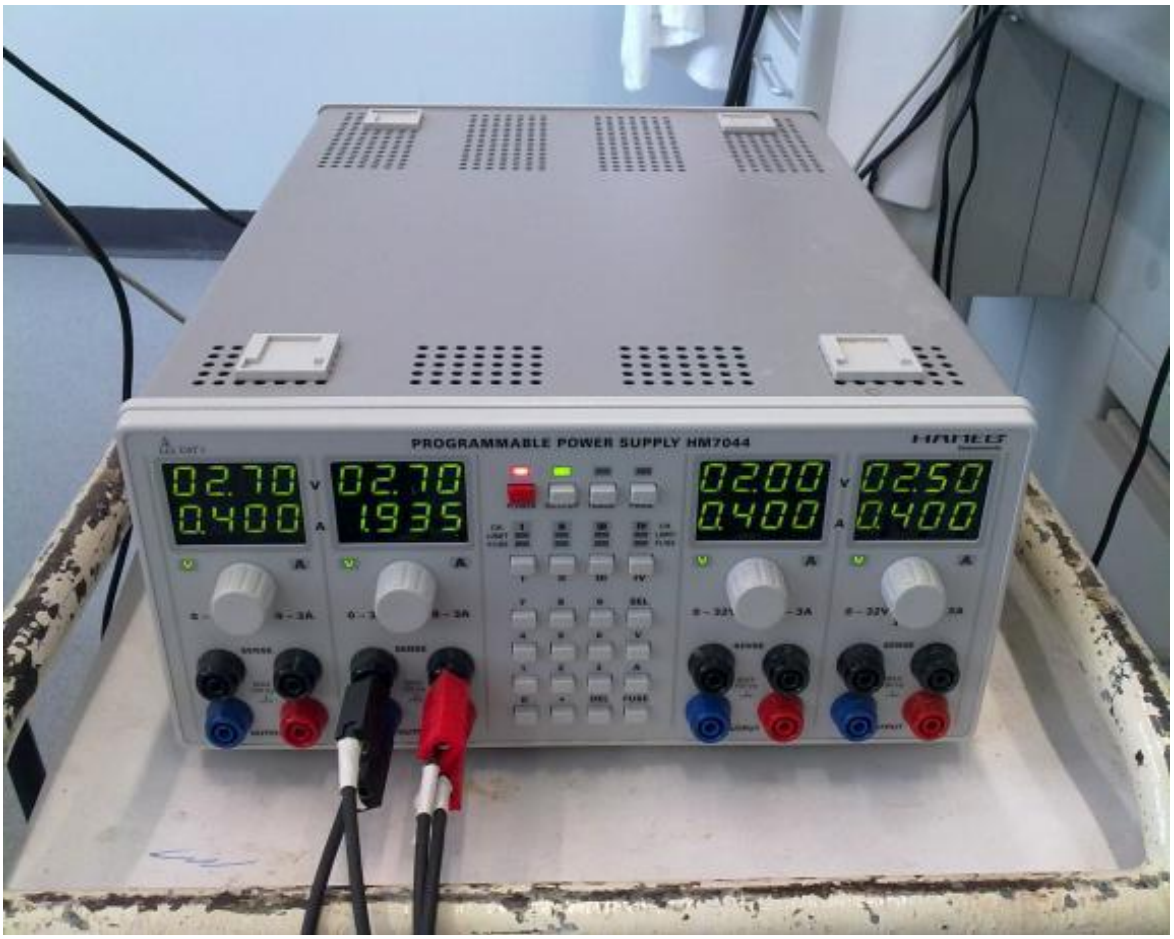

Figure 2. 5. Photograph of the Hameg power supply.

Figure 2. 6. Photograph of the Masterflex pump.

(a)

(b)

Figure 2. 7. Photographs of (a) Astranet UV-Vis fibre optic spectrophotometer and (b) a flow cell.

2.7 Scanning Electron Microscope (SEM) and Energy Dispersive X-ray Analysis (EDX)

Scanning electron microscopy (SEM) micrographs were obtained using a JEOL 5300 LV instrument fitted with Rontec and Si (Li) Energy Dispersive X-ray (EDX) detectors cooled by liquid nitrogen. The SEM operated at 25 kV, but the magnification was limited to 5000x due to charging of the sample. All SEM/EDX runs were carried out by the Materials Analytical Unit, Newcastle University.

2.8 Cyclic Voltammetry

Cyclic voltammetry was first reported in 1938 and described theoretically in 1948 by Randles and Sevcik [139]. In cyclic voltammetry, the potential is ramped and cycled between two chosen limits at a steady rate (scan rate ν) and the current monitored. The voltammetry of an electrochemical system gives invaluable information as to the presence of electroactive species in solution or at the electrode surface [139]. A cyclic voltammogram is a plot of current vs. the (time dependent) potential [139]. The electrochemical cell in which cyclic voltammetry is carried out usually consists of three electrodes immersed in the electrolyte: the working electrode (WE), the counter electrode (CE) and the reference electrode (RE). The potential of the WE is monitored and controlled with respect to the RE by a potentiostat[139] . The electrochemical cell (ca. 100 cm^3) used in this work was of a standard, 3-electrode design with a 1.5 cm^2 Pt mesh counter electrode and a saturated calomel electrode (SCE) reference (Sentek). An Autolab potentiostat was employed to maintain and control the potential of the Ni/Sb-SnO_2 working electrode with respect to the SCE. Cyclic voltammetry was carried out using only the small scale (0.8 cm × 0.8 cm) anodes.

2.8.1 Cyclic voltammetry and slow electron transfer

It is easy to discern from a cyclic voltammogram (CV) if an electrochemical process (2.1)

$$aRed \leftrightharpoons bOx + ze^- \qquad (2.1)$$

is completely irreversible because the reverse reaction is prevented from occurring, for example Ox is a gas whilst Red is a solution species (*eg*. Cl_2 and Cl^-, or H_2O and O_3). However, it is often difficult to assess whether a process such as (2.1) is facile; *eg*. the rates of the forward and back reactions are both sufficiently fast that, during the cyclic voltammetry experiment, equilibrium is constantly maintained and hence the Nernst equation always holds true[139, 140]:

$$E = E^0 + (RT/zF)\ln([Ox]^b/[Red]^a) \qquad (2.2)$$

Where E^0 is the potential at which the surface coverage by the oxidised form is 0.5, R is gas constant, which is 8.31 (J mol^{-1} K^{-1}), T is temperature (K), z is number of moles of electrons exchanged in the electrochemical reaction (mol), and F is Faraday's constant (96480 C mol^{-1}). In the case of the anodic scan of a cyclic voltammogram at a scan rate ν:

$$E = E_c + \nu = E^0 + (RT/zF)\ln([Ox]/[Red]) \qquad (2.3)$$

Where E_c is the cathodic potential limit.

In an ideal cell, a fast (or facile) one electron system (Ox/Red) will have a separation of 57 mV at 298K between the anodic and cathodic peaks irrespective of scan rate[140]. However, most cells do have uncompensated resistance and hence the peak separation increases with scan rate due to the fact that current also increases with scan rate, hence the potential drop (V = IR) increases which, in turn, moves the peaks apart. Thus, a plot of peak separation (ΔE) *vs* scan rate is usually made and the scan rate extrapolated to 0 to give the actual peak separation which should be 57 mV.

If there was no Ox present (equation (2.1)) then the peak current of a facile process varies with scan rate ν according to the Randles-Sevcik equation (2.4)[140]:

$$I_p = 2.69 \times 10^5 An^{3/2} D_{red}^{1/2} [Red] \nu^{1/2} \qquad (2.4)$$

Where I_p is the peak current (A), A is the (true) area of the electrode (cm^2) and D_{red} is the diffusion coefficient (cm^2 s^{-1}).

In the case of slow electron transfer, equation (2.2) no longer holds true as the forward and back reactions in equation (2.1) are no longer fast enough to maintain equilibrium. In this case, in an ideal cell, a slow system (Ox/Red) will have a peak separation ΔE that shifts with scan rate. A plot of peak separation *vs.* scan rate for a cell having uncompensated resistance will give a value of ΔE greater than 57 mV at ν = 0. Under these conditions[140]:

$$I_p = 3.01 \times 10^5 An^{3/2} \beta^{1/2} D_{red}^{1/2} [Red] \nu^{1/2} \qquad (2.5)$$

Where β is the asymmetry parameter; if the transition state of the process in equation (2.1) is "reactant-like" $\beta \rightarrow 0$, if it is "product like" $\beta \rightarrow 1$. If the transition state lies midway between Red and Ox, β = 0.5, and this is often assumed[33, 139].

2.8.2 Cyclic voltammetry with ferrocyanide

In order to investigate electron transfer across a particular electrode/electrolyte, $Fe(CN)_6^{4-}$ is often employed as the redox active solution species, as it undergoes a one – electron oxidation. Where the Red/Ox equation of ferrocyanide can be written as follows:

$$Fe(CN)_6^{4-} \leftrightarrows Fe(CN)_6^{3-} + e^- \qquad (2.6)$$

As mentioned above, the separation ΔE between the anodic and cathodic peaks of the cyclic voltammogram of ferrocyanide on the Ni/Sb – SnO_2 anode will depend upon the resistance of the electrolyte and the kinetics of electron transfer across the interface.

In the ferrocyanide cyclic voltammetry experiments reported in this thesis, 0.1 M $K_4Fe(CN)_6.3H_2O$ in 0.5 M Na_2SO_4 in Millipore water was prepared. The cyclic voltammetry was performed between 0 V and 0.45 V or 0.6 V at scan rates of 10 mV s^{-1}, 50 mV s^{-1}, 100 mV s^{-1}, and 500 mV s^{-1}.

Cyclic voltammetry in the absence of a redox active species in solution can be employed to characterize the capacitive behaviour of porous electrodes ([141] and references therein), with the capacitive current (I_{cap}) given by:

$$I_{cap} = C\,\nu \qquad (2.7)$$

Where C is the capacitance of the interface. Often, C is observed to be potential-dependent due to effects such as ion adsorption, and hence I_{cap} varies with $\nu^{1/n}$, where n is a positive number, due to the effects of distributed resistance in the pores of the electrode ([141] and references therein). The latter causes C to decrease with increasing scan rate. Despite these complications, cyclic voltammetry is acceptable as a means of comparing the *relative* capacitance, and hence *relative* area, of a family of electrodes. In addition, Sb-doped SnO_2 has been shown to exhibit conventional, double-layer capacitance behaviour, as opposed to pseudo capacitance due to redox active surface species[142] with less than *ca*. 10% decrease in C on increasing the scan rate from 0.004 V s^{-1} to 0.1 V s^{-1}.

2.8.3 Fractal anodes

Fractal systems have structures that look the same on all length scales – in other words, the complexity does not decrease as you 'zoom in'. In essence, the Randles-Sevcick treatment of cyclic voltammograms, where peak current, I_p, varies as $\nu^{1/2}$, is the limit of a more general treatment which has [143-145]:

$$I_p = B \nu^{\alpha} \quad (2.8)$$

where B is constant and α is given by Nyikos and Pajkossy, [146]:

$$\alpha = (d_f - 1)/2 \quad (2.9)$$

d_f is the dimensionality of the electrode; for an ideal, smooth electrode, $d_f = 2$ and $\alpha = 0.5$, which is the Randles-Sevcick approach. A more general way of treating cyclic voltammogram data is to plot $\ln(I_p)$ against $\ln(\nu)$, the slope of which gives α and hence d_f. Fractal electrodes would be expected to give values tending towards 3, planar electrodes $d_f = 2$.

2.8.4 Cyclic voltammetry in acid

Cyclic voltammetry of the Ni/Sb – SnO_2 anodes was carried out to determine the potential at which the oxygen and/or ozone generation started (onset potential). For this purpose, the (small scale) Ni/Sb – SnO_2 anode, 1.5 cm^2 Pt mesh and SCE reference electrode were immersed in the same electrochemical cell in which the ferrocyanide cyclic voltammetry was performed. The cathodic potential limit was always 0 V and the anodic limit was varied.

2.9 The Electrochemical Cells for Ozone Generation

Three types of electrochemical cell were employed: 1 cm pathlength quartz cuvette, glass and polycarbonate (area exposed to electrolyte = 6.0 cm × 4.0 cm), depending upon whether 0.8 cm × 0.8 cm, 2.5 cm × 2.5 cm or the "framed" (7 cm × 5 cm) electrodes, respectively were being investigated.

The 1 cm pathlength quartz cuvette employed in this study is similar to that employed by Wang et al.[75] with only 2 electrodes, namely the anode and the cathode, see fig. 1.10.

The glass cell used is the same glass cell employed by Christensen et al[42], and it comprised two Pyrex glass halves of oval section having ground glass flanges. The sections were clamped together on either side of the Nafion 117 membrane, sealing being achieved by means of silicone O-rings between the ground glass flanges and membrane. The volume of each half of the cell was *ca.* 100 cm^3, see fig. 2.8. 1 M $HClO_4$ was employed as the anolyte and catholyte, which were kept separate by the membrane; the latter was stationary and supplied from a glass reservoir *via* polyethylene tubing (Portex 800/012/425/800 7.0

Figure 2. 8. Photograph of the glass electrochemical cell.

mm × 10.5 mm). The counter electrode (cathode) was a 5.0 cm × 5.0 cm platinised Ti mesh, and the cell voltage and/or current density across the ozone anode and Pt/Ti cathode was controlled with Hameg HM 7044 power supply unit.

The polycarbonate cell was designed to allow the use of an MEA. The electrolytes employed were acid or Millipore water anolyte and acid or Millipore water catholyte. A schematic representation of a polycarbonate cell and the MEA are shown in fig. 2. 9(a) and anode and cathode with the Ti frames are in fig. 2. 9(b).

2.10 Electrochemical Ozone Generation:

All experiments were conducted at room temperature, 20-25 ^{O}C.

2.10.1 Small scale anodes

The small scale anodes were employed to generate ozone in the quartz cuvette cell. This cell was a sealed, 1 cm pathlength UV Vis cuvette, containing 3 cm^3 electrolyte (1 M $HClO_4$). The cathode was a 0.64 cm^2 platinised Ti mesh held vertically against one of the opaque sides of the cuvette; the anode was held flat on the floor of the cuvette. The absorbance of ozone was monitored using either Astranet spectrophotometer with cuvette holder or Shimadzu 1240 mini spectrophotometer.

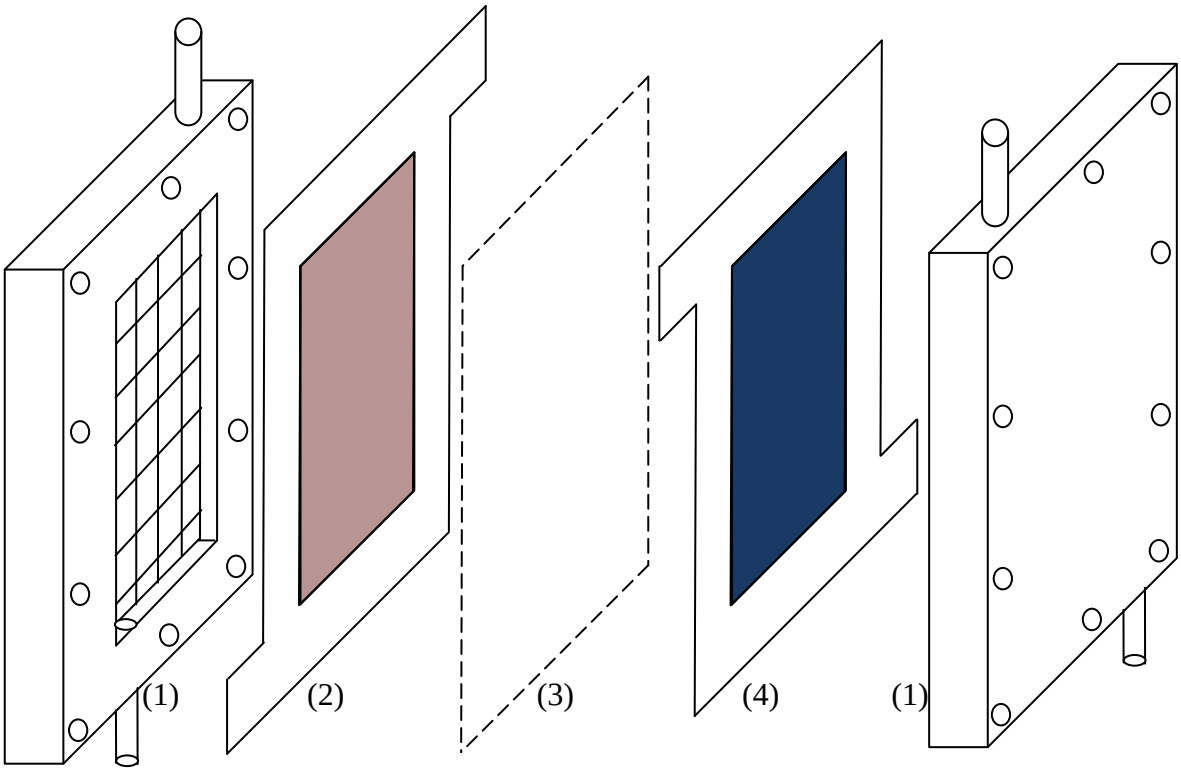

(a)

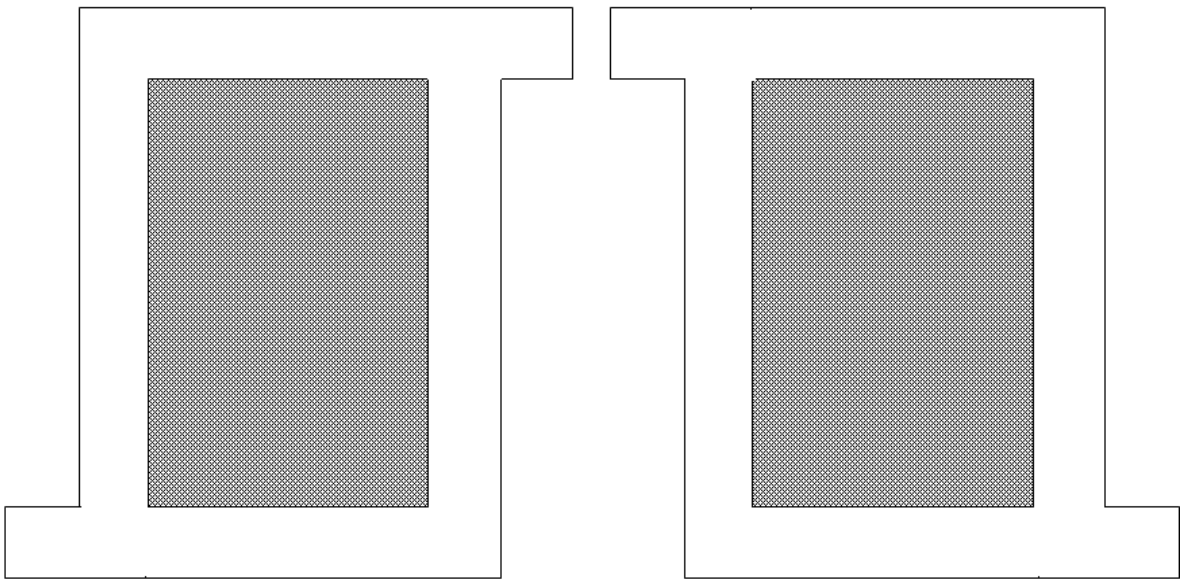

(b)

Figure 2. 9. (a) The membrane electrode assembly and the polycarbonate (PC) electrochemical cell: (1) one half of the PC electrochemical cell, (2) the anode spot-welded on Ti frame, (3) the Nafion 117 membrane, (4) the cathode spot-welded on Ti frame. (b) The cathode and anode meshes with the Ti frames.

The cuvette holder (see fig. 2.10) was connected by the fibre optic cables to the Astranet spectrophotometer. The cuvette cell (with the anode and the cathode) was inserted in the cuvette holder and the absorbance of ozone was monitored online using the Astranet spectrophotometer.

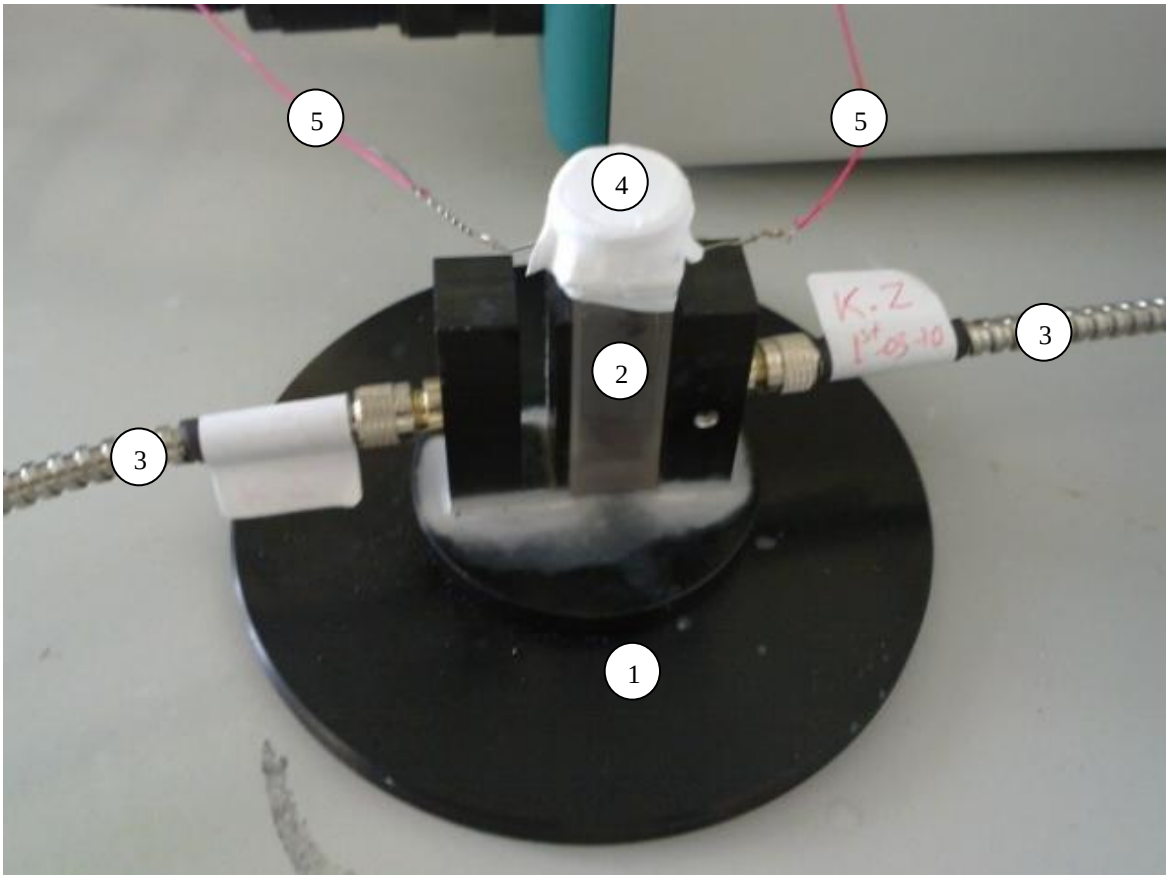

Figure 2. 10. (1) The Astranet cuvette holder, (2) cuvette cell, (3) fibre optic cables, (4) cuvette seal and (5) wires connecting the electrodes to the power supply.

In some experiments, a Shimadzu spectrophotometer was employed, in which case the cuvette cell (with the anode and the cathode) was inserted in the cuvette holder of the spectrophotometer and the ozone was monitored after the generation of ozone was stopped to avoid any bubble interference.

The potential of the anode was controlled with respect to the Pt/Ti cathode by Autolab type II potentiostat/galvanostat. Ozone activity was assessed using a pulsed potential protocol in which the potential was stepped from open circuit to 2.7 V for 30 s and then switched to open circuit again for an additional 270 s. A baseline was collected during the initial time at open circuit and spectra taken during the second period at open circuit, the latter to avoid interference by gas bubbles [45].

2.10.2 Larger scale anodes

The ozone was generated electrochemically in the glass cells (2.5 cm × 2.5 cm anodes) and MEA – based cell (7 cm × 5 cm anodes) using two methods: flow (single pass) mode (fig. 2.11) and recycle mode (fig. 2.12).

In the flow system employed in the work reported in this thesis (see fig. 2.11), both anolyte and catholyte were supplied from a glass reservoir via polyethylene tubing (Portex 800/012/425/800 7.0 mm x 10.5 mm), with the catholyte static. The anolyte was pumped from the cell to a pyrex glass gas separator via PE tubing using a Masterflex Digital Standard Cartridge Pump (Cole-Palmer), flow rate 30 cm^3 min^{-1} unless otherwise stated. Dissolved ozone was then monitored by a 1 cm pathlength UV-Vis cell (Astranet). Nitrogen gas from a cryogenic boil-off was employed to dilute the gas exiting from the separator at a carefully-controlled rate (typically 80 cm^3 min^{-1}) using a Cole-Palmer WU series flowmeter system and the gas phase ozone concentration monitored using a second 1 cm pathlength UV-Vis cell (Astranet). The gas-phase ozone then exhausted into a fume hood.

Under recycle conditions (see fig. 2.12), the anolyte was pumped from the cell to a

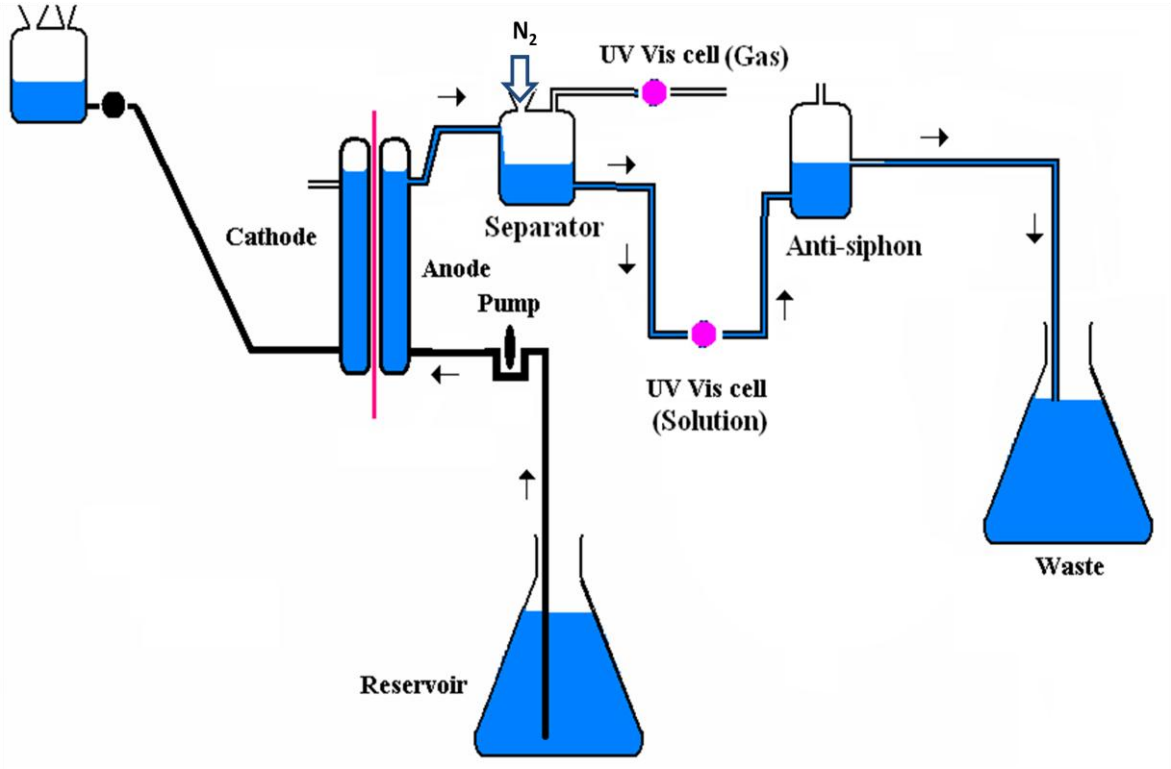

Figure 2. 11. The flow (single pass) system for generating ozone in the glass cell or the polycarbonate (MEA – based) cell.

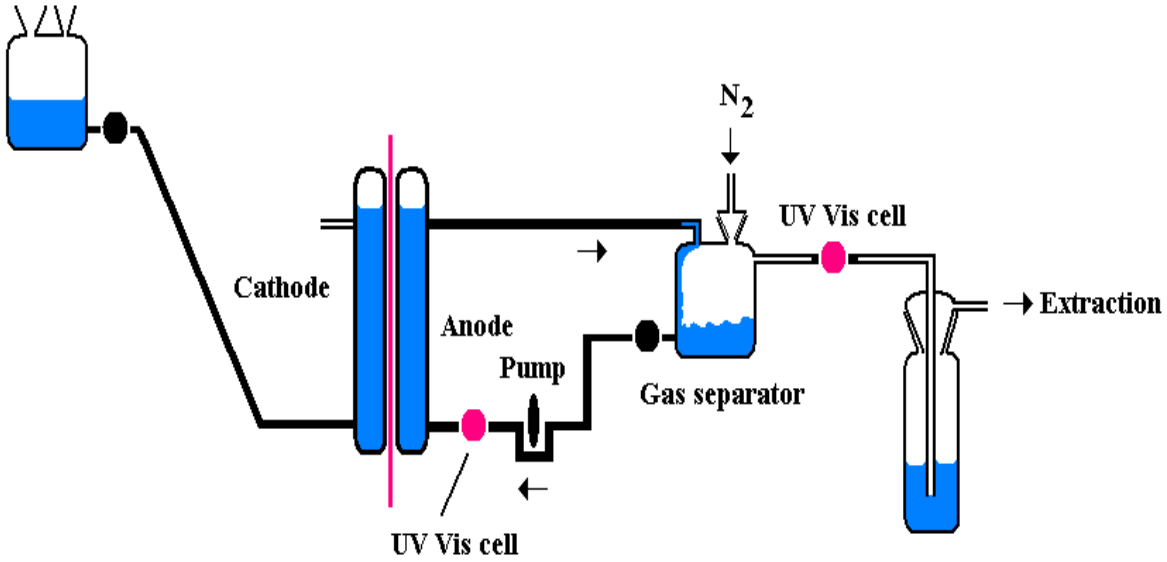

Figure 2. 12. The recycle system for generating ozone in the glass cell or the polycarbonate (MEA – based) cell.

Pyrex glass gas separator via PE tubing, and back to the cell using a Masterflex Digital Standard Cartridge Pump (Cole-Palmer). The dissolved ozone was monitored using a 1 cm pathlength UV-Vis cell (Astranet). Nitrogen gas from a cryogenic boil-off was again employed to dilute the gas exiting from the separator and monitored using a 1 cm pathlength UV-Vis cell (Astranet). The ozone then exhausted into a fume hood. It was assumed that, once the anolyte becomes saturated with ozone, all the ozone produced subsequently is released into the gas phase.

2.11 Ozone Generation Using Membrane Electrode Assemblies

Seven MEA's were used to generate ozone, as will be discussed in Chapter 5. These consisted of different anodes and cathodes. The anodes included SNATO and NATO prepared using precursors containing different Sn/Sb/Ni ratios and prepared at different furnace temperatures. The cathodes included air breathing cathode (supplied by either Clarizon Ltd or Johnson Matthy (JM)) and hydrogen evolution cathodes (Pt/Ti). As discussed above, Nafion 117 membrane was used as separator between the cathode and the anode. The MEA's were tested either in flow mode or in recycle mode. Those MEA's are presented in table 2.5.

The rate of ozone production rate generatied by the MEA's was calculated according to:

$$OPR\ (mg\ h^{-1}) = I \times \eta \times t \times 48 \times 1000 \times 3600/6F = 299\ I \times \eta \qquad (2.10)$$

Where I is the current (A), η is the current efficiency (as a decimal), t is the time (s), 48 is

MEA's	Anode Name	Anode Size	Cathode Name	Cathode Size
MEA1	SNATO03S	4 cm × 6 cm	Clarizon	4 cm × 6 cm
MEA2	NATO13A	2.5 cm × 2.5 cm	Clarizon	4 cm × 6 cm
MEA3	NATO16C	4 cm × 6 cm	JM	4 cm × 6 cm
MEA4	NATO17D	4 cm × 6 cm	JM	4 cm × 6 cm
MEA5	NATO07J	2.5 cm × 2.5 cm	JM	4 cm × 6 cm
MEA6	NATO17E	4 cm × 6 cm	Pt/Ti	4 cm × 6 cm
MEA7	NATO17J	4 cm × 6 cm	Pt/Ti	4 cm × 6 cm

Table 2. 5. Summary of the anode and cathode sizes and names used to fabricate the MEA's investigated in Chapter 5.

ozone molecular weight (g mol^{-1}), 6 is the number of electrons involved and F is Faraday's constant.

Power consumption by the MEA's can be calculated from:

$$P\ (kWh\ kg^{-1}\ O_3) = V \times 6 \times F/48/3600/\eta = 3.35\ V/\ \eta \qquad (2.11)$$

Where V is the cell voltage (V). Again η is the current efficiency (as a decimal).

2.12 Calculation of Ozone Generation Current Efficiency

2.12.1 Current efficiency using the cuvette cell

The electrochemical generation of ozone on small scale anodes took place in the cuvette cell. The ozone is generated as a result of water discharge according to equation (1.1).

Assuming 100% efficiency, the number of moles of O_3 generated ($n_{O3,100\%}$) according to Faraday's law is:

$$n_{O3,100\%} = \frac{Q}{zF} \qquad (2.12)$$

Where: Q is the charge passed (C), z is the number of electrons involved in the reaction (z = 6) and F is Faraday's constant.

The number of actual moles of O_3 produced ($n_{O3,ac}$) is:

$$n_{O3,ac} = C_{O3}.V \qquad (2.13)$$

Where C_{O3} is the concentration of the ozone in solution, expressed in mol L^{-1}, V is the volume of the solution, which is 3 cm^3 (volume of the cuvette). According to the Beer – Lambert Law:

$$A_{O3} = \in_{O3}.b.C_{O3} \quad (2.14)$$

$$C_{O3} = \frac{A_{O3}}{\in_{O3}.b} \quad (2.15)$$

$$n_{O3,ac} = \frac{A_{O3}.V}{\in_{O3}.b} \quad (2.16)$$

Where A_{O3} is ozone absorbance, $\in_{O3}$ is the molar absorbtivity of ozone , 3000 L mol^{-1} cm^{-1} [22], b is the path length of the sample (cm) - that is, the path length of the cuvette in which the sample is contained (b = 1 cm).

$$n_{O3,ac} = \frac{A_{O3}.3/1000}{3000.1} = \frac{A_{O3}}{1000000} = \frac{A_{O3}}{10^6} \quad (2.17)$$

The current efficiency (%) is:

$$\eta\ \% = \frac{n_{O3,ac}}{n_{O3,100\%}} \times 100 \quad (2.18)$$

$$\eta\ \% = \frac{A_{O3}.z.F}{10^6.Q} \times 100 \quad (2.19)$$

$$\eta\ \% = \frac{A_{O3}.6.96480}{10^6.Q} \times 100 \quad (2.20)$$

$$\eta\ \% = 58 \times \frac{A_{O3}}{Q} \quad (2.21)$$

$$Q = \int_{t=0}^{t=n} I.t \quad (2.22)$$

Where I is the current (A) and t is the time (s).

2.12.2 Current efficiency using the glass or polycarbonate cells

For ozone in a gas or solution stream at a flow rate of *f* (cm^3 min^{-1}), the number of moles of ozone generated per second is:

$$n_{O3,ac} = \frac{A_{O3}}{\in_{O3}.b} \times \frac{f}{60} \times \frac{1}{1000} = \frac{A_{O3}.f}{\in_{O3}.b.60000} \quad (2.23)$$

The number of moles of ozone generated in 1 s at a current I assuming 100% current efficiency is:

$$n_{O3,100\%} = \frac{I}{6.F} \quad (2.24)$$

The current efficiency η% is:

$$\eta\,\% = 100\left[\frac{n_{O3,ac}}{n_{O3,100\%}}\right] \quad (2.25)$$

$$\eta\,\% = 100\left[\frac{\left(\frac{A_{O3}.f}{\in_{O3}.b.60000}\right)}{\left(\frac{I}{6.F}\right)}\right] \quad (2.26)$$

$$\eta\,\% = \frac{A_{O3}.f.F}{100.\in_{O3}.I} \quad (2.27)$$

$$\eta\,\% = \frac{96480.A_{O3}.f}{300000.I} \quad (2.28)$$

$$\eta\,\% = \frac{0.32.A_{O3}.f}{I} \quad (2.29)$$

In flow mode, current efficiencies were calculated for both the gas phase and dissolved ozone.

2.13 Durability Studies

To assess the durability of the anodes, they were electrolysed in a 250 cm^3 beaker at 100 mA cm^{-2} in 1M $HClO_4$ using a 5 cm x 5 cm Pt/Ti mesh as counter electrode. The cell voltage was monitored throughout the electrolysis. At intervals, the activity and selectivity of the anodes were assessed in the glass cell in flow mode at 100 mA cm^{-2} in 1M $HClO_4$; the total current efficiency was calculated from the gas and solution ozone absorbances at steady state (each experiment was run for *ca*. 15 – 20 minutes).

2.14 Dye Decolourisation

2.14.1 Dyes

Reactive Blue 50 (RB50) dye was the main dye used in the decolourisation (colour removal) experiments reported in this thesis. For the purpose of comparison, the decolourisation of Naphthol Green B (NGB) and Congo Red (CR) dyes was also studied.

The UV – Vis spectra of 100 mg dm^{-3} in Millipore water of the three dyes are shown in fig. 2.13. A summary of the wavelength of the various peaks in fig. 2.13 and the molecular formula and structures of the three dyes is presented in table 2.6.

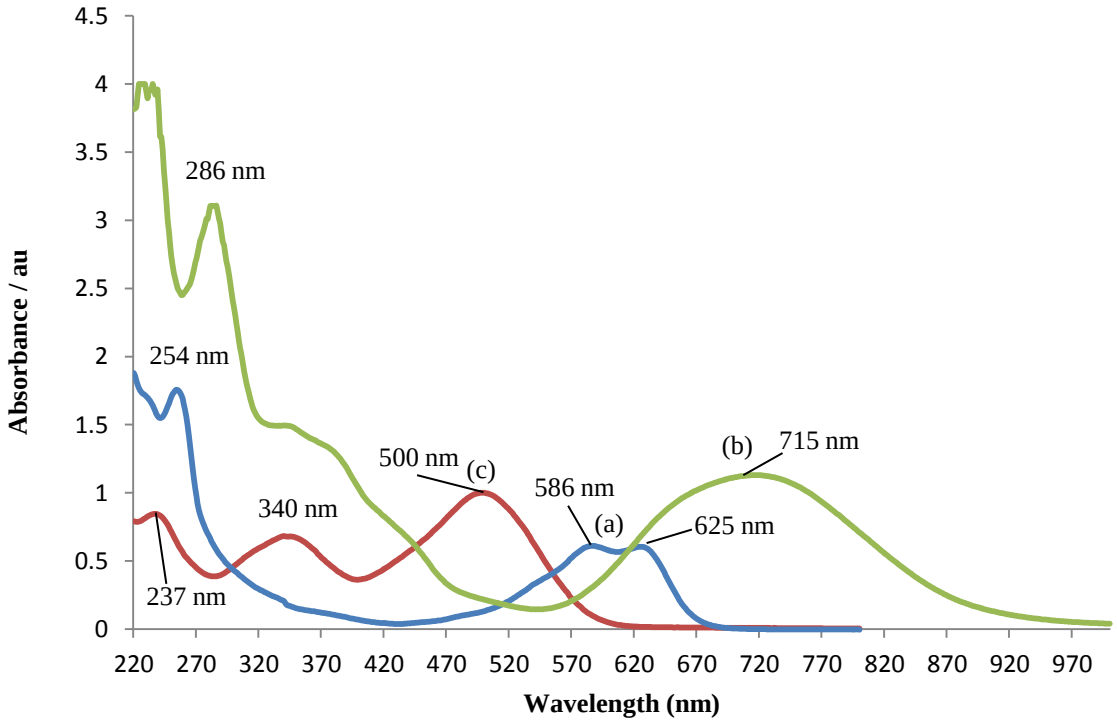

Figure 2. 13. UV-Vis spectra of 100 mg dm^{-3} of (a) RB50, (b) NGB and (c) CR solutions in Millipore water.

In general, the UV – Vis spectra of the types of dyes under investigation show bands in the visible region (associated with colour) and in the UV region (associated with aromatic rings); in particular, bands near 254 nm are associated with benzene rings[111, 123]. Kusmierek et al.[123] reported that absorption bands in the near UV region (280nm – 380 nm) may be attributed to the unsaturated system of benzene and naphthalene. Martinez – Huitle et al.[147] postulated that UV band at 310 nm was due to naphthalene. In the case of the RB50 (see fig. 2.13 and table 2.6), bands at 625 nm and 586 nm have been attributed to the anthraquinone moiety of the dye, and the band at 254 nm to the benzene ring [111, 123, 147]. The UV – Vis spectrum of CR (see fig. 2.13 and table 2.6) has a band at 500 nm, due to the presence of the diazo bonds, and bands at 340 nm and 237 nm due to naphthalene and benzene rings, respectively[111, 123, 147]. The UV – Vis spectrum of NGB (see fig. 2.13 and table 2.6) has a band at 715 nm, due to the nitroso chromophore, and bands at 280 nm may be due to the naphthalene rings.

It may be seen from table 2.6 that the RB50 has several functional groups: 2 sulphonates

Dye	Molecular Formula	Structure	Visible Peaks:	UV Peaks:
RB50	$C_{26}H_{23}Br_2N_3O_9S_2Na_2$ (ChemNet)	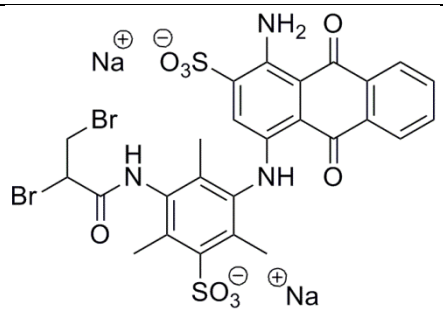	625 nm & 586 nm	254 nm
NGB	$C_{30}H_{15}FeN_3Na_3O_{15}S_3$ (Sigma – Aldrich)	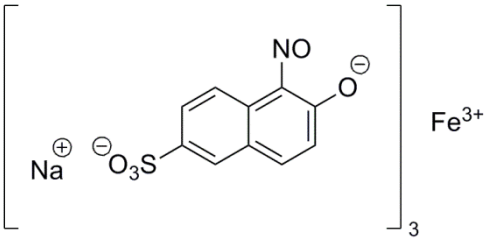	715 nm	286 nm
CR	$C_{32}H_{22}N_6Na_2O_6S_2$ (Sigma – Aldrich)	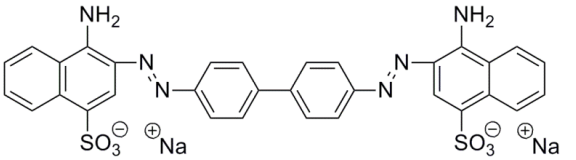	500 nm	340 nm & 237 nm

Table 2. 6. Molecular formula, structure and the visible & UV bands of RB50, NGB and CR.

(to render the soluble in water), 3 × CH_3, NH_2 and 2 × Br; the CR has 2 × sulphonates and 2 × NH_2 groups, whereas the NGB has 3 × sulphonates and 3 × NO functional groups.

An aqueous stock solution of each dye consisting of 1000 mg dm^{-3} was prepared. Several concentrations of the dyes were studied, and the required concentrations were obtained by diluting the stock solutions using Millipore water at room temperature.

2.14.2 The dye decolourisation methods

The dye solutions were decolourised by the means of four methods; electrochemical, ozonation, irradiation with UV_{245nm} light and the combination of O_3/UV_{254nm}. The optimum conditions for each decolourisation process were investigated using the RB50 solution, and then these conditions were then applied to decolourise the NGB and CR solutions.

2.14.3 Analytical method

The methods used to measure pH and chemical oxygen demand (COD), for the dye solutions are stated below. All of the experiments were carried out in accordance with the American Public Health Association (APHA) standard methods[148].

pH

The pH of the samples was measured using a HI 8520 (Hanna Instrument) pH meter. The pH meter was calibrated prior to use.

Chemical Oxygen Demand (COD)

The 'Closed Reflux Titrimetric Method'[148] was used to measure COD (procedure 5220 C), summarised as follows:

The COD was analyzed using HACH COD reactor. Two HACH test tubes (COD tubes) were used. The first test tube was used as blank, and the second was used for the sample. 2 cm^3 of Millipore water was added into the first COD tube, and 2 cm^3 of the sample was added to the second tube. 2 cm^3 of the digestion solution (an acidic solution of 0.075N potassium dichromate containing mercuric sulphate) and 3.5 cm^3 of sulphuric acid/silver sulphate solution were added to the two tubes. The two tubes were capped tightly and inverted gently several times to mix completely, and then they were placed in the preheated (to 150 ^oC) block for 2 hours. The tubes were then removed from the block, cooled and their contents were transferred in turn to 100 cm^3 conical flask. The content of the flask was titrated with 0.025N ferrous ammonium sulphate using ferroin indicator (the end point is blue-green to reddish-brown). The COD was then calculated as follows:

$$COD\ (mg\ dm^{-3}) = (a - b) \times c \times 8000/v \qquad (2.30)$$

$$= 100 \times (a - b) \qquad (2.31)$$

Where a is the volume of ferrous ammonium sulphate used for titrating the blank (cm^3), b is titration volume of the sample (cm^3), c is the normality of ferrous ammonium sulphate (0.025 N) and v is the sample volume (cm^3)

2.15 Electrochemical Decolourisation of Dye Solutions

Only the small (0.8 cm × 0.8 cm) anodes were used to investigate the dye decolourisation. Therefore, as described in section 2.9, the quartz cuvette cell was used and the cathode was a (0.8 cm × 0.8 cm) Pt/Ti mesh.

All of the electrochemical decolourisation experiments were carried out at constant current density, during which the cell voltage and absorbance (of the visible and UV peaks of the dye solutions described in section 2.14.1) were monitored at 0, 1, 3, 5 min and then at 5 min intervals for one hour in all experiments.

Figure 2.14 shows a picture of the electrochemical decolourisation system using the small scale Ni/Sb – SnO_2 anodes. It may be seen from the picture that the cuvette cell was placed in a cuvette holder connected to the Astranet spectrophotometer, which was connected to a laptop to measure the absorbance during the electrolysis. The baseline was collected using Millipore water with electrolyte prior to any readings being taken. In some experiments, the cuvette was inserted in the cuvette holder of the Shimadzu spectrophotometer as described in section 2.10.1.

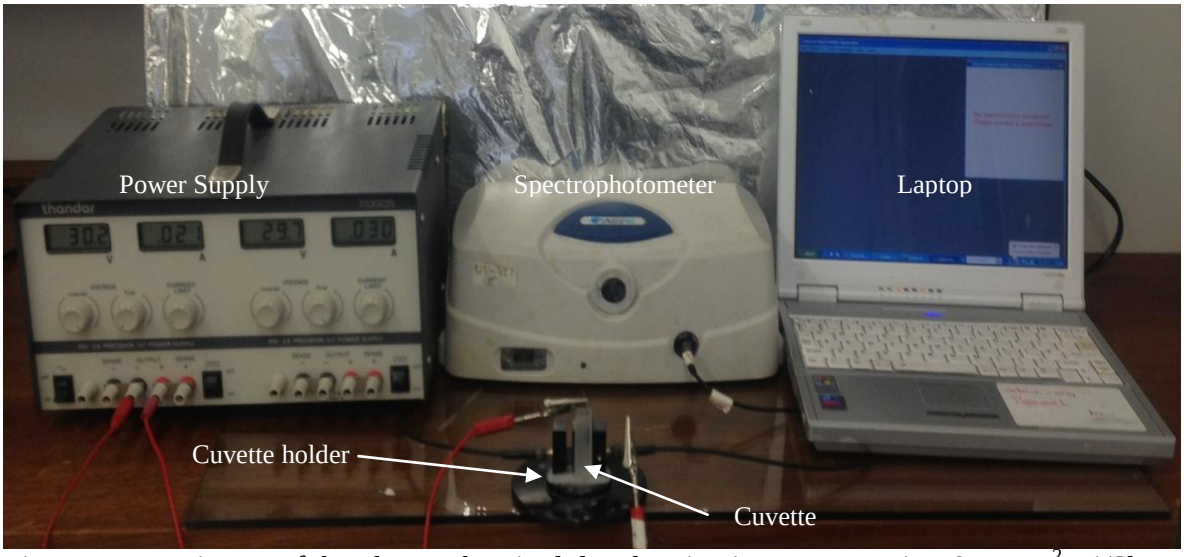

Figure 2. 14. Picture of the electrochemical decolourisation system using 0.64 cm^2 Ni/Sb – SnO_2 anodes.

To determine the optimum condition of the RB50 electrochemical decolourisation in the cuvette, several parameters were investigated including: current density, electrolyte type and concentration (added salts to the dye solution to increase its conductivity), pH (buffered), initial dye concentration, COD removal and decolourisation current efficiency. During the experiments, the cell voltage, absorbance at 625 nm, 586 nm and 254 nm were recorded, and at the end of the experiment COD was performed. Then decolourisation was estimated by the ratio $(A/A_0)_{625}$ and $(A/A_0)_{586}$, and benzene ring removal (dye degradation) by the ratio $(A/A_0)_{254}$.

2.15.1 The effect of current density

The current density required to effect efficient decolourisation reflects the cost of the method as it directly reflects power consumption. To investigate the effects of the current density on the electrochemical decolourisation in the cuvette, 3 cm^3 of 100 mg dm^{-3} RB50 solution in 3 g dm^{-3} aqueous Na_2CO_3 electrolyte was electrolysed at a constant current

density of: 10 mA cm^{-2}, 25 mA cm^{-2}, 50 mA cm^{-2}, 75 mA cm^{-2} and 100 mA cm^{-2} for 1 hour.

2.15.2 The effect of electrolyte

To investigate the effect of the electrolyte on the decolourisation of RB50 solution (at the optimum current density), 3 cm^3 of 100 mg dm^{-3} RB50 solution in 3 g dm^{-3} aqueous $NaClO_4$, NaCl, $NaHCO_3$, or Na_2SO_4 was electrolysed. The electrolyte that gave the best decolourisation was then selected and its concentration was varied to optimise it. To investigate the optimum electrolyte concentration, again 3 cm^3 of 100 mg dm^{-3} RB50 solution in 1 g dm^{-3}, 3 g dm^{-3}, 5 g dm^{-3} and 7.5 g dm^{-3} aqueous solution of the optimum electrolyte.

2.15.3 The effect of buffered pH

The effect of pH on the decolourisation of RB50 solution under the optimum conditions of current density and electrolyte was investigated using 3 cm^3 of 100 mg dm^{-3} RB50 solution buffered at pH 2, pH 7 and pH 11. The buffers were prepared according to Lide[149] as follows:

pH = 2, in 100 cm^3 volumetric flask, 25 cm^3 of 0.2 M KCl, 6.5 cm^3 of 0.2 M HCl, 10 mg of the RB50 powder and the optimum salt concentration were added together and supplemented by Millipore water to 100 cm^3, and mixed well.

pH = 7, in 100 cm^3 volumetric flask, 50 cm^3 of 0.1 M H_2KO_4P , 29.1 cm^3 of 0.2 M NaOH, 10 mg of the RB50 powder and the optimum salt concentration were added together and supplemented by Millipore water to 100 cm^3, and mixed well.

pH = 11, in 100 cm^3 volumetric flask, 50 cm^3 of 0.05 M $NaHCO_3$, 22.7 cm^3 of 0.2 M NaOH, 10 mg of the RB50 powder and the optimum salt concentration were added together and supplemented by Millipore water to 100 cm^3, and mixed well.

3 cm^3 of each buffered solution was electrolysed in the cuvette as stated above.

2.15.4 The effect of initial dye concentration

To investigate the effect of initial dye concentration on the decolourisation of RB50 solution, 3 cm^3 of 50 mg dm^{-3}, 100 mg dm^{-3}, 200 mg dm^{-3}, 300 mg dm^{-3} or 500 mg dm^{-3} RB50 at the optimum concentration of the best electrolyte and at the optimum current density was electrolysed in the cuvette.

2.15.5 COD and decolourisation current efficiency

At the optimum conditions obtained so far, the COD was measured at several time intervals. The RB50 solution was electrolysed for 5 min, the experiment stopped and the COD was measured. A fresh sample of RB50 solution was then electrolysed for 10 min and the COD determined. The experiment was repeated for electrolysis time of 15, 20, 30, 45 and 60 min.

The decolourisation current efficiency at time t is given by:

$$CE\% = (COD_0 - COD_t).F.V/8.I.t \qquad (2.32)$$

Where COD_0 and COD_t are the chemical oxygen demand at time 0 and time t, F is the Faraday's constant, V the solution volume (3×10^{-3} dm), I is the current (A).

2.15.6 The electrochemical decolourisation of NGB and CR solutions

The NGB and CR solutions were decolourised under the optimized conditions determined as above.

2.16 Dye Decolourisation by Ozone

Ozone was generated using an MEA in recycle mode system, as described above (see sections 2.3 and 2.10.2). This will be called the MEA - based Ozone Generation System (MEA – OGS) as shown in fig. 2.12. Where 1 M $HClO_4$ was used as catholyte and anolyte.

2.16.1 Dye ozonation system

The ozonation system, shown in fig. 2.15, consisted of the MEA – OGS, a gas diffuser, UV – Vis flow cells and a bubble column reactor (BCR). The BCR was a Pyrex tube of 1 m length and 3 cm diameter.

The dye solution was placed in the bubble column reactor. The ozone with oxygen and nitrogen gases from the MEA-OGS passed through a UV – Vis cell, then through a gas diffuser to generate fine bubbles to facilitate ozone gas dissolution at the bottom of the BCR. Any unreacted ozone, oxygen and nitrogen along with any other gases generated from the decolourisation process then left the BCR and passed through a UV – Vis cell. Samples of the treated dye solution were taken at several intervals for UV – Vis analysis using Shimadzu spectrophotometer and for COD analysis.

The effect of ozone dose and pH were investigated. The experiment at the optimum ozone

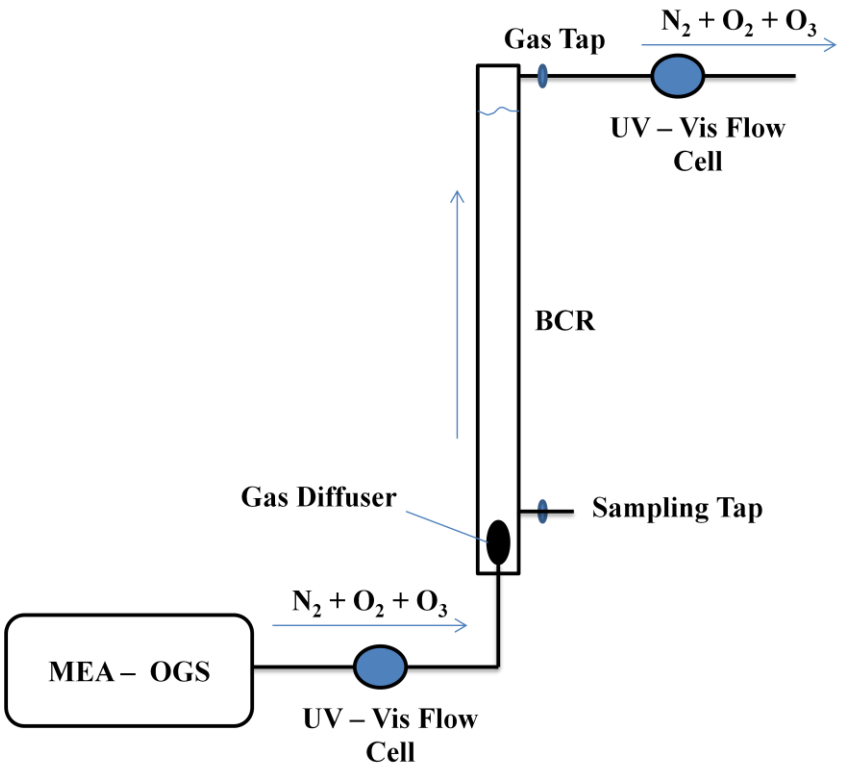

Figure 2. 15. The ozonation system

dose and pH was repeated using 500 cm^3 of 100 mg dm^{-3} NGB or CR dissolved in Millipore water.

The effect of ozone dose

To investigate the effect of ozone dose on the decolourisation process, 500 cm^3 of 100 mg dm^{-3} RB50 in Millipore water was ozonated in the BCR at ozone doses of 0.4 mg min^{-1}, 0.7 mg min^{-1}, 1.2 mg min^{-1}, 1.3 mg min^{-1} and 1.9 mg min^{-1}, for one hour. These doses were obtained by operating the MEA – OGS at a constant current of 0.6 A, 1.2A, 1.8 A, 2.4A, and 3 A, respectively. N_2 was used as carrier gas with a flow rate of 1000 cm^3 min^{-1}. The ozone dose was calculated according to:

$$O_3 \text{ Dose (mg min}^{-1}) = 16 \times 10^{-3} \times A \times f \qquad (2.33)$$

where A is the absorbance of the gas phase ozone at the exit of the MEA – OGS and *f* is the carrier gas (N_2) flow rate (cm^3 min^{-1}).

The effect of pH

To investigate the effect of pH on the ozonation process, 500 cm^3 of 100 mg dm^{-3} RB50 dissolved in Millipore water buffered at pH 2, pH 7 and pH 11 was ozonated at the

optimum ozone dose for one hour. The pH buffered solution was prepared as discussed in section 2.15.3.

2.17 Decolourisation by Ultraviolet Irradiation

Figure 2.16 shows the ultraviolet (UV) irradiation system used for decolourising the dye solutions. It may be seen from the figure that the system consisted of a UV – lamp (TUV 16W 4P SE UNP, Philips, UK, λ_{max} = 254 nm) inserted into a quartz tube, surrounded by a Pyrex tube. This configuration allows the dye solutions to be exposed to the maximum intensity of UV – light. N_2 gas at 1000 cm^3 min^{-1} was injected and diffused at the bottom of the reactor.

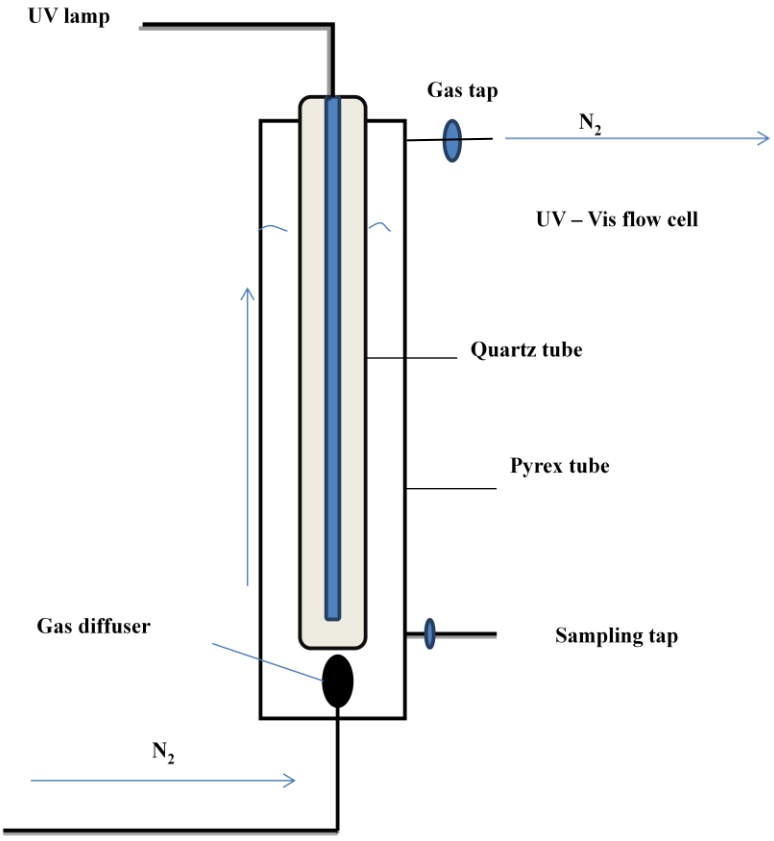

Figure 2. 16. The UV irradiation system

500 cm^3 of 100 mg dm^{-3} RB50, NGB or CR solutions dissolved in Millipore water were irradiated for 1 hour, separately. UV – Vis spectra were taken of samples (3 cm^3) every 5 min using the Shimadzu spectrophotometer. COD analysis was performed at the end of each experiment.

2.18 Decolourisation by Ozonation / Ultraviolet Radiation

Figure 2.17 shows the ozone / UV irradiation (O_3/UV) system. It may be seen from the figure that the system consisted of the UV irradiation system shown in fig. 2.16 connected to the MEA – OGS.

To investigate the efficiency of the O_3/UV system on decolourising dye solutions, 500 cm^3 of 100 mg dm^{-3} of RB50 was subjected to simultaneous ozone and UV exposure for one hour under the optimum ozonation conditions determined as in section 2.16.1. The sampling was carried out as discussed above. NGB and CR solutions under the same conditions were decolourised by the O_3/UV combination.

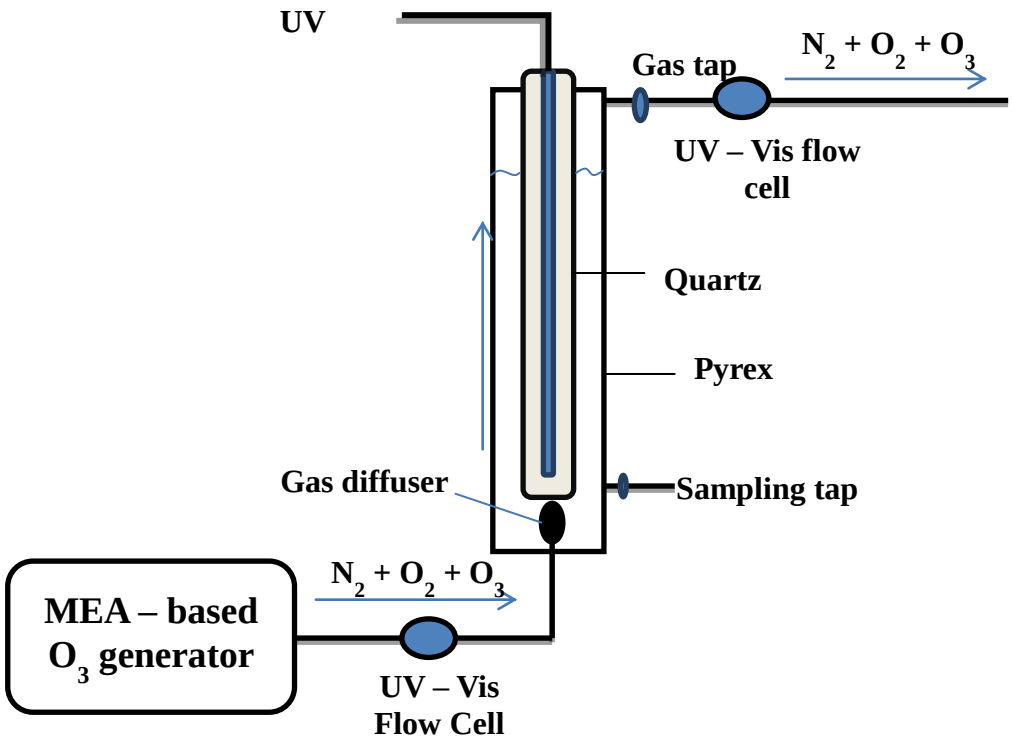

Figure 2. 17. The ozonation / UV irradiation system

2.19 Removal Efficiency

The decolourisation and benzene ring destruction was estimated by the removal ratio as follows:

$$R = (A_0/A_t) \qquad (2.34)$$

Where A_0 is the initial absorbance at the specified wavelength (625 nm & 254 nm, 500 nm and 715 nm for RB50, CR and NGB, respectively) before treatment; A_t is the

corresponding absorbance at time t during treatment. Complete benzene ring destruction was considered when the peak (of RB50 UV – Vis spectra) at 254 nm disappeared.

The COD removal was determined as:

$$R\ (\%) = 100 \times (COD_0 - COD_t)/COD_0 \qquad (2.35)$$

Where: COD_0 is initial COD before treatment; COD_t is the COD at time t during treatment.

In the following chapter, the structure, selectivity and activity of 0.8 cm × 0.8 cm Ni/Sb – SnO_2 anodes will be discussed.

CHAPTER THREE

3 Structure and Activity of Small (0.8 cm × 0.8 cm) Ozone Anodes

3.1 Introduction

In the following discussion, data are included on small 0.8 cm × 0.8 cm standard Ni/Sb-SnO_2 (SNATO) anodes, without or with Au (AuSNATO) or Pb (PbSNATO), and NATO anodes in order to investigate the surface composition (by SEM and EDX), electrochemical behaviour (*ie*. capacitive current and ferrocyanide oxidation) and ozone activity.

3.1.1 The Anodes

The work reported in this chapter was carried out on small scale anodes including the anode series KZ01 – KZ06. As was shown in table 2.3 and the Appendix II, all of the anodes were 0.8 cm × 0.8 cm Ti meshes first coated with an electrodeposited interlayer (EDIL) (except the KZ06 series), and then with the electrocatalyst (Ni/Sb – SnO_2) using the thermal deposition method described in section 2.2.1. The electrocatalyst was deposited from an ethanolic precursor solution containing $SnCl_4$. $5H_2O$, $SbCl_3$, and $NiCl_3.6H_2O$ of a ratio Sn: Sb: Ni = 500: 8: 3, with or without $HAuCl_4$ or $Pb(Ch_3COOH)_4$. The coating process was repeated up to 20 times (see Appendix II). All of the anodes underwent the same heat treatment during the coating process, unless otherwise stated. The loading of the electrocatalyst varied according to the number of coatings.

3.1.2 Why dope with Pb/Au?

Chan's discovery of the ozone activity of the Ni/Sb-SnO_2 anode [75, 93] is unprecedented in the ozone electrochemical literature; hence one must look elsewhere for a starting point from which to build a model. To this end, the methods employed to extend the service life of Sb-SnO_2 anodes may be used as a starting point. These anodes have a highly restricted service life[99, 150]; *eg*. in accelerated lifetime tests conducted at 1 A cm^{-2}, the service life of such anodes may be as little as 3 – 10 hours[99]. However, Montilla and co-workers[99, 150, 151] have reported that addition of Pt at an optimum concentration of 3 at.% increases the service life by up to 2 orders of magnitude.

Pt has a low overpotential for oxygen evolution[152], and hence would be unsuitable for use

in ozone anodes; thus Pb and Au (which have higher oxygen overpotentials than Pt) were considered as possible dopants.

3.2 Cyclic Voltammetry Experiments: Capacitive Currents

Cyclic voltammetry is commonly employed to characterize the capacitive behaviour of porous electrodes ([141] and references therein), with the capacitance current given by equation (2.7) (see discussion in section 2.8.2).

Figure 3.1 shows a typical set of cyclic voltammograms as a function of scan rate, obtained using the SNATO02H anode. The cyclic voltammograms in the figure are representative of all small scale anodes (KZ01 – KZ06). It may be seen from the figure that increasing the scan rate resulted in increasing current at the same potential, as expected.

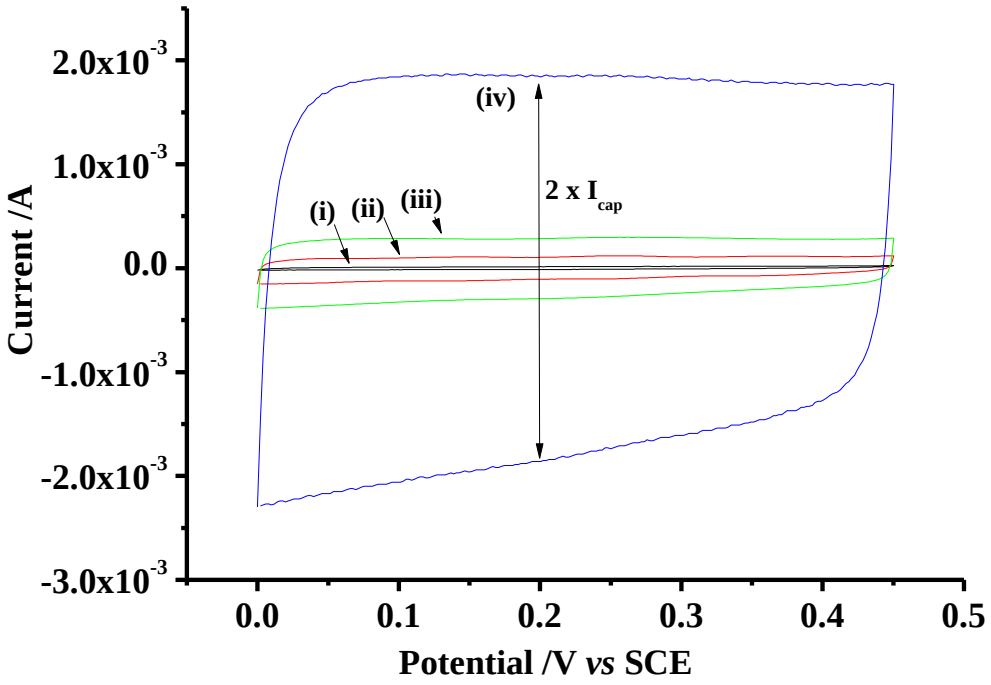

Figure 3. 1. Typical cyclic voltammograms of the 0.8 cm × 0.8 cm anode SNATO02H immersed in 0.5 M Na_2SO_4 as a function of scan rate, (i) to (iv): 10, 50, 100 and 500 mV s^{-1}, respectively.

Figure 3.2 shows a plot of I_{cap} measured between 0.1 V and 0.45 V from cyclic voltammograms of the SNATO anodes immersed in aqueous 0.5 M Na_2SO_4 at 0.5 V s^{-1}. As may be seen from the figure, there appears to be a clear, linear relationship between catalyst loading and the surface area of the catalyst coating exposed to electrolyte. The data in fig. 3.2 were collected at the high scan rate to optimize discrimination between the

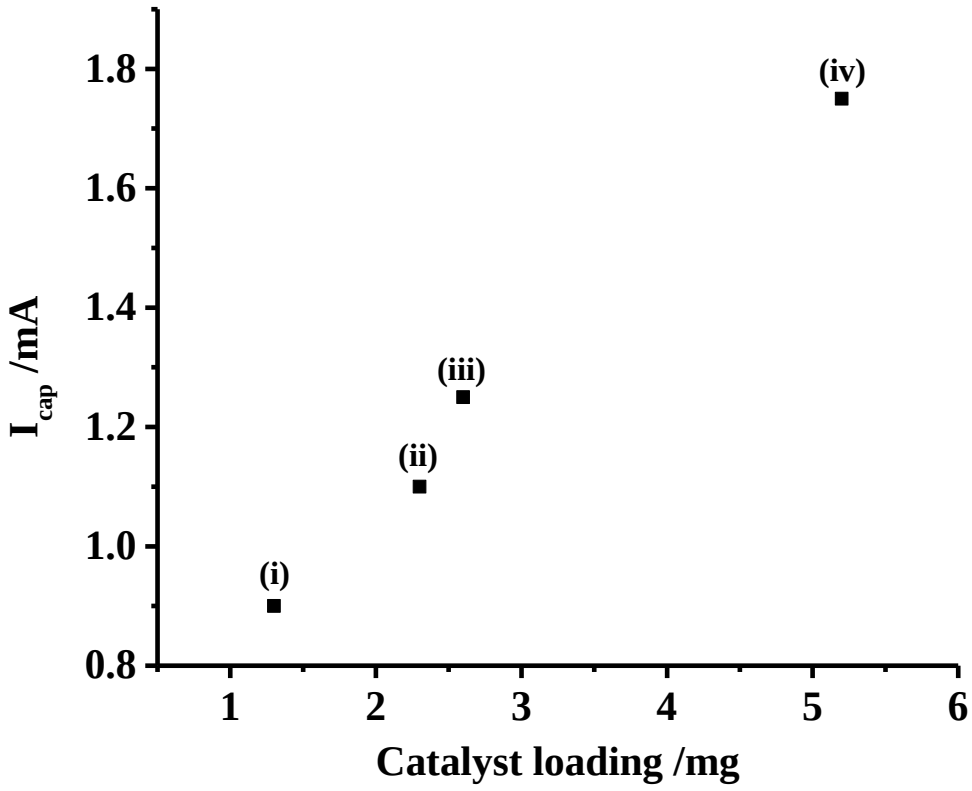

Figure 3. 2. Plot of capacitive current vs. catalyst loading for 0.8 cm × 0.8 cm SNATO anodes. The anodes were: (i) SNATO02D, (ii) SNATO02F, (iii) SNATO02G and (iv) SNATO02H. The electrolyte was aqueous 0.5M Na_2SO_4.

electrodes; however, the same trend was observed in the cyclic voltammograms recorded at 50 mV s^{-1}. If the capacitive currents in fig. 3.2 are taken as order-of-magnitude indications of the true values, then the specific capacitance varies from 0.8 to 1.5 Fg^{-1} for electrodes SNATO02D to SNATO02H; this is not an unreasonable range when compared to 10 – 16 Fg^{-1} exhibited by higher surface area, Sb-SnO_2 xerogels [142] and suggests a doubling in real, accessible area on increasing catalyst loading from 1.3 to 5.1 mg, and this was generally observed. The average values of I_{cap} obtained for all SNATO, AuSNATO and PbSNATO anodes are summarised in tables 3.1 – 3.3, respectively. The capacitive current (I_{cap}) presented in the tables were measured at 0.2 V and measured at highest scan rate of 500 mV s^{-1}.

3.3 SEM and EDX Characterization of the Anodes

As discussed in section 2.2, Ti meshes were used as substrate for the anodes. Therefore, it became clear that morphologies at the nodes (crossing of strands) and at the strands were

N° of coats	EDIL /mg	Catalyst loading /mg	I_{cap} /mA	ΔE / V	O_2/O_3 Onset potential /V	d_f	I_{30s} /mA	η /%
5	0.1	0.8	0.9	0.13	1.79	1.72	33	10
7	0.5	2.3	1.1	0.13	1.82	1.76	43	12
10	0.8	2.1	1.3	0.10	1.81	1.82	47	22
15	0.9	2.9	1.5	0.12	1.78	1.84	50	26
20	0.8	3.5	1.8	0.10	1.81	1.86	54	30

Table 3. 1. Summary of the data (the average value) obtained by cyclic voltammetry in 0.5 M Na_2SO_4 with and without ferrocyanide and 1 M $HClO_4$ using SNATO anodes.

Au ratio	N° of coats	EDIL /mg	Catalyst loading /mg	I_{cap} /mA	ΔE / V	O_2/O_3 Onset potential /V	d_f	I_{30s} /mA	η /%
0.1	20	0.8	4.6	1.96	0.12	1.84	1.83	77	19
0.3	20	0	4.3	1.6	0.15	1.78	1.74	85	14
1.5	20	0.3	3.5	1.65	0.12	1.81	1.8	60	10
2.25	20	0.5	4.7	1.63	0.12	1.75	1.77	66	6.6

Table 3. 2. Summary of the data (the average value) obtained by cyclic voltammetry in 0.5 M Na_2SO_4 with and without ferrocyanide and 1 M $HClO_4$ using AuSNATO anodes.

Pb ratio	Coats No	EDIL /mg	Catalyst loading /mg	I_{cap} /mA	ΔE / V	O_2/O_3 Onset potential / V	d_f	I_{30s} /mA	η / %
0.5	5	0.1	0.8	0.56	0.12	1.87	1.79	42	16
	10	2	1.9	1.7	0.12	1.91	1.82	59	16
	15	1.8	3.2	1.6	0.12	1.89	1.82	59	16
	20	1.7	4.7	1.7	0.12	1.91	1.78	89	22
1.5	20	0	4.4	1.2	0.12	1.92	1.77	72	33

Table 3. 3. Summary of the data (the average value) obtained by cyclic voltammetry in 0.5 M Na_2SO_4 with and without ferrocyanide and 1 M $HClO_4$ using PbSNATO anodes.

different. The data in fig. 3.2 suggest that the thicker electrodes at least are porous, and this is supported by the SEM data: fig. 3.3(a) shows a typical micrograph of SNATO02D, and fig. 3.3(b) a micrograph of SNATO02H, which are also representative of all SNATO electrodes, the micrographs were taken from areas on the strands of the coated meshes. As may be seen, the thicker anodes have the typical 'cracked earth' morphology, with large fissures giving 3-dimensional access to the catalyst layer.

The variation in catalyst coating may be inferred from figs. 3.3(a) and (b), and more clearly from a comparison of figs. 3.4(a) and (b) which shows representative EDX spectra of anodes SNATO02D and SNATO02H, respectively. The coating on SNATO02D is sufficiently thin to allow detection of the underlying Ti substrate. The data shown in

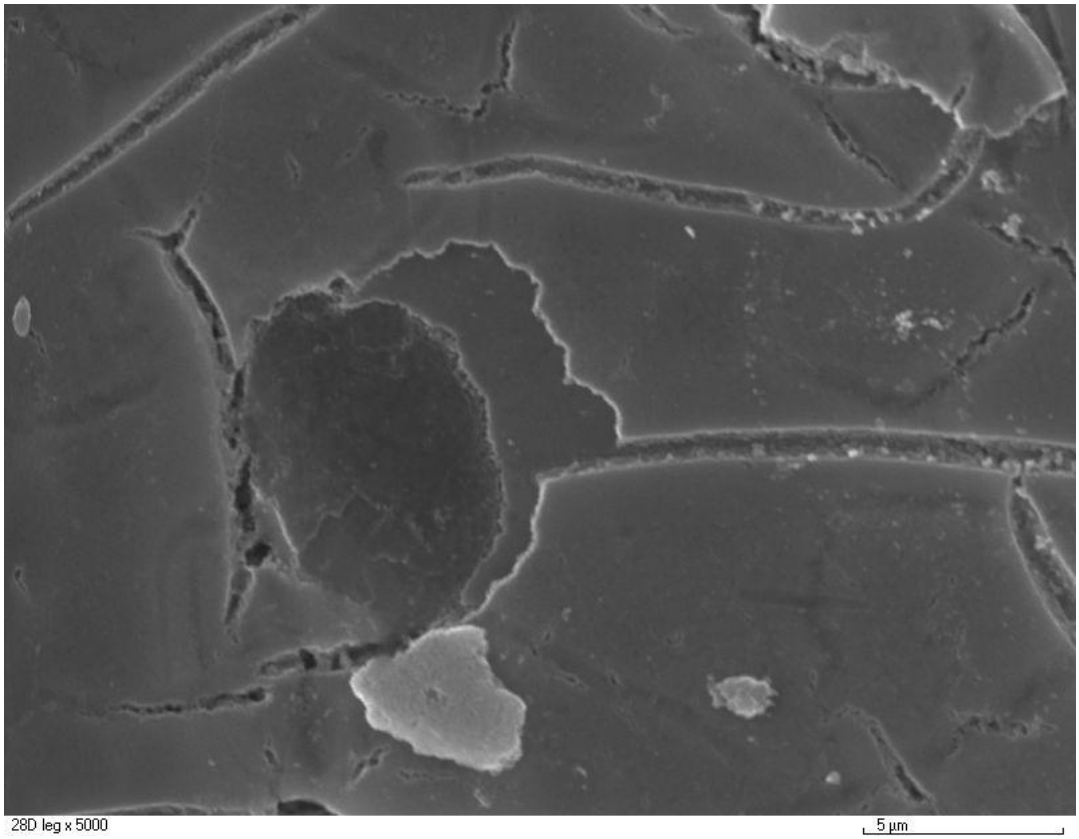

(a)

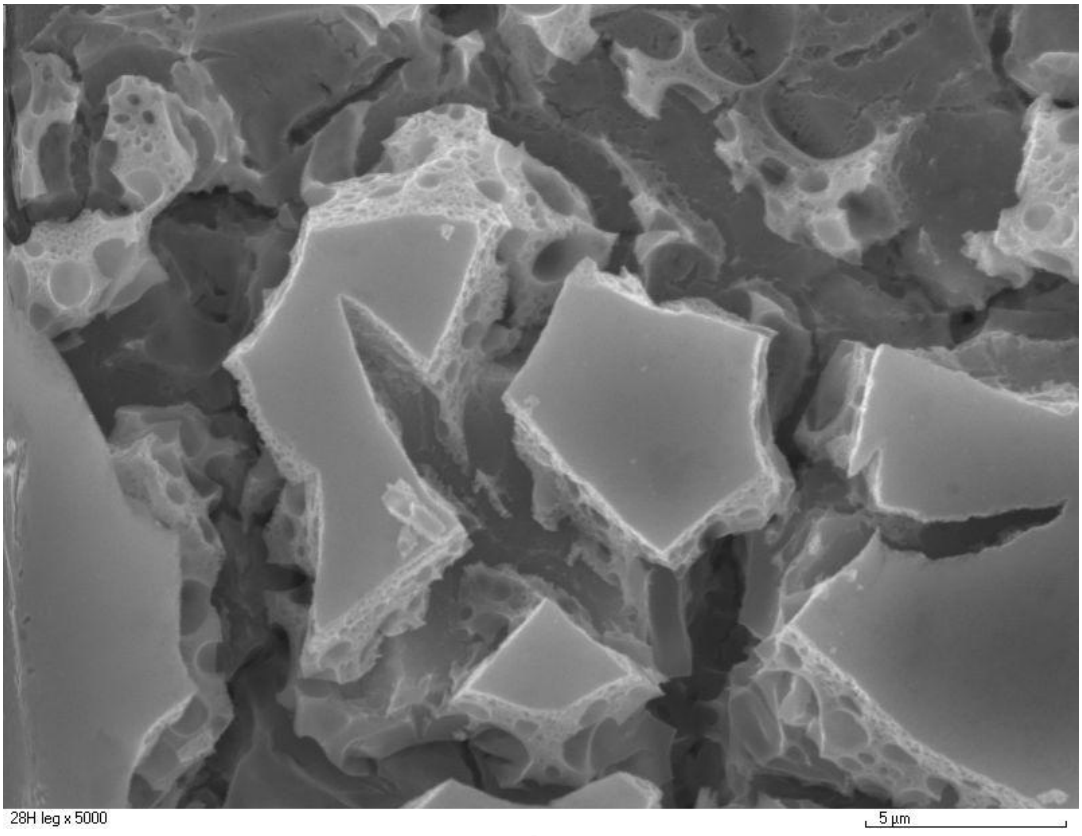

(b)

Figure 3. 3. SEM micrographs (× 5000, bar = 5 µm) of a wire strand of (a) SNATO02D and (b) SNATO02H.

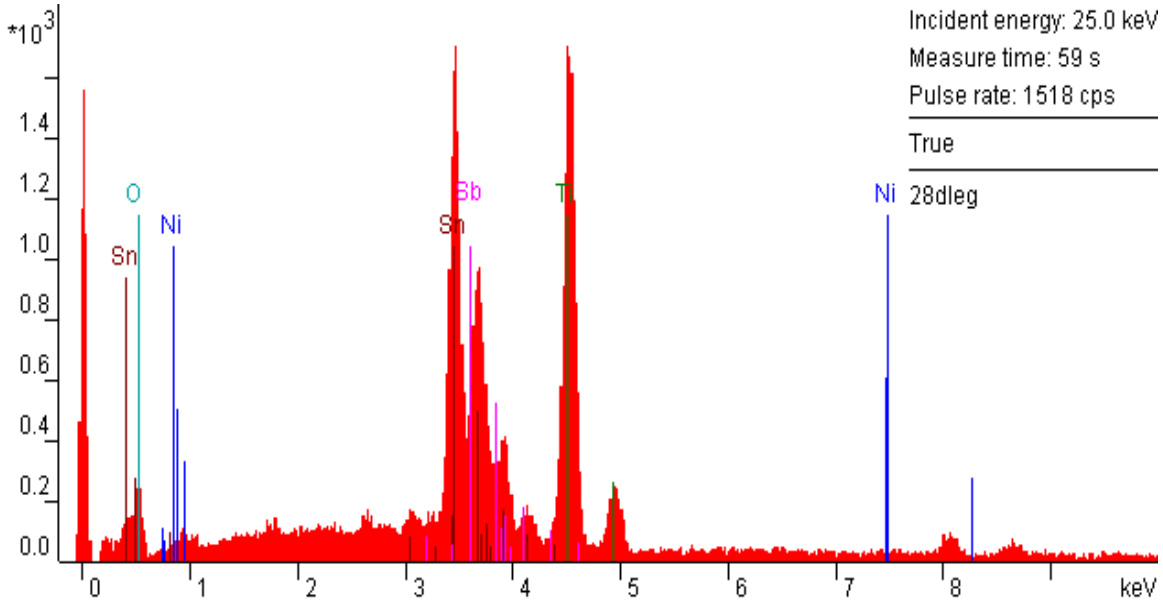

(a)

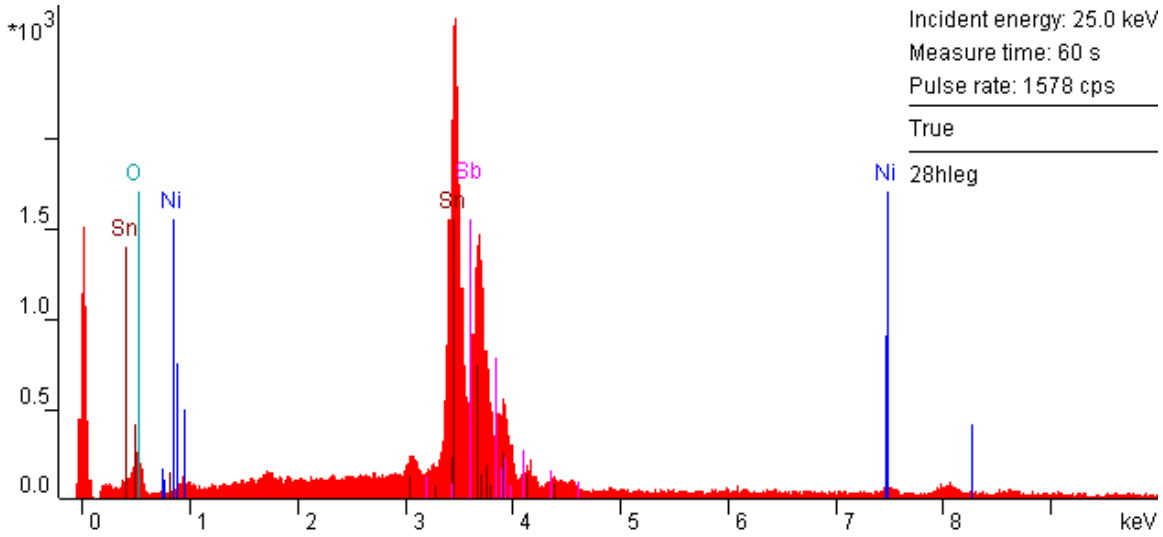

(b)

Figure 3. 4. EDX spectra of the anodes in fig. 3.3, taken from the strands of the meshes, SNATO02D and (b) SNATO02H.

figs. 3.3 and 3.4 are representative of the all anodes made in the same way.

Figure 3.5 shows typical micrographs of (a) a node and (b) a strand of AuSNATO01D anode, (c) a node and (d) a strand of PbSNATO04P anode. These micrographs are representative of all AuSNATO and PbSNATO anodes. It may be noted that the nodes were more cracked than the strands may be due to higher thickness of catalyst. As may be seen, all anodes have the typical 'cracked earth' morphology.

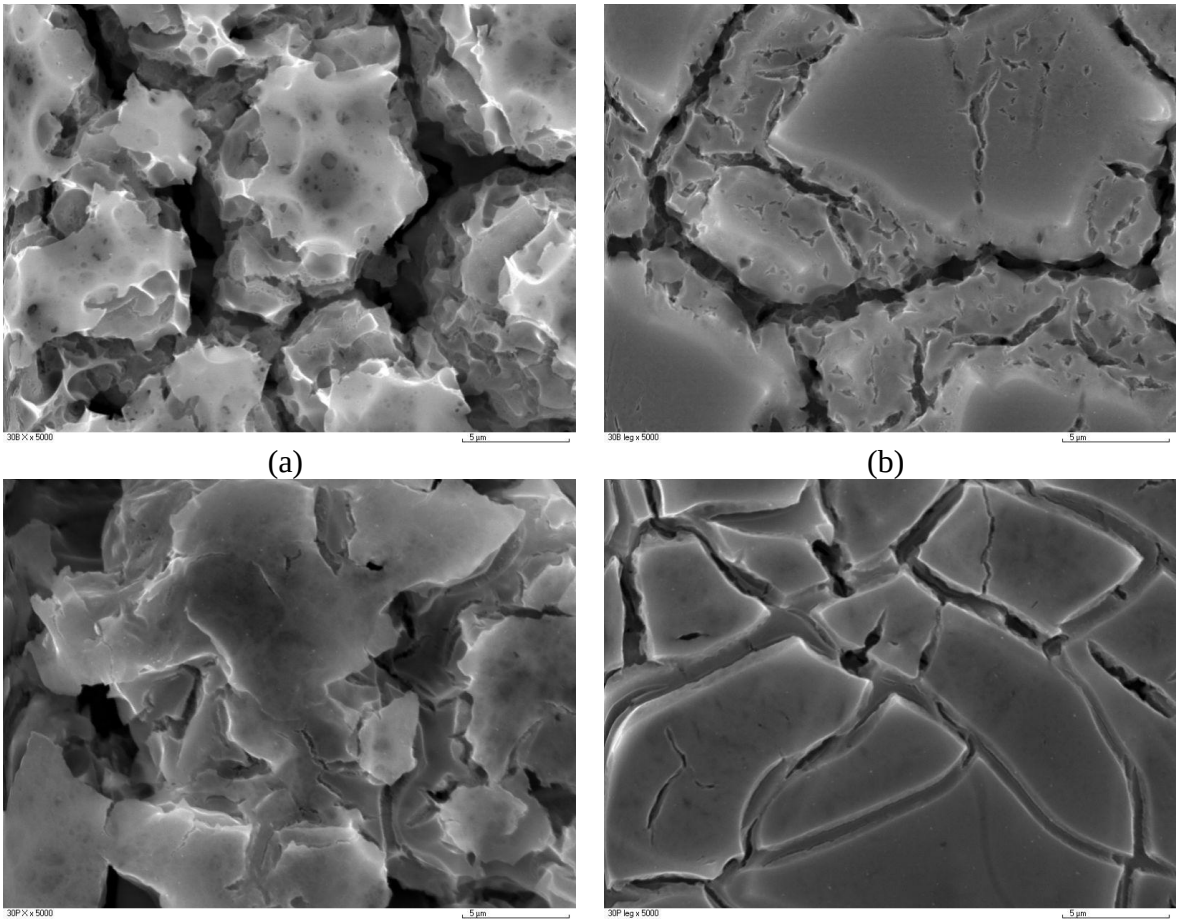

Figure 3. 5. Typical SEM micrographs (× 5000, bar = 5 µm) of: (a) node of AuSNATO04B anodes, (b) strand of AuSNATO04B anodes, (c) node of PbSNATO04P anodes and (d) strand area of PbSNATO04P anodes.

The cracked earth morphology was observed for all small anodes (SNATO, AuSNATO and PbSNATO), and it was observed by other research groups and generally attributed to thermal shock [90-92] during the sudden cooling caused by withdrawing the anodes from furnace [75, 99].

The variation in catalyst coating between the node and strand areas may be inferred from figs. 3.5(a)&(c) (for nodes) and (b)&(d) (for strands), and more clearly from a comparison of figs. 3.6(a)&(c) and (b)&(d) which shows representative EDX spectra of AuSNATO (a)&(b) and PbSNATO (c)&(d) anodes at nodes (a)&(c) and at strand areas (b)&(d). The coating on the strands is thinner than that of the nodes so that underlying Ti substrate appeared in their EDX spectra.

SEM and EDX of all anodes were taken before they were used for ozone generation.

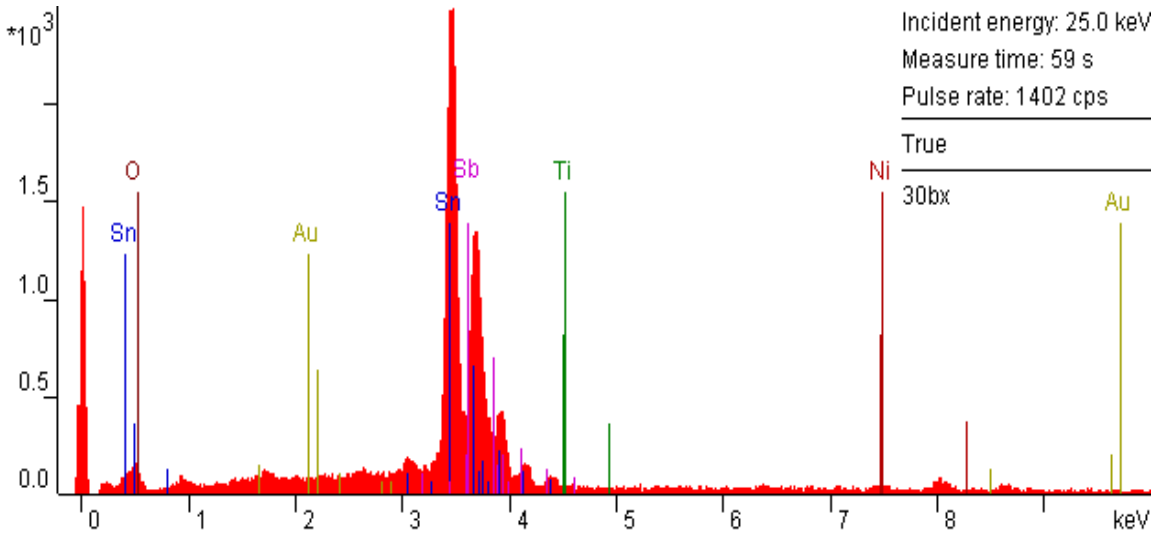
*10^3
1.5
1.0
0.5
0.0
O
Sn
Au
Sb
Sn
Ti
Ni
Au
Incident energy: 25.0 keV
Measure time: 59 s
Pulse rate: 1402 cps
True
30bx
0
1
2
3
4
5
6
7
8
keV

(a)

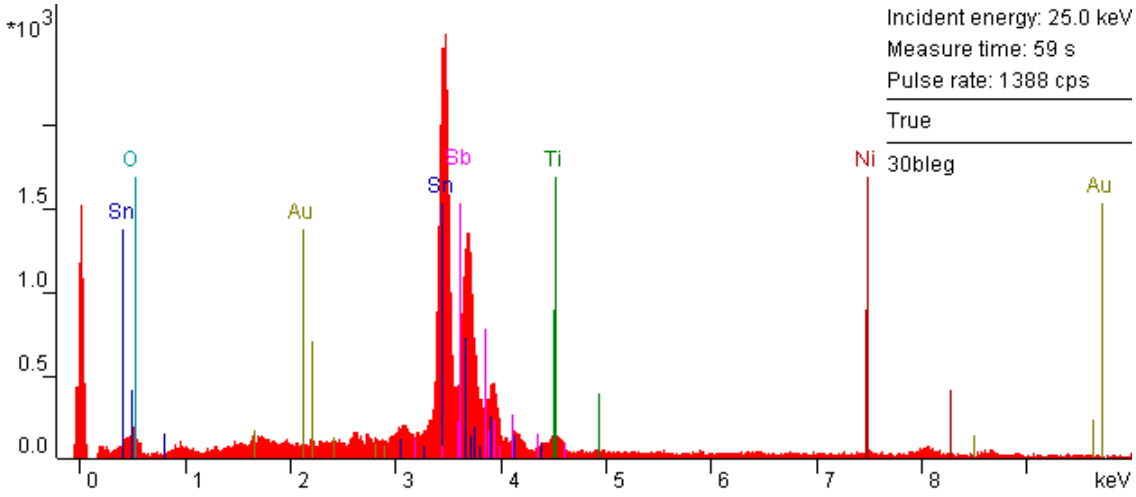
*10^3
1.5
1.0
0.5
0.0
O
Sn
Au
Sb
Sn
Ti
Ni
Au
Incident energy: 25.0 keV
Measure time: 59 s
Pulse rate: 1388 cps
True
30bleg
0
1
2
3
4
5
6
7
8
keV

(b)

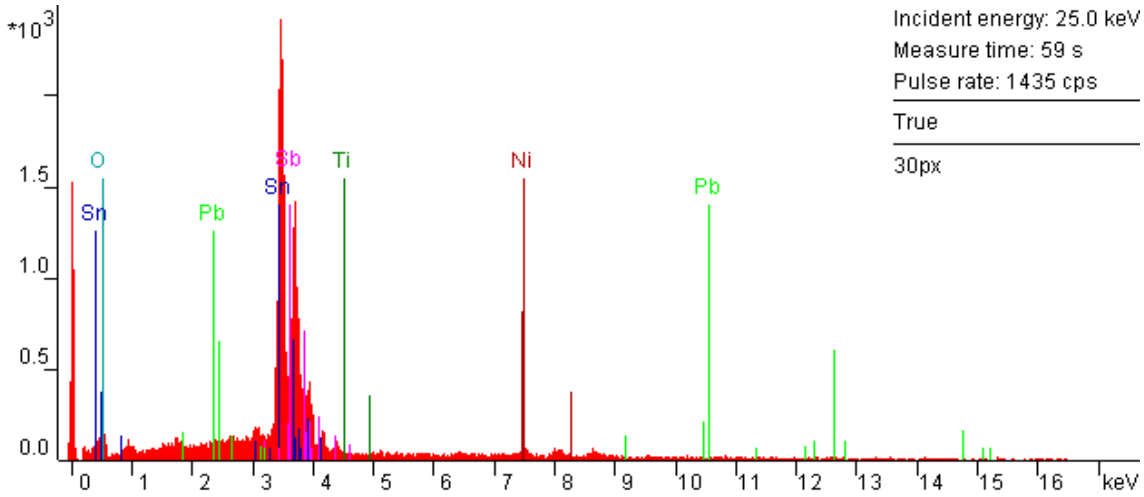
*10^3
1.5
1.0
0.5
0.0
O
Sn
Pb
Sb
Sn
Ti
Ni
Pb
Incident energy: 25.0 keV
Measure time: 59 s
Pulse rate: 1435 cps
True
30px
0
1
2
3
4
5
6
7
8
9
10
11
12
13
14
15
16
keV

(c)

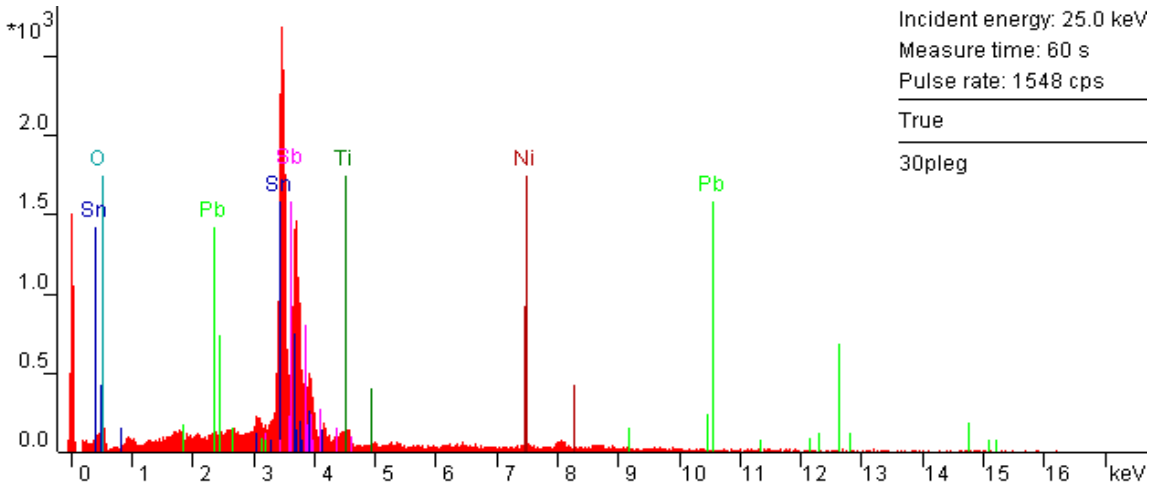

(d)

Figure 3. 6. Typical EDX spectra of the anodes in fig. 3.5 of (a) node of AuSNATO04D anodes, (b) strand area of AuSNATO04D anodes, (c) node of PbSNATO04P anodes and (d) strand area of PbSNATO04P anodes.

3.4 Cyclic Voltammetry in the Presence of $K_4Fe(CN)_6$

The oxidation of $Fe(CN)_6^{4-}$ in 0.5 M Na_2SO_4 was employed to investigate the relative rates of electron transfer across the electrode/electrolyte interface[138]. Cyclic voltammograms of the SNATO02H anode immersed in 0.5 M Na_2SO_4 + 0.1 M $K_4Fe(CN)_6$ as a function of scan rate, ν, are shown in fig. 3.7(a) as typical of all small anodes (SNATO, AuSNATO and PbSNATO), and the separation of the anodic and cathodic peaks, ΔE, from plots of ΔE *vs* ν extrapolated to ν = 0 are presented in tables 3.1 – 3.3. In general, all of the small (0.8 cm × 0.8 cm) anodes (i.e. 71 anodes) investigated showed ΔE values of 120 ± 20 mV and it is clear from tables that electron transfers across the electrode/electrolyte interfaces are slow [33].

Figure 3.7(b) shows a plot of the anodic peak current, $I_{p,a}$, *vs* the catalyst loading from the experiments represented by fig. 3.7(a). As can be seen, the peak current due to ferrocyanide oxidation increases with catalyst loading, in agreement with the data in fig. 3.2, again suggesting that the electrodes are increasingly porous.

In order to account any possible three-dimensionality of the Ni/Sb - SnO_2 electrodes, the fractal approach developed by Strømme and co-workers [153] may be applied. The method is relatively insensitive to electrolyte and film resistance, and has been applied to the study of a variety of electrode types including fractal gold [143], metal/graphite/polymer composites [144], silica co-gel hybrids [145] as well as ion transport through Sn oxide films [154]. The method yields the simple expression shown in equation (2.8), see section 2.8.3.

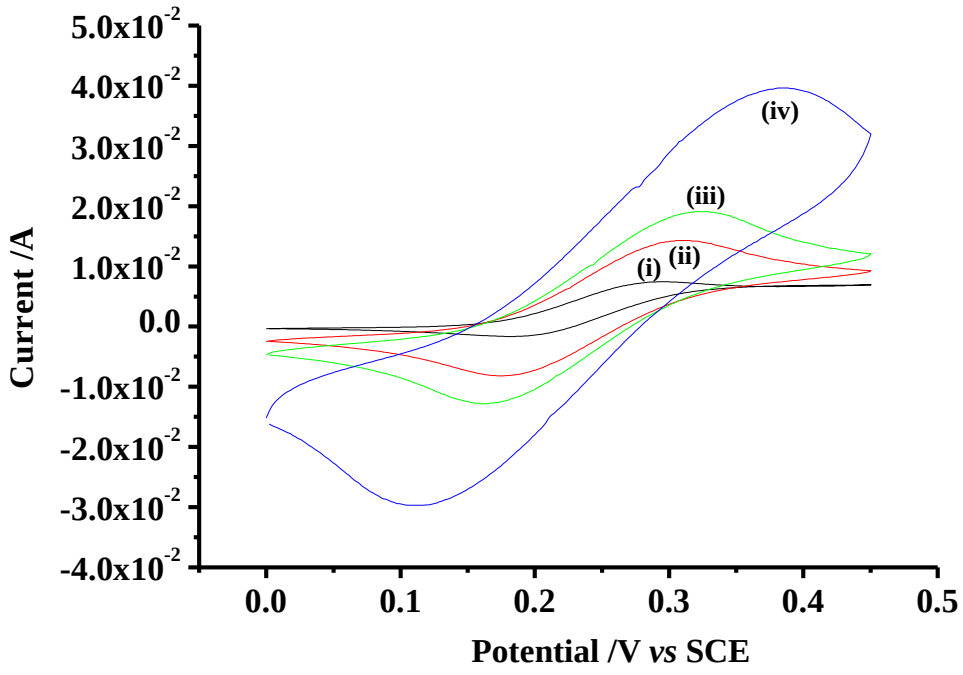
5.0x10-2
4.0x10-2
3.0x10-2
2.0x10-2
1.0x10-2
0.0
-1.0x10-2
-2.0x10-2
-3.0x10-2
-4.0x10-2
Current /A
0.0
0.1
0.2
0.3
0.4
0.5
Potential /V vs SCE
(i)
(ii)
(iii)
(iv)

(a)

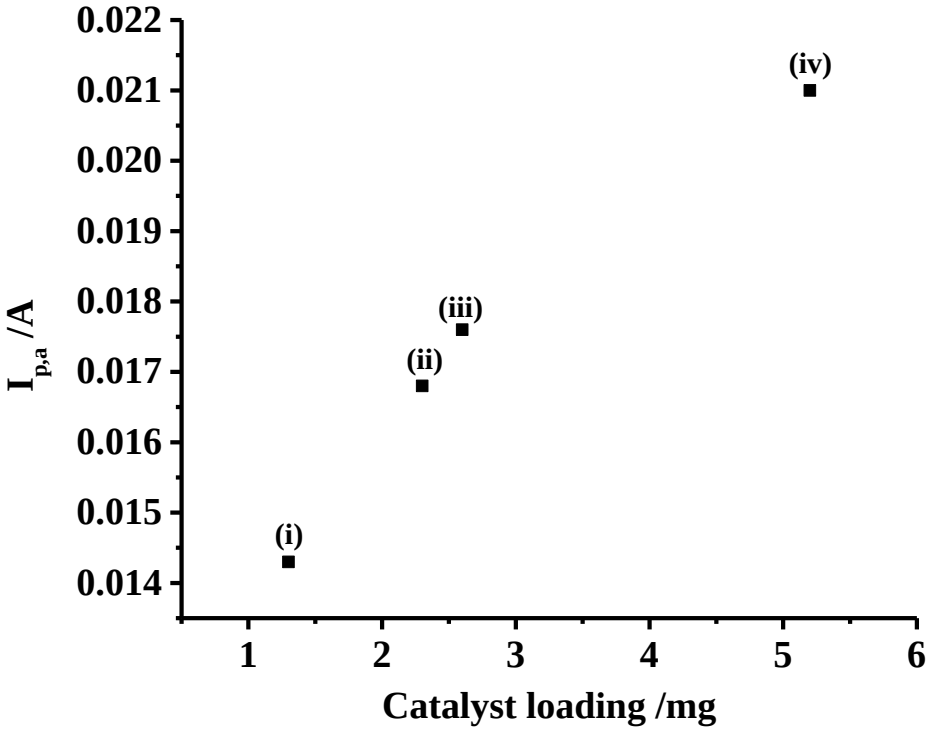
0.022
0.021
0.020
0.019
0.018
0.017
0.016
0.015
0.014
Ip,a /A
1
2
3
4
5
6
Catalyst loading /mg
(i)
(ii)
(iii)
(iv)

(b)

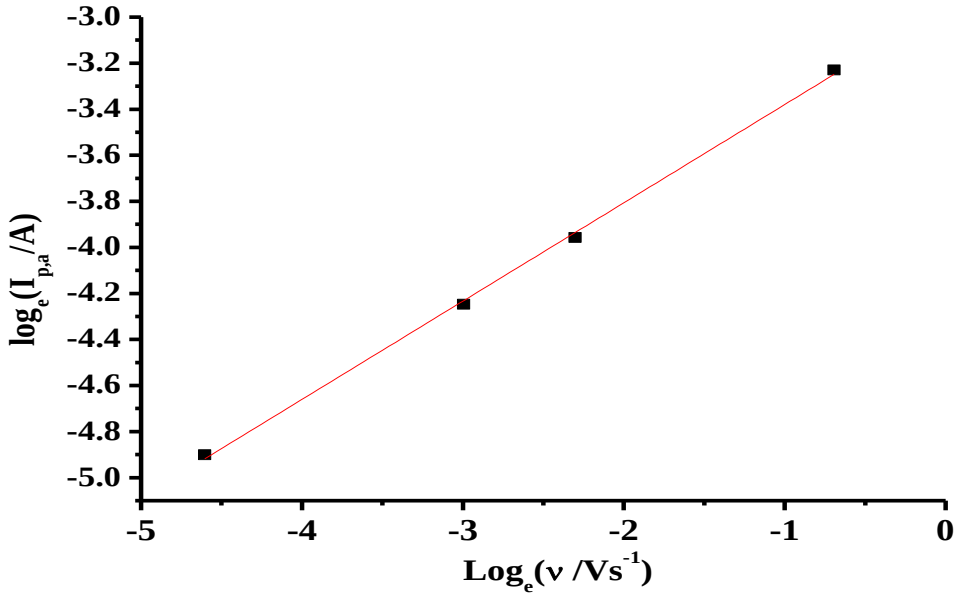

(c)

Figure 3. 7. (a) Cyclic voltammograms of the 0.8 cm x 0.8 cm SNATO02H anode immersed in 0.5M Na_2SO_4 + 0.1M $K_4Fe(CN)_6$ as a function of scan rate, (i) to (iv): 10, 50, 100 and 500 mV s^{-1}, respectively. (b) Plot of peak anodic current ($I_{p,a}$) at a scan rate of 100 mV s^{-1} vs catalyst loading from the experiments represented by fig. 3.7(a). The anode used were: (i) SNATO02D, (ii) SNATO02F, (iii) SNATO02G and (iv) SNATO02H. (c) Plot of Ln($I_{p,a}$) vs Ln(scan rate) from the cyclic voltammograms of the SNATO electrodes in the experiments represented by fig. 3.7(a).

Figure 3.7(c) shows a plot of ln($I_{p,a}$) *vs* ln(ν) for the SNATO02H anode in fig. 3.7(a), where $I_{p,a}$ is the peak anodic current in the cyclic voltammograms, and the plot is again typical of all the SNATO, AuSNATO and PbSNATO anodes investigated. The dimensionalities obtained from the plots are given in tables 3.1 – 3.3. It may be seen from the table that all small (SNATO – based) electrodes investigated gave d_f = 1.8 ± 0.2, irrespective of added dopant. Strømme et al.[153] found that $Fe(CN)_6^{4-}$ oxidation at In_2O_3 electrodes gave d_f = 1.42 , whilst Agrisuelas et al.[144] showed that the dissolution of Ni from Ni/graphite /polypropylene electrodes gave d_f = 1.82. These authors interpreted dimensionalities < 2 in terms of electro-inactive regions on the electrode due to: (i) the physical composition of the electrode when electro-active material is dispersed in an inert matrix; and/or (ii) the high electric field at sharp features forcing the electrochemical reaction to take place only at protrusions and edges. In case of the anodes reported in this chapter, a modified version of (i) may also be appropriate where inhomogeneous doping by Sb results in resistive areas of coating. The lack of variation in d_f suggests that the dimensionality of the SNATO, AuSNATO and PbSNATO electrodes is a characteristic of

Sb-doped SnO_2, a postulate supported by the observation that a Sb-SnO_2 film having no added Ni at a loading of 3.3 mg gave d_f = 1.88. The fractal data appear to be in complete contrast to the increasing porosity with catalyst loading suggested by the data in figs. 3.2 and 3.7(b).

3.5 Cyclic Voltammograms in 1 M $HClO_4$

Figure 3.8 shows a typical cyclic voltammogram of all SNATO anodes immersed in 1.0 M $HClO_4$; the voltammogram is essentially featureless until the onset of O_2/O_3 evolution around 1.7V *vs* SCE, in agreement with Wang *et al.* [75].

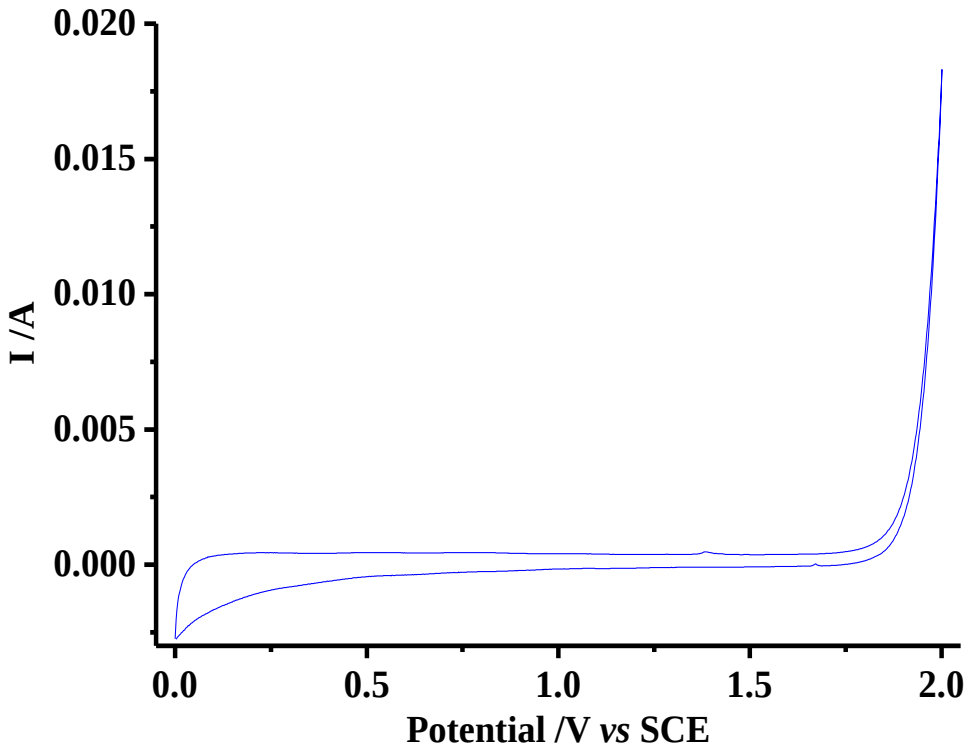

Figure 3. 8. Cyclic voltammogram of the 0.8 cm x 0.8 cm SNATO02H anode in 1M $HClO_4$ at a scan rate of 100 mV s^{-1}.

Figure 3.9 shows a typical cyclic voltammogram which is representative of all the AuSNATO anodes immersed in 1.0 M $HClO_4$ at different anodic potential limits. These limits were 0 – 1.2 V, 0 – 1.7 V, 0 – 2 V and 0 – 2.5 V, and the cyclic voltammograms are shown in figs. 3.9(a) – (f). It may be seen from the figures that, up to an anodic limit of 1.2 V, there was no reduction peak and the onset of Faradic current was at ca. 1.1 V (fig. 3.9(a)). When the upper potential limit was > 1.2 V and < 2 V, a reduction peak at ca. 0.85 V appeared along with a clear oxidation peak at ca. 1.35 V (see figs. 3.9(b) – (d)).

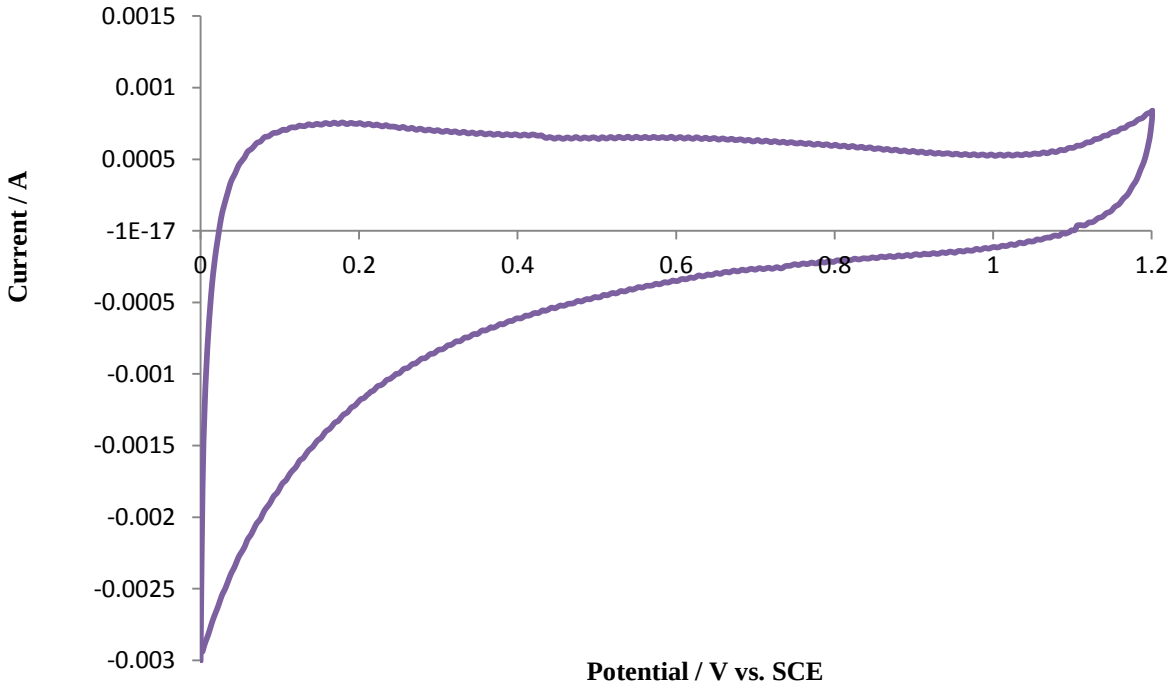
0.0015
0.001
0.0005
-1E-17
-0.0005
-0.001
-0.0015
-0.002
-0.0025
-0.003
0
0.2
0.4
0.6
0.8
1
1.2
Current / A
Potential / V vs. SCE

(a)

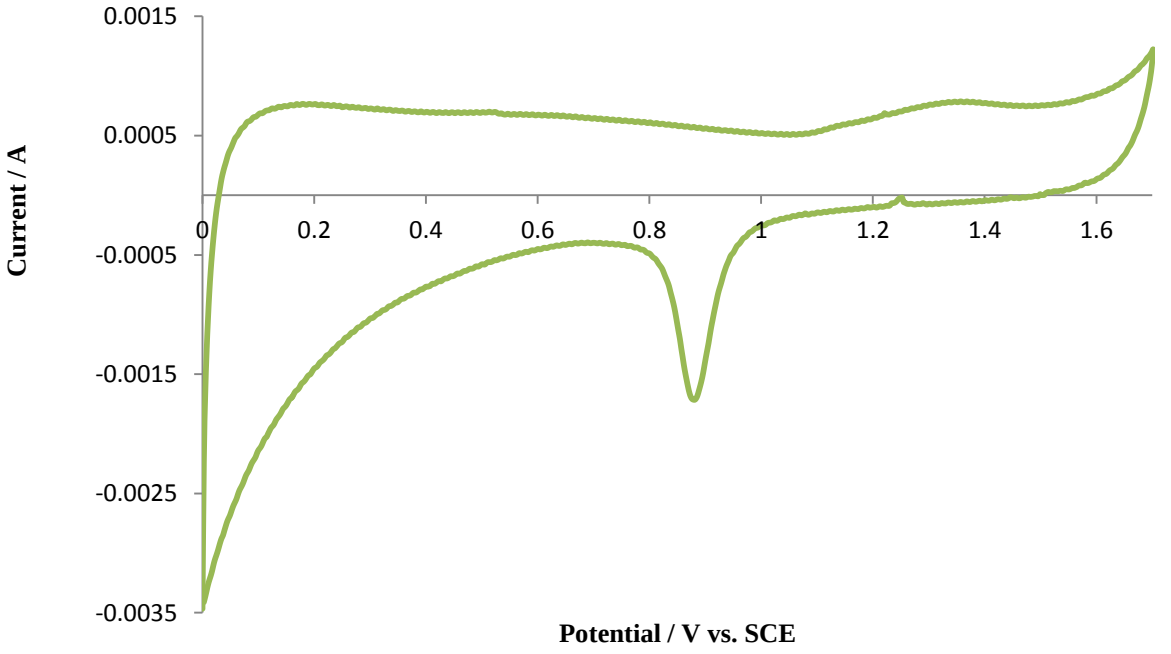
0.0015
0.0005
-0.0005
-0.0015
-0.0025
-0.0035
0
0.2
0.4
0.6
0.8
1
1.2
1.4
1.6
Current / A
Potential / V vs. SCE

(b)

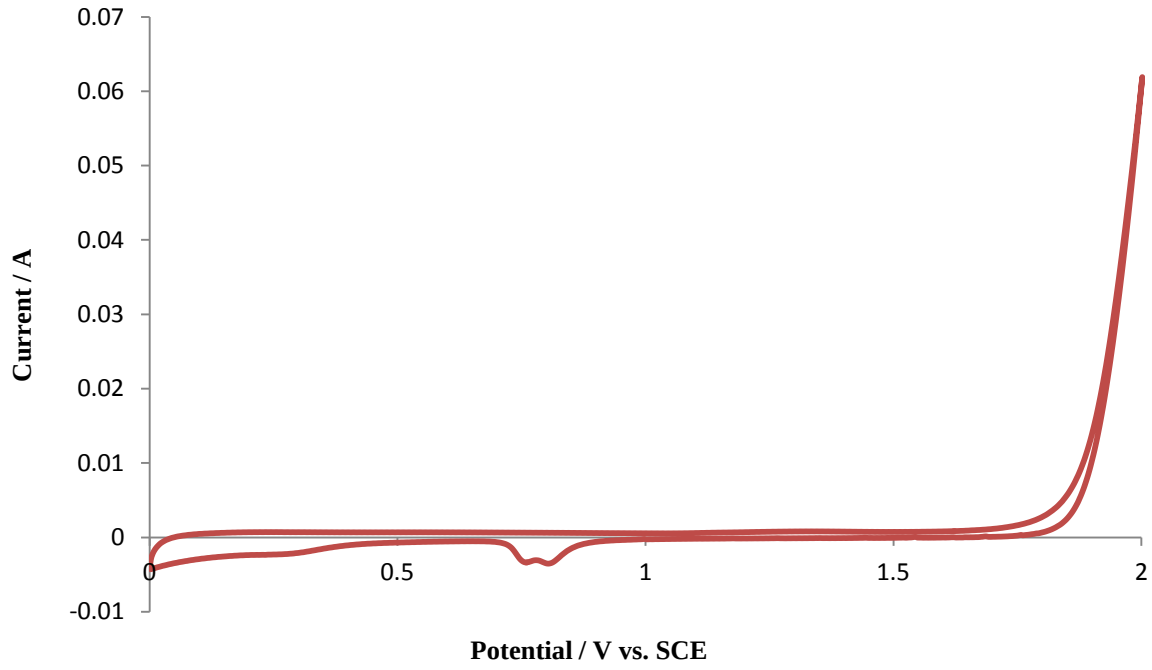
0.07
0.06
0.05
0.04
0.03
0.02
0.01
0
-0.01
Current / A
0
0.5
1
1.5
2
Potential / V vs. SCE

(c)

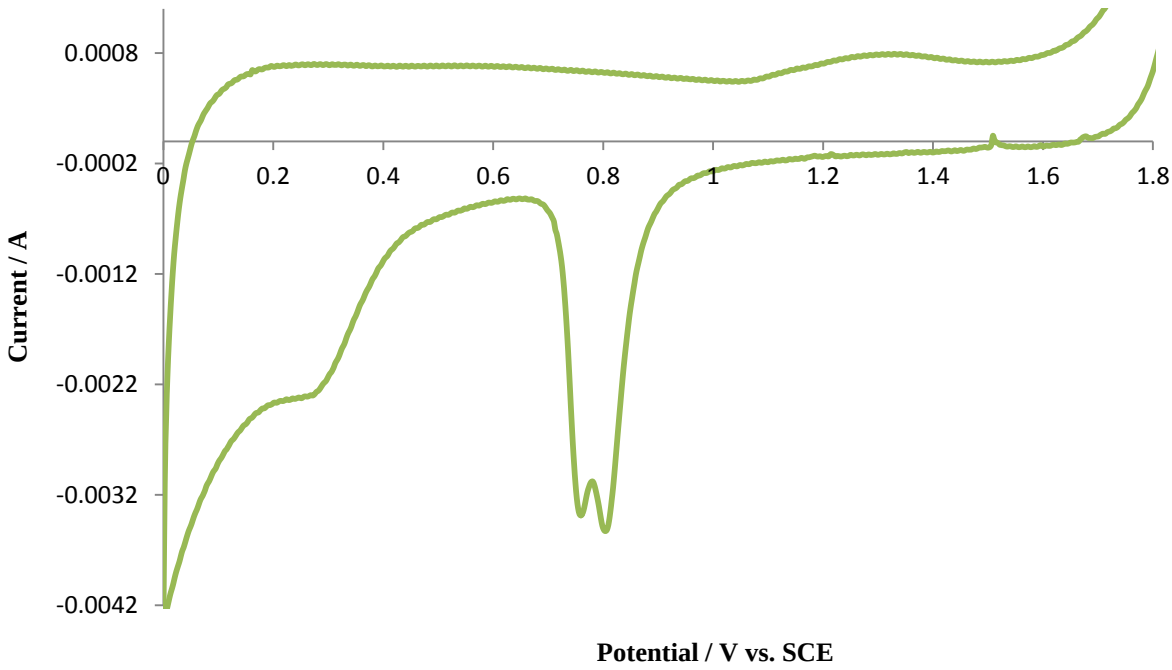
0.0008
-0.0002
-0.0012
-0.0022
-0.0032
-0.0042
Current / A
0
0.2
0.4
0.6
0.8
1
1.2
1.4
1.6
1.8
Potential / V vs. SCE

(d)

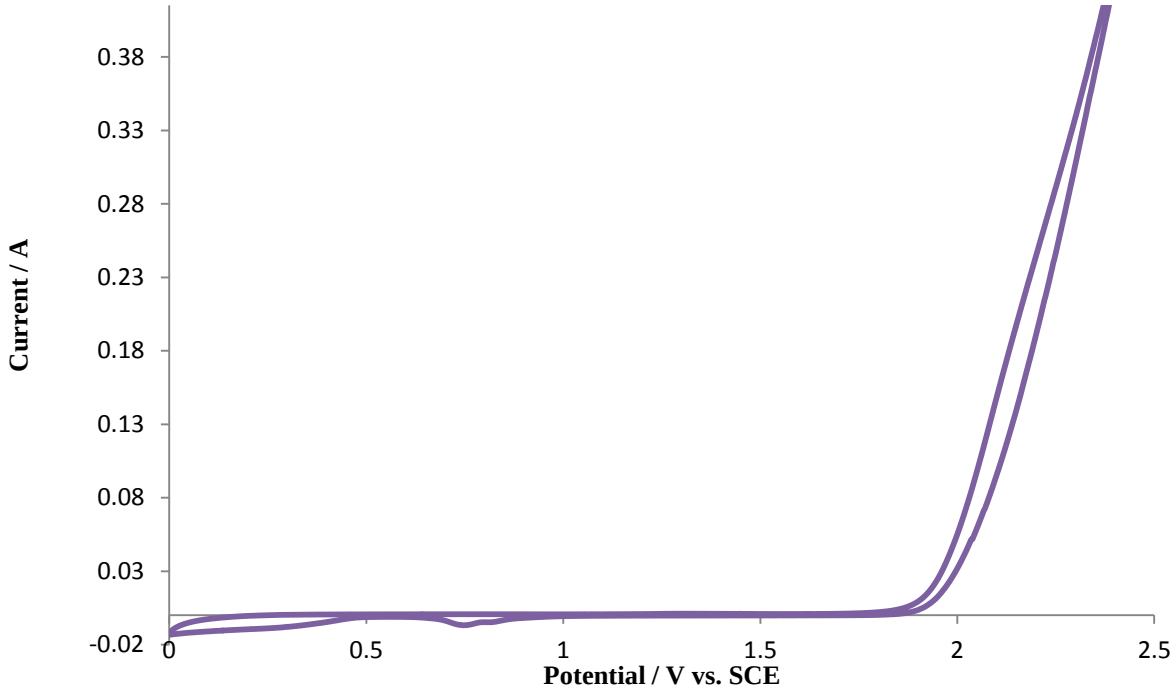

(e)

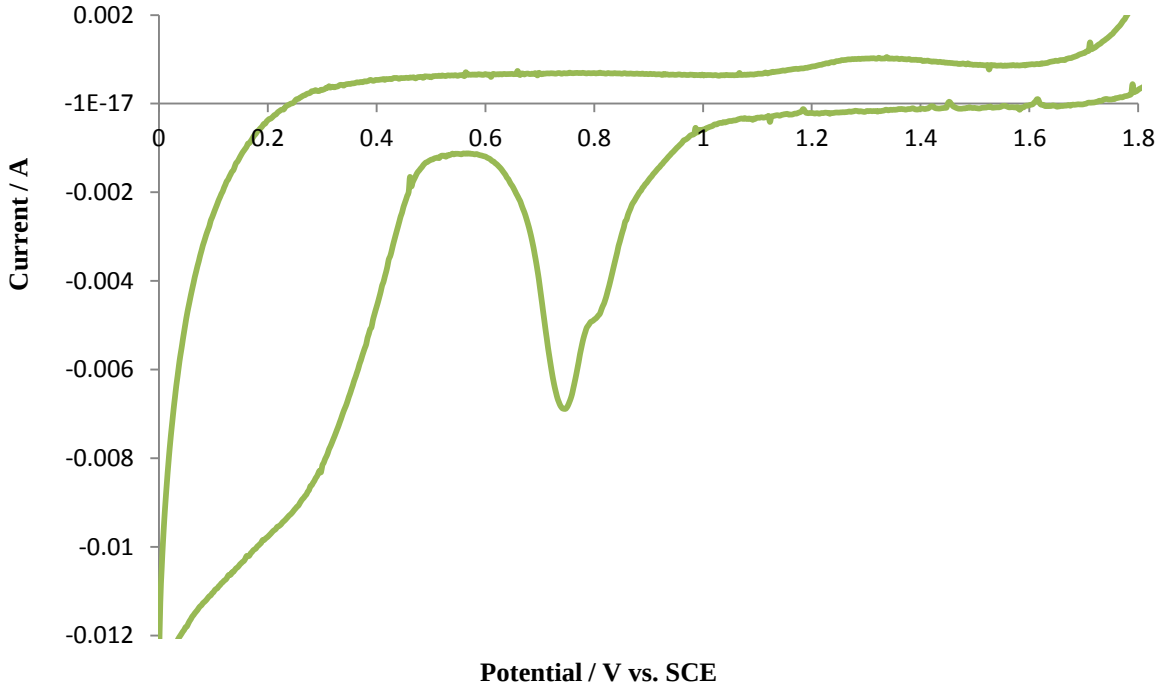

(f)

Figure 3. 9. Plots of cyclic voltammograms scan of AuSNATO01D anode in 1M $HClO_4$, voltage limits of (a) 0 – 1.2 V, (b) 0 – 1.7 V, (c) 0 – 2 V and (e) 0 – 2.5 V. (d) is zoom in (c) and (f) is zoom in (e). Three electrodes system, the cathode was 1.5 cm × 1 cm Pt mesh and the reference electrode was SCE, at room temperature

Using anodic limits ≥ 2 V, (figs. 3.9(c) - (f)), the voltammograms showed two reduction peaks. It may be seen from figs. 3.9(b), (d) and (f) that the higher the anodic limit, the larger the area under the reduction peak; thus the peak currents at ca. 0.85 V were ca. – 0.0017 A, – 0.0035 A and – 0.007A when the anodic limits were 1.7 V, 2 V and 2.5 V, respectively. However, in all cases, the oxidation peak did not change, with a peak potential of ca. 1.35 V and peak current of ca. 0.001 A. The O_2/O_3 onset potential in figs. 3.9(a) – (f) was ca. 1.8 V.

Figure 3.10 shows a typical cyclic voltammogram of a PbSNATO anode (PbSNATO04P) immersed in 1.0 M $HClO_4$; the voltammogram is essentially featureless until the onset of O_2/O_3 evolution around 1.9 V *vs* SCE.

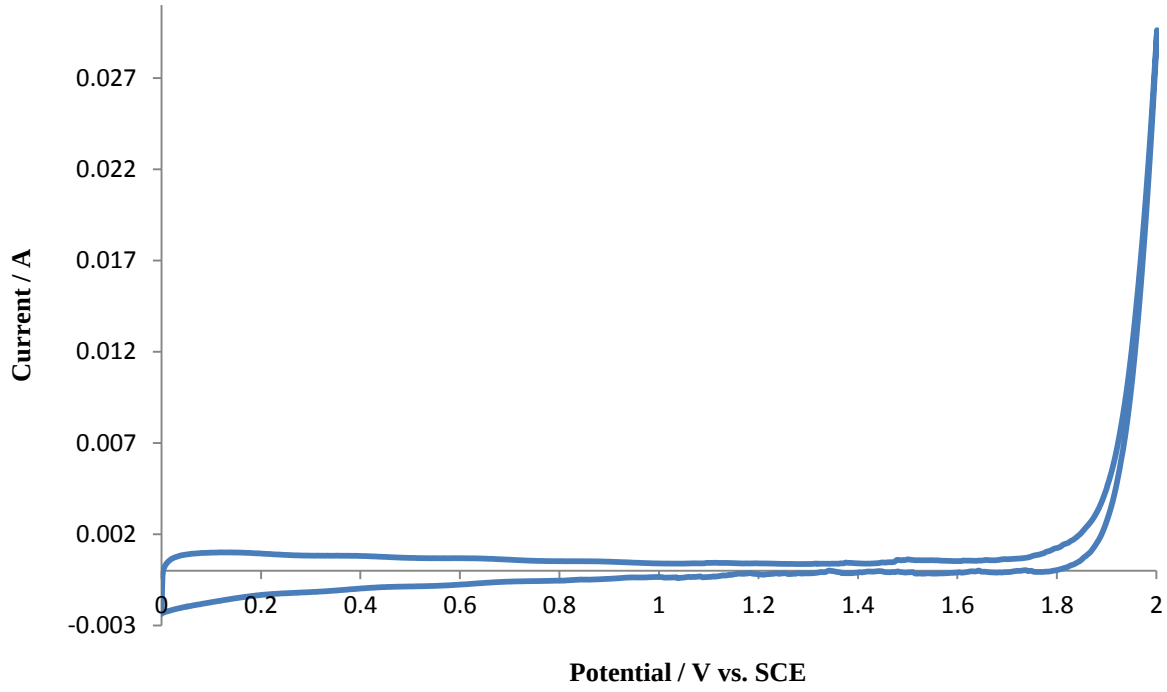

Figure 3. 10. Plots of cyclic voltammogram scan of PbSNATO04P anode in 1M $HClO_4$, voltage limits of 0 – 2 V in three electrode system, the cathode was 1.5 cm × 1 cm Pt mesh and the reference electrode was SCE, at room temperature

The oxidation and reduction peaks shown in fig. 3.9 (for AuSNATO anodes) do not appear in the cyclic voltammograms of SNATO anodes (see fig. 3.8) or in those of PbSNATO anodes (see fig. 3.10), therefore, it does not seem unreasonable to assume that the oxidation and the reduction peaks in fig. 3.9 are due to the presence of Au in the surface of the anode; reflecting possible surface enrichment by Au.

3.6 Current and Current Efficiency of the Electrochemical Ozone Production

The ozone activities of the various anodes were determined in the cuvette cell using 0.8 cm × 0.8 cm SNATO, AuSNATO or PbSNATO anode and a 0.8 cm × 0.8 cm Pt/Ti mesh cathode. Ozone current efficiency was calculated from the O_3 absorbance at 258 nm after a 30 s, 2.7 V potential pulse (see section 2.10.1) by collecting spectra in the subsequent 30 s to 300 s period; typical spectra so obtained are shown in fig. 3.11(a), and a representative plot (of all SNATO, AUSNATO and PbSNATO anodes) of the current observed during the potential pulse in fig. 3.11(b).

Tables 3.1 – 3.3 present the average values of ozone generation current and current efficiency (see discussion below).

Figure 3.12(a) shows a plot of the current measured for the SNATO electrodes, taken just before the cell was switched to open circuit, *vs* the catalyst loading of each electrode, whilst fig. 3.12(b) shows the corresponding current efficiencies assuming a 6-electron ozone generation[42] (see equation (1.1)).

As may be seen from fig. 3.12(a), the current behaves in the same manner as in figs. 3.2

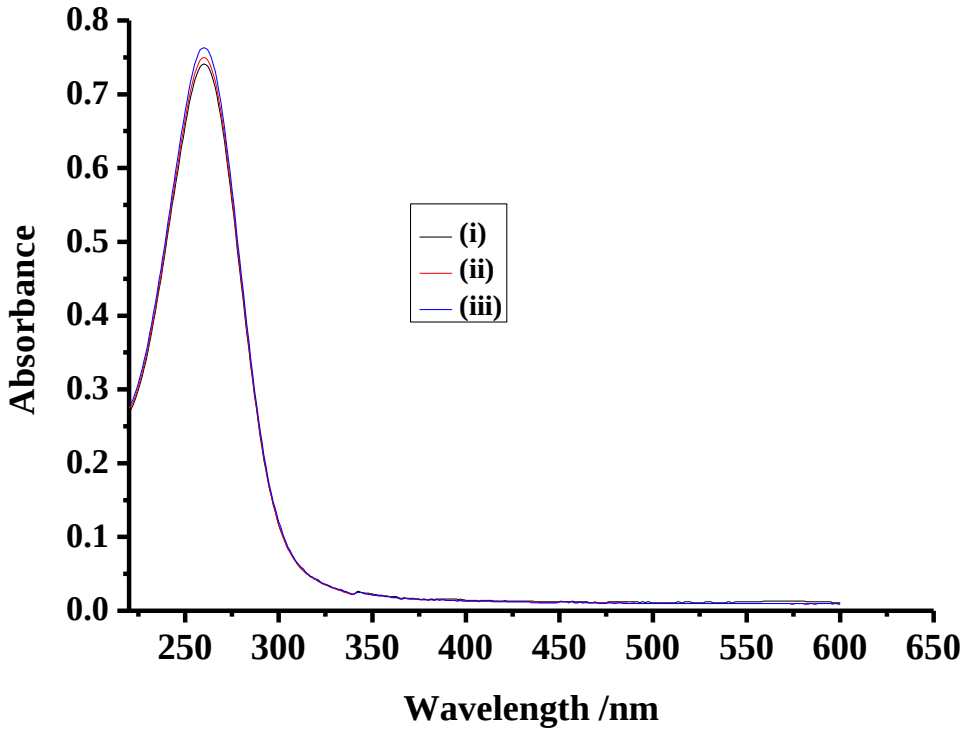

(a)

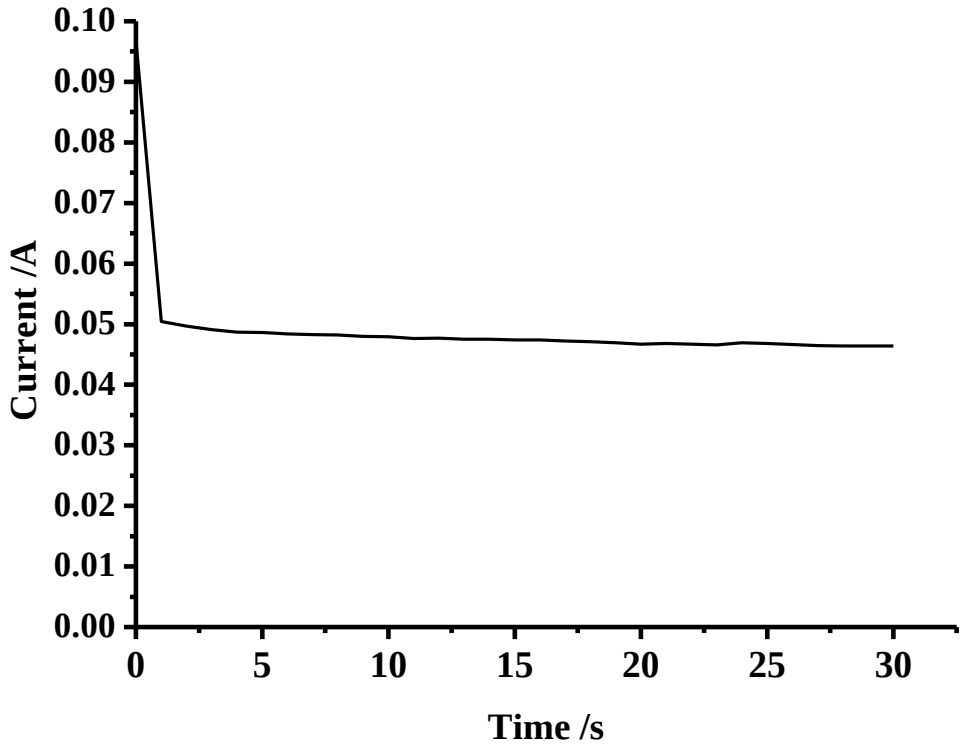

(b)

Figure 3. 11. (a) UV Vis spectra collected (i) 60 or 120 s, (ii) 180 s and (iii) 300 s after a 30 s, 2.7 V potential pulse using SNATO02H immersed in 1M $HClO_4$. (b) The current observed during the potential pulse in fig. 3.11(a).

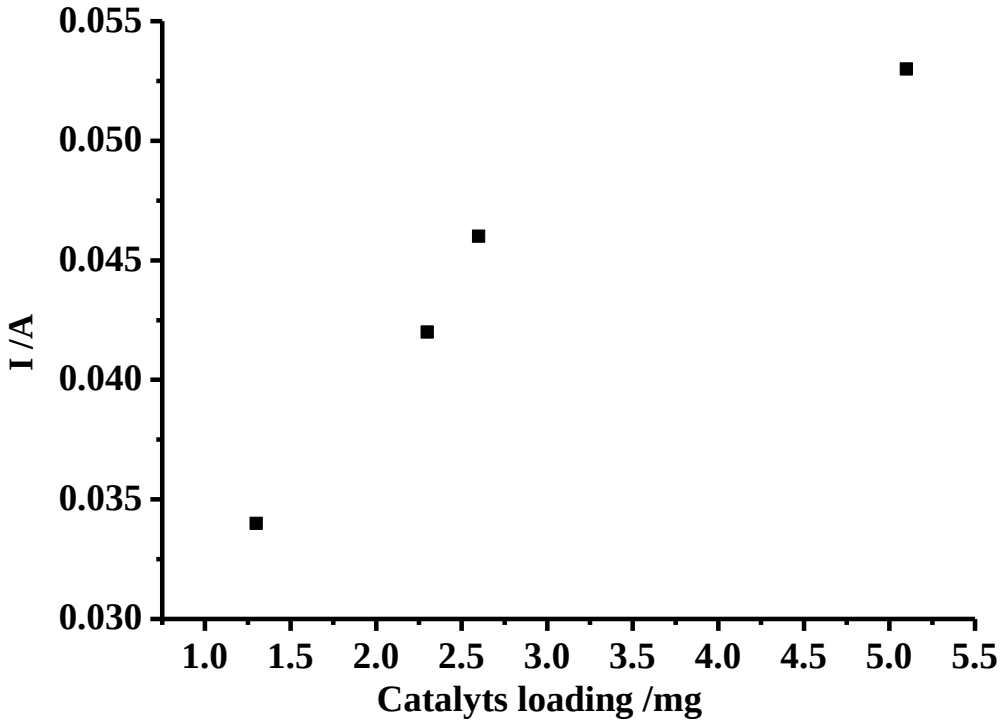

(a)

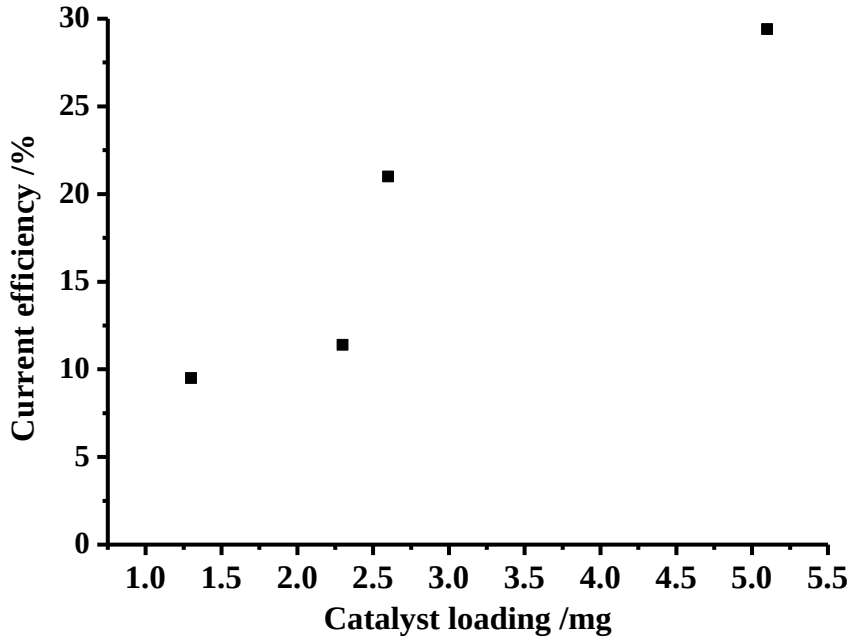

(b)

Figure 3. 12. (a) A plot of the current at 30 s vs loading of catalyst on the SNATO anodes in the UV Vis cuvette cell. Electrolyte was 3 cm^3 1M $HClO_4$. (b) Plot of ozone current efficiency vs loading of catalyst for the electrodes in fig. 3.12(a). In each case, the order of the anodes was SNATO02D, lowest current/current efficiency, SNATO02F, SNATO02G and SNATO02H, highest current/current efficiency.

and 3.7(b), increasing with loading, and in contrast to the fractal analysis. Interestingly, as may be seen from fig. 3.12(b), the ozone current efficiency also increases with catalyst loading, suggesting an increasing fraction of the catalyst is active for O_3 evolution (relative to oxygen evolution) as the thickness of the coating increases.

Figure 3.13 shows plots of current and current efficiency as a function of electrode potential for the SNATO02D and SNATO02H anodes; in order to allow direct comparison between all four sets of data, the current data were scaled down by a factor of 0.33. In the case of the SNATO02H data, it can be seen from the figure that, whilst the current increases steadily with potential, the current efficiency rises to an asymptotic value at high potentials. The latter is in contrast to the data of Wang et al.[75] who observed a definitive maximum at 2.2 V vs Ag/AgCl, equivalent to ca. 2.4 V in our experiments. Wang et al.[75] observed the current efficiency to remain constant after 8 coating cycles, possibly as the loading of catalyst on the Ti substrate did not increase above ca. 1.4 – 1.5 mg. The current efficiency of the SNATO02D anode shows the same behaviour as the thicker anode. The current passed by the SNATO02D anode at 2.8V was only ca. 25% lower than that observed using the SNATO02H electrode at the same potential, but the optimum current

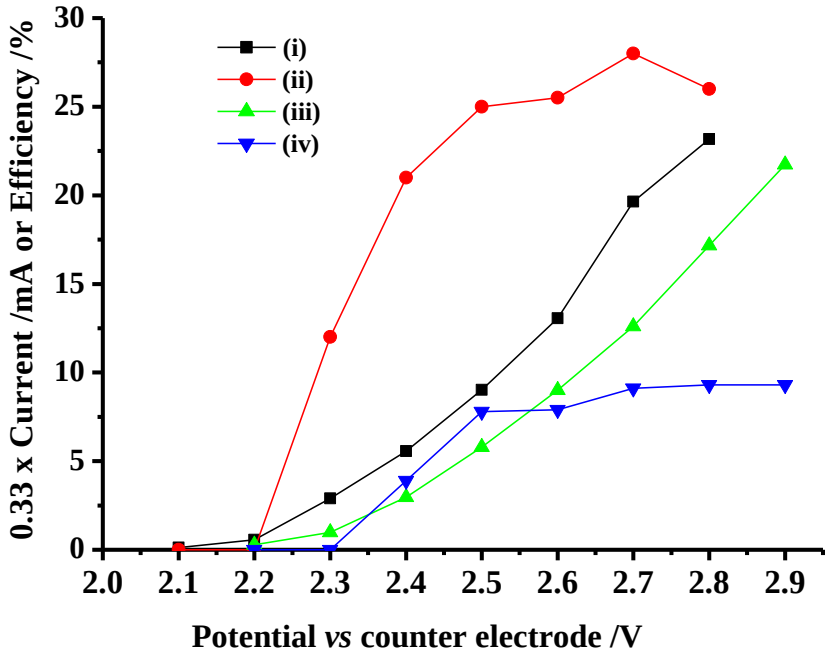

Figure 3. 13. Plots of current (■) & (▲), and current efficiency (●) & (▼), as a function of the potential of the (■) & (●) SNATO02H and (▲) & (▼)SNATO02D anodes vs *the Pt/Ti mesh counter electrode in the cuvette cell. The current data have been reduced by a factor of 3 for clarity.*

efficiency of the former anode was *ca*. 9% compared to 26% for the SNATO02H electrode. As may be seen from the figure, SNATO02H shows an onset for O_3 evolution *ca*. 100 mV lower than that of SNATO02D anode

3.7 The Effect of Gold Ratio

The Au ratio (Sn: Sb: Ni: Au = 500: 8: 3: Au) in the precursor solutions was varied between 0.1 and 2.25. The effect of the Au content on the electrochemical characteristics of the AuSNATO anodes is summarised table 3.2. The data from the table were used to plot figs. 3.14 and 3.15.

Figure 3.14 shows plots of the average values of the capacitive current I_{cap} and dimensionality d_f vs. the Au ratio in AuSNATO anodes. It may be seen from the figure that the average values of I_{cap} increased to ca. 2 mA with increasing Au content up to 0.1, then decreased to ca. 1.6 mA up to 0.3, after which the I_{cap} remained unchanged with increasing Au content. In addition, the average values of d_f increased to ca. 1.83 with increasing Au content up to 0.1, then decreased to ca. 1.74 with increasing Au content up to 0.3, after which d_f remained almost unchanged.

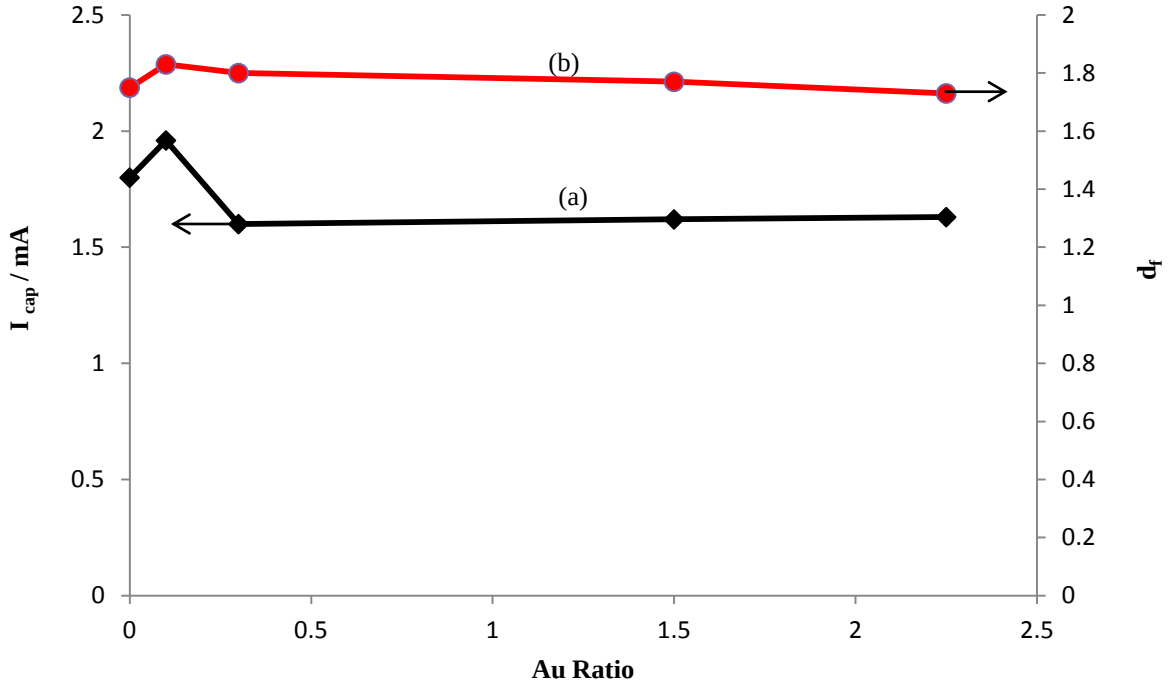

Figure 3. 14. Plots of the average values of (a) I_{cap} and (b) d_f vs. the Au ratio in AuSNATO anodes, the data obtained from table 3.2.

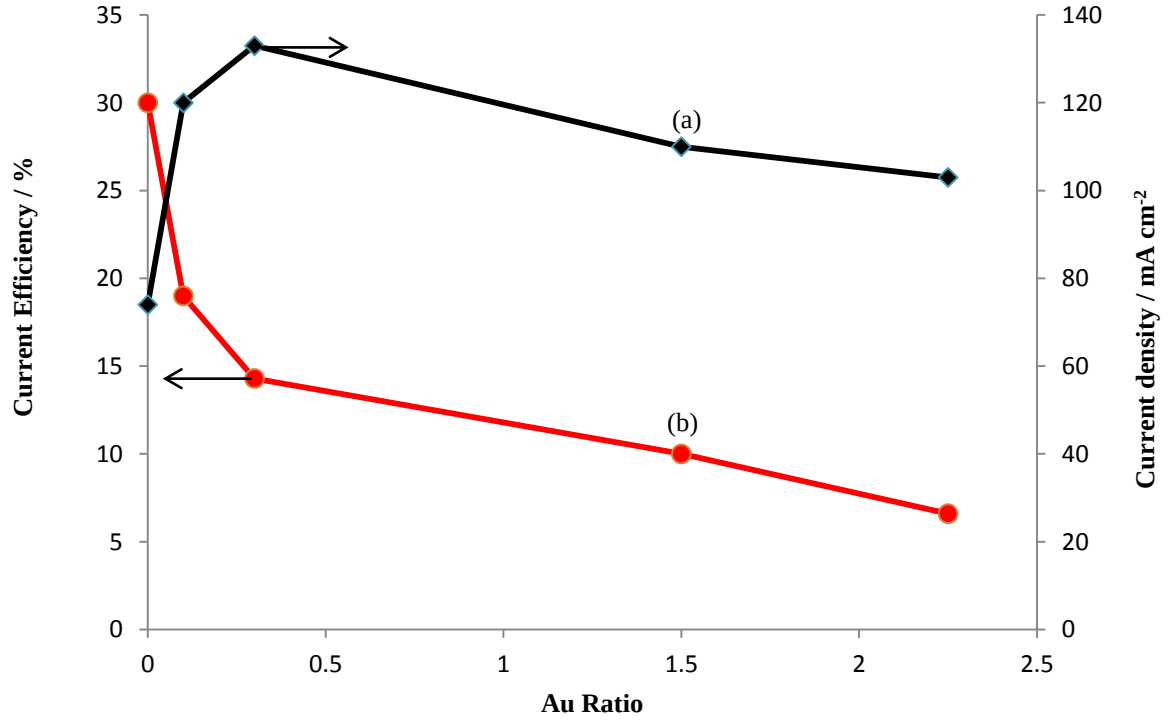

Figure 3. 15. Plots of the average values of (a) current and (b) ozone current efficiency vs. the Au ratio in AuSNATO anodes, the data obtained from table 3.2.

Figure 3.15 shows a plot of the average values of the ozone current and current efficiency measured for the AuSNATO electrodes, taken just before the cell was switched to open circuit, *vs* the Au ratio. As may be seen from the figure, the current increased to ca. 133 mA cm^{-2} with increasing Au content up to 0.3, after which the current decreased with increasing Au content. In contrast, the current efficiency decreased with increasing Au ratio up to 0.3, after which the current efficiency decreased slowly with increasing Au content. It is clear from fig. 3.15 that, whilst the current did not decrease as the Au content increased up to 0.3, the current efficiency for ozone decreased in an exponential way with increasing Au content. Thus, as the Au content increased, ozone active sites were switching to oxygen suggesting strongly that Au favours oxygen production. For Au content > 0.3, both the current and the current efficiency decreased suggesting that the increase in Au value decreased the active sites on the anode surface for both oxygen and ozone.

3.8 The Effect of Lead

3.8.1 The effect of lead on the electrochemical characteristics of the anodes

For Pb ratio (Sn: Sb: Ni: Pb = 500: 8: 3: Pb) of 0.5, the coating process was repeated 5, 10, 15 and 20 times. Figure 3.16 shows the catalyst loading as a function of the number of coatings, each data point is the average of all anodes (10 samples) prepared in an identical fashion. It may be seen from the figure that the catalyst loading increased linearly with increasing coating number, as expected.

Figure 3.17 shows a plot of average values of I_{cap} and d_f vs. catalyst loading. As may be seen from the figure, there appears to be a clear relationship between catalyst loading and the surface area of the catalyst coating exposed to electrolyte, in that the I_{cap} increased to ca. 1.75 mA with increasing catalyst loading up to 2 mg, after which the I_{cap} remained essentially constant. In addition, it may be seen from the figure that the dimensionality d_f remained almost constant with the catalyst loading, behaviour that has been seen previously observed for SNATO anodes (see section 3.4).

Figure 3.18 shows the average values of current and ozone current efficiency vs. catalyst loading for PbSNATO anodes. It may be seen from the figure that the current generally increased with increasing the catalyst loading, suggesting that the PbSNATO anodes are porous. However, the current efficiency did not change with increasing catalyst loading up to ca. 3.2 mg after which it did increase. In general, the increase in current suggests that the

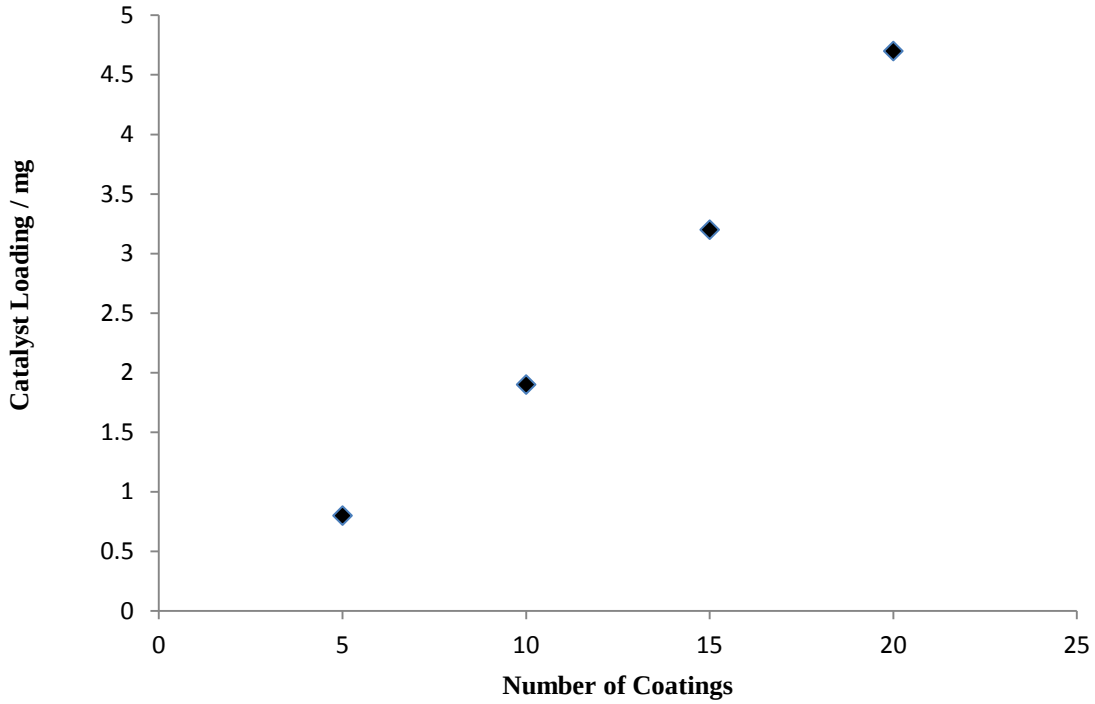

Figure 3. 16. Plots of the catalyst loading vs. number of coats for 0.8 cm × 0.8 cm PbSNATO anodes, the data were obtained from table 3.3.

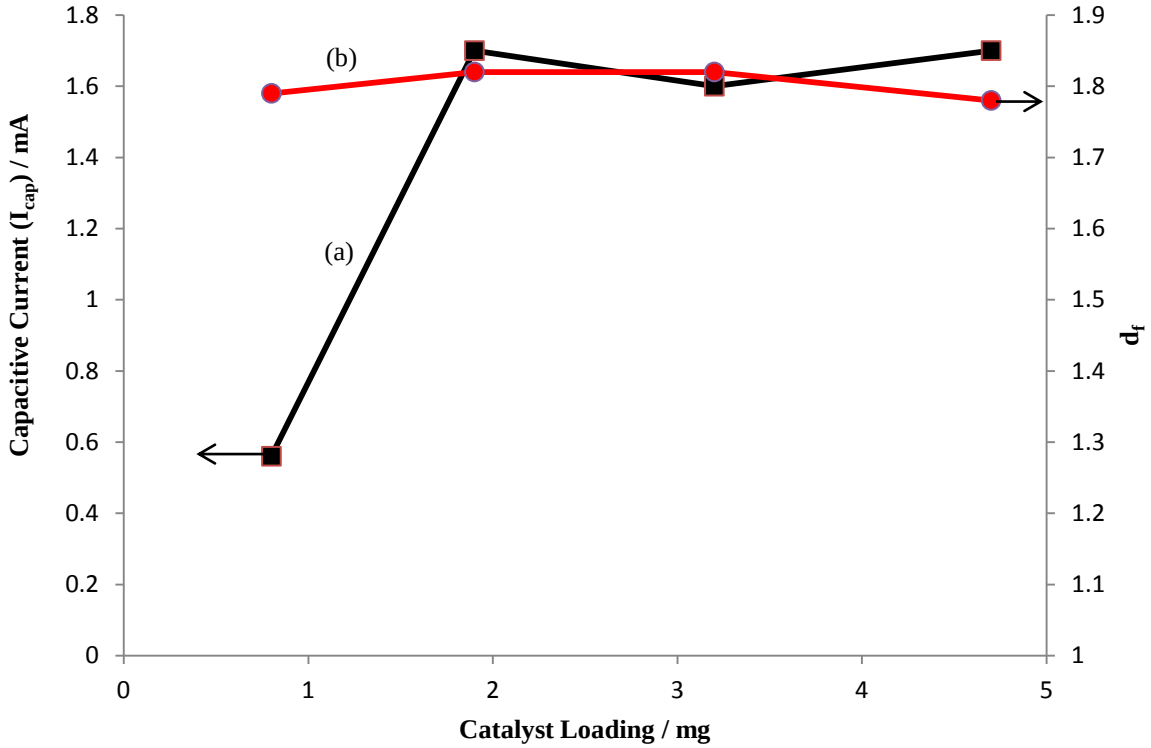

Figure 3. 17. Plots of the average values of (a) I_{cap} and (b) d_f vs. catalyst loading for PbSNATO anodes, the data were obtained from table 3.3.

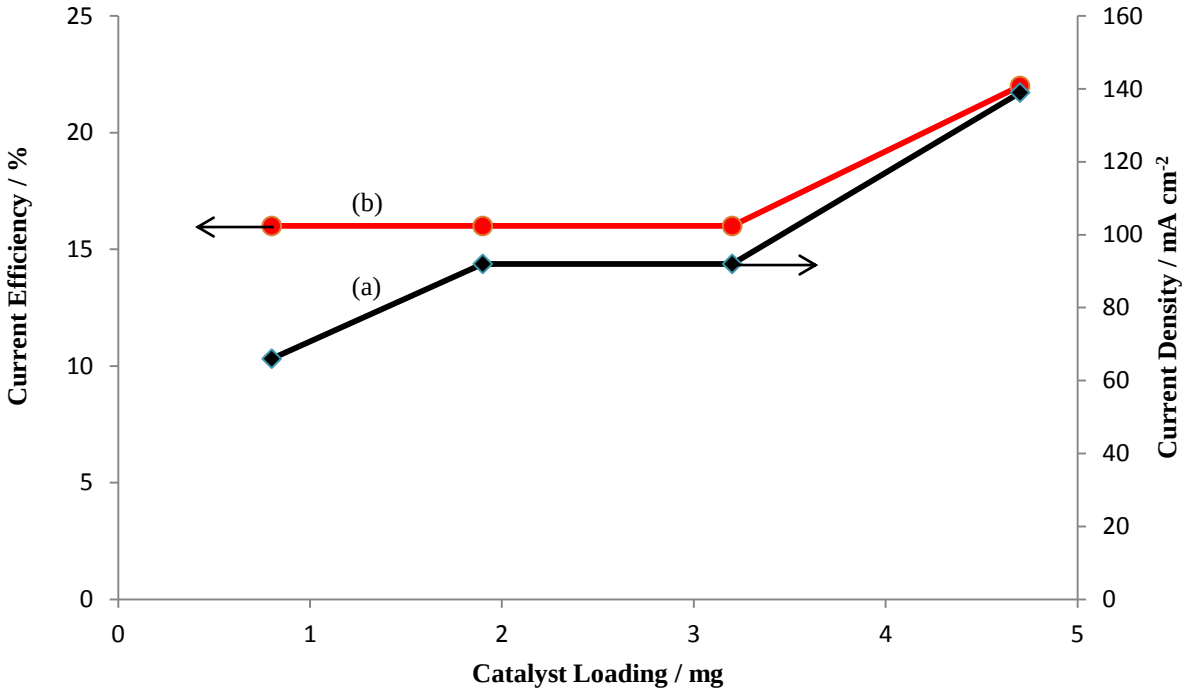

Figure 3. 18. Plots of the average values of (a) current and (b) current efficiency vs. catalyst loading for PbSNATO anodes, the data were obtained from table 3.3.

number of active sites (ozone and oxygen) is increasing with loading. However, the ratio of ozone/oxygen active sites seems to stay constant with increasing catalyst loading up to 3 mg, after which the ratio ozone/oxygen active sites increased with increasing catalyst loading.

3.9 The Electrodeposited Inter Layer (EDIL)

3.9.1 The characteristics of the EDIL

As discussed in section 2.2.1, an interlayer (IL) was employed with most of the small scale anodes (KZ01 – KZ05 anode series). Overall, the use of an EDIL showed the following characteristics: (i) it is irreproducible (see tables 3.1 – 3.3) , (ii) it is not uniform and cannot cover all the Ti substrate and (iii) only Sb (and its oxides) is being deposited. These factors led to the EDIL being investigated in more detail. Thus, in separate experiments, EDIL electrodepositions from ethanolic solution of only $SnCl_4$, only $SbCl_3$ and $SnCl_4$ & $SbCl_3$ were studied using the same concentrations of that discussed in section 2.2.1, and under the same deposition conditions, i.e. 5 mA/cm^2 for 1 min and then 2.5 mA/cm^2 for 20 min. Two electrodes were prepared from each solution, and the films so obtained were characterized by SEM and EDX.

Table 3.4 presents the mass of EDIL deposited on different electrodes, where Sn, Sb and

Sn/Sb refer to the electrodeposition solution used (i.e. only $SnCl_4$, only $SbCl_3$ or both $SnCl_4$ and $SbCl_3$, respectively). The key observations that can be made from the data in the table are: (i) tin does not deposit, (ii) the electrodeposition of Sb is irreproducible and (iii) whilst no deposition occurs from the $SnCl_4$ solution, the presence of $SnCl_4$ did enhance the mass of the EDIL electrodeposited. It is not clear from the experiment why the latter is the case, however, the Sn facilitates the deposition of EDIL.

Electrode	**Sn1**	**Sn2**	**Sb1**	**Sb2**	**Sn/Sb1**	**Sn/Sb2**
EDIL mass (mg)	0	0	0.7	0.4	1.5	0.9

Table 3. 4. The EDIL masses for different electrodes prepared from only $SnCl_4$ -containing, only $SbCl_3$ - containing and $SbCl_3/SnCl_4$ -containing electrodeposition solutions.

To confirm the findings of table 3.4, the electrodes prepared from each solution were analysed using EDX and SEM. Figures 3.19(a) – (i) show the SEM images of the electrode after the EDIL process at different magnifications, and the EDX analysis at the same point where the SEM had been taken. The SEM's and EDX of the electrode prepared using the $SnCl_4$ solution are shown in figs. 3.19(a) - (c); the SEM's and EDX of the electrode prepared from the $SbCl_3$ solution are shown in figs. 3.19(d) - (f), and the SEM's and EDX of the electrode prepared from the $SnCl_4/SbCl_3$ solution are shown in figs. 3.19(g) - (i). It may be seen from the SEM image at 150 magnification, shown in fig. 3.19(a), that only the etched Ti mesh may be seen; no EDIL can be seen, and the SEM image at 5000 magnification confirms this (see fig. 3.19(b)), as does the EDX analysis, see fig. 3.19(c). Thus, no EDIL was deposited on the Ti mesh when using $SnCl_4$ solution. In contrast, the SEM images of the electrode prepared using $SbCl_3$ solution at both magnifications (i.e. × 150 and × 5000, see figs. 3.19(d) and (e)) showed that small spheres were attached to the Ti mesh. These spheres did not cover all the Ti mesh, and EDX analysis (fig. 3.19(f)) showed that these spheres were only Sb, thus, the underlying Ti appeared in the EDX spectrum (see fig. 3.19(f)). The SEM images of the meshes coated from the $SnCl_4$ + $SbCl_3$ solution shown in figs. 3.19(g) and (h) at two magnifications (i.e. × 150 and × 3500) show similar spheres to those shown in figs. 3.19(d) and (e). Again, the EDX analysis (fig. 3.19(i)) showed that the spheres were comprised only of Sb.

To confirm the finding that only Sb was deposited from the $SnCl_4$ + $SbCl_3$ solution, the SEM image of the second electrode, prepared the same way, is shown in fig. 3.20(a).

Two spots were randomly selected from the SEM image, EDX analysis at these two spots

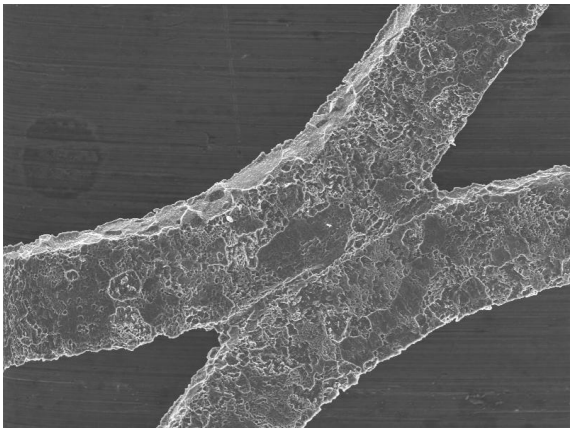

(a) × 150

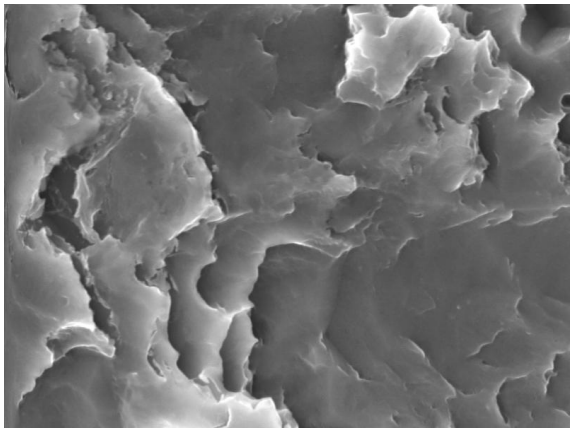

(b) × 5000

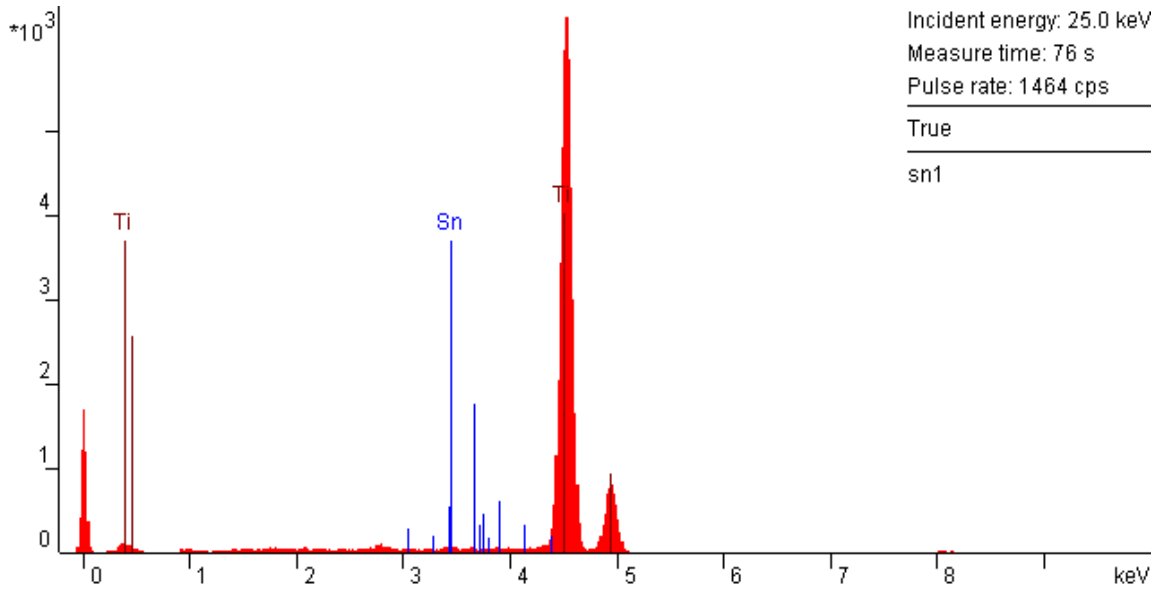

(c)

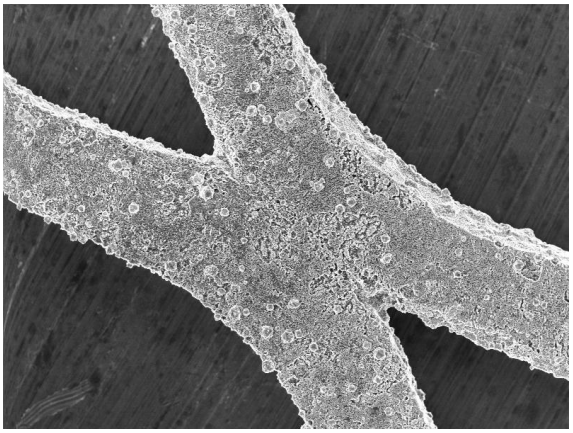

(d) × 150

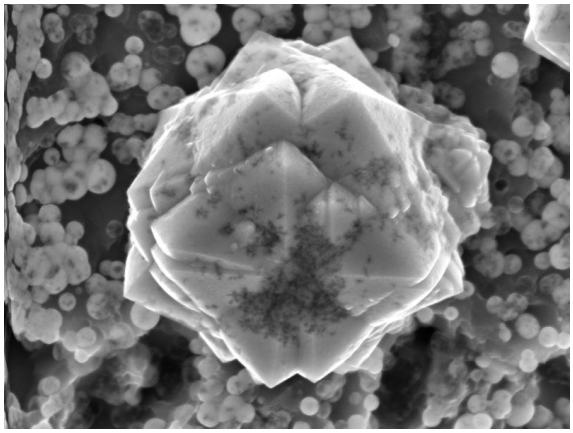

(e) × 5000

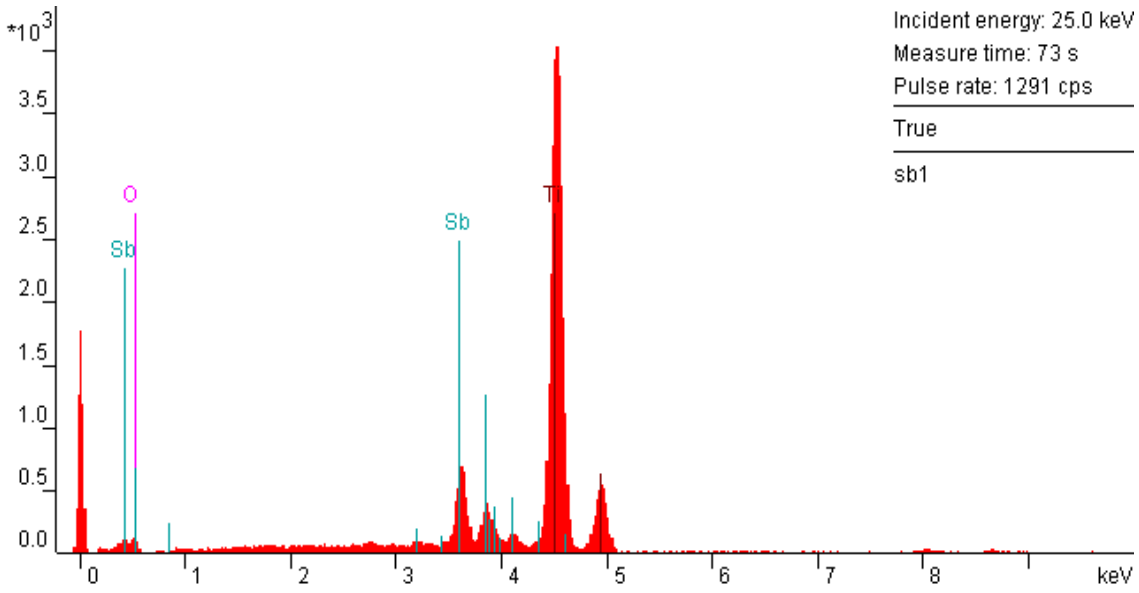
*10^3
3.5
3.0
2.5
2.0
1.5
1.0
0.5
0.0
O
Sb
Sb
Ti
0
1
2
3
4
5
6
7
8
keV
Incident energy: 25.0 keV
Measure time: 73 s
Pulse rate: 1291 cps
True
sb1

(f)

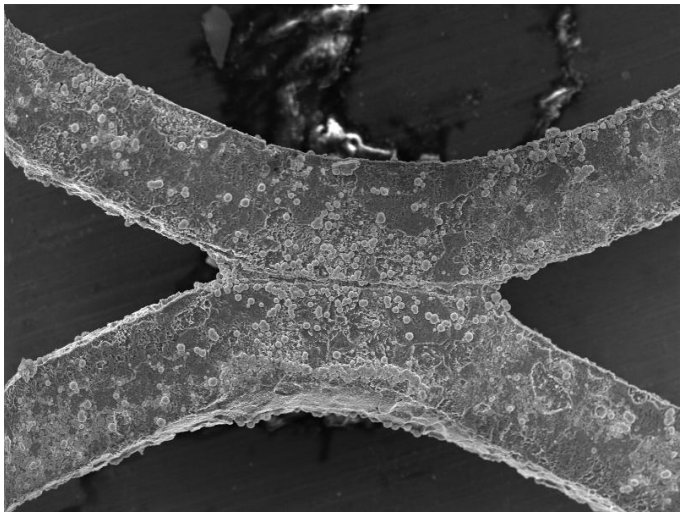

(g) × 150

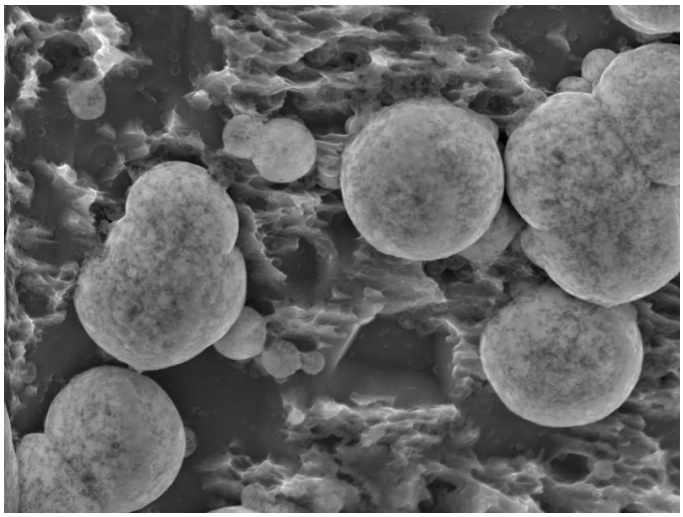

(h) × 3500

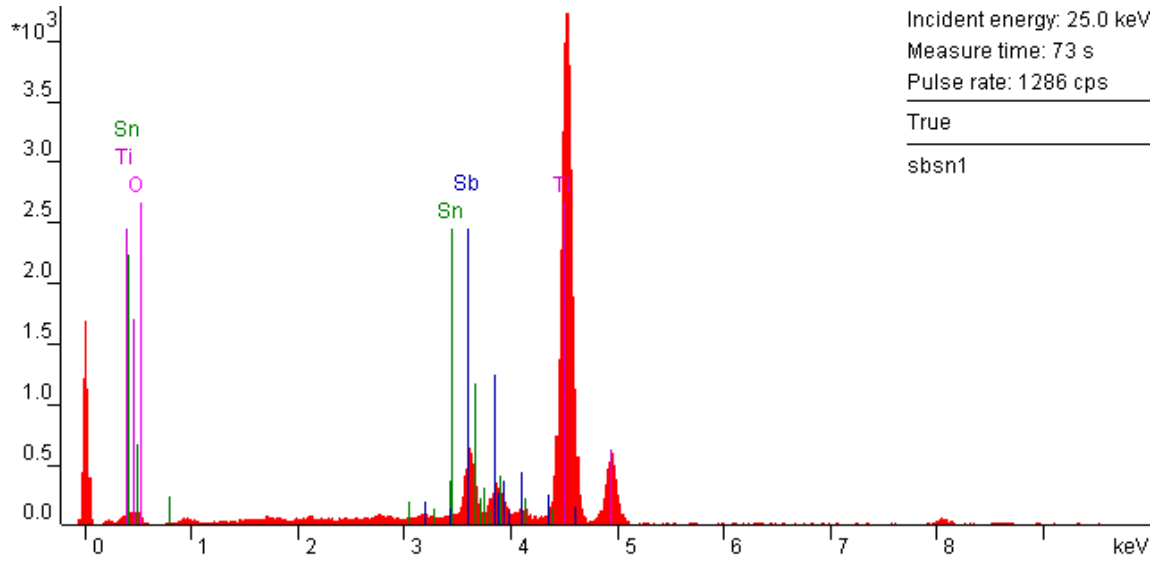

(i)

Figure 3. 19. SEM images and EDX spectra of Ti mesh after ED process from $SnCl_4$ solution: (a) SEM × 150, (b) SEM × 5000 and (c) EDX, from $SbCl_3$ solution: (d) SEM × 150, (e) SEM × 5000 and (f) EDX, and from $SnCl_4$ + $SbCl_3$ solution: (g) SEM × 150, (h) SEM × 3500 and (i) EDX. See text for more details

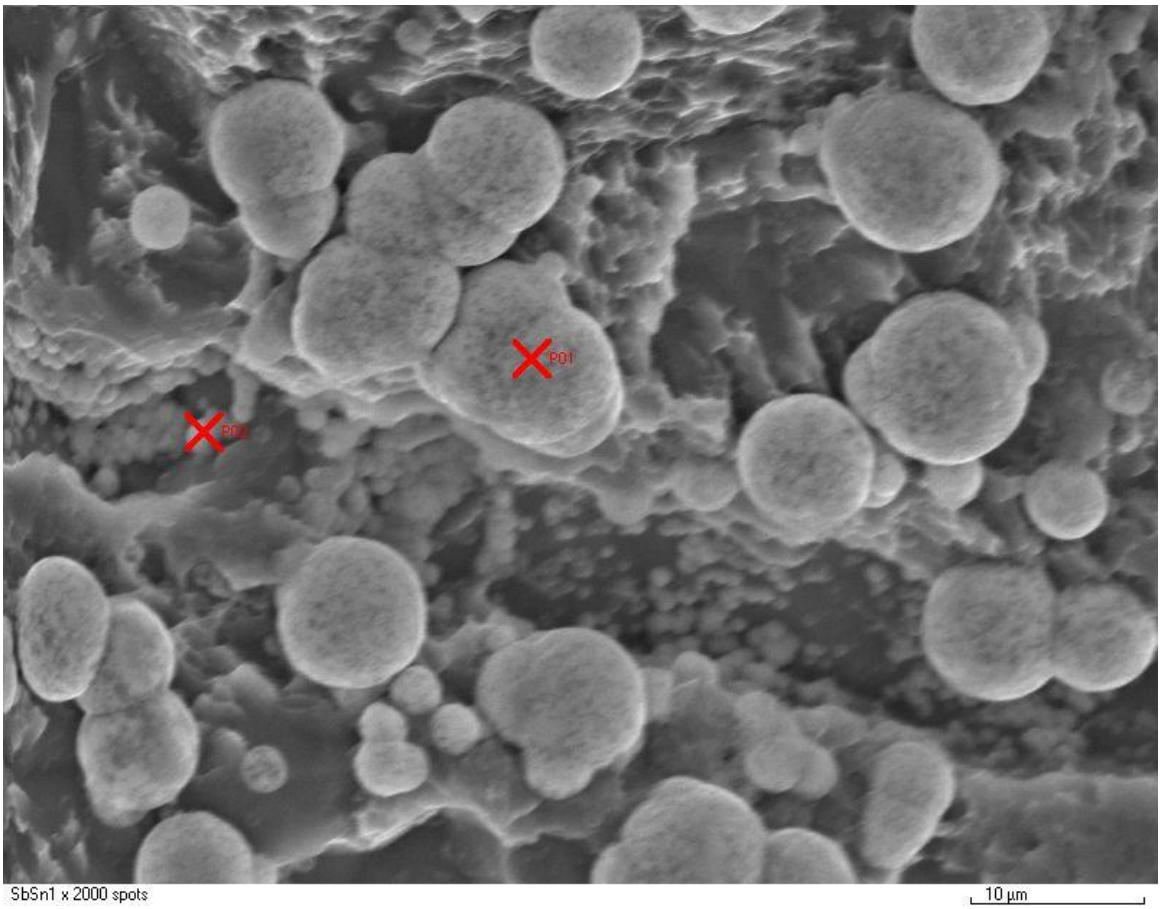

(a) × 2000

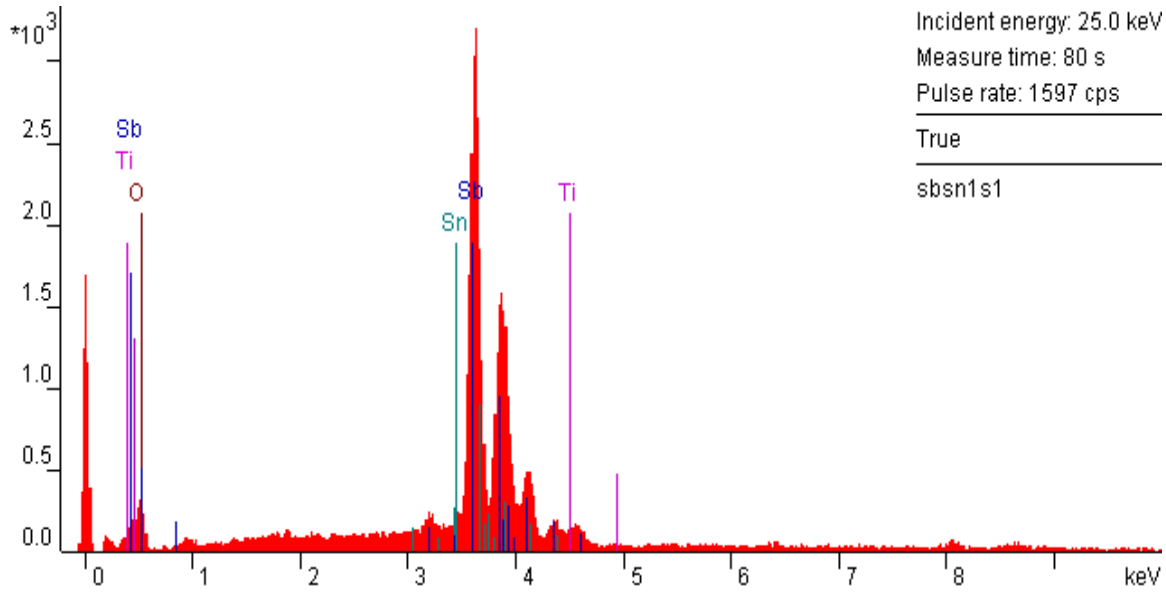

(b)

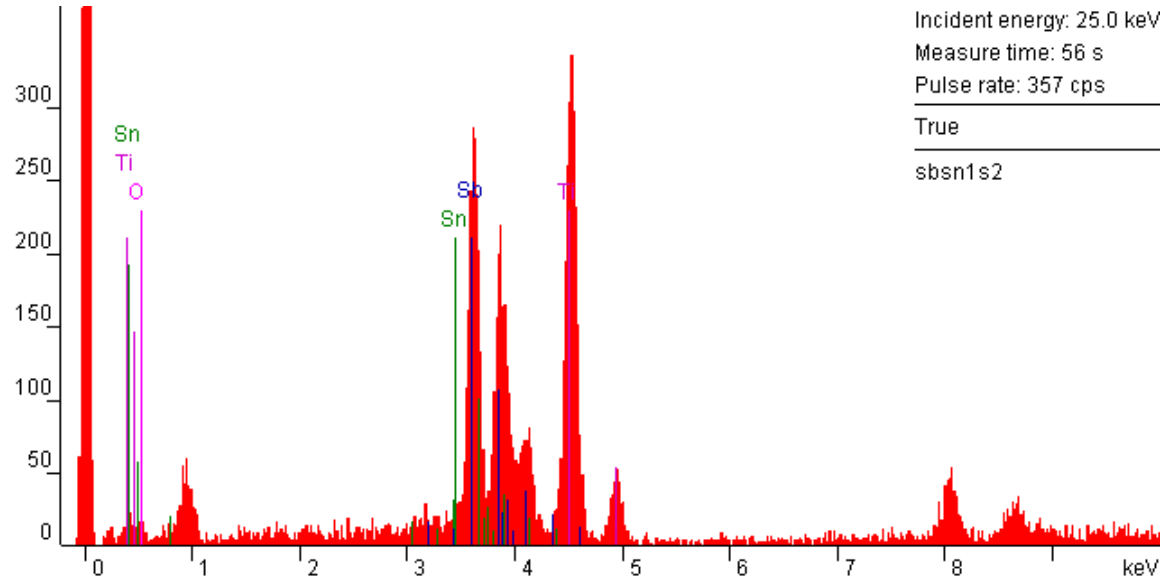

(c)

Figure 3. 20. (a) SEM image of Ti mesh after ED process from $SnCl_4$ + $SbCl_3$ solution, two random spots were allocated on this SEM image, (b) EDX spectrum of spot 1 from (a) and (c) EDX spectrum of spot 1 from (a). See text for the ED process conditions.

were carried out, and the EDX spectra so obtained are shown in figs. 3.20(b) and (c), respectively. It may be seen from figs. 3.20(b) and (c) that only Sb has been deposited and it was not thick enough to stop the Ti from appearing in the EDX spectra. Again, it may be seen from figs. 3.19 and 3.20 that the EDIL did not cover all the Ti mesh substrate (as it should do). Hence, the EDIL does not fulfil its primary aim, that of protecting the Ti mesh from oxidation, and the EDIL was not employed in the remaining electrodes reported in this thesis.

3.10 Anode Preparation Using Sb and Ni Oxides (NATO Anodes)

As will be discussed in detail in the following chapter, Chapter 4, new precursors were employed in the coating solution to prepare Ni/Sb – SnO_2 anodes. This precursor solution was made up of $SnCl_4.5H_2O$, Sb_2O_3 and NiO dissolved in 97.5% ethanol and 2.5% HCl, with a new ratios of Sn: Sb: Ni = 67: 4.3: 1, as discussed in section 2.2.2. The main idea of this work was to improve the durability (service life) of Ni/Sb – SnO_2 anodes. In this regard, not only the precursor components were changed but also the furnace temperature at which the anodes were annealed. The anodes studied here were from the KZ06 series. In this chapter, preliminary work to investigate the effect of the new precursors and the furnace temperature on the electrochemical characteristics and ozone activity of 0.8 cm × 0.8 cm anodes prepared using the new precursor solution will be described and this discussion continued in the next chapter.

3.10.1 The electrochemical characteristics of the anodes prepared using NiO&Sb_2O_3

As discussed in sections 3.2 - 3.5, the electrochemical characteristics of the anodes were investigated using cyclic voltammetry in 0.5 M Na_2SO_4 with and without 0.1M ferrocyanide, and in 1 M $HClO_4$, and the cyclic voltammograms so obtained were similar to those shown in figs. 3.1, 3.7(a) and 3.8, respectively. These figures can be taken as representative of the KZ06 series under investigation in this section. The main parameters obtained were: I_{cap} (mA), ΔE (V), d_f and the O_3/O_2 onset potential, and they are summarised in table 3.5. In addition, SEM images and EDX analysis were performed on representative samples of those anodes. The values included in the table 3.5 are the average of two electrodes prepared the same way.

Temp / ^oC	Coats No	Catalyst /mg	I_{cap} /mA	ΔE /V	O_2/O_3 Onset potential /V	d_f	I_{30s} /mA	η / %
550	8	1.2	0.40	0.13	1.8	1.64	51	23
460	8	1.2	0.30	0.15	1.8	1.70	51	20
390	8	0.7	0.47	0.15	1.8	1.63	40	18

Table 3. 5. Summary of the data and parameters obtained by SEM, EDX, cyclic voltammograms in 0.5 M Na_2SO_4 with and without 0.1 M ferrocyanide and in 1 M $HClO_4$ using the small scale NATO anodes.

3.10.2 Catalyst loading with furnace temperature

The new anodes (NATO) were prepared without any EDIL and with only 8 catalyst coatings. The average values of the catalyst loading at different furnace temperatures of

390 ^{o}C, 460 ^{o}C and 550 ^{o}C are shown in table 3.5. As may be seen from the table, the catalyst loading varied with the furnace temperature. For more detailed picture of these differences, the data from the table were used to plot fig. 3.21 which shows the variation in catalyst loading and d_f with furnace temperature.

It may be seen from fig. 3.21 that the catalyst loading increased to ca. 1.2 mg with increasing furnace temperature up to 460 ^{o}C, then it reached a plateau. In addition, the dimensionality (d_f) increased from 1.63 to 1.7 with increasing furnace temperature up to 460 ^{o}C, and then decreased to 1.64 at 550 ^{o}C. It is not clear why more catalyst can deposit on the Ti substrate at 460 ^{o}C than that at 390 ^{o}C.

3.10.3 I_{cap} and ozone generation current & current efficiency with furnace temperature

As discussed above, I_{cap} was obtained from the cyclic voltammograms in 0.5 M Na_2SO_4. The variation in I_{cap} with furnace temperature for the NATO anodes is shown in fig. 3.22. It may be seen from the figure that the I_{cap} decreased from ca. 0.47 mA at 390 ^{o}C to ca. 0.3 mA with increasing furnace temperature up to 460 ^{o}C, then it increased to 0.40 mA at 550 ^{o}C. It is not directly clear why this is the case. It is well known that the I_{cap} is proportional

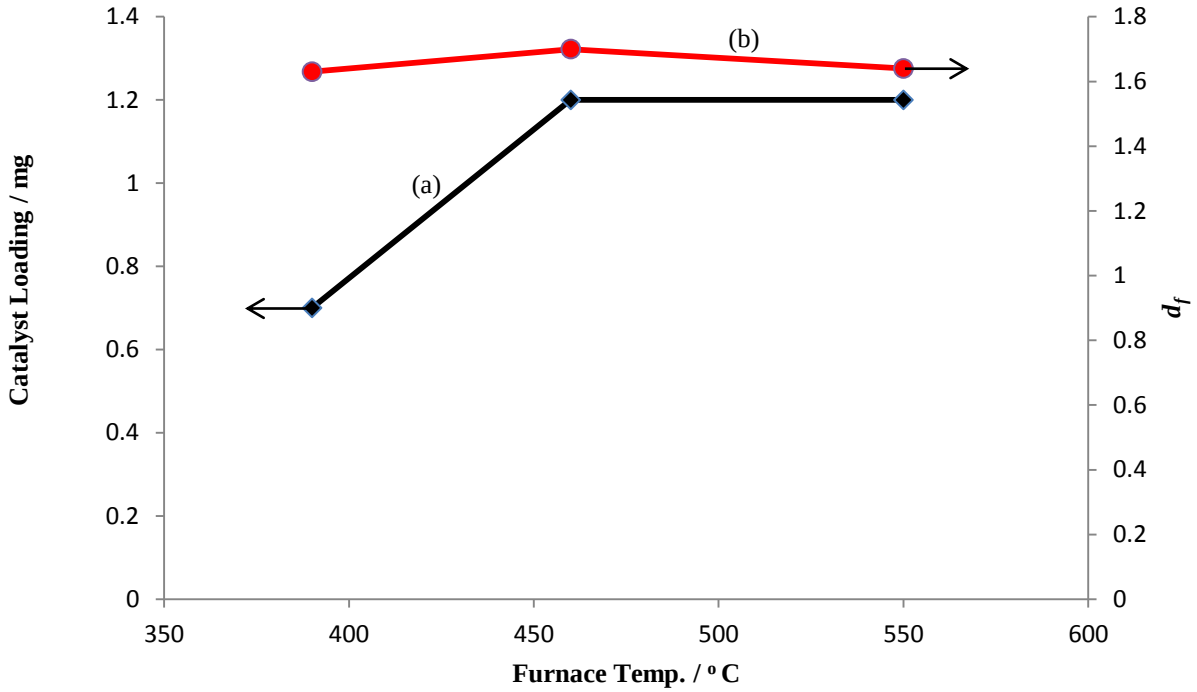

Figure 3. 21. Plots of (a) catalyst loading and (b) d_f vs. furnace temperature for the 0.8 cm × 0.8 cm anodes prepared using Sb and Ni oxides (NATO), the data obtained from table 3.5.

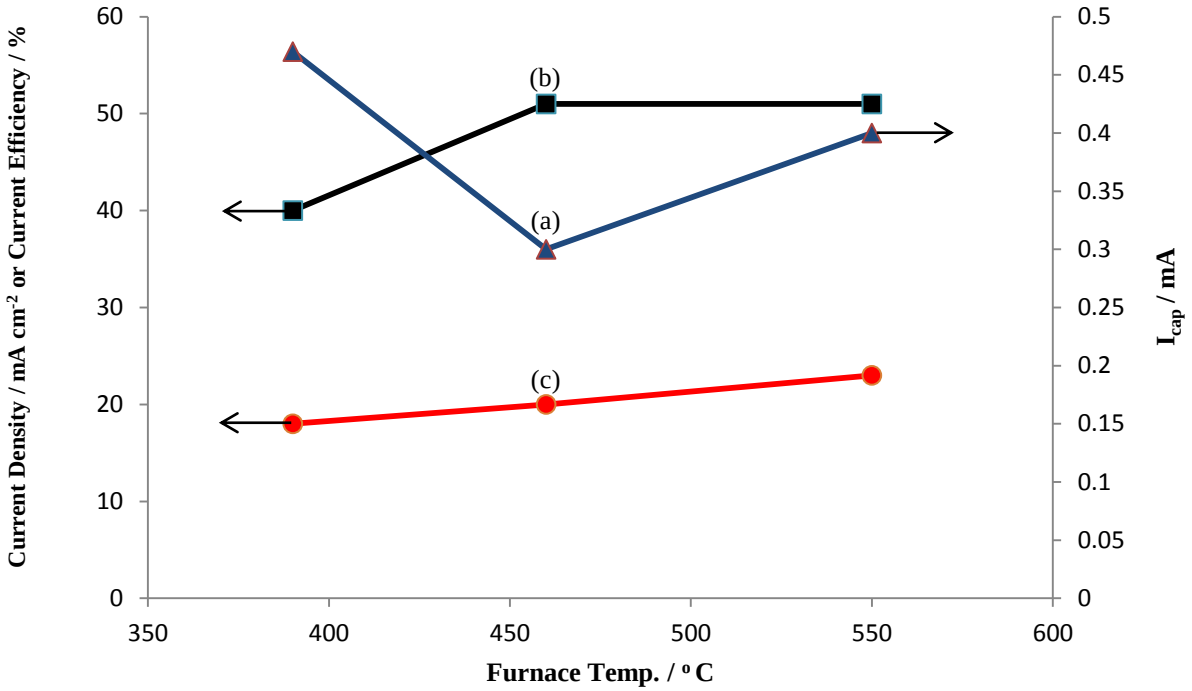

Figure 3. 22. Plots of (a) capacitive current I_{cap}, (b) current and (c) ozone current efficiency vs. furnace temperature for the 0.8 cm × 0.8 cm anodes prepared using Sb and Ni oxides (NATO), the data obtained from table 3.5.

to the real surface area of the anode, and d_f is also related to the real surface area. It may be seen from figs. 3.21 and 3.22 that I_{cap} and d_f are showing diametrically opposed variation with furnace temperature which makes interpretation of the data more difficult.

It may be seen from fig. 3.22 that the current increased to ca. 80 mA with increasing the furnace temperature up to 460 ^oC, after which it reached a plateau. The increase in current from 390 ^oC to 460 ^oC indicates that the number of active sites (ozone and oxygen) generally increased with increasing the temperature up to 460 ^oC, above which no real change in the number of active sites took place. In contrast, the current efficiency increased slightly but almost linearly with the furnace temperature; suggesting a concomitant increase in the ratio of ozone/oxygen active sites.

3.11 Conclusions

The 0.8 cm × 0.8 cm SNATO with or without Au or Pb and NATO anodes were investigated with respect to their surface composition, electrochemical characteristics and the ozone activity. In general, the SEM images and EDX analyses showed little or no differences between the SNATO, AuSNATO, PbSNATO and NATO anodes. The cyclic voltammograms in 0.5 M Na_2SO_4 with and without ferrocyanide were used to estimate the

electron transfer in anode/electrolyte interface (ΔE / V), the capacitive current (I_{cap} / mA) and dimensionality (d_f) of the anodes. The presence of Au or Pb resulted in little or no difference between these values and the values obtained with SNATO and NATO anodes. However, the cyclic voltammograms in acid, showed that the Au is present on the AuSNATO anode surface and resulted in reduction and oxidation peaks that were not observed with SNATO, PbSNATO and NATO anodes, suggesting a possible Au surface enrichment. In terms of the ozone current efficiency, the Au resulted in decrease of the ozone/oxygen active site ratio or switching off the ozone active sites. In contrast, Pb had little or no effect on the current efficiency.

The data suggest that, as the thickness of the SNATO coating on the Ti mesh is increased, the electroactive area exposed to the electrolyte, the fraction of sites active for ferrocyanide oxidation in neutral solution, and O_2 & O_3 gas evolution in acid electrolyte all increase; in the case of ozone evolution by a factor of 2.5 between SNATO02D (catalyst loading of 1.3 mg) and SNATO02H (5.1 mg). In addition, the nature of the ozone-active sites apparently changes with the thicker anodes being more active (lower onset potential).

The electrochemical data is consistent in suggesting that at least the SNATO and PbSNATO electrodes are increasingly active in general electrochemical terms as the catalyst coating is increased. At first sight the SEM data supports this, showing the thicker anodes have the cracked earth morphology with fissures of the order of μm across.

For all anodes, namely SNATO, AuSNATO, PbSNATO and NATO, there was apparent absence of any participation of the walls of the fissures in the catalyst layer in $Fe(CN)_6^{4-}$ oxidation as the anodes all behave as 2-dimensional electrodes with electro-inactive regions. However, the clear increase in the current with catalyst loading (SNATO and PbSNATO) during electrolysis of aqueous perchloric acid, suggests the participation of pores and cracks that are of a size not visible to SEM. The increase in the fraction of surface active for ozone evolution with catalyst loading may be attributed to surface Ni enrichment. It may be the case dipcoating a layer upon the previous coating removes a little of the surface layer of the previous deposition cycle. If there is a tendency for the nickel to segregate to the surface, it is at least feasible that increasing the number of deposition cycles will lead to a steady increase in the nickel concentration at the surface.

The furnace temperature at which the new NATO anodes were calcined had a significant

effects on the ozone current efficiency. Where the anodes prepared at furnace temperatures ≥460 ^oC seemed to be superior in performance. No further durability (service life) investigation was done on the small scale anodes, and this was decided to be covered in the following chapter.

The data in fig. 3.13 suggest that high cell voltages (2.7 V or 2.8 V) are the most effective in terms of the amount of ozone produced, through the constant efficiency but high currents observed. That is why 2.7 V was used for ozone generation on the all the remaining small scale anodes.

In the following chapter, as mentioned above, the effect of the composition of the new precursor containing Sb and Ni oxides instead of their respective chlorides and the furnace temperature on the structure, selectivity, activity and durability of 2.5 cm × 2.5 cm Ni/Sb – SnO_2 anodes will be investigated.

CHAPTER FOUR

4 Activity, Selectivity and Durability of 6.25 cm^2 NATO Anodes

4.1 Introduction

This chapter reports the effect of employing Ni & Sb oxide precursors (instead of chlorides) in the preparation of Ni/Sb-SnO_2 anodes on the activity and selectivity of ozone production in 1.0 M $HClO_4$. The effect of catalyst loading, Ni content in the precursor solution, furnace temperature and constant current density *vs* constant cell voltage operation are reported. The durability of anodes prepared using NiO and Sb_2O_3 at 550 °C was also investigated.

4.1.1 The anodes

The work reported in this chapter was carried out on 2.5 cm × 2.5 cm NATO anodes from the anode series KZ07 – KZ16. As may be seen in table 2.3 and Appendix II, all the anodes were 2.5 cm × 2.5 cm Ti meshes coated with an electrocatalyst (Ni/Sb – SnO_2) using the thermal deposition method as described in section 2.2.2. The electrocatalyst was deposited from an ethanolic precursor solution containing $SnCl_4$. $5H_2O$, Sb_2O_3, and NiO at a ratio of Sn: Sb: Ni = 67: 4.3: ×, and × was varied from 0.1 to 2. The coating process was repeated up to 20 times (see Appendix II). However, most of the anodes had only 8 coatings. All of the anodes underwent the same heat treatment during the coating process, unless otherwise stated.

4.1.2 Resistivity of catalyst layer

Undoped SnO_2 should be an insulator with resistivity of *ca*. 7.25 x 10^{-3} Ω cm. SnO_2 anodes are usually doped with Sb to improve the conductivity of the electrodes (resistivities *ca*. 10^{-5} - 10^{-4} Ω cm [155, 156]), with the Sb (as Sb^{5+} [157]) replacing Sn^{4+} due to their similar ionic radii [156] and hence no change occurs in lattice parameters[158]. Resistivity initially falls with Sb doping, but then increases at higher dopant levels due to the incorporation of Sb(III) centres[101, 159] which act as trap sites for the electrons generated by Sb(V) [156]. There is some disagreement as to where the minimum resistivity occurs in Sb-doped SnO_2 anodes, e.g.: Kötz and co-workers [157] report this as being between 4 and 9 mol.% Sb, whereas Lehmann & Widmer [160] and Chopra et al.[161] suggest 0.4 – 3 mol.% Sb. Hence, it does not seem unreasonable to postulate that the resistivity of the catalyst layer is likely to be an

important factor in ozone activity.

4.1.3 The service life of Ni/Sb – SnO_2 anodes

Although there is a number of reports in the literature on the durability (or service life) of Ti/Sb – SnO_2 anodes [99-101, 138, 150, 151], there is a lack of detailed studies on the durability of Ni-doped Sb – SnO_2 anodes. As discussed before, in the absence of Ni, the service life of Ti/Sb – SnO_2 anodes is defined as the electrolysis time at which the anode potential increases rapidly to more than 5 V vs. the reference electrode under the operational conditions employed[92, 101]. Correa-Lozano et al.[101] found that the service life of Ti/Sb – SnO_2 anodes was only 12 h at 1000 A m^{-2}, but could be increased to 1150 h by reducing the current density to 60-200 A m^{-2} [100]. A number of papers report attempts to improve the durability of these anodes, for example: Vicent et al. [138] studied the addition of Pt to improve the service life of Ti/Sb – SnO_2 anodes at 40 mA cm^{-2} in 0.5 M K_2SO_4, and showed that a service life of 760 h could be obtained. Montilla et al.[99, 150, 151] also found that the addition of trace amounts of Pt to the coating solution improved the service life of Ti/Sb – SnO_2 anodes from 300 h at 10 mA cm^{-2} in 0.5 M Na_2SO_4 solution buffered at pH = 6.9 to 990 h at 50 mA cm^{-2}. XPS data, taken together with the results of electrochemical experiments, were interpreted by Montilla and co-workers as strong evidence for the deactivation of Sb-SnO_2 *via* the formation of a passivating OH-containing layer at the SnO_2/electrolyte interface. Pt was postulated as preventing this, and hence significantly extending the service life; with added Pt, deactivation was postulated as occurring through long term attack on the Ti substrate and the formation of a passivating layer at the Ti/catalyst interface, possibly TiO_2.

To date, the only literature reports on the durability of Ni/Sb-SnO_2 anodes are by Shekarchizade and Amini[92], who reported a service life of about 600 min for the best anodes at 200 mA cm^{-2} in 0.1 M H_2SO_4, and Parsa et al.[91] who added carbon nanotubes to the coating solution and achieved up to 17 hours (compared to 3 h without the nanotubes [90]) during which the voltage increased up to 3.49 V at 53.5 mA cm^{-2} in 0.1 M $HClO_4$.

It is interesting that small changes in the composition of the precursor solution (such as adding carbon nanotubes) can have such a marked effect upon durability. Rather than explore the effect of additives, given that all the work reported on Ni/Sb-SnO_2 to date has been carried out using anodes prepared from chloride precursors and furnace temperatures $\leq$ 520 ^oC [4, 42, 50, 64, 75-77, 90-93], it does not seem unreasonable to explore the effect of: (i)

changing the Ni and Sb precursors from chlorides to oxides (given that SnO_2 is commonly doped with Sb using Sb_2O_3 [162, 163]) and (ii) furnace temperature.

The activity and selectivity of the anodes so produced were characterised in terms of: catalyst loading, Ni content in the precursor solution, furnace temperature and constant current/voltage operation. In addition, the durability of the anodes was investigated by electrolysis in 1M $HClO_4$. Further, it is clear that the development of Ni/Sb-SnO_2 anodes is still at a somewhat early stage, with some fundamental questions remaining unanswered; specifically, how durable can these materials be and what magnitude of current density can they sustain? This chapter seeks to address these questions.

4.2 EDX and SEM

Typical SEM images of the NATO14M anode prepared using a precursor solution containing 93.3, 6.0 and 0.7 at.% Sn, Sb and Ni, respectively, are shown in figs. 4.1(a) and (b). Figure 4.1(a) shows an image taken of a node (intersection of two strands) of the mesh, and fig. 4.1(b) of an area on a strand, both at × 5000 magnification. It was generally observed that the coating on nodes exhibited a cracked morphology; an observation made by other workers[90-92, 99], whilst the coating on strands presented a smoother appearance, suggesting a thicker coating on the intersections. The latter postulate is supported by EDX spectra of the same regions of the mesh, see figs. 4.2(a) & (b). The peak near 4.52 eV in fig. 4.2(b) may be attributed to the underlying Ti substrate, detected due to the thinner catalyst coating on the strands.

4.3 Activity and Selectivity vs Catalyst Loading

Figure 4.3 shows a plot of catalyst loading *vs* number of dipcoats; these anodes (KZ14 series) were NATO14A – P which were made to explore the effect of catalyst layer thickness on activity *etc*; each data point is the average of two anodes prepared in an identical fashion (see Appendix II). The at.% ratio of Sn:Sb:Ni was 93.3:6.0:0.7 in the dipcoating solution. There is a fairly linear relationship between the number of coating cycles and the amount of catalyst deposited. Figure 4.4 shows (i) the corresponding current densities (measured in flow mode) and (ii) the total (gas + solution) current efficiencies. Figure 4.4 shows that, up to a catalyst loading of ca. 1.0 mg cm^{-2}, current density and current efficiency increase, suggesting that there is an increase in the number of ozone and oxygen active sites, and that the ratio of the former to the latter also increases, *ie*. a greater proportion of the sites are active for ozone as the loading increases. This, in turn, suggests

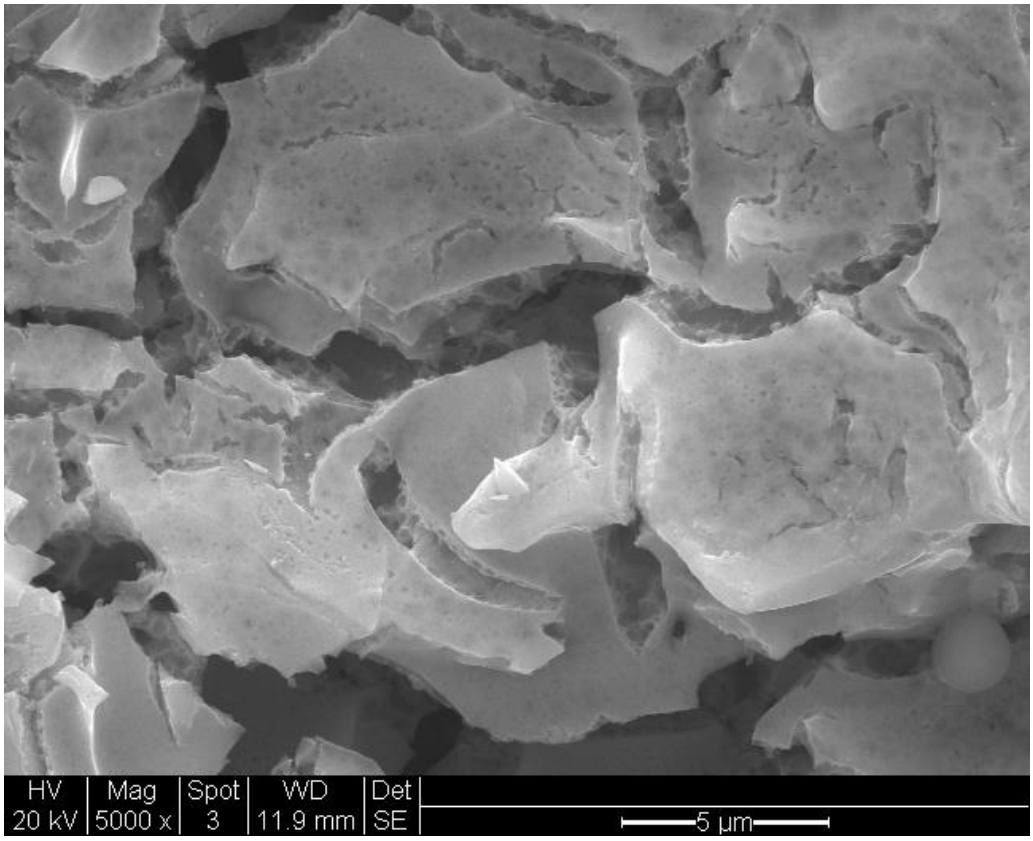

(a)

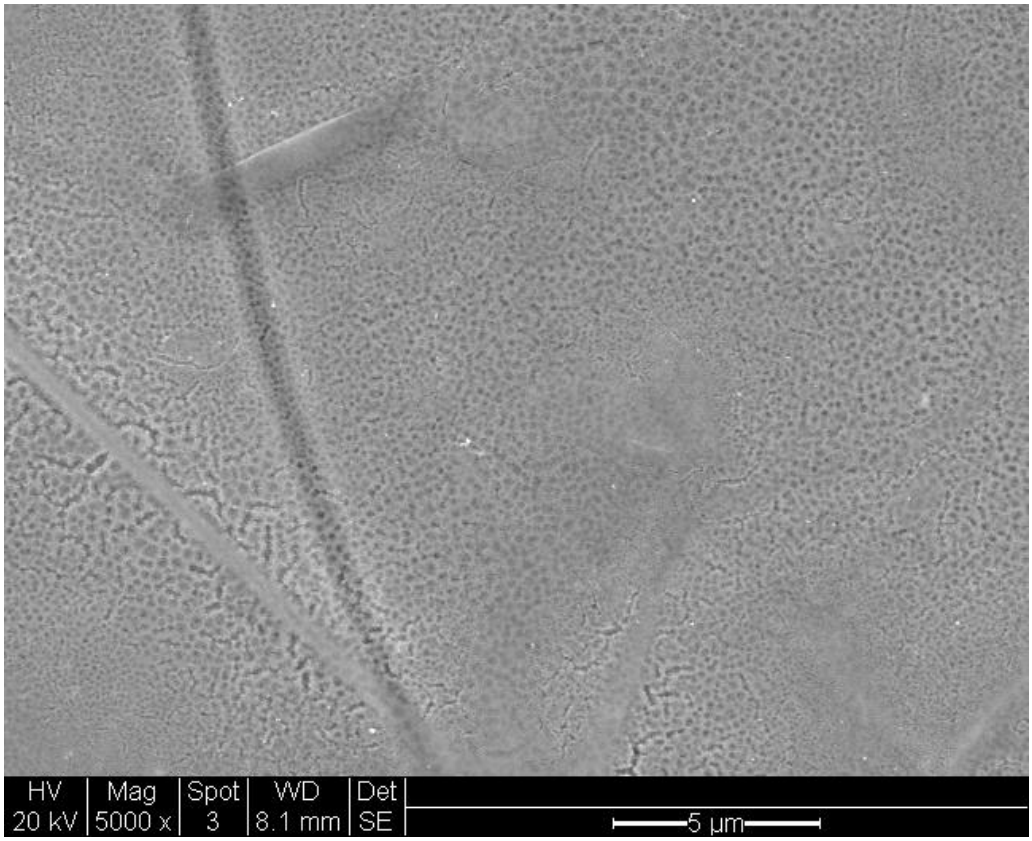

(b)

Figure 4. 1. Typical SEM images (× 5000, bar = 5 µm) of two areas of NATO14M anode: (a) a node, and (b) a strand.

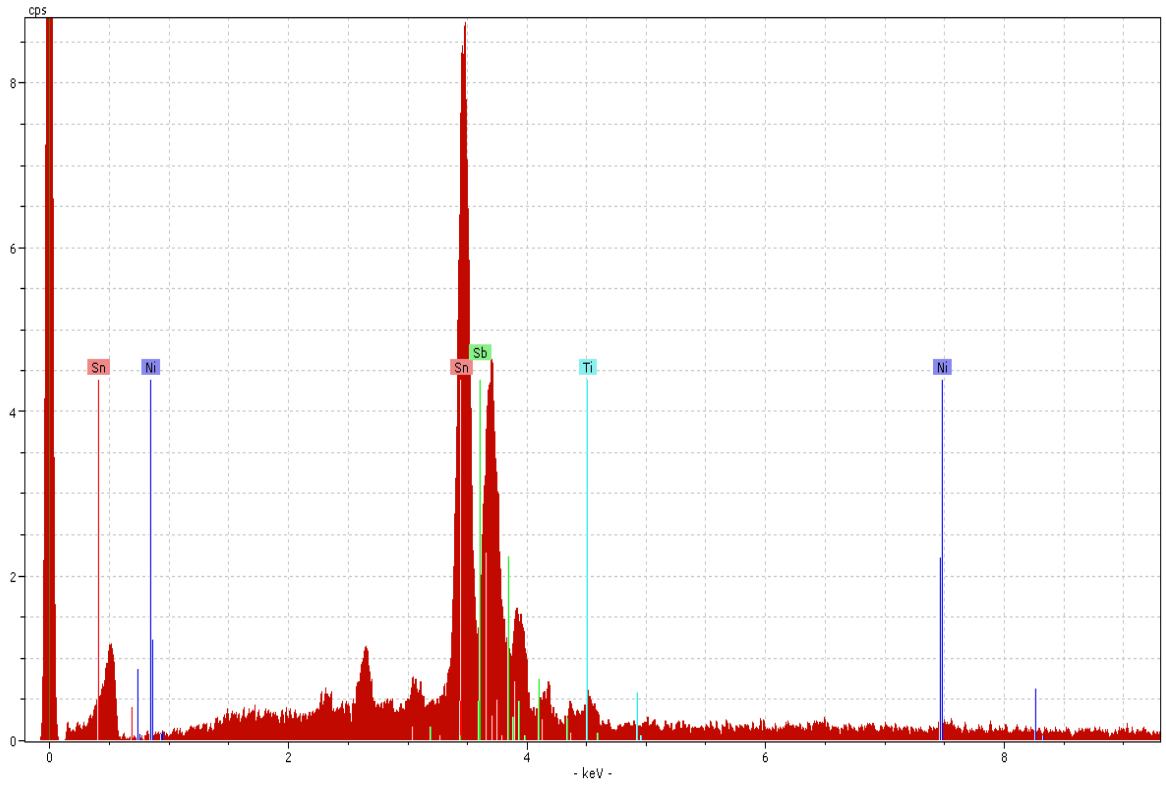

(a)

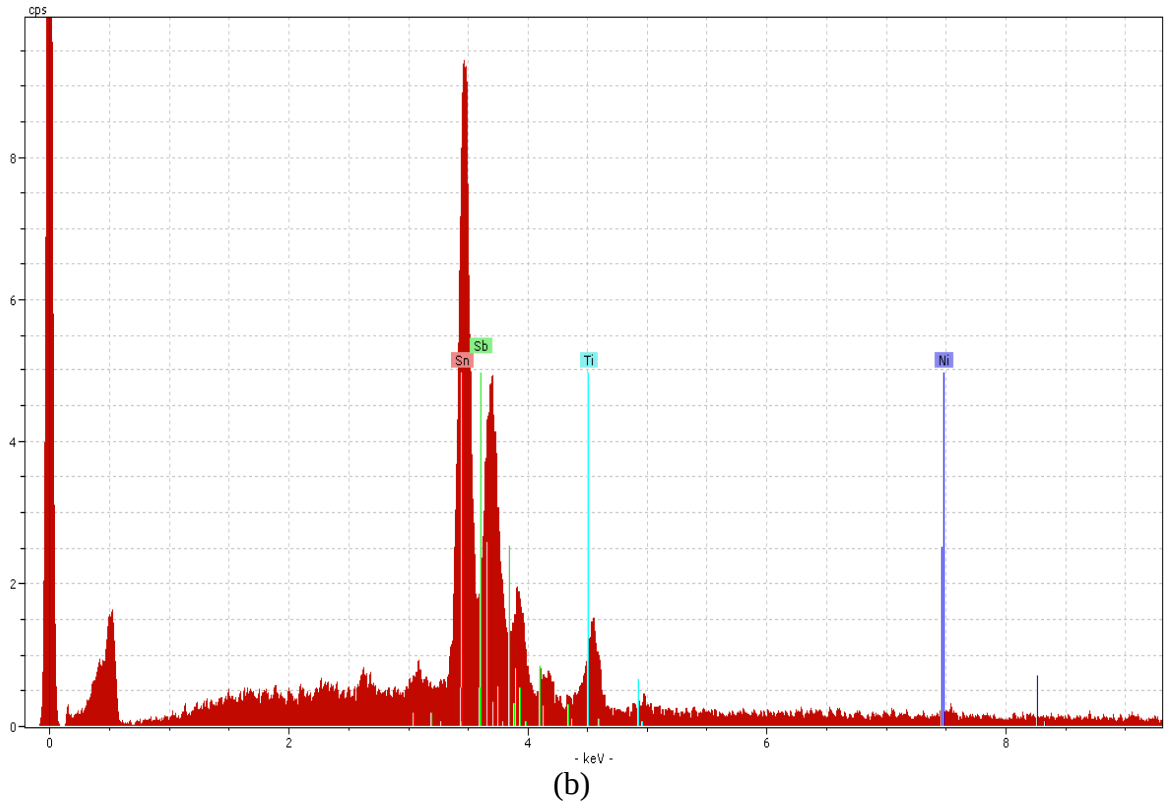

(b)

Figure 4. 2. (a) & (b) EDX spectra of the same regions of the electrode in fig. 4.1.

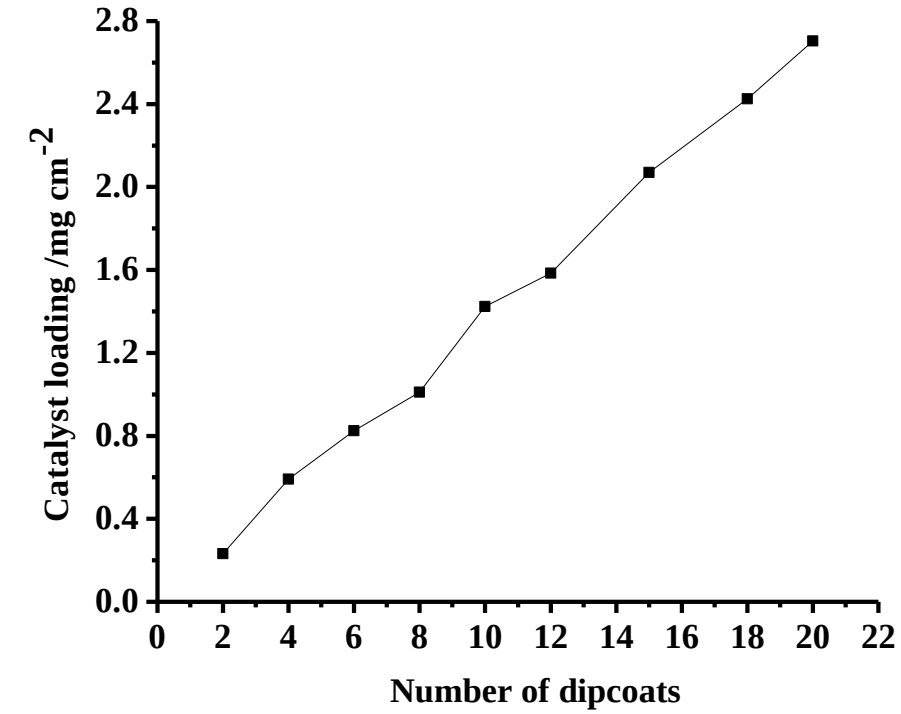

Figure 4. 3. Plot of catalyst loading vs number of dipcoats. Each datapoint is the average of two anodes prepared by the same method. The anodes were from KZ14 series.

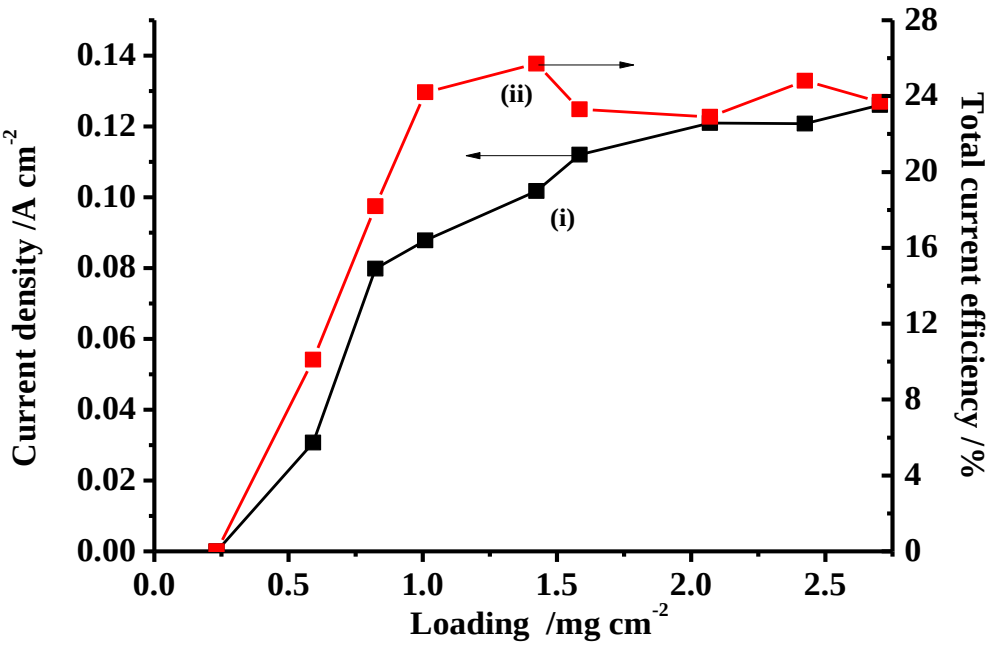

Figure 4. 4. Plots of (i) current density and (ii) current efficiency for the anodes in fig. 4.3. Current densities were measured at a cell voltage of 2.7V in single pass mode at an anolyte (1M $HClO_4$) flow rate of 30 cm^3 min^{-1} in the glass cell, and total current efficiencies were calculated from the current passed and the gas & dissolved ozone absorbances.

that the catalyst is porous such that the active sites are not confined to the 'geometric' surface of the anode, and that there is, perhaps, some surface enrichment by Ni, favouring ozone formation over oxygen evolution, as was observed in previous studies [76]. Figure 4.4 also shows that, after 8 dipcoats, (corresponding to 1.0 mg cm^{-2}), the ozone current efficiency remained constant, but the current density continued to increase with catalyst loading, albeit more slowly in agreement with the work of Wang at al.[75] and in contrast to Parsa et al.[90] who found that the ozone current efficiency increased with increasing catalyst loading, although they prepared only 3 electrodes (according to optimum composition of Wang et al.[75]) with 4, 8 and 12 coating cycles without stating the catalyst loading on the mesh. Thus, above this critical loading, the number of O_2 and O_3 active sites continues to increase, but the ratio of the two now remains constant.

4.4 Comparison of Constant Current vs Constant Voltage Operation

Figures 4.5(a) and (b) show the effect of current density and cell voltage on current efficiency (solution, gas and total) at constant catalyst loading; also shown in the figures are the cell voltages observed at each current density or the current density observed at each cell voltage. The anode (NATO14H) had the composition Sn: Sb: Ni = 93.3 at.%: 6.0 at.%: 0.7 at.%, and comprised 10 coats (loading 1.4 mg cm^{-2}). There are clearly very marked differences in terms of the current efficiencies observed during the two sets of experiments. It should be noted that each data point in figs. 4.5(a) and (b) represents a steady state measurement after $\geq$ 15 minutes at that particular cell voltage or current density. To date, Parsa et al.[91] is the only research group to have studied the effects of constant current density on the ozone current efficiency using co-doped Ni/Sb – SnO_2 (with and without carbon nano-tube anodes), and found that the current efficiency increased up to ca. 25 mA cm^{-2}, after which it declined sharply. In a separate paper, Parsa et al.[90] reported that ozone current efficiency also exhibited a maximum as a function of cell voltage, an observation supported by Wang et al.[75] and in contrast to the data presented here.

Figure 4.5(c) compares the total current efficiencies observed as a function of current density and cell voltage (both plotted against current density imposed or observed, respectively) and the power consumption. From fig. 4.5(c) it can be seen that, under both constant voltage and constant current density operation, the total current efficiency rises to a maximum with increasing current density, then remains essentially constant. This

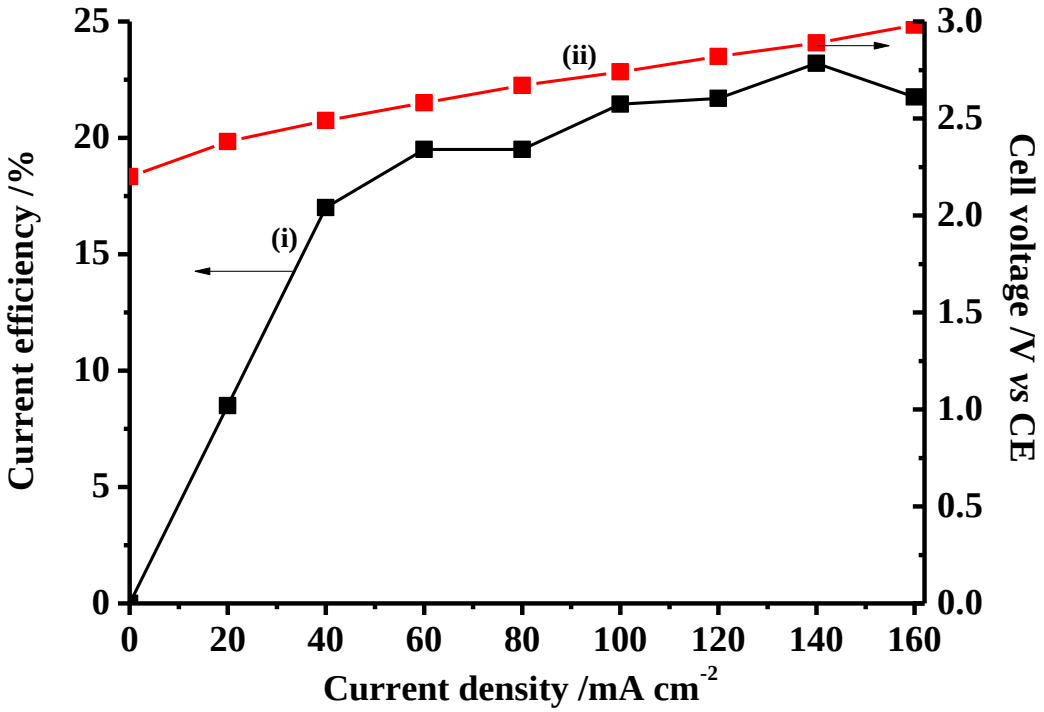
Current efficiency /%
Cell voltage /V vs CE
Current density /mA cm^{-2}
(i)
(ii)
0
5
10
15
20
25
0.0
0.5
1.0
1.5
2.0
2.5
3.0
0
20
40
60
80
100
120
140
160

(a)

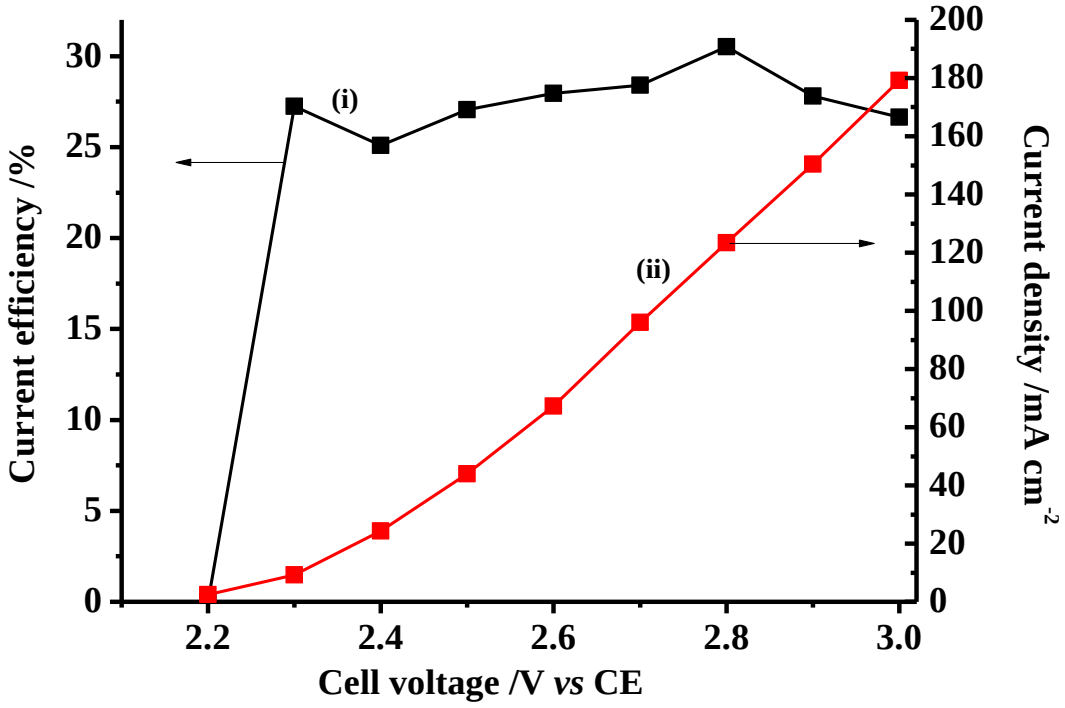
Current efficiency /%
Current density /mA cm^{-2}
Cell voltage /V vs CE
(i)
(ii)
0
5
10
15
20
25
30
0
20
40
60
80
100
120
140
160
180
200
2.2
2.4
2.6
2.8
3.0

(b)

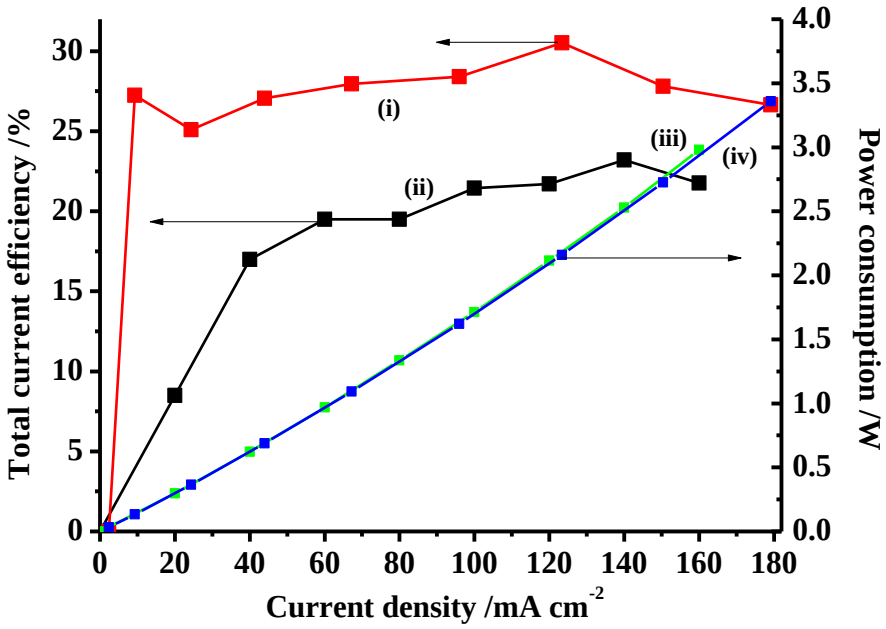

(c)

Figure 4. 5. Plots of (i) total (gas+solution) current efficiency and (ii) cell voltage or current density for experiments carried out in the glass cell using flow mode in 1M $HClO_4$ at (a) constant current density and (b) constant cell voltage. The anolyte flow rate was 60 cm^3 min^{-1}, and the anode was NATO14H . Each data point was measured once the system had reached steady state, typically ca. 15 minutes from the start of each experiment. (c) Plots of current efficiency and power consumption (cell voltage × current) for the experiments in (a) and (b): (i) & (iv) at constant cell voltage, (ii) & (iii) constant current density.

transition happens near ca. 10 mA cm^{-2} at constant voltage and ca. 60 mA cm^{-2} at constant current density. Moreover, the maximum current efficiency observed is higher at constant voltage. In general, PbO_2 anodes also show increasing current efficiency up to some limiting current density (typically 1 A cm^{-2}, but this value depends upon the electrolyte [29]), before levelling out and becoming independent of current [29-31, 46, 47, 49]. There are exceptions, however; for example, Onda and co-workers[48] and Awad and Saleh [74] who observed ozone current efficiency passing through a maximum with increasing current density. Boron doped diamond (BDD) electrodes also show current efficiency both becoming independent of current density [45] and passing through a clear maximum [62]. In contrast to PbO_2, BDD and NATO anodes, TiO_2 [78, 79], Pt [39], C [40] and TaO_x [12, 59] show increasing current efficiency with current density; however, this may be due to insufficient current density being applied and hence the transition in behaviour not being attained. IrO_2-Nb_2O_5 shows an onset current density for ozone evolution that varies with IrO_2 content [37] .

It is not immediately clear why constant voltage should yield higher current efficiencies than constant current.

As can be seen from fig. 4.5(c), the variation in power consumption observed is identical for the two sets of data, reflecting the fact that the same electrochemical cell and system were employed and that there is a 1:1 correlation between imposed current density and the cell voltage observed on the one hand, and imposed cell voltage and the current density observed on the other. The data in fig. 4.5(c) suggest that local heating effects are not observed. Early workers in electrochemical ozone generation (see[29, 164] for an excellent review of the early work) took significant care to cool their anodes to avoid heating as it was shown that current efficiency generally increased as temperature was decreased[39, 40, 65], with temperatures down to -60 ºC being found to be particularly effective[40, 65]. Lash and co-workers[65] showed that high current densities resulted in local heating of the anode which obscured the actual effect of such current densities on current efficiency; the authors were able to deconvolute the effect of local heating by careful cooling of the anode. However, all the above workers employed significantly higher current densities than those reported in this chapter.

4.5 Optimisation of the Ni Concentration

Figure 4.6 shows the effect of Ni concentration in the dipcoating solution on the current density and current efficiency. Each anode comprised 8 dipcoats with mean loadings of 0.94 ± 0.10 mg cm^{-2}, and each datapoint was the average of two 15 – 20 minute experiments with the ozone efficiency measured at steady state. As may be seen from the figure, the current density remains essentially constant as the concentration of Ni is increased in the catalyst to *ca*. 1.04 at.%; however, there is a 45% increase in current efficiency over this range, *ie*. from 20 to 29%. This suggests relatively little change in the total number of active sites but a very marked increase in the ratio of O_3 to O_2 sites, in line with the postulated key role of Ni in the O_3 active site. At higher concentrations, the current efficiency appears to remain constant, or decrease slightly, whereas the current density shows a sharp decline. The data in fig. 4.6 are in broad agreement with the work of Shekarchizade and Amini[92] and Wang et al.[165]; the former found that ozone current efficiency increases with increasing Ni in the coating solution up to an optimum, although they observed the optimum Ni concentration to be ca. 0.2 at.% (and an optimum Sb concentration of *ca*. 2 at.%). Wang et al.[165] observed an optimum efficiency at a

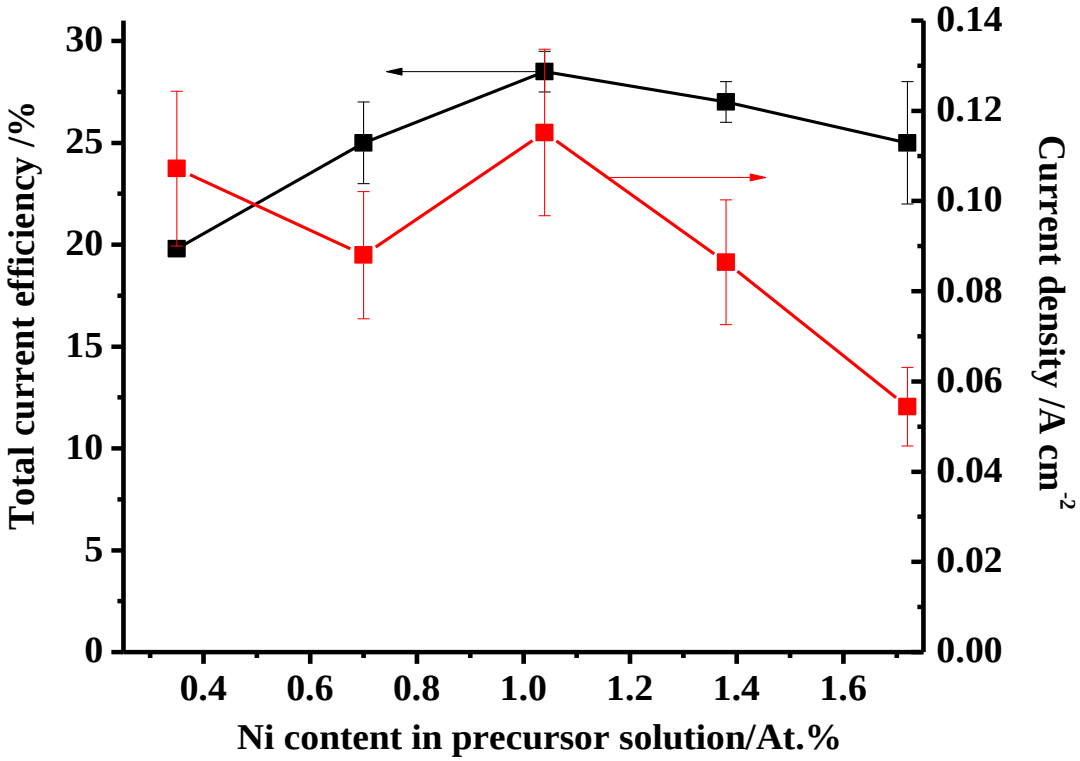

Figure 4. 6. Plots of current density and total current efficiency vs nickel concentration in the catalyst coating solution (at.%) for NATO anodes of KZ08 – 10, 12, 14 and 15 series. Each anode comprised 8 dipcoats, 0.94 ± 0.10 mg cm^{-2} and calcined at 550 ^{o}C, and each data point was the average of several distinct, ca. 15 minute experiments using several anodes of identical composition in the glass cell at 2.7V using 1M $HClO_4$ as anolyte and catholyte in flow mode measuring both gas and dissolved ozone. Anolyte flow rate 30 cm^{3} min^{-1}.

concentration of 0.71 at.% Ni in the coating solution.

Interpreting the data in fig. 4.6 poses a challenge as, as well as the uncertainty regarding the actual content of Ni in the catalyst films, whilst there is a wealth of literature on the physicochemical characteristics of Ni-doped SnO_2 due to potential application in varistors [166] and solid state gas sensors[167, 168], apart from the brief treatment in Shekarchizade and Amini[92] there is no such data in the literature on Ni and Sb-doped SnO_2. Thus, it does not seem unreasonable to use the literature on Ni doped SnO_2 as a starting point; on this basis, the significant increase in current efficiency up to 1.04 at.% may simply reflect the replacement of the Sn by Ni (due to their similar size, *ie*. 0.072 nm and 0.071 nm, respectively[166-168]) throughout the catalyst, and hence the increase in active ozone sites at the electrode/electrolyte interface. The constant current density is due to the fact that the

minimum in resistivity for Sb-doped SnO_2 is fairly broad[161].

From the Ni-doped SnO_2 literature, it is clear that the physicochemical properties of SnO_2 undergo major changes around 1 at.% Ni [166-168]. In particular, Aragón and co-workers [168] employed Raman spectroscopy and have shown that, at Ni ≤ 1 mol.%, the Ni primarily forms a solid solution with SnO_2 with some segregation to the surface, but at ≥ 2%, the latter process dominates. It does not seem unreasonable to postulate that the decrease in current density at Ni > 1.04 at.% is due to the resistivity rising with increasing Ni (moving out of the minimum resistivity due to the increased doping by Ni on top of the effect of the fixed Sb doping) and to an excessive surface concentration of Ni. Figure 4.7 shows current/voltage plots for the anodes NATO15A, C and E (see Appendix II) with 0.35, 1.04 and 1.72 at.% Ni: it can be seen from the figure that, whilst the plots for 0.35 and 1.04 at.% Ni are similar, with the latter giving a slightly higher current at 2.7 V, the plot for 1.72 at.% Ni is significantly more resistive as well as giving lower current, in agreement with the discussion above. In contrast, Shekarchizade and Amini[92] and Wang et al.[165] both report

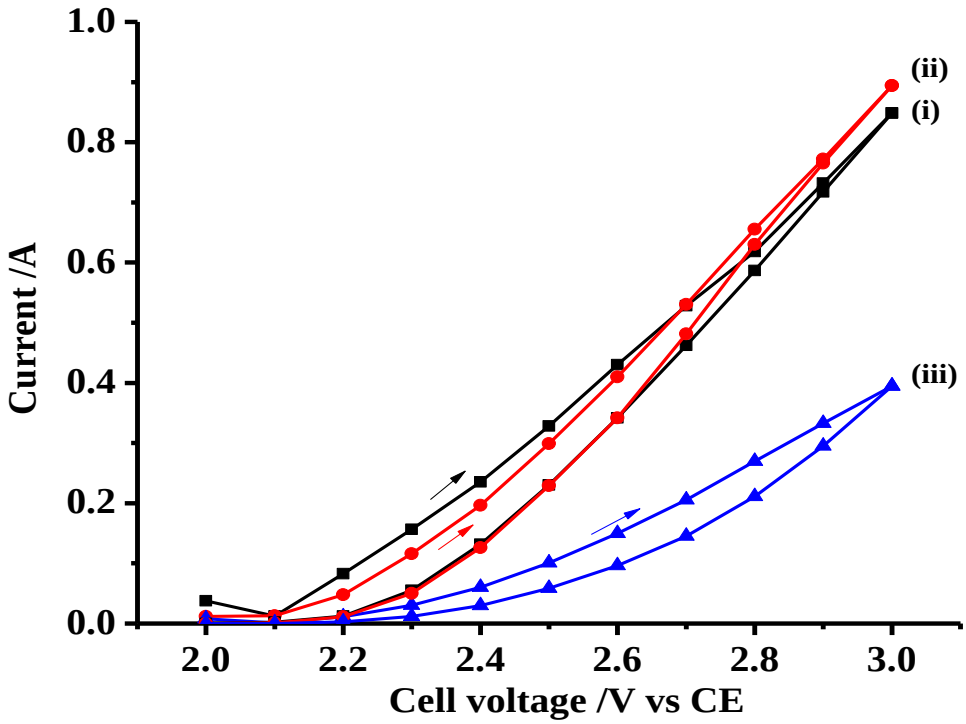

(b)

Figure 4. 7. Current/voltage plots for the anodes having (i) 0.35 (NATO15A), (ii) 1.04 (NATO15C) and (iii) 1.72 (NATO15E) at. % Ni in the coating solution. The cell voltage was stepped up from 2 to 3 V and the current measured after ca. 1 minute for each step; the voltage was then stepped down from 3 V and the measurements repeated.

that the resistance of Ni/Sb-SnO_2 anodes increases with increasing content (rather than passing through a maximum) and attribute the decline in efficiency after the maximum to this increase.

4.6 The Effect of Furnace Temperature

Figure 4.8(a) shows plots of catalyst loading vs furnace temperature for Ni/Sb-SnO_2 films having (i) 0.7 at.% and (ii) 1.4 at.% Ni, 8 coats. The anodes prepared at 390 ^{o}C, 550 ^{o}C and 460 ^{o}C were of KZ11, KZ12 and KZ13 series (see Appendix II), respectively. Each datapoint is the average of the masses of three anodes prepared in an identical manner; the ranges of the loading values are shown on the plot. As may be seen, the furnace temperature seemed to affect the loading of catalysts in a way that depended very little upon the concentration of Ni. Figure 4.8(b) shows the current density data for the experiments on the anodes shown in fig. 4.8(a); whilst there is little variation with furnace temperature for the anodes with 1.4 at.%, the anodes with 0.7 at.% show a clear maximum in current density at 460 ºC. This maximum is reflected in the plot of total current efficiency *vs* furnace temperature in fig. 4.8(c) which also shows a clear maximum at 460 ºC. All the anodes had loadings above the *ca*. 1.0 mg cm^{-2} threshold for constant current efficiency; furthermore, the catalyst loadings of the anodes decreased as

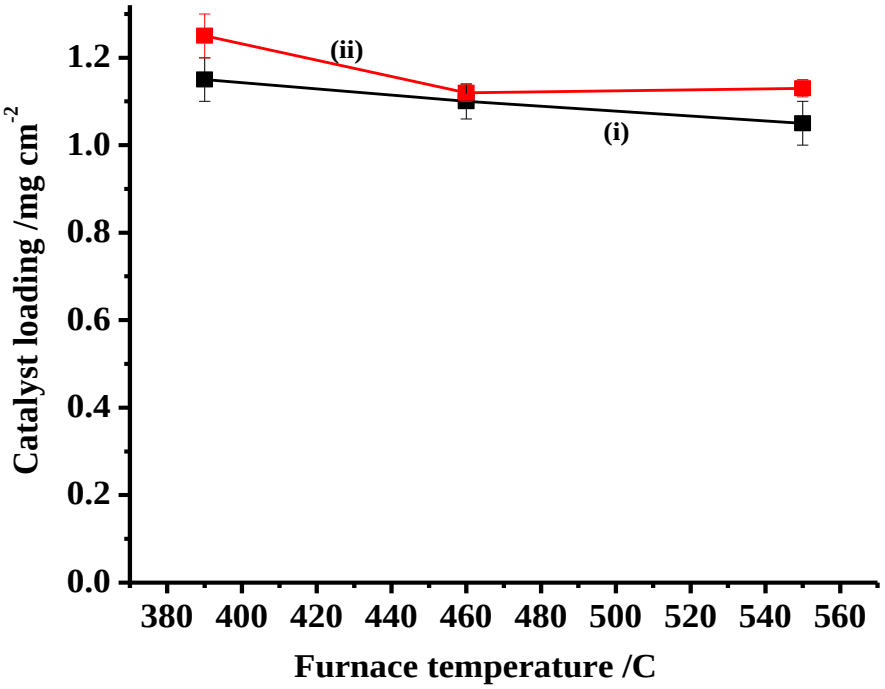

(a)

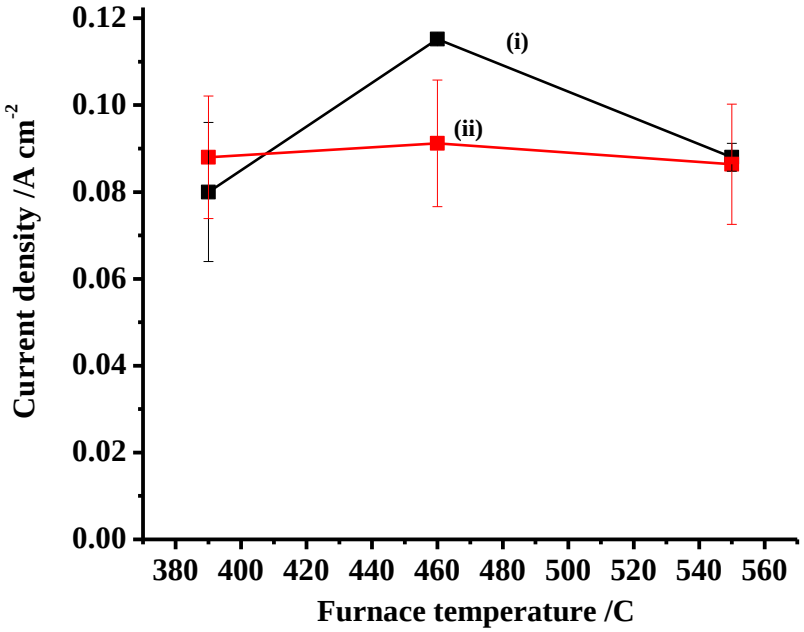

(b)

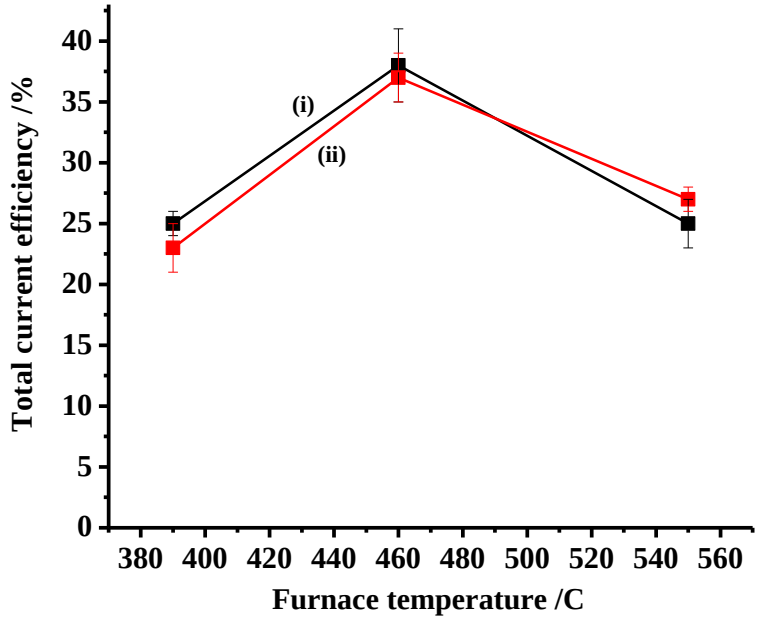

(c)

Figure 4. 8. Plots of (a) catalyst loading, (b) current density and (c) total current efficiency as a function of furnace temperature for Ni/Sb-SnO_2 anodes having (i) 0.7 at.% and (ii) 1.4 at.% Ni, 8 coats. Each datapoint is the average of two experiments (15 minutes) using three anodes prepared in an identical manner. The current densities and ozone efficiencies were measured at 2.7V in single pass mode using the glass cell and 1M $HClO_4$ as anolyte and catholyte; anolyte flow rate 30 cm^3 min^{-1}.

furnace temperature increased. This supports the postulate that current density is an important parameter in determining current efficiency. However, the anodes with 1.4 at.% also show a clear maximum in current efficiency, without this being mirrored in the plot of current density, or that showing the variation in catalyst loading; in addition, the current efficiency remains constant in fig. 4.6 at higher Ni content whilst the current density decreases sharply. Hence, current density cannot be the *only* factor governing current efficiency. This in agreement with Rufino et al.[169] and Da Silva et al. [8] who reported that ozone current efficiency is affected by temperature, real current density (i.e taking into account electrochemically active surface area), electrode and electrolyte composition.

4.7 Durability

The anodes prepared at 460 ºC clearly show higher current efficiencies than those prepared at 550 ºC, albeit comparable current densities. The question then arises as to whether furnace temperature affects durability and, if so, in what way? Figure 4.9 shows the results of a durability study carried out as described in section 2.13 on anodes prepared from the same dipcoating solution (containing Ni and Sb oxides as precursors, and at 550 °C) in an identical manner. The anode failed after *ca*. 200 hours electrolysis in 1M $HClO_4$ at 100 mA cm^{-2}. A second anode prepared in an identical manner to that in fig. 4.9 also failed after 200 hours electrolysis. Anodes prepared at 390 ºC and 460 ºC failed within *ca*. 40 hours; this may be related to the fact that the crystallinity of SnO_2 increases with furnace temperature from 450 °C to 550 °C [101]. Nevertheless, even the latter lifetime was a significant improvement on the durability of the anodes prepared using all-chloride precursors, as well as on the lifetime of anodes reported in the literature. Thus, Shekarchizade and Amini[92] prepared their anodes at 520 °C and have shown that the Ni and Sb concentrations in the coating solution are key factors affecting the service life of the anodes; however, the highest service life the authors observed was ca. 600 min at a Sb concentration of ca. 12 % and Ni concentration of ca. 0.2 %, but the authors reported that this composition did not give the highest current efficiency. The authors reported that anodes having the optimum composition with respect to current efficiency (2% Sb and 0.2% Ni) showed a service life of only 300 min. The very significant difference between the service life of the anodes discussed in this chapter and those studied by Shekarchizade and Amini is most likely related to the use of Sb_2O_3 and NiO instead of the chloride salts and possibly the slightly higher furnace temperature.

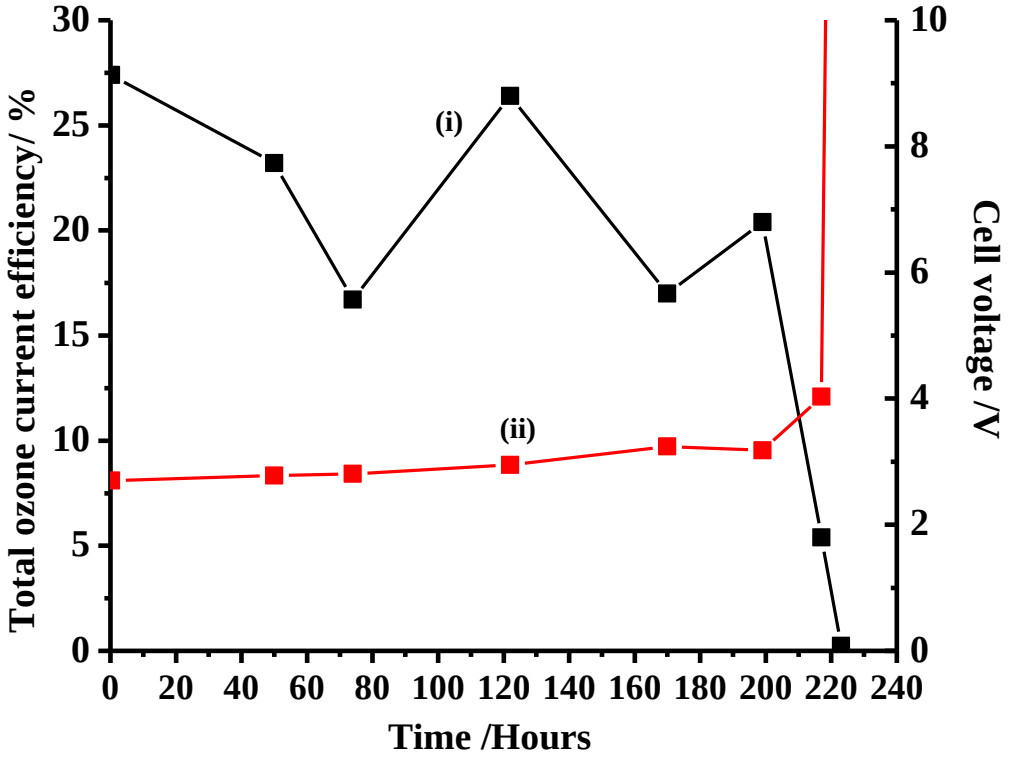

Figure 4. 9. Plots of (i) total current efficiency and (ii) cell voltage taken at intervals during a durability experiment in which an anode was electrolysed in a 250 cm^3 beaker at 100 mA cm^{-2} in 1M $HClO_4$ using a 5 cm × 5 cm Pt/Ti mesh as counter electrode. The cell voltage was monitored throughout the electrolysis. At intervals, the activity and selectivity of the anode were assessed, see text for details. The anode was NATO14O.

Again, of necessity, using the literature on Sb-SnO_2 anodes, the deactivation of Ni/Sb-SnO_2 electrodes could be due, in broad terms, to one or all of the following processes: (1) physical loss of catalyst due (i) spallation (stress cracking from formation of TiO_2 under the coating[101]) and/or (ii) corrosion (etching away of the surface as observed by Foller and Tobias[170]); (2) formation of a 'passivating' layer at the catalyst/electrolyte interface[99, 150, 151, 157]. The dissolution of Ni from Ni(II)O could be a very real problem [9]. However, Kelsall has formulated the phase diagram in fig. 4.10 [171] based on thermodynamic calculations using the potentials for the various Ni redox couples in[9, 172, 173]; (note: reference[9] gives the Ni(III) species as $Ni(OH)_3$; this is more likely to be NiOOH [174]) at pH 0 (the typical pH of the experiments reported in this chapter) and at a cell voltage of 2.7 V *vs* the counter electrode (which evolves H_2), Ni would be expected to be in the form of the stable Ni(III) species which (as was discussed above) may also be the active site for ozone evolution.

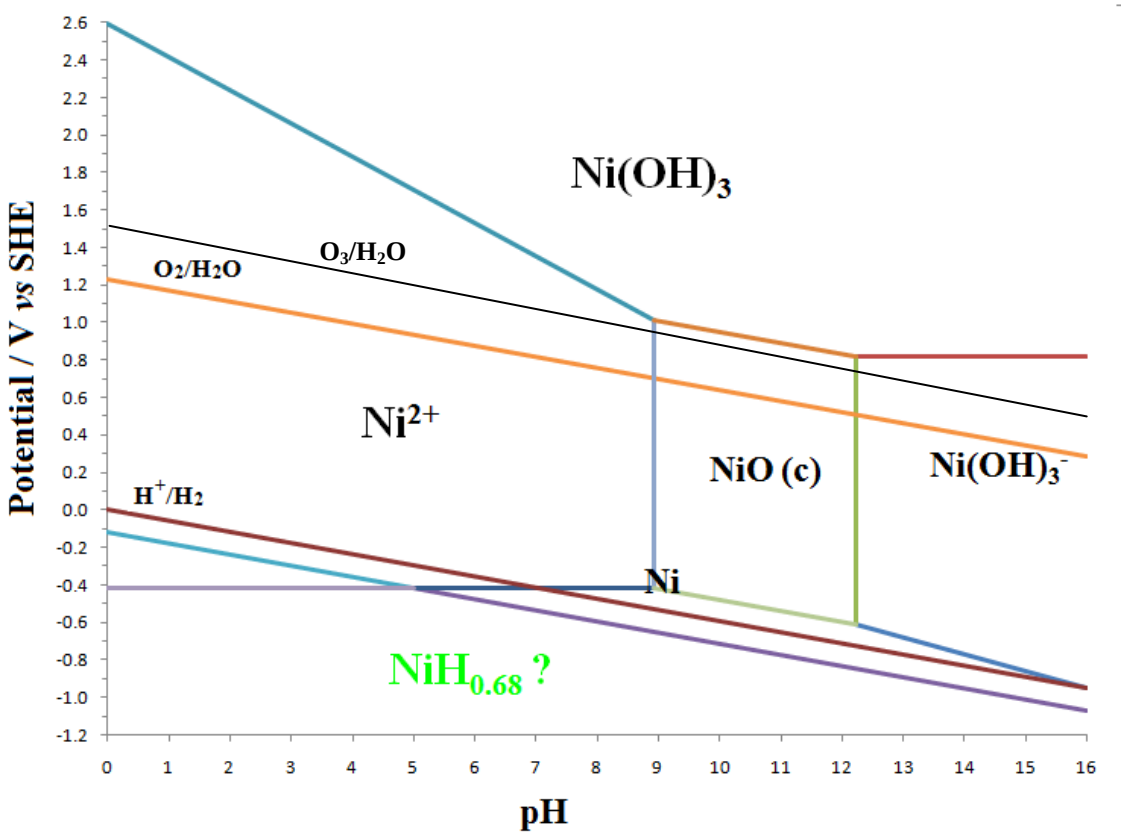

Figure 4. 10. Phase diagram for Ni, constructed on the basis of the data in [9, 172, 173] see text for details.

At the end of the durability experiment shown in fig. 4.9 (and the repeat with the second anode) powder was noted in the bottom of the beakers; SEM images of these powders suggested that they were catalyst that had spalled off the Ti mesh, see fig. 4.11. The loss of catalyst was supported by EDX spectra of the meshes which showed only Ti present. This suggests that failure was due to relatively rapid, complete spalling of the catalyst, either due to stress or to the oxidation of the underlying Ti to TiO_2.

It should be noted that with further modification of the precursor solutions, durability can be increased to more than 650 h. Figure 4.12 shows the results of a durability study carried out on NATO18Q anode (see Appendix II for more details about the anode) prepared from the dipcoating solution (containing Ni and Sb oxides as precursors, and at 550 °C) in standard(general purposes) ethanol. Anode NATO18Q was not the only anodes that gave such service life, where the service life of anode NATO10E exceeded 600 hours.

4.8 Conclusions

The use of a slightly higher furnace temperature and/or Ni and Sb oxides as precursors (instead of chlorides) significantly increases both the current density that Ni/Sb-SnO_2

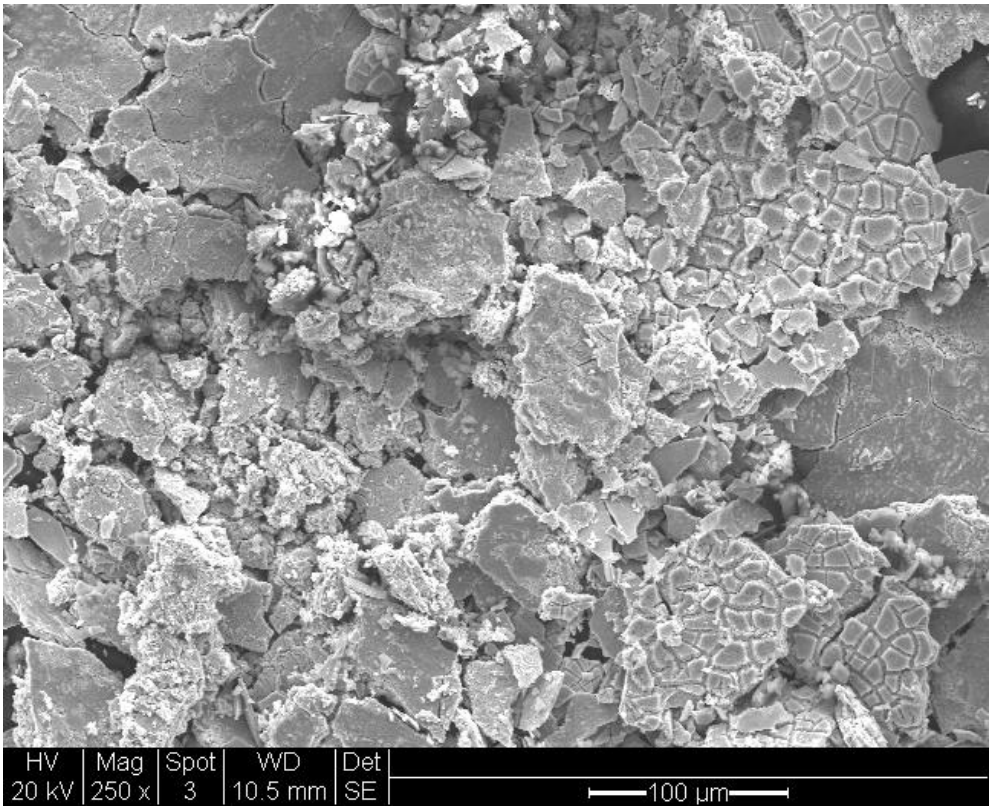

Figure 4. 11. SEM image of the powder collected from the bottom of the cell after the durability study depicted in fig. 4.9. Magnification x 250: bar = 100 µm.

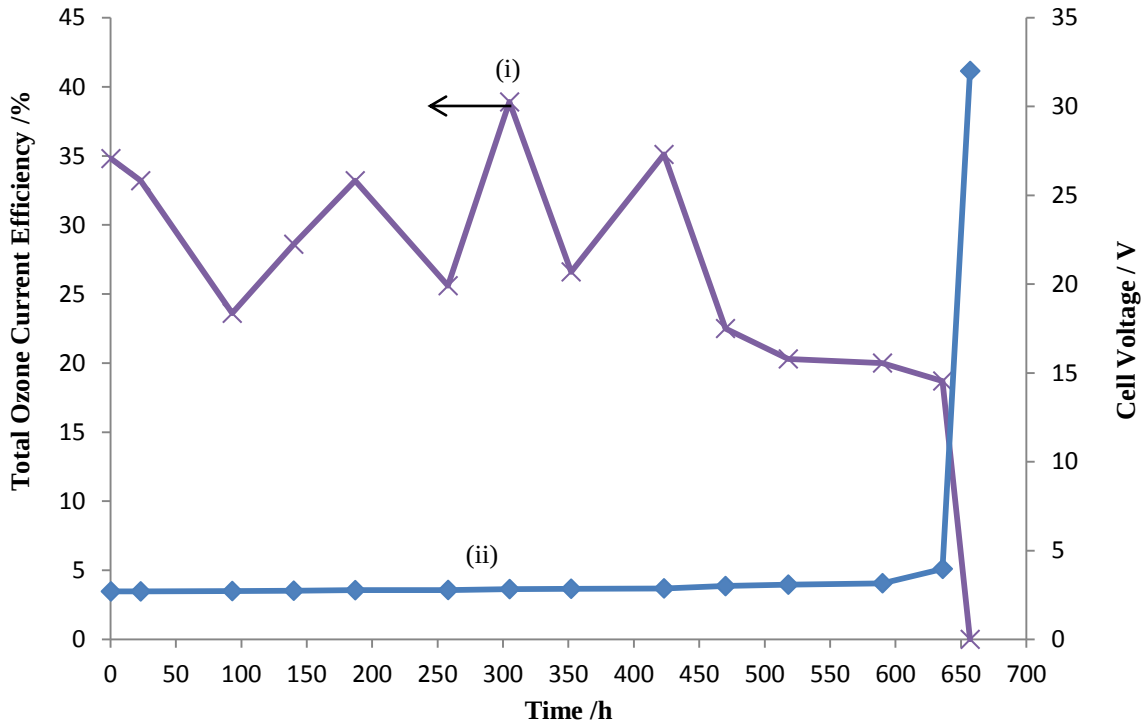

Figure 4. 12. Plots of (i) total current efficiency and (ii) cell voltage taken at intervals during a durability experiment in which an anode was electrolysed in a 250 cm^3 beaker at 100 mA cm^{-2} in 1M $HClO_4$ using a 5 cm × 5 cm Pt/Ti mesh as counter electrode. The cell voltage was monitored throughout the electrolysis. At intervals, the activity and selectivity of the anode were assessed, see text for details. The anode was NATO18Q.

anodes are able to sustain and their durability. The former is more than doubled (the highest current densities yet reported), and durability increased from a few tens of hours to 200 hours (also the highest reported). Whilst the maximum current efficiency of ca. 38% is not as high as the 50% observed using anodes made from chloride precursors, the ca. 25 – 30% routinely observed is comparable.

The dipcoating procedure results in thicker catalyst layers at the intersection of strands of mesh than on the strands themselves and the morphologies of the layers at these positions are different. Overall, catalyst loading increases linearly with the number of dipcoating cycles, forming a porous layer, with the active, Ni-containing sites not confined to a two-dimensional surface up to *ca*. 1 mg cm^{-2}.

Nickel is essential for the generation of ozone, but excessive amounts reduce both current efficiency and current density, the latter due to increased resistance; the optimum appears to be 1.04 at.% Ni.

Furnace temperature has a marked effect upon current efficiency, with a temperature of 460 °C being optimum; however, this (and lower) temperatures result in poor durability compared to those anodes prepared at 550 °C.

In the following chapter, the effect of scale up to 4 cm × 6 cm Ni/Sb – SnO_2 anodes and their use in Membrane Electrode Assemblies (MEA's) will be discussed. The effects of air breathing and hydrogen evolving cathodes, the current density, the flow rate and the electrolyte on the ozone current efficiency and production rate and the power consumptions will be investigated.

CHAPTER FIVE

5 Ozone Generation Using Membrane Electrode Assemblies (MEA's)

5.1 Introduction

The objectives of the work reported in this chapter were to investigate the effect of the following factors on the ozone current efficiency, power consumption and production rate:

(i) The scale up of Ni/Sb-SnO_2 (NATO) anodes from 6.25 cm^2 to 24 cm^2,

(ii) The use of the membrane electrode assemblies (MEA's) to generate ozone in electrolyte – free water (Millipore water),

(iii) The use of different cathodes and anodes in the MEA,

(iv) The nature of the electrolyte and

(v) Anolyte flow rate.

All the MEAs discussed in this chapter had a NATO anode pressed on one side of a Nafion 117 membrane, with either an air breathing cathode or platinised titanium (Pt/Ti) mesh (hydrogen evolving) cathode. The air breathing cathodes were supplied either by Johnson Matthey (JM) or Clarizon Ltd. Clarizon cathodes were initially employed; however, as is discussed below, it was thought that there could have been a problem with these, and hence it was decided to try JM cathodes.

Two types of anode were employed in the work described in this chapter, made either using Ni and Sb chloride precursors or oxide precursors (see section 2.11 and table 2.5), and these are summarised in table 5.1.

MEA	Ni/Sb-SnO_2 anode		Anode size cm × cm	Cathode 4 cm × 6 cm			Anodes prepared at:
	Chlorides	Oxides		Clarizon	JM	Pt/Ti	
MEA1	√		4 × 6	√			Furnace at 460^{O}C
MEA2		√	2.5 × 2.5	√			Furnace at 460^{O}C
MEA3		√	4 × 6		√		Furnace at 460^{O}C
MEA4		√	4 × 6		√		Furnace at 550^{O}C
MEA5		√	2.5 × 2.5		√		Furnace at 550^{O}C
MEA6		√	4 × 6			√	Furnace at 550^{O}C
MEA7		√	4 × 6			√	Furnace at 550^{O}C

Table 5. 1. Summary of the anode and cathodes employed in the MEA's studied in this chapter.

5.2 Ozone Generation Using Membrane Electrode Assemblies (MEA's) with Air Breathing Cathodes

The effect of two parameters were investigated in this section, the cell voltage and the anolyte flow rate on the ozone current efficiency, production rate and power consumption using different anodes and cathodes.

5.2.1 The effect of cell voltage

All the MEAs in this section were tested for ozone generation from Millipore water in flow mode at different cell voltages. The corresponding current and ozone absorbances at 258 nm and 255 nm in the solution and gas phases, respectively, were measured and the latter values at steady state were then used to calculate current efficiencies (gas, solution, and total), power consumption and ozone production rate.

MEA1 was tested over the range 1.4 V – 1.8 V. The corresponding current density and current efficiencies are presented in fig. 5.1. It may be seen from the figure that whilst the onset of current was at <1.4 V, ozone was only produced at cell voltages > 1.4 V. The current efficiency for dissolved ozone increased to ca. 3.5% at 1.6 V and then remained constant, whereas the gas phase ozone current efficiency increased more slowly, also to ca. 3.5%; this most likely reflects a delay caused by the arrangement of the system. Given that the distribution of ozone between solution and gas depends primarily upon the arrangement of the system, further discussion will focus only on the total ozone production. The total ozone current efficiency simply reflected the sum of these two contributions. As may be seen, the current increased steadily as the cell voltage increased, as expected.

Figure 5.2 shows the power consumption in kWh kg^{-1} O_3 and the ozone production rate of the unit area of the anode in mg h^{-1} cm^{-2} vs. cell voltage for the experiments in fig. 5.1. It may be seen from the figure that the ozone production rate increased with increasing voltage, achieving a value of ca. 0.38 mg h^{-1} cm^{-2} at 1.6 V and ca. 0.83 mg h^{-1} cm^{-2} at 1.8 V. In contrast, the power consumption seems to decrease with increasing voltage up to 1.6 V, reaching a value of 80 kWh kg^{-1} O_3, which remained constant at higher voltage.

It may be concluded from figs. 5.1 and 5.2 that cell voltages > 1.6 V had little or no effect on current efficiency or power consumption, but increased the ozone production rate, due to the increased current.

The current efficiency and power consumption reported for MEA1 may be attributed to the

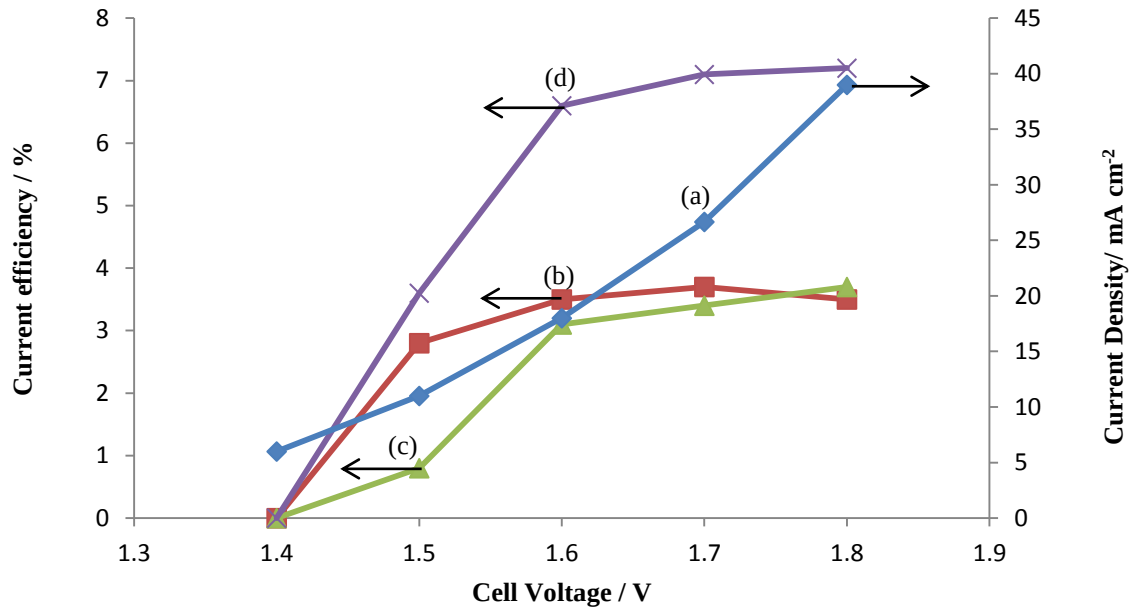

Figure 5. 1. Plots of: (a) current density, (b) solution current efficiency, (c) gaseous current efficiency and (d) total current efficiency vs. cell voltage obtained using MEA1 in flow mode. The anolyte was Millipore water at a flow rate of 60 cm^3 min^{-1}. The N_2 flow rate was 80 cm^3 min^{-1}, at room temperature.

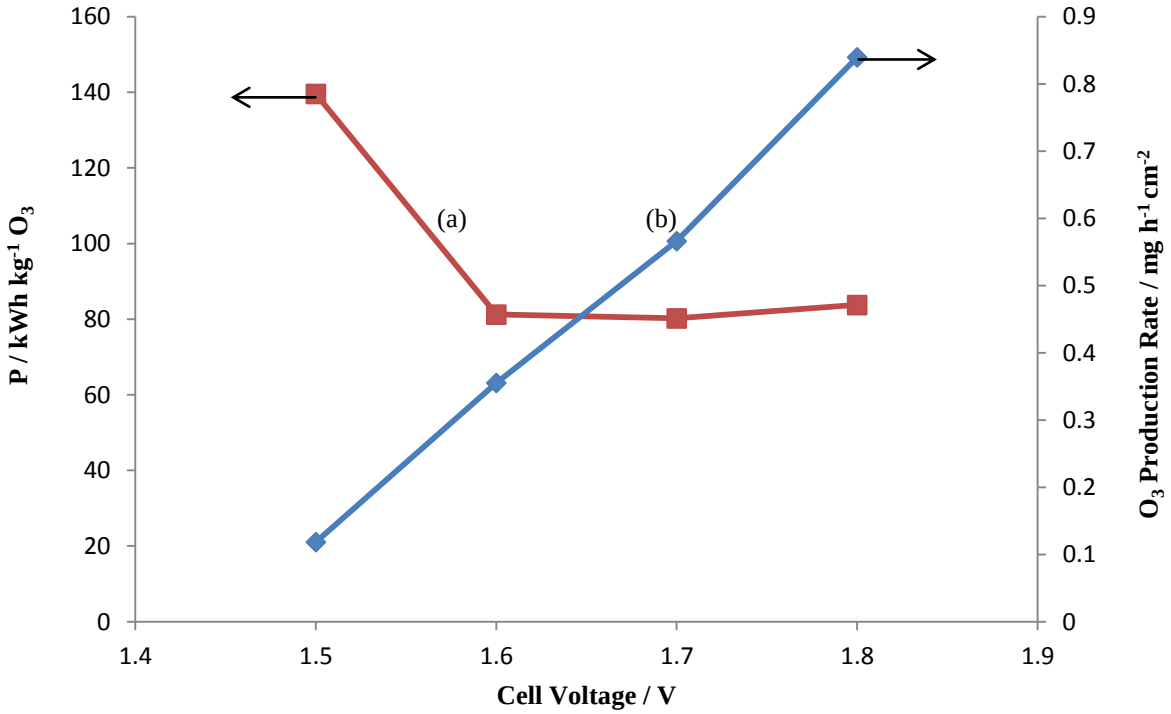

Figure 5. 2. Plots of: (a) power consumption P and (b) ozone production rate vs. cell voltage for the experiments in fig. 5.1.

MEA configuration (for example: the anode area). Therefore, it was decided to look at the anode area, although the real cathode (Pt particles) area are much greater than the geometric 24 cm^2 anode area. It was thought that using smaller size anode than cathode might be helpful in increasing the current efficiency and reduce the power consumption. Hence, an anode of 6.25 cm^2 was pressed against the Nafion with the same kind of cathode to fabricate MEA2 (see table 5.1).

The evolution of ozone using MEA2 was investigated over the same cell voltage range as MEA1. Figure 5.3 shows the current efficiencies (gas, solution and total) and the current density vs. cell voltage. It may be seen from fig. 5.3 that the current and current efficiencies increased with increasing voltage, with the total current efficiency attaining more than 15% (i.e. twice that of MEA1; the current densities were roughly the same at 1.8 V of ca. 40 mA cm^{-2}). However, there was no gaseous ozone up to 1.6 V. As was observed with MEA1, the onset of ozone was at a higher cell voltage than the onset of Faradic current; the current then increased steadily with voltage as was also seen using MEA1. The total ozone current efficiency increased with cell voltage, in contrast to the behaviour of MEA1.

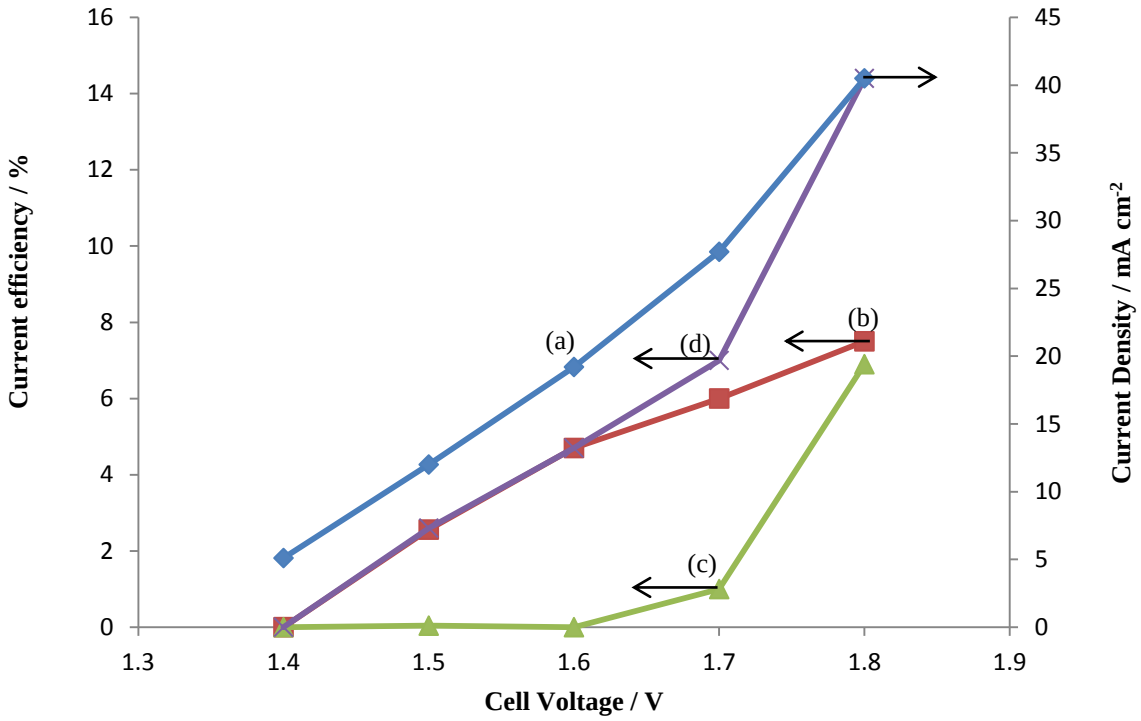

Figure 5. 3. Plots of: (a) current density, (b) solution current efficiency, (c) gaseous current efficiency and (d) total current efficiency vs. cell voltage obtained using MEA2 in flow mode. The anolyte was Millipore water at a flow rate of 60 cm^3 min^{-1} at room temperature.

Figure 5.4 shows the power consumption and ozone production rate vs. cell voltage for the experiments in fig. 5.3; it may be seen from the figure that these followed different trends. Whilst the ozone production rate increased with cell voltage, the power consumption decreased almost linearly, reaching a value of < 40 kWh kg^{-1} O_3. However, the increase of ozone production rate was slower at < 1.7 V than that at >1.7 V, due to the onset of gas phase ozone only occurring at 1.7 V. it may be seen from the figure that the OPR for MEA2 (1.8 mg h^{-1} cm^{-2}) was more than twice as that of MEA1 (0.8 mg h^{-1} cm^{-2}) at 1.8 V. the results, shown in figs. 5.3 and 5.4, suggest using smaller anode size resulted in improving the performance of the MEA in terms of current efficiency and OPR which doubled and power consumption that was reduced by ca. 50% at 1.8 V.

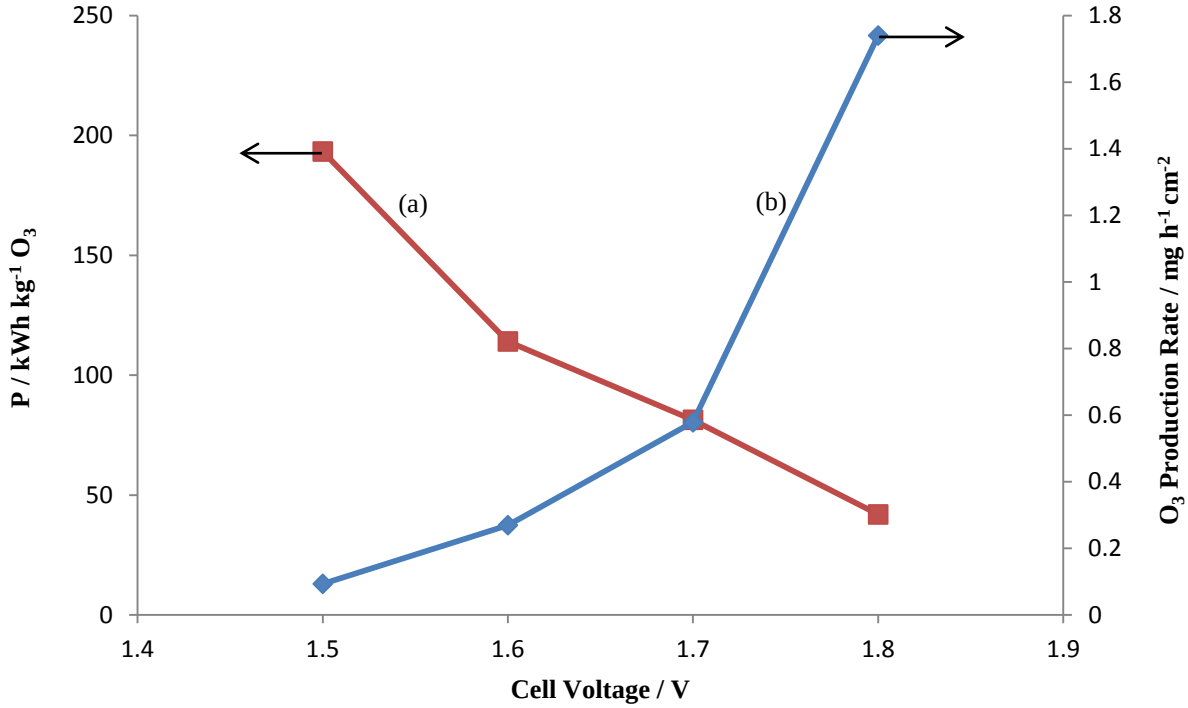

Figure 5. 4. Plots of: (a) power consumption and (b) ozone production rate vs. cell voltage for the experiments in fig. 5.3.

It was postulated that the efficiency of air breathing cathode could have an effect on performance; hence, cathodes made by JM were used instead of those made by Clarizon. Thus, MEA3 was pressed and tested at cell voltages of 1.3 V – 1.8 V, and the corresponding current and current efficiencies are presented in fig. 5.5. It may be seen from the figure that the current increased with increasing voltage. As was obtained with MEA1 and MEA2, the onset of ozone production was at higher cell voltage than the onset of Faradic current. However, the total current efficiency increased with cell voltage increase to a maximum of 17% at 1.5 V (at current density of ca. 30 mA cm^2), after which

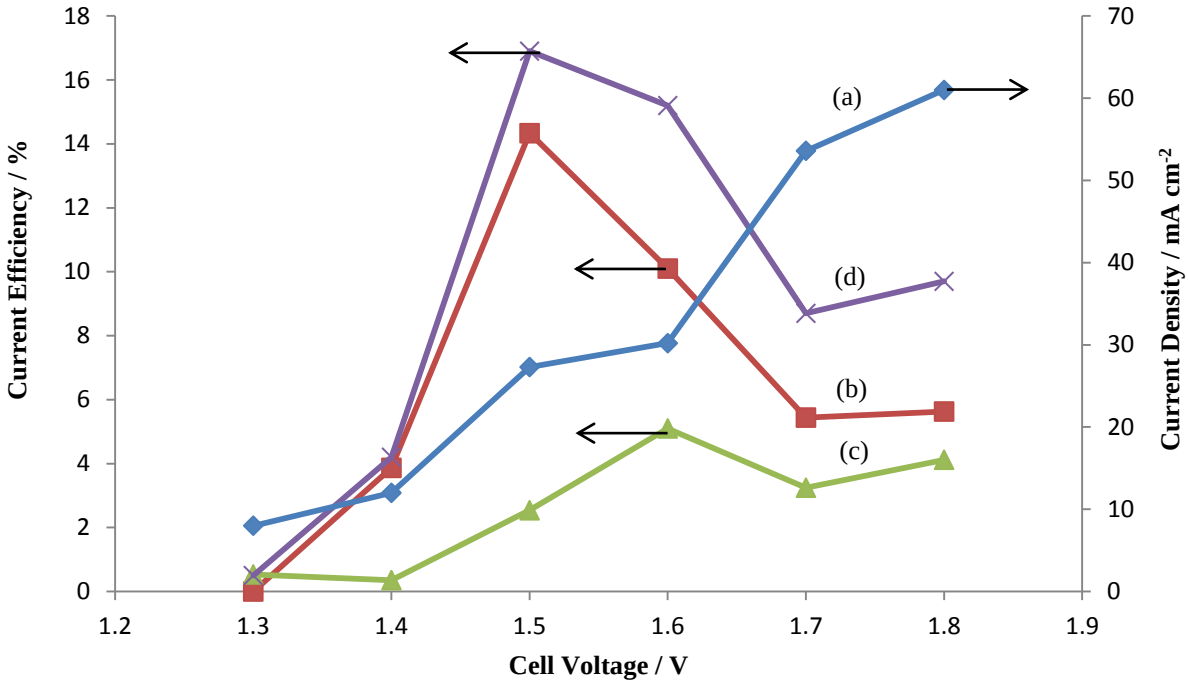

Figure 5. 5. Plots of: (a) current density, (b) solution current efficiency, (c) gaseous current efficiency and (d) total current efficiency vs. cell voltage obtained using MEA3 in flow mode. The anolyte was Millipore water at flow rate of 60 $cm^3 min^{-1}$ at room temperature.

it decreased to ca. 9% at 1.8 V (at current density of ca. 60 mA cm^2).

Figure 5.6 shows the power consumption and ozone production rate vs. cell voltage for the experiments in fig. 5.5. It may be seen from the figure that the power consumption decreased with increasing voltage reaching a minimum of ca. 30 kWh kg^{-1} O_3 at 1.5 V, then it increased slowly with increasing voltage. The OPR increased to ca. 1.4 mg h^{-1} cm^{-2} with increasing voltage up to 1.5 V (significantly higher than the 0.8 and less than 1.8 mg h^{-1} cm^{-2} observed using MEA1 and MEA2, respectively), then it increased slowly at higher cell voltages, reaching 1.8 mg h^{-1} cm^{-2} at 1.8 V.

It may be seen from figs. 5.1 – 5.6 that the maximum current efficiencies of MEA1, 2 and 3 were ca. 7%, 15% and 17% obtained at current densities of ca. 40 mA cm^2 for MEA's 1 and 2 and ca. 30 mA cm^2 for MEA3, whilst the power consumption at the same cell current densities were ca. 80, 45 and 30 kWh kg^{-1} O_3, respectively. Thus, the performance of MEA3, in terms of current efficiency and power consumption, was superior to that of MEA1 and MEA2, and it was better than that of MEA1 and similar to that of MEA2 with respect to the OPR; supporting the initial postulate that the type of air breathing cathode can have a significant effect upon the performance of the MEA. However, it was found

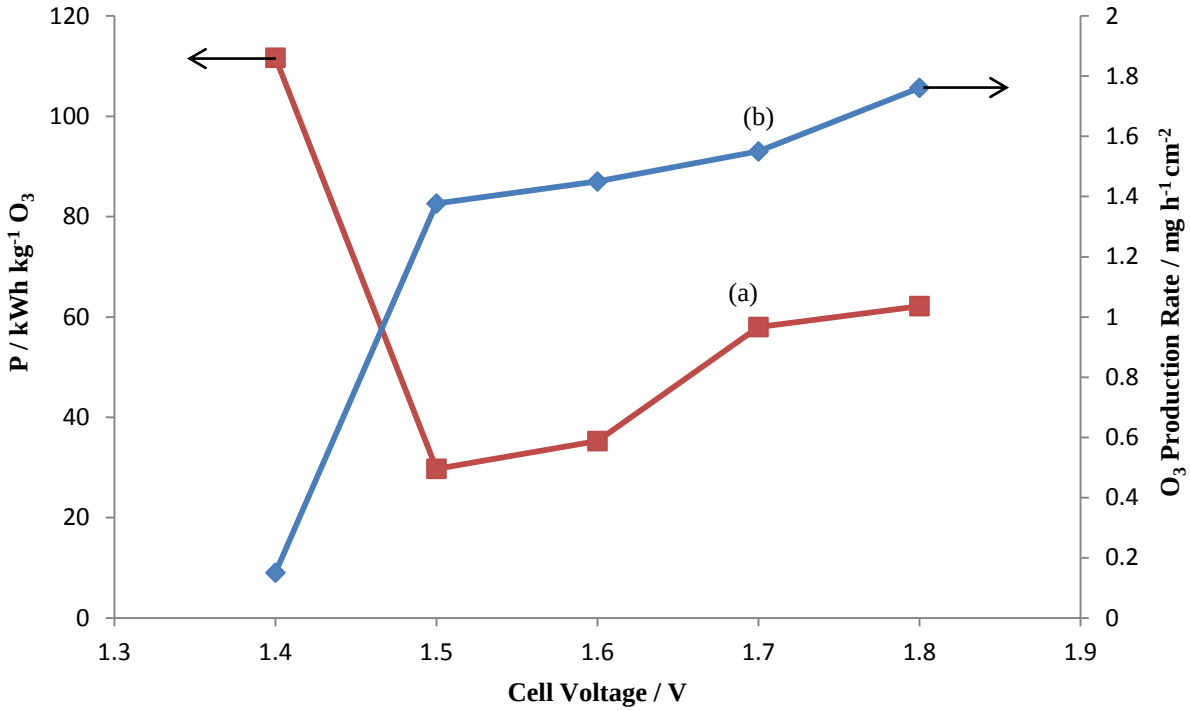

Figure 5. 6. Plots of: (a) power consumption and (b) ozone production rate vs. cell voltage for the experiments in fig. 5.5.

that the JM cathode apparently suffered from flooding, as will be discussed below.

To confirm that the improvement in the MEA3 performance was due to the new JM cathode and not due to the anode, a new anode that was fabricated slightly differently was used (see table 5.1). MEA4 was pressed and tested at a cell voltage of 1.2 V – 1.8 V, and the corresponding current and current efficiencies are presented in fig. 5.7. It may be seen from the figure that both the current and the current efficiencies increased with increasing voltage, as was the case for MEA2. The highest current efficiency of 13% was achieved at 1.8 V (at current density of ca. 40 mA cm^2). As was obtained with MEA's 1, 2 and 3, the onset of ozone production was at higher cell voltage than the onset of Faradic current.

Figure 5.8 shows the power consumption and ozone production rate vs. cell voltages for the experiments in fig. 5.7. It may be seen from the figure that the power consumption decreased whilst the ozone production increased with increasing voltage as was observed using MEA2. The power consumption was < 50 kWh kg^{-1} O_3 at 1.8 V, and was > 100 kWh kg^{-1} O_3 at 1.6 V. The OPR reached ca. 1.4 mg h^{-1} cm^{-2} at 1.8 V.

Only few papers were found in the literature dealing with ozone generation using MEA's with air breathing cathodes: Katoh et al.[44], Wang et al. [4] and Cui et al.[50]. Katoh and co - workers[44] studied ozone generation from DI water in a flow – through MEA cell using a 56

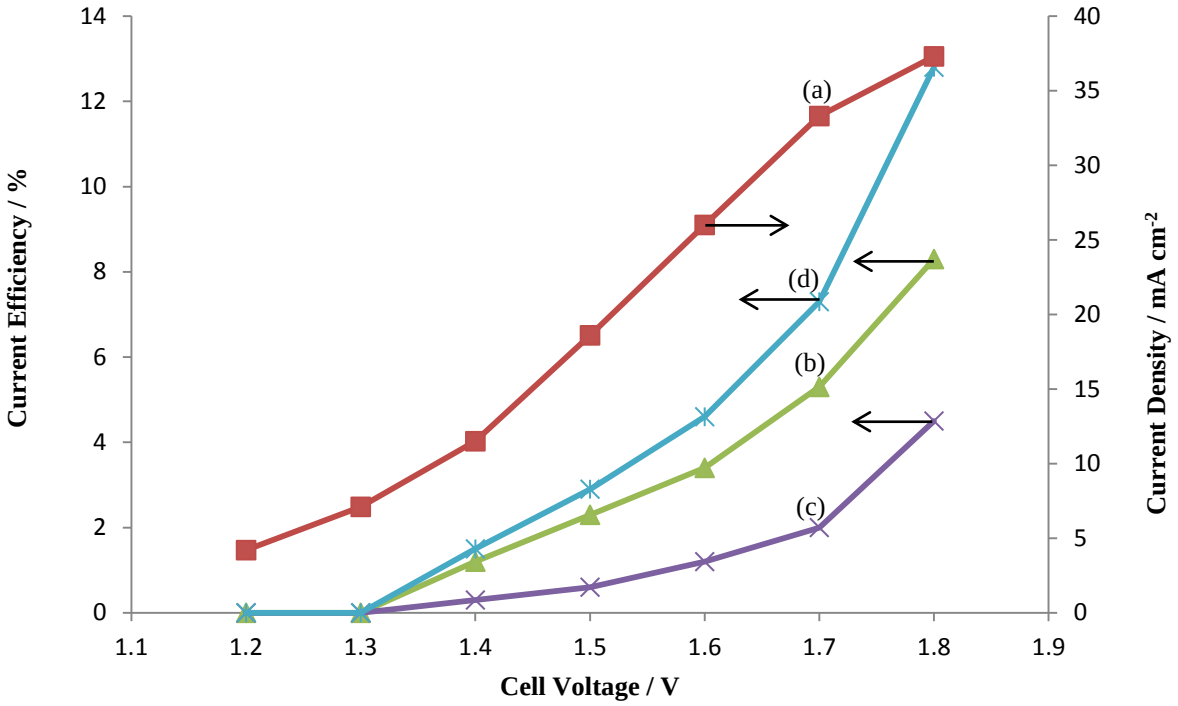

Figure 5. 7. Plots of: (a) current density, (b) solution current efficiency, (c) gaseous current efficiency and (d) total current efficiency vs. cell voltage obtained using MEA4 in flow mode. The anolyte was Millipore water at flow rate of 60 $cm^3 min^{-1}$ at room temperature.

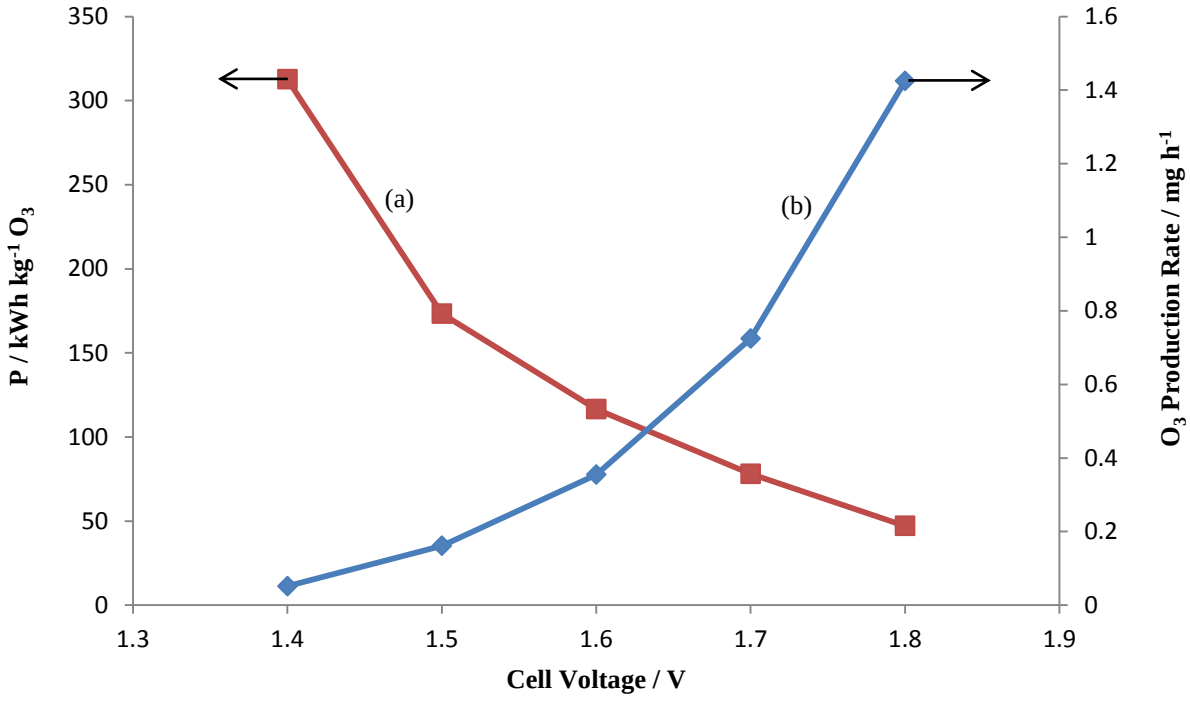

Figure 5. 8. Plots of: (a) power consumption and (b) ozone production rate vs. cell voltage for the experiments in fig. 5.7.

cm^2 Pt/Ti (porous plate) anode. Wang et al. [4] employed a MEA cell with 24 cm^2 Ni/Sb – SnO_2 anode in MEA and stationary anolyte (pure water). Cui and co – workers[50] used a single MEA – based flow through cell, with a 104 cm^2 Ni/Sb – SnO_2 anode, and also investigated the performance of a 4 –cell stack.

For the four MEA's tested, namely MEA1, 2, 3 and 4, the general trend of the current density was to increase with increasing voltage. This is in agreement with the work of Wang et al. [4] who used constant voltage over the range of 1.6 V – 2.3 V, Cui et al. [50] who employed constant current densities of 19.2 – 58 mA cm^{-2} (corresponding to 3 V – 6.5 V), and Katoh et al.[44] who used constant current densities of 0.1 – 1 A cm^{-2}. Wang et al. [4] found that the current increased almost linearly with the cell voltage achieving a value of ca. 4 mA cm^{-2} at 1.6 V and ca. 12 mA cm^{-2} at 2 V, and Cui et al. [50]& Katoh et al.[44] also reported a linear increase in voltage with increasing current density.

In terms of current efficiency vs. cell voltage, and at low voltages (for example, <1.6 V for MEA1 and <1.5 V for MEA3), the four MEA's generally showed increasing current efficiency with increasing voltage. However, at higher voltages (>1.6 V for MEA1 and >1.5 V for MEA3), the MEA's behaved differently. In the case of MEA's 1 and 3, the current efficiency either reached a plateau (MEA1) or decreased (MEA3) with increasing voltage. In contrast, in the case of MEA's 2 and 4, the current efficiencies increased with increasing voltage. In general, at low voltages where both current density and current efficiency increased with voltage, it is clear that the ratio of ozone active sites to oxygen site is increasing. At higher voltages, three distinct types of behaviour are observed which may be represented by fig. 5.9. Thus, the ozone current efficiency remains constant (Type (I), MEA1), decreases (Type (II), MEA3) or continues to increase (Type (III), MEA's 2 and 4).

Type (I) behaviour shows that the ratio of ozone to oxygen sites is constant and that the rates of formation of the two products (O_2 + O_3) are increasing. Type (II) behaviour shows that either (i) the ozone sites are switching to oxygen, switching off, (ii) ozone is being produced at such a rate that decomposition reactions are taking place according to scheme 5.1[175], (iii) the presence of high concentrations of O_3 inhibits the O_3 evolution process at Ni/Sb-SnO_2 anodes, possibly by replacing key adsorbed intermediates by adsorbed O_3 [64] and/or (vi) that local heating is taking place[17, 31, 62].

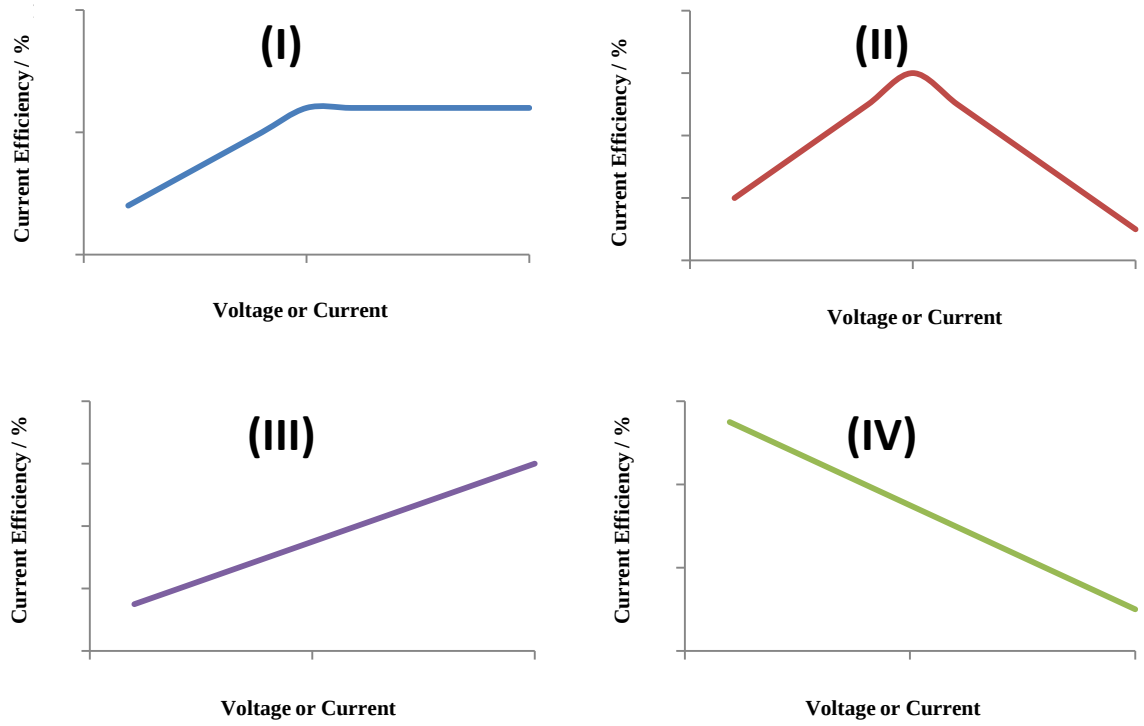

Figure 5. 9. Representation of the general types of the behaviour observed in the literature for electrochemical ozone generation current efficiency using MEA – based cells vs. constant current or constant voltage irrespective of the anode and cathode used.

$$O_3 + OH^- \rightarrow O_2 + HO_2^- \qquad (5.1)$$

$$O_3 + HO_2^- \rightarrow O_3^{\cdot -} + HO_2^{\cdot} \qquad (5.2)$$

$$HO_2^{\cdot} \leftrightarrows O_2^{\cdot -} + H^+ \qquad (5.3)$$

$$O_2^{\cdot -} + O_3 \rightarrow O_3^{\cdot -} + O_2 \qquad (5.4)$$

$$O_3^{\cdot -} + H^+ \leftrightarrows HO_3^{\cdot} \qquad (5.5)$$

$$HO_3^{\cdot} \rightarrow OH^{\cdot} + O_2 \qquad (5.6)$$

$$O_3 + O_3 \rightarrow 3O_2 \qquad (5.7)$$

Scheme 5.1. The ozone self decomposition chain reaction

It should be noted that, for all the MEA's tested in this section, the Faradic current onset took place at voltages lower than that of ozone, reflecting that the oxygen is being produced before the ozone. However, the ozone sites switched on at cell voltages > 1.3 V for MEA's 3 and 4, and it was at >1.4 V for MEA1 and MEA2. In contrast, the current

onset was at < 1.3 V for MEA's 3 and 4, and it was at <1.4 V for MEA's 1 and 2.

Figure 5.9 actually represents the four types of behaviour generally reported in the literature observed using MEA – based ozone cells irrespective of anode or cathode size or composition or cathode type (air breathing or hydrogen evolving). Type (I) behaviour has also been reported by Stucki et al. [17, 31] and Tatapudi and Fenton[49], Type (II) by Wang et al. [4], Tatapudi and Fenton[51], Arihara et al.[45], Kraft et al.[62] and Onda et al.[48], Type (III) by Katoh et al.[44], Han et al.[47] and Da Silva et al.[7, 46]. In addition, a fourth dependence of current efficiency has been observed by Cui et al. [50] and Arihara et al.[61], where the ozone current efficiency decreases steadily with voltage or current, Type (IV).

Katoh and co-workers[44] found that the current efficiency increased with increasing current density (Type(III)), albeit more slowly at higher currents, achieving 19% at 1.5 A cm^{-2} and voltage of 3 V. The authors suggested that local heating in the air breathing cathode could result in local hot spots on the anode. If this is the case, then the steady increase in the current efficiency with current observed using MEA2 and 4 rules out this as possibility. Furthermore, the Type (II) behaviour observed using MEA3 is in agreement with the work of Wang et al. [4] who found that the current efficiency passed through a maximum of 15% at 2 V, after which it decreased with increasing voltage. They interpreted this in terms of a model in which, at higher voltage, the generation of oxygen rather than the ozone increased, and/or ozone decomposition was promoted. However, in their second paper (Cui et al. [50]), the authors reported that increasing the current density resulted in a decrease in current efficiency. This was interpreted in terms of the increasing decomposition of ozone to oxygen. The highest current efficiency achieved by this group was 17% at a current of 2 A. Furthermore, Cui et al. [50] found that the current efficiency passed through a maximum of 22% when 4 MEA's were assembled together in series or parallel to make a stack. In contrast, the Type (I) behaviour observed using MEA1 has not been reported before for MEA's with air breathing cathodes; it has been reported for other combinations of MEA, as will be discussed in section 5.3.1.

Although the fact that MEA2 had an anode that was 25% the area of the anodes employed in the remaining MEA's studied in this section, the maximum current efficiency observed (ca. 15%) was twice that observed using MEA1 (ca. 7%) and was comparable to that of MEA's 3 (ca. 17%) and 4 (ca. 13%). However, the current density (ca. 40 mA cm^{-2}) of MEA2 was higher than those of the other MEA's (ca. 19 mA cm^{-2}, ca. 27 mA cm^{-2} and ca.

38 mA cm^{-2} for MEA1, 3 and 4, respectively), and the ozone production rate per unit anode area at the voltage associated with the maximum current density was also higher; 1.8 mg h^{-1} cm^{-2} compared to 0.8, 1.4 and 1.4 mg h^{-1} cm^{-2} for MEA's 1, 3 and 4, respectively. In addition, the power consumed at the highest current efficiency of MEA2 (ca. 40 kWh kg^{-1} O_3) was less than that of MEA1 (ca. 80 kWh kg^{-1} O_3), similar to that of MEA4 (ca. 40 kWh kg^{-1} O_3) and more than that of MEA3 (ca. 30 kWh kg^{-1} O_3).

Looking at the results in previous chapters (3 and 4), it might be concluded that the anodes made using metal oxides and at 460 ^{O}C gave higher current efficiency but lower service life. This might be helpful in understanding why the current efficiency of MEA3 (the anode annealed at 450 ^{O}C) is higher than that of MEA4 (the anode annealed at 550 ^{O}C). However, looking at the performance of MEA3 and MEA4 against the MEA1 and MEA2 suggest that the JM air breathing cathode is better than that of Clarizon.

In general, as discussed in sections 1.1.2 and 1.1.6, it is generally believed that the solubility of ozone in water depends upon pH[13-15], decreasing as pH increases; leading to ozone self autolysis at higher pH, and consequently decreasing the ozone current efficiency[7, 13, 75]. This may be the main reason why the ozone current efficiency in acid/acid cell is higher than in the MEA – based cells employing Millipore water as anolyte.

In terms of the power consumption, the MEA's tested showed three different types of behaviour. The first (MEA1) showed power consumption decreasing with increasing voltage to a minimum at 1.6 V, after which it reached a steady state of ca. 80 kWh kg^{-1} O_3. The second behaviour was exhibited by MEA3 which showed a decreasing power consumption with increasing voltage to a minimum of ca. 30 kWh kg^{-1} O_3 at 1.5 V after which it increased. The third behaviour was shown by MEA's 2 and 4, where the power consumption decreased with increasing voltage; achieving ca. 40 and 50 kWh kg^{-1} O_3, respectively at 1.8 V. The second behaviour has been reported by Wang et al. [4] who observed that the power consumption passed through a minimum of ca. 50 kWh kg^{-1} O_3 and 160 kWh kg^{-1} O_3 at 2 V and 1.6 V, respectively. In their second paper, Cui et al. [50] reported that the ozone production rate and the power consumption increased with increasing the current density for both the individual MEA and the 4 cells stack. They found that the lowest power consumption for the single MEA of 59 kWh kg^{-1} O_3 was recorded at a current density of 19.2 mA cm^{-2} (corresponding to a cell voltage of ca. 4 V)

and flow rate of 4 dm^3 min^{-1}, and 42.4 kWh kg^{-1} O_3 at a current of 24.3 mA cm^{-2} (cell voltage of 2.7 V) and flow rate of 5.4 dm^3 min^{-1} for the stack. However, the other types of power consumption vs. cell voltage behaviours have not been reported for MEA with air breathing cathodes, but they have been reported for hydrogen evolution cathodes (see below section 5.3.1 for more details).

Comparing the power consumptions of MEA1 – MEA4, it might be seen that the best is MEA3 that consumed the lowest power at the highest current efficiency, and it was lower than that of MEA2 even anode size of MEA2 was 4 times less than that of MEA3. The best MEA configuration so far, in terms of current efficiency and power consumption, is MEA3 (4 cm × 6 cm NATO anode made of metal oxides at 460 ^{O}C, Nafion 117, and 4 cm × 6 cm JM air breathing cathode).

In terms of the different current efficiencies and power consumption vs. cell voltages behaviours reported for the MEA's tested in this section, it may be clear that those MEA's employed different cathodes and anodes; resulting in different behaviour. For example, MEA's 2 and 4, at the voltage range studied, did not suffer from local heating; therefore, they showed Type (III) behaviour of current efficiency vs. voltage (see fig. 5.9). In contrast, MEA's 1 and 3 have been clearly affected by either local heating and/or ozone decomposition; showing Type (I) and (II), respectively.

The ozone production rates (OPR) reported in this section generally increased with increasing voltage. For MEA1, the OPR increased linearly with the cell voltage; achieving ca. 0.4 and 0.8 mg h^{-1} cm^{-2} at 1.6 V and 1.8 V, respectively. However, the OPR increased slower at low cell voltages up to 1.7 V, then it increased faster at cell voltages >1.7 V for both MEA2 and MEA4; achieving a value of ca. 1.8 and 1.4 mg h^{-1} cm^{-2}, respectively at 1.8 V. In contrast, the OPR for MEA3 increased with increasing voltage at lower voltages; achieving ca. 1.4 and 1.8 mg h^{-1} cm^{-2} at 1.5 V and 1.8 V, respectively, then it increased slowly after 1.5 V. In contrast to all of these findings, Wang et al. [4] reported that the OPR passed through a maximum at 2 V after which it decreased with increasing voltage, achieving 0.04 mg h^{-1} cm^{-2} at 1.6 V and 0.54 mg h^{-1} cm^{-2} at 2V. In their second paper, Cui et al. [50] reported that the OPR increased with increasing current density for both the individual MEA and the 4 cells stack, and this is in general agreement with our findings. However, the greatest OPR for the single MEA of 2.1 mg h^{-1} cm^{-2} was achieved at 57.6 mA cm^{-2} (corresponding to a cell voltage of ca. 5.5 V) and flow rate of 4 dm^3 min^{-1}; and

for the stack, 1.1 mg h^{-1} cm^{-2} was achieved at a current of 20.6 A, corresponding to cell voltage of 3.3 V and flow rate of 5.9 dm^3 min^{-1}. Thus, at 1.8 V, MEA's 1, 2 and 4 generated 0.8, 1.8 and 1.4 mg h^{-1} cm^{-2} of ozone, respectively. Interestingly, the OPR for MEA3 increased to 1.4 mg h^{-1} cm^{-2} at 1.5 V (at which the maximum current efficiency was observed), then continued to increase achieving 1.8 mg h^{-1} cm^{-2} at 1.8 V. Thus, it does not seem unreasonable to postulate that the reason for the decrease in current efficiency using MEA3 may be due to the decomposition of ozone (see equation 5.7)

Cathode flooding investigation

As discussed in section 1.1.2, water balance in air breathing cathodes is crucial[55] since water is produced at the cathode *via* the oxygen reduction reaction;

$$O_2 + 4H^+ + 4e^- \rightarrow 2H_2O \qquad (5.8)$$

in addition, every proton drags between 1 and 5 water molecules with it as it passes through the polymer electrolyte membrane from anode to cathode (electro-osmotic drag[55, 56]). As a result, the pores of the cathode may become flooded with water, which blocks access to the oxygen gas and hence increases cell voltage (under constant current operation) or decreases current (under constant voltage operation).

For all the MEA's tested in this section, the cathodes were air breathing and it was thought that they might suffer from water flooding. In this regard, it is imperative to mention two important observations: the first is that the cathodes of all MEA's 1, 2, 3 and 4 were wet after the tests, and the second was when retesting these MEA's under the same conditions (of constant voltage and flow rate), the performance in terms of current and current efficiency was significantly reduced, as will be discussed below. This was thought to be due to either cathode flooding or anode deterioration. To investigate this postulate, MEA2 was tested again only at constant voltage of 1.6 V for 10 min the day after of the tests reported in fig. 5.3. The MEA2 was then taken apart and the anode tested in the glass (acid/acid) cell at the same conditions of constant voltage and flow rate. So, the first test of the MEA2 at 1.6 V will be called "the first run", the next day test will be called "the second run" and the MEA2's anode test in acid/acid cell will be called "the third run". The three runs were performed at constant voltage of 1.6 V, in flow mode with anolyte flow rate of 60 cm^3 min^{-1}. The electrolyte (anolyte and catholyte) in the first and the second runs was Millipore water and it was 1 M $HClO_4$ for the third run.

Figure 5.10 shows the current density vs. time for the ozone generation using MEA2 or its anode during the three runs. It may be seen from the figure that the current density reached the steady state with 1 minute for the first and the second runs, and within 3 minutes in the third run.

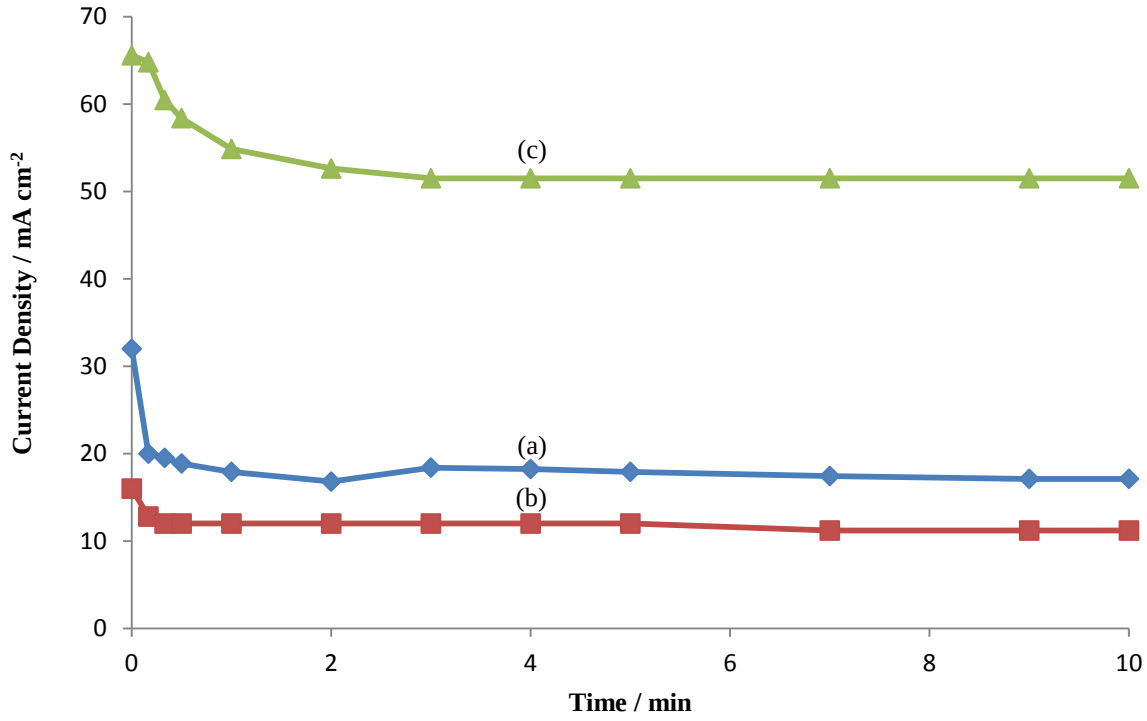

Figure 5. 10. Plots of current density vs. time during ozone generation using MEA2 in flow mode at constant potential of 1.6 V . Where: (a) the first run, (b) the second run and (c) the third run (anode stripped from MEA, Pt/Ti cathode in glass cell, see text). The electrolyte was Millipore water for (a)&(b) and 1 M $HClO_4$ for (c), the anolyte flow rate was 60 cm^3 min^{-1}, N_2 flow rate to the gas separator was 80 cm^3 min^{-1}, at room temperature.

It may be seen from the figure also that the steady state current dropped from ca. 18 mA cm^{-2} in the first run to ca. 64% of its value in the second run (ca. 11 mA cm^{-2}), and it increased 3 times to ca. 52 mA cm^{-2} in the third run. The current drop in the second run might be due to either the cathode flooding and/or to anode catalyst deterioration. However, the current clearly increased with the anode tested in acid/acid cell (the third run), this increase suggests that the anode catalyst is still active and no problem whatsoever had happened to the MEA2 anode. This leads to conclude that the cathode was flooded after the first run.

Figure 5.11 shows the current efficiency vs. time for the experiments in fig. 5.10. It may be seen from the figure that the current efficiency reached steady state with 1 minute for the

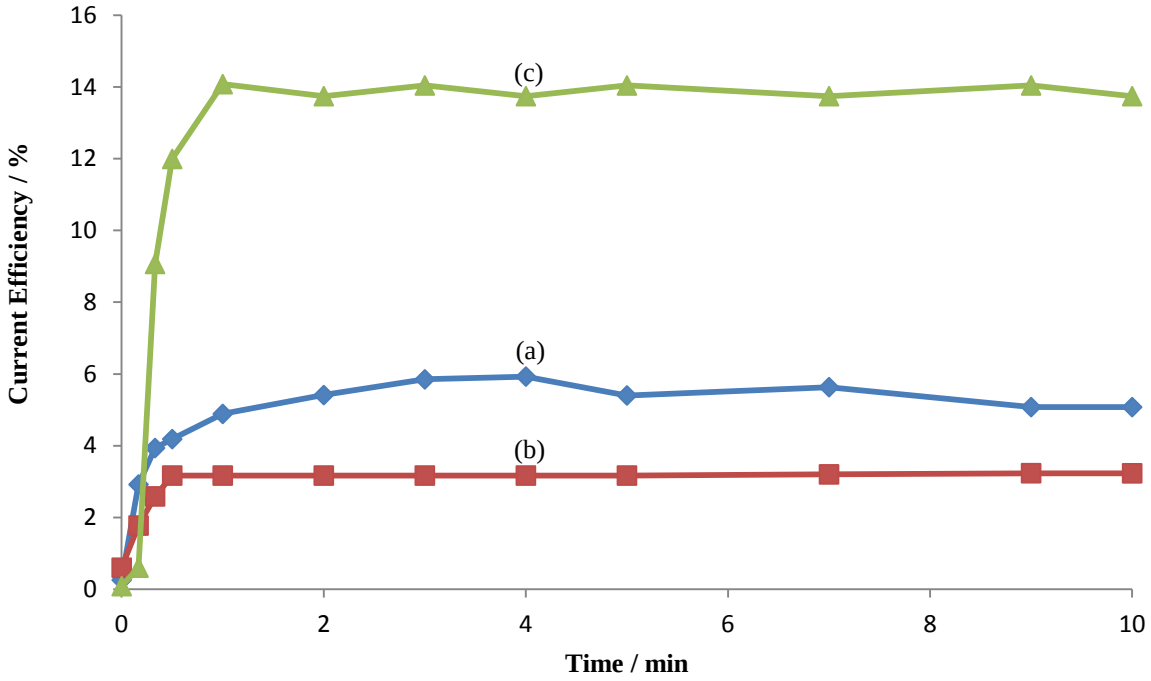

Figure 5. 11. Plots of current efficiency vs. time for the experiments in fig. 5.10, where: (a) the first run, (b) the second run and (c) the third run (see text for details).

three runs. It may also be seen from the figure that the steady state current efficiency dropped from ca. 6% in the first run to ca. 3.5% in the second run, and it increased to ca. 15 % in the third run. The decrease in current efficiency from the first run to the second run is most likely due to cathode flooding, and the current efficiency increase in the third run confirms the fact that the anode is not mainly responsible.

5.2.2 Anolyte flow rate dependence

Two MEAs were used to investigate the effect of flow rate on ozone current efficiency, production rate and power consumption.

Based on the results discussed in section 5.2.1, MEA5 was prepared (see table 5.1) and the effect of anolyte flow rate assessed, in addition to MEA4. These MEA's were tested at constant cell voltage in flow mode during which the steady state current and ozone current efficiency were monitored.

The performance of MEA4 at 1.8 V was assessed as a function of anolyte flow rate between 30 cm^3 min^{-1} and 300 cm^3 min^{-1} (corresponding to linear velocity of ca. 0.3-3 cm s^{-1}). Figure 5.12 shows the current and current efficiencies (gas, solution and total) vs. flow rate for the MEA4. It may be seen from the figure that the current decreased slightly with increasing the flow rate. In addition, the solution and total current efficiencies increased

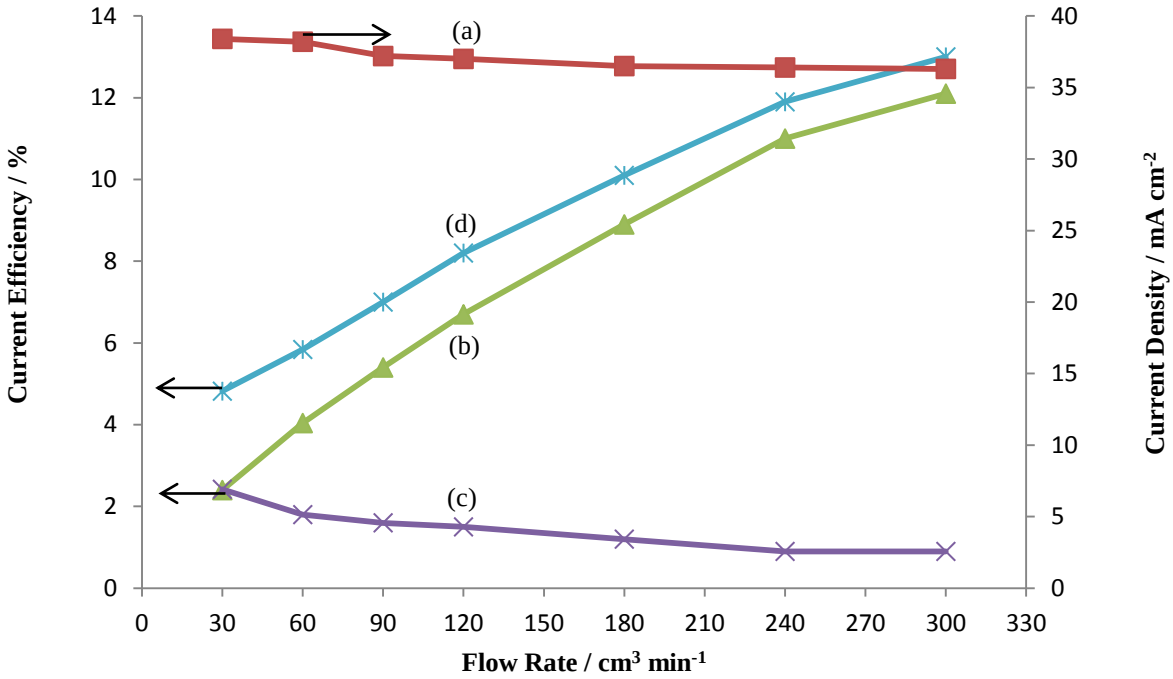

Figure 5. 12. Plots of: (a) current density, (b) solution current efficiency, (c) gaseous current efficiency and (d) total current efficiency vs. flow rate obtained using MEA4 in flow mode at 1.8 V. The anolyte was Millipore water, at room temperature.

with increasing the flow rate, in contrast, the gaseous current efficiency slightly decreased with increasing flow rate, this may be due to the fact that more ozone was entrained in solution as flow rate increased [50]. The highest current efficiency of ca. 13% was achieved at flow rate of 300 cm^3 min^{-1} (3 cm s^{-1}), the highest flow rate employed.

The effect of flow rate on the performance of MEA5 was assessed at 1.6 V over the range 60 cm^3 min^{-1} to 240 cm^3 min^{-1} (corresponding to linear velocity of ca. 0.6-2.4 cm s^{-1}). Figure 5.13 shows the steady state current and total current efficiency vs. flow rate for MEA5. It may be seen from the figure that the current decreased slightly, whereas the current efficiency increased with increasing flow rate reaching a value of 36% at 240 cm^3 min^{-1} (2.4 cm s^{-1}).

The power consumption and the ozone production rates from the flow rate experiments using MEA4 and MEA5 are shown in fig. 5.14. Bearing in mind that the area of the anode of MEA5 was ca. 25% of that of MEA4, it may be seen from the figure that the power consumption decreased with increasing the flow rate, achieving values of 46 kWh kg^{-1} O_3 and ca. 16.7 kWh kg^{-1} O_3 at 300 cm^3 min^{-1} (3 cm s^{-1}) and 240 cm^3 min^{-1} (2.4 cm s^{-1}) for MEA4 and MEA5, respectively. It may be seen from fig. 5.14 that the ozone production rates increased with increasing flow rates for both MEAs, reaching values of ca. 1.4 mg h^{-1}

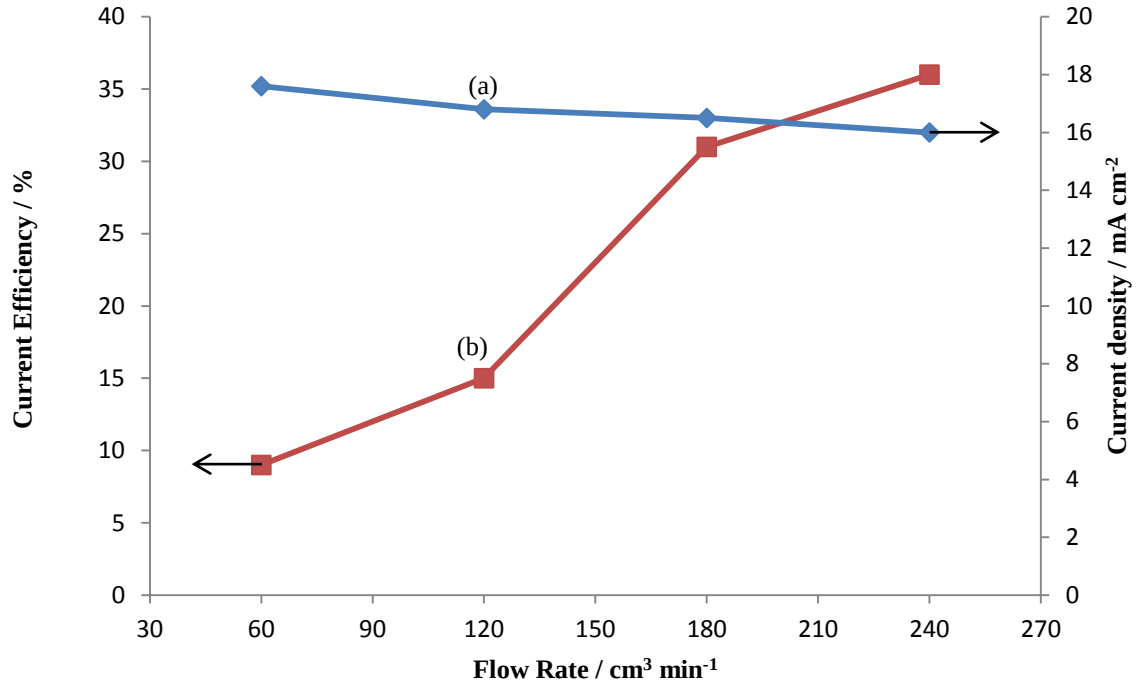

Figure 5. 13. Plots of: (a) current density and (b) total current efficiency vs. flow rate when generating ozone in the MEA5, tested in flow mode system at 1.6 V. The electrolyte was Millipore water, at room temperature.

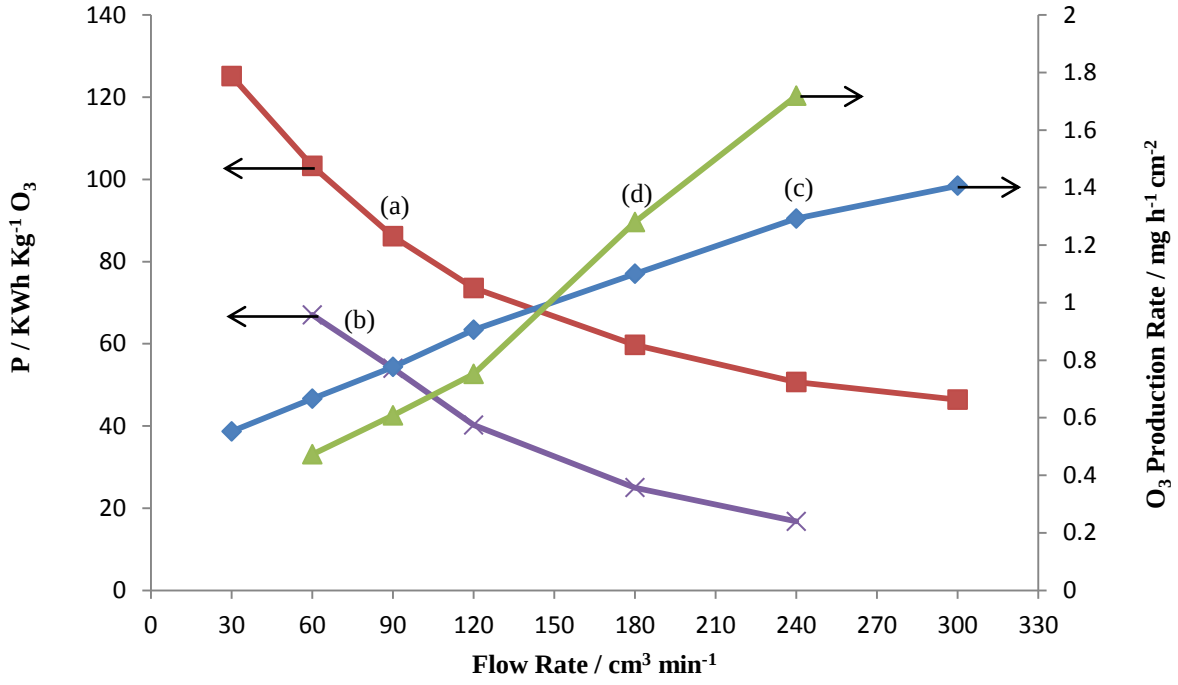

Figure 5. 14. Plots of: (a) & (b) power consumption and (c) & (d) ozone production rate vs. flow rate for the experiments in figs. 5.12 (a)&(c) (MEA4) and figs. 5.13 (b)&(d) (MEA5).

cm^{-2} and ca. 1.7 mg h^{-1} cm^{-2} for MEA4 and MEA5 at the highest flow rate employed, respectively.

As discussed above in section 5.2.1, air breathing cathodes have not been used frequently in ozone MEA cells due to various problems (especially flooding), see for example [4, 44] and [50].

For the two MEA's investigated, the flow rate (linear velocity) had little or no effect on current. However, the current decreased very slightly with increasing the flow rate for the three MEA's tested. To date, the effect of anolyte flow rate at constant cell voltage on the performance of Ni/Sb – SnO_2 – based MEA's has not been investigated previously, and the only research group investigate the effects of flow rate using MEA cells with air breathing cathodes was Cui and co – workers [50] who employed constant current. Therefore, it does not seem unreasonable to use the findings of Cui et al. [50] as a starting point. The authors found that increasing the flow rate resulted in decreasing cell voltage at constant current due to the fact that water convection reduced mass transfer resistance at the Nafion/anode/water interface and lowered the electrode polarization.

In terms of the effect of flow rate (linear velocity) on ozone current efficiency, the ozone current efficiency increased with increasing flow rate/liner velocity, and this was the case of both MEA4 and MEA5 that achieved ca. 13% and 36% at flow rates of 300 and 240 cm^3 min^{-1} (3 and 2.4 cm s^{-1}), respectively. These findings are not in complete agreement with the work of Cui et al. [50] who reported that the current efficiency increased linearly with the increasing flow rate initially, then became constant at higher flow rates. They claimed that the improvement in current efficiency in solution with increasing flow rate was a result of forced convection.

With respect to the effect of flow rate/linear velocity on power consumption for the MEA's investigated in this section MEA's 4 and 5, it was found that the power consumption decreased with increasing flow rate; achieving ca. 46 and 16.7 kWh kg^{-1} O_3 at 300 cm^3 min^{-1} and 240 cm^3 min^{-1} for MEA4 and MEA5, respectively. These values are much less than those found by Cui et al. [50], who found that the energy consumption dramatically decreased with increasing flow rate due to the decrease in voltage (as discussed above). The authors reported that the lowest energy consumption of 59 kWh kg^{-1} O_3 was achieved at 2 A constant current (corresponding to cell voltage value of 3 V) and 4 dm^3 min^{-1} flow

rate.

The OPR for the MEA's investigated in this section increased with increasing flow rate/liner velocity; achieving ca. 1.4 and 1.6 mg h^{-1} cm^{-2} at 300 cm^3 min^{-1} and 240 cm^3 min^{-1} (3 and 2.4 cm s^{-1}) for MEA4 and MEA5, respectively. This is in agreement with the work of Cui et al. [50] who reported the highest ozone production rate of 2.1 mg $h^{-1}cm^{-2}$ at the highest flow rate (4 dm^3 min^{-1} / 10.4 cm s^{-1}).

5.3 Ozone Generation in MEA with Hydrogen Evolution (Pt/Ti) Cathodes

The ozone generation experiments reported in this section were performed at either constant voltage or constant current in flow or recycle mode. The ozone absorbance in gas and solution phases were measured in addition to the corresponding current (at constant cell voltage) or voltage (at constant current). The current efficiency, power consumption, and ozone production rate were calculated accordingly. In addition, the effects of flow rate and electrolyte (anolyte and catholyte) type were investigated in recycle mode.

5.3.1 Ozone generation flow mode system

MEA6 was fabricated (see table 5.1) to investigate the effects of constant cell voltage in flow mode. MEA6 consisted of a 24 cm^2 NATO anode (prepared from metal oxides and at 550 ^{O}C) and Pt/Ti cathode pressed on either sides of Nafion 117 membrane. The corresponding steady state current density and current efficiencies (gas, solution and total) were calculated and are presented in fig. 5.15. It may be seen from the figure that the current density increased with increasing voltage up to 2.8 V after which it increased very little. Ozone was produced at voltages > 2.3 V. The current efficiency for dissolved ozone increased to ca. 25% at 2.5 V and then decreased with increasing voltage, whereas the gas phase ozone current efficiency increased slowly to ca. 10 % at 2.6 V, then remained steady with increasing voltage; most likely reflecting delay caused by the arrangement of the system. The total current efficiency simply reflects the sum of these two contributions. Given that the distribution of ozone between solution and gas depends upon the system, further discussion will focus only on the total ozone production. The maximum current efficiency was about 33%. The behaviour of the ozone current efficiency with cell voltage suggests that the ozone active sites on the anode surface were switched on at voltages > 2.3 V, and the ratio of ozone/oxygen active sites increased with increasing voltage at voltages between 2.3 – 2.5 V. However, at voltages > 2.5 V, the ratio of ozone/oxygen sites decreased with increasing voltage, or amount of ozone produced was less due to: (i) local

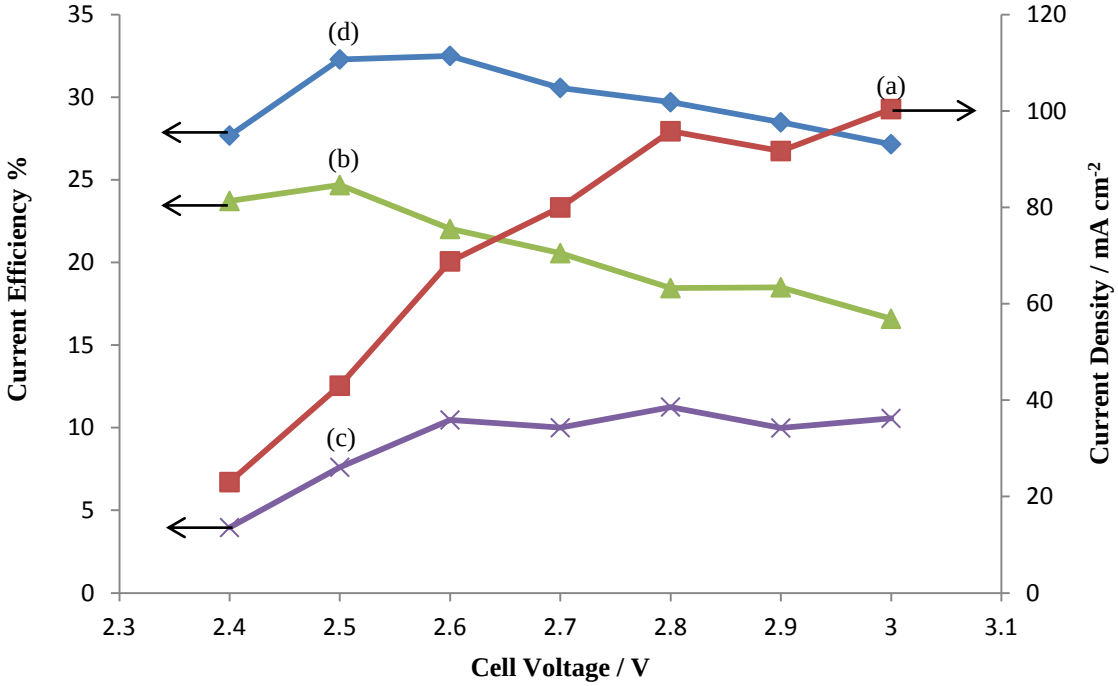

Figure 5. 15. Plot of: (a) current density, (b) solution current efficiency, (c) gaseous current efficiency and (d) total current efficiency vs. cell voltage when generating ozone in the MEA6, tested in flow mode system at 200 cm^3 min^{-1}. The electrolyte was Millipore water, at room temperature.

heating effects that increase with increasing current density leading to a decrease in ozone efficiency [17, 29, 62, 74, 176, 177], (ii) the switching of ozone active sites to oxygen [75, 78, 177], (iii) the decomposition of ozone as a result of its reaction with OH radicals:

$$OH^{\bullet} + O_3 \rightarrow O_2 + HO_2^{\bullet} \qquad (5.9)$$

with such radicals being produced at significant rates at higher current densities [61, 62, 177] and/or (iv) ozone decomposition:

$$O_3 + O_3 \rightarrow 3O_2 \qquad (5.10)$$

Equation (5.10) represents the sum of the equations given by Gardoni et al. [175] for ozone decomposition in neutral and alkaline media.

To date, an MEA consisting of a NATO anode/Nafion117/(Pt/Ti) cathode has not been investigated for ozone generation previously. Therefore, it does not seem unreasonable to use the literature on MEA's that used different anodes as starting point.

The current increase with increasing voltage has been reported by Tatapudi and Fenton[49]

who studied ozone generation from deionised (DI) water in a flow through MEA – based cell, using PbO_2 powder anode and Pt powder cathode deposited on Nafion 117 at constant voltage over the range 2 V to 5 V. The authors found the current passed through a maximum at 4 V and they explained the subsequent decrease in current in terms of a change in the morphology of the PbO_2 powder. However, Tatapudi and Fenton in another paper[51] changed the configuration of their MEA, where the anode was PbO_2 powder pressed on carbon fibre paper, and the cathode was gold, graphite or carbon pressed on carbon fibre paper, separated by Nafion 117 at constant voltage over the range 2 V to 5 V. The authors found that a minimum voltage of 3 V was required for Faradic current to pass, with current increasing with increasing voltage.

As discussed above, in terms of the current efficiency vs. cell voltages (or current), there were four types of behaviour in the literature (see fig. 5.9). Type (I)[17, 31, 49] has been reported by Stucki et al.[17, 31] who studied ozone generation from DI water using an MEA consisting of a Pt cathode and a porous titanium coated with PbO_2 anode, operating in recycle mode at a constant current of 0 – 3 A cm^{-2} from water. The authors found that the current efficiency increased with increasing current density up to 1.3 A cm^{-2} then reached a plateau due to local heating. Tatapudi and Fenton[49] found that the current efficiency reached a plateau after 4.5 V. Type (II)[45, 48, 51, 62] has been reported by Kraft et al.[62] who studied the ozone generation in MEA using boron doped diamond (BDD) as anode and cathode separated by Nafion N324 from water (1 μS cm^{-1}) at 0.1 – 5 A in a flow – through reactor. The authors found that the current efficiency passed through a maximum at 1 – 1.5 A after which the current efficiency decreased with increasing current. They interpreted the decrease in current efficiency in terms of either: (i) the production of hydrogen peroxide that accelerated ozone decomposition and/or (ii) local heating leading to lower ozone production or faster ozone decay. In addition, Tatapudi and Fenton[51] found that the current efficiency passed through a maximum at 4.7 V and then decreased. They did not suggest any reason why. Current efficiency passing through a maximum with increasing current during tests on MEA – based ozone cells has been reported many times for a range of different types of anode and cathode; see for example[45] and [48]. Type (III) has been reported by Han et al.[47] and Da Silva et al.[7, 46] who used MEA's consisting of PbO_2 anodes and Pt cathodes at different constant currents from DI water[47], H_2SO_4 [7] and water[46]. The authors found that the current efficiency increased with increasing current. Type (IV) has been reported by Arihara et al.[61] who used an MEA consisting of a BDD anode and Pt cathode

separated by Nafion N324 at current of 1 -10 A from pure water. The authors found that the current efficiency decreased with increasing current. They explained their findings in terms of a model in which the autolysis of the ozone at higher concentrations was dominant. The current efficiency findings (in fig. 5.15) are in agreement with Type (II) behaviour (the work of Tatapudi and Fenton[51], Arihara et al.[45], Kraft et al.[62] and Onda et al.[48]).

Figure 5.16 shows the power consumption and ozone production rate for the experiments in fig. 5.15. It may be seen from the figure that the power consumption decreased with increasing voltage to a value of ca. 25 kWh kg^{-1} O_3 at 2.5 V after which it increased almost linearly with increasing the cell voltage. This is in general agreement with the work of Stucki et al.[17, 31] who found that the power consumption decreased to a minimum of ca. 65 kWh kg^{-1} O_3 at about 1 A cm^{-2} after which it increased, and the work of Onda et al.[48] who used MEA consisted of PbO_2 anode and Pt cathode separated by Nafion 117 membrane at constant current of 0.25 – 2 A cm^{-2}. The authors reported that the power consumption decreased to a minimum of 130 kWh kg^{-1} O_3 at 1 A cm^{-2}, after which it increased. They compared their results to that obtained by Stucki et al.[17, 31], interpreting the difference in terms of the difference between MEA and that of Stucki et al. In contrast, Arihara et al.[45]

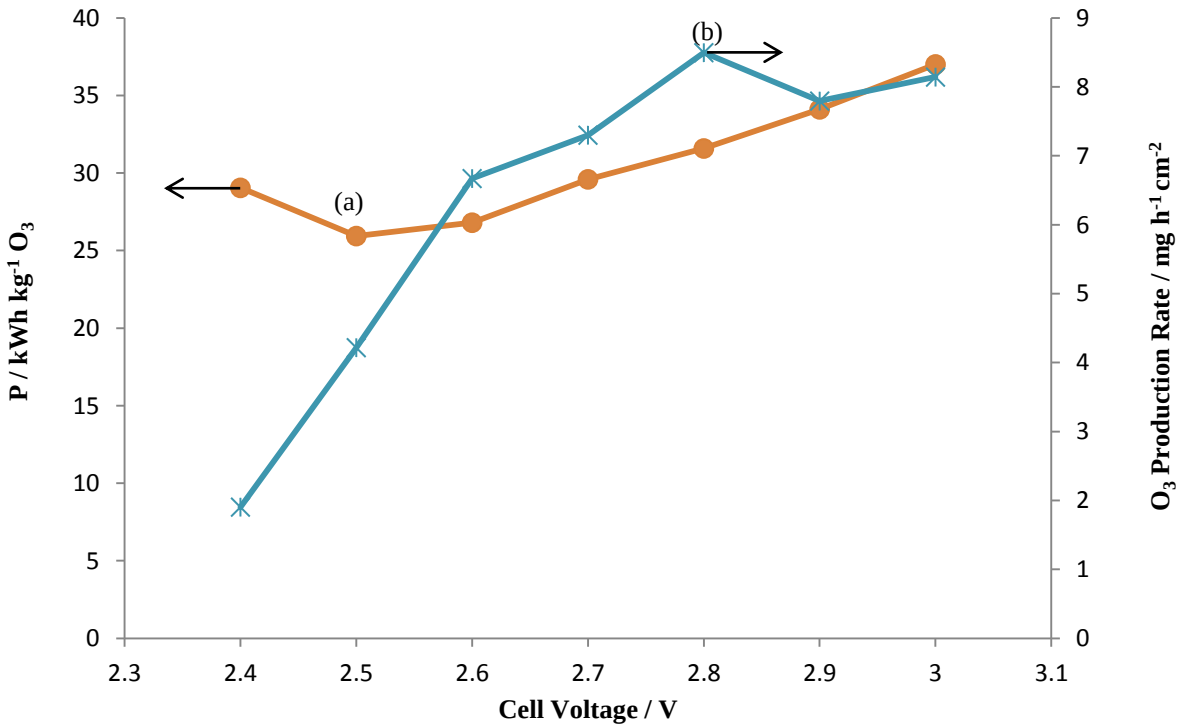

Figure 5. 16. Plots of: (a) power consumption and (b) ozone production rate vs. cell voltage for the experiments in fig. 5.15.

used an MEA consisting of a porous BDD plate as anode and Pt mesh as cathode from pure water at constant current of 1 – 10 A, and found that the power consumption increased with increasing current. On the other hand, Da Silva et al.[7, 46] found that the power consumption decreased with increasing current.

It may be seen from fig. 5.16 that ozone production rate increased with increasing voltage up to 2.8 V then remained almost constant. This behaviour is in general agreement with the work of Kraft et al.[62] who reported that the ozone production rate increased with increasing current although the ozone production rate increased slowly at higher currents. In addition, Arihara et al.[61] and Da Silva et al.[7, 46] found that the ozone production rate increased with increasing current.

5.3.2 Anolyte flow rate effect in recycle mode

The effects of the anolyte flow rate/linear velocity on ozone generation were investigated in recycle mode in 1 M $HClO_4$ at constant current densities from 10 mA cm^{-2} to 100 mA cm^{-2}. Figure 5.17 shows plots of cell voltage vs. current density at anolyte flow rate of 200 cm^3 min^{-1} (2 cm s^{-1}) and 100 cm^3 min^{-1} (1 cm s^{-1}) using MEA7 (see table 5.1). It may be seen from the figure that the voltage increased with increasing current density. This was expected and it had been reported previously as discussed above, see for example [4, 7, 44-47, 50]. In addition, it may be seen from the figure that the flow rate/linear velocity had little or no effect on the voltage. This is in general agreement with the work of Stucki et al.[31] and Da Silva et al.[46] who employed an anolyte flow rates of 10 to 90 dm^3 h^{-1} (1.15 – 1.4 cm s^{-1}, respectively). In contrast, Nishiki et al.[52] who employed an MEA comprising a BDD anode, Nafion and stainless steel wire cathode at flow rates of 50 to 600 cm^3 min^{-1} at 0.5 A and 1 A. The authors reported that, at low flow rates, the voltage increased with increasing flow rates, then became independent of the flow rate at higher values. They explained this as due to the increase of local temperature at the interface of the membrane and the electrodes (local heating).

Figure 5.18 shows the current efficiency vs. current density for the experiments in fig. 5.17. It may be seen from the figure that the current efficiencies at the two flow rates studied(100 and 200 cm^3 min^{-1}/ 1 and 2 cm s^{-1}) increased with increasing current density up to 60 mA cm^{-2} achieving a value of 37%, after which the current efficiencies reached a plateau. This has been reported previously, as discussed above, see for example: [17, 31, 49-51]. In addition, it may be seen from the figure that the flow rate had little or no effect on the

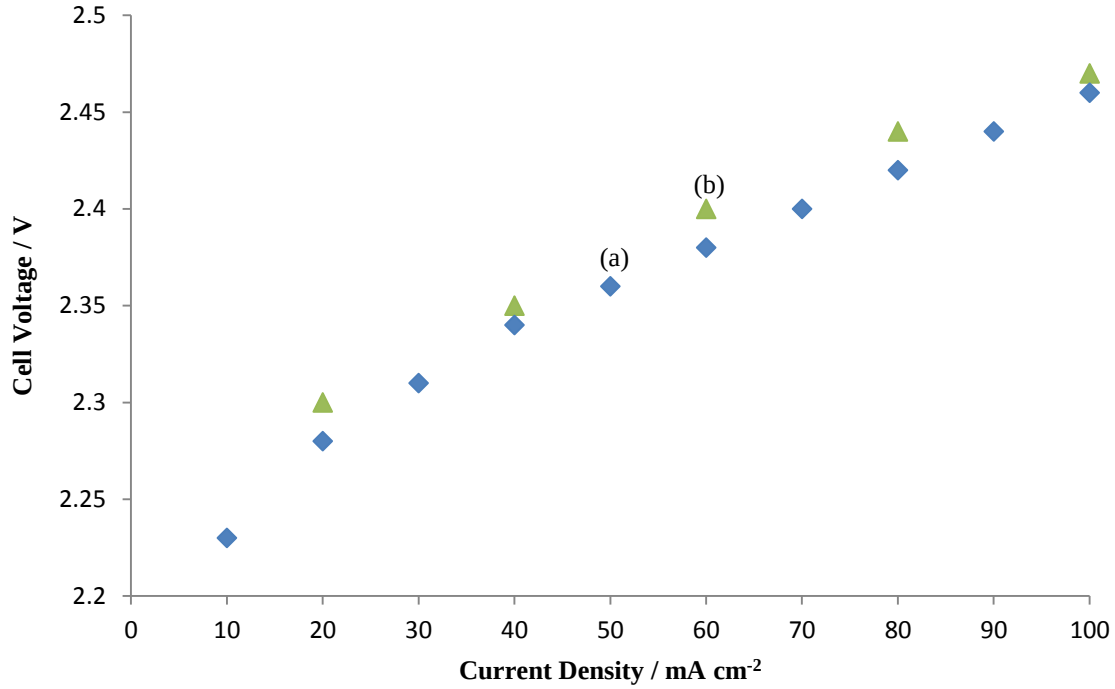

Figure 5. 17. The cell voltage changes with current density at different recycle flow rates: (a) 200 cm^3 min^{-1} and (b) 100 cm^3 min^{-1}, MEA7 was used for ozone generation in recycle mode system, 1 M $HClO_4$ was used as both anolyte and catholyte, at room temperature.

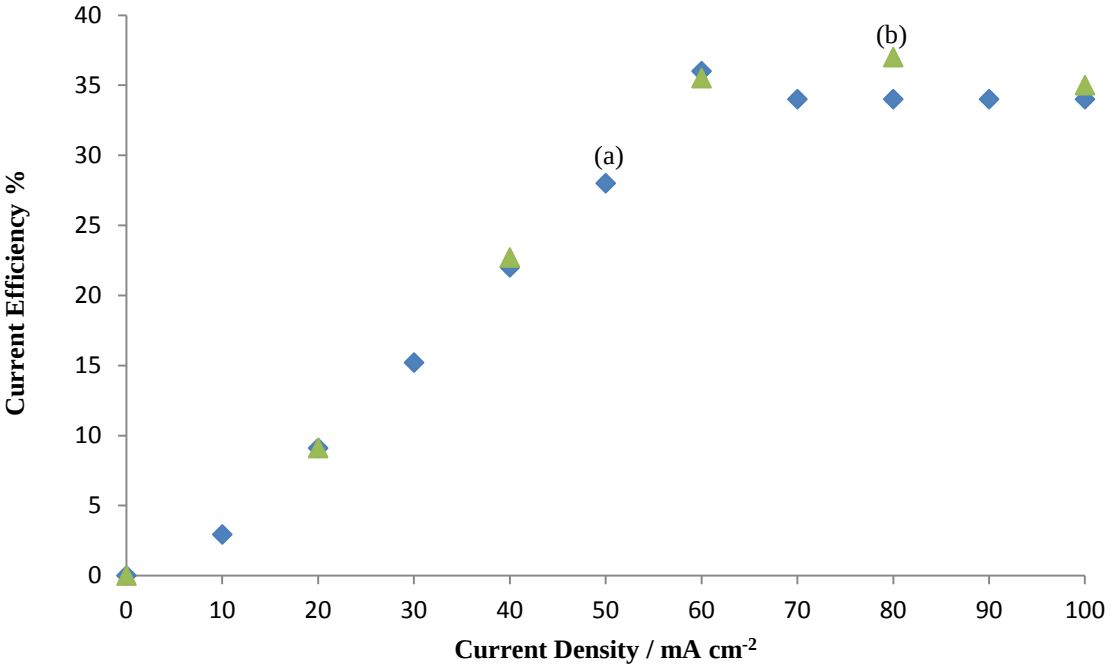

Figure 5. 18. The current efficiency as function of current density at different recycle flow rates: (a) 200 cm^3 min^{-1} and (b) 100 cm^3 min^{-1}, MEA7 was used for ozone generation in recycle mode system, 1 M $HClO_4$ was used as both anolyte and catholyte, at room temperature.

ozone current efficiency. This is in contrast to the work of Nishiki et al.[52], Onda and Naya[176], Kraft et al.[62] and Onda et al.[48] who found that current efficiency increased with increasing flow rate/linear velocity due to the local heat removal at higher flow rates/linear velocities. On the other hand, Cui et al. [50], Stucki et al.[31] and Da Silva et al.[46] found that although current efficiency increased with increasing flow rate initially, at higher flow rates, the current efficiency became independent of flow rate due to 'local overheating'.

Figure 5.19 shows the power consumption and ozone production rates vs. current density at flow rates of 200 cm^3 min^{-1} and 100 cm^3 min^{-1} for the experiments in figs. 5.17 and 5.18. It may be seen from the figure that power consumption decreased with increasing current density up to 60 mA cm^{-2} achieving a value of 22 kWh kg^{-1} O_3, the lowest ever reported for an MEA with hydrogen evolving cathode, after which the power consumption at both the flow rates studied reached a plateau. This in general agreement with the work of Da Silva et al.[7, 46]. In contrast, Stucki et al.[17, 31] and Onda et al.[48] found the power consumption to pass through a clear minimum after which it increased, and Arihara et al.[45] who reported that the power consumption increased with increasing current. In addition, it may be seen from the figure that the flow rate had little or no effects on power consumption. This is in contrast to the work of Onda et al.[48] who found the power consumption decreased with

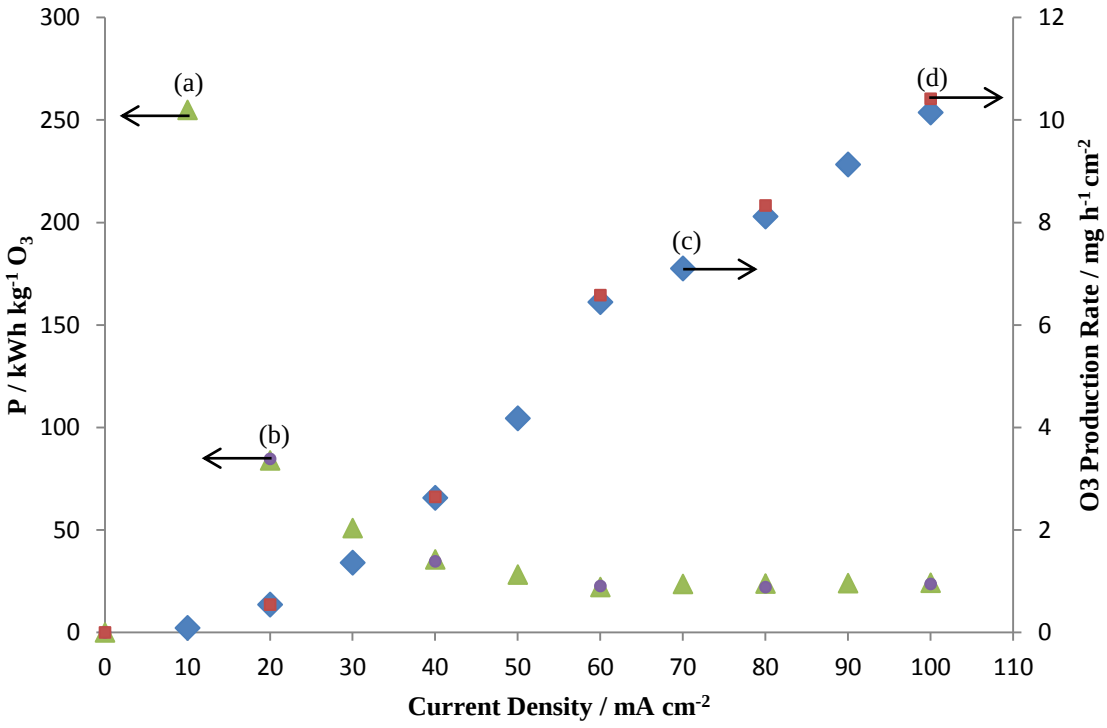

Figure 5. 19. Plots of: (a) power consumption at 200 cm^3 min^{-1}, (b) power consumption at 100 cm^3 min^{-1}, (c) ozone production rate at 200 cm^3 min^{-1} and (d) ozone production rate at 100 cm^3 min^{-1} for the experiment in fig. 5.18.

increasing flow rate.

It may be seen from fig. 5.19 that the ozone production rate increased with increasing the current density. This is in agreement with the work of Arihara et al.[61] and Da Silva et al.[7, 46]. In addition, the flow rate had little or no effects on ozone production rate due to the fact that in recycle system, and based on Henry's law of gas partial pressure, once the solution reached a saturation state with O_3, all remaining ozone will leave the solution.

5.3.3 Electrolyte effects

As discussed in section 1.1.6, the use of Nafion membrane poses some problems such as calcification, therefore, the choice of the electrolyte and especially the anolyte is very important issue. This fact made the use of electrolyte-free water as anolyte a common practice (see for example,[4, 50]). In addition, Nafion is an acidic membrane that is designed to conduct protons from the anode to the cathode. Therefore, it doesn't seem unreasonable to postulate that the use of acidic electrolyte might improve the current of the

MEA cell, and consequently, the current efficiency and the ozone production rate. To check this postulate, it was decided to investigate the effects of the Millipore water and 1 M $HClO_4$ as anolytes and catholytes on the performance of the MEA.

Figure 5.20 shows the cell voltage and the total current efficiency vs. time when using Millipore water as anolyte. The catholyte was either Millipore water or 1 M $HClO_4$. It may be seen from the figure that the cell voltage reached a steady state within one minute of operation for both catholyte used. However, the current efficiency increased with time up to a value of ca. 15% and 6% after 6 min of using $HClO_4$ and Millipore water as catholyte, respectively. The increase in current efficiency for the acid as catholyte was faster than that of the Millipore water. It is clear from the figure that the use of acid as catholyte resulted in a superior performance in terms of cell voltage and current efficiency than the use of Millipore water; this may be due to the fact that the acid is much more ionically conductive than the Millipore water and/or MEA delamination.

Figure 5.21 shows the cell voltage vs. time when using 1 M $HClO_4$ as anolyte. The catholyte was either Millipore water or 1 M $HClO_4$. It may be seen from the figure that the cell voltage in both cases reached a steady state within one minute of operation. In addition, in terms of cell voltage, the best performance of MEA7 was observed using 1 M $HClO_4$ as catholyte followed by Millipore water, this may be due to the higher conductivity of the

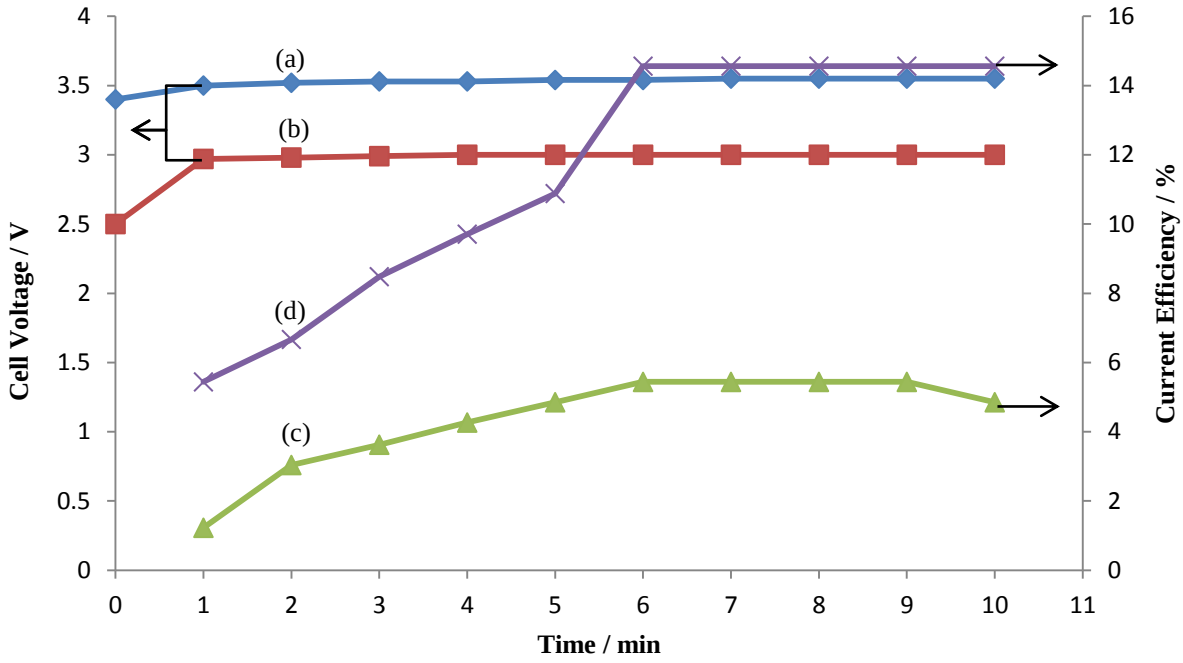

Figure 5. 20. Plot of (a) & (b) cell voltage and (c) & (d) current efficiency vs. time, MEA7 was used for ozone generation in recycle mode system at 50 mA cm^{-2}, Millipore water was used as anolyte. The catholyte was Millipore water for (a) & (c), and 1 M $HClO_4$ for (b) and (d), anolyte recycle flow rate is 200 cm^3 min^{-1}, at room temperature.

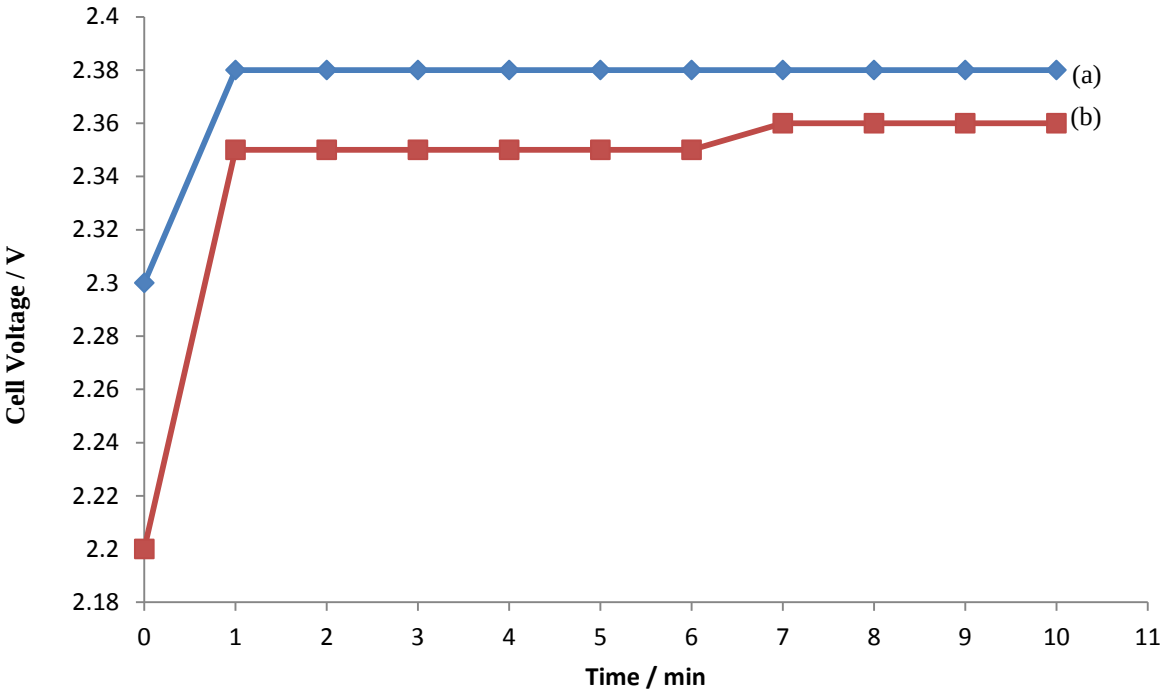

Figure 5. 21. Plot of cell voltage vs. time, MEA7 was used for ozone generation in recycle mode system at 50 mA cm^{-2}, 1 M $HClO_4$ was used as anolyte and the catholyte were: (a) Millipore water and (b) 1 M $HClO_4$, at 50 mA cm^{-2}, anolyte recycle flow rate is 200 cm^3 min^{-1}, at room temperature.

acid. It became clear that using acid as anolyte and/or catholyte resulted in increasing the current and current efficiency. This is most likely to be due to MEA delamination.

Figure 5.22 shows the current efficiency vs. time for the experiments in fig. 5.21. It may be seen from the figure that whatever the catholyte was, the current efficiency increased with time to reach a steady state at 4 – 5 min; achieving a value of ca. 27%. It may be seen from the figure that at the steady state, the catholyte had little or no effects on the current efficiency. In contrast, Kraft et al.[62] found that the current efficiency decreased with increasing electrolyte conductivity, explaining that by the fact that at higher electrolyte conductivity, the active area of the BDD anode increases leading to lower real current densities that resulted in lower ozone production efficiency.

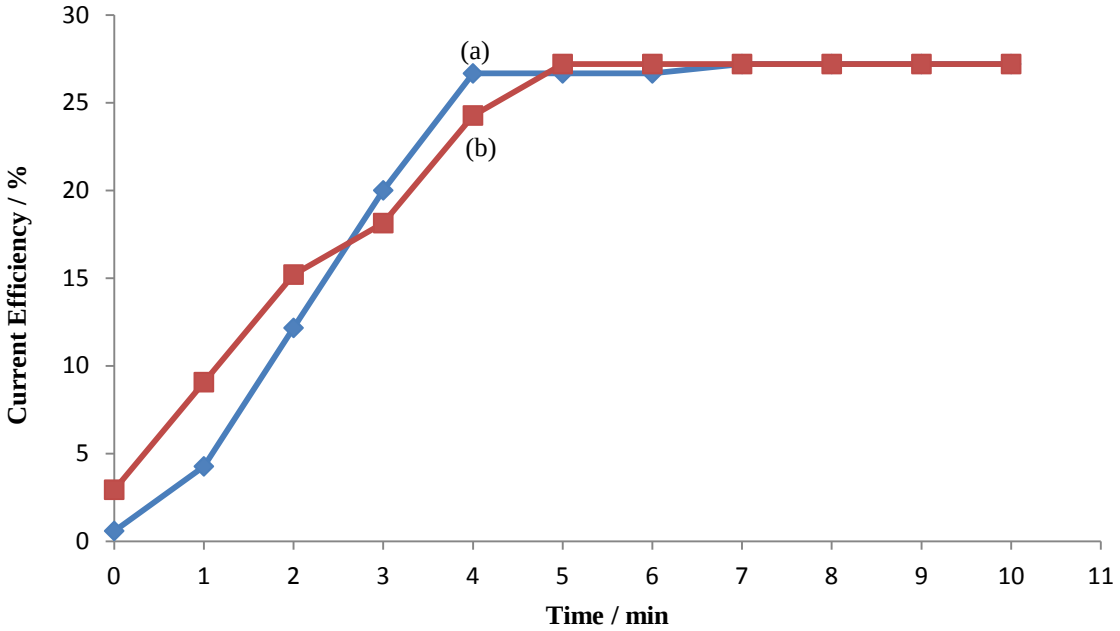

Figure 5. 22. Plot of current density vs. time, MEA7 was used for ozone generation in recycle mode system at 50 mA cm^{-2}, 1 M $HClO_4$ was used as anolyte and the catholyte were: (a) Millipore water and (b) 1 M $HClO_4$, at 50 mA cm^{-2}, anolyte recycle flow rate is 200 cm^3 min^{-1}, at room temperature.

Table 5.2 summarises the effect of the electrolyte on the performance of MEA7. It may be seen from the table that when 1 M $HClO_4$ was used as anolyte, the steady state cell voltage was about 2.4 V regardless of the catholyte used, but it was more than 3 V when Millipore water was used as anolyte. The lowest cell voltage recorded was when using 1 M $HClO_4$ as catholyte and anolyte, simultaneously. This might be due to the fact that more protons (H^+) are available in the acid than in the Millipore water; making the conductivity much higher. It may be seen from table 5.2 that the current efficiency when 1 M $HClO_4$ was used as

Anolyte	**Millipore Water**		**1 M $HClO_4$**	
Catholyte	Millipore Water	1 M $HClO_4$	Millipore Water	1 M $HClO_4$
Cell Voltage / V	3.55	3	2.38	2.36
Current Efficiency / %	5.4	14.6	27.2	27.2
Power consumption / kWh kg^{-1} O_3	219	69	29	29
O_3 production rate / mg h^{-1} cm^{-2}	0.8	2.2	4.1	4.1

Table 5. 2. Summary of steady state cell voltage, current efficiency, power consumption and ozone production rate for the experiments in figs. 5.20 – 5.22.

anolyte is twice as that when using Millipore water as anolyte. In addition, the current efficiency when using the acid as catholyte with Millipore water as anolyte is almost 3 times as that when using Millipore water as anolyte and catholyte, this suggest the MEA delamination (the anode and/or the cathode were separated from the Nafion at least partially).

The power consumption was at its highest levels when Millipore water was used as anolyte and catholyte (see table 5.2). It may be seen from the table that the use of acid as anolyte reduced the power consumption considerably no matter what the catholyte was. Furthermore, the use of the acid as catholyte with Millipore water as anolyte reduced the power consumption (see table 5.2).

In terms of the ozone production rate, it may be seen from table 5.2 that it is affected by the electrolyte, and especially the anolyte. It is clear from the table that the highest ozone production rate achieved when the 1 M $HClO_4$ was used as anolyte and catholyte. In addition, the use of acid as catholyte only was helpful in improving the ozone production rate.

5.4 Conclusions

In general, the use of air breathing cathodes posed a major problem of flooding and made the use of MEA constrained. The problem of flooding could not be solved by using smaller size anode than cathode nor by using differently fabricated air breathing cathode, although these two ideas were helpful in improving the performance of the MEA in terms of ozone current efficiency and power consumption. The anode's type and fabricating methodology had an effect on the performance of the MEA. In contrast, the MEA that was fabricated using the optimum component (smaller anode than cathode, JM cathode, anode made of

metal oxides and annealed at 550 ^{O}C) could achieve 36% current efficiency at 240 cm^3 min^{-1} flow rate with power consumption of only 16.7 kWh kg^{-1} O_3, which has not been reported in the literature of MEA whatever the anode was.

The hydrogen evolving cathodes do not suffer from flooding as the catholyte is aqueous, and the main product is H_2 gas. The H_2 gas is an energy source that can be exploited. MEA's with hydrogen evolution cathodes could achieve current efficiencies as high as 37% under optimum conditions. The anolyte flow rate had little or no effects on the performance of the MEA. Using acid as anolyte and/or catholyte improved the performance of the MEA.

In the following chapter, the efficiency of the small (0.8 cm × 0.8 cm) NATO anodes in decolourisation of industrial wastewater containing dyes will be investigated. The optimum operation conditions; including the effect of current density, the effect of electrolyte type and concentration, the effect of pH, the effect of initial dye concentration on both the decolourisation and COD removal will also be discussed.

CHAPTER SIX

6 Electrochemical Dye Decolourisation on NATO Anodes

6.1 Introduction

As was seen in previous chapters, Ti/Ni/Sb – SnO_2 anodes have shown very high activity and selectivity for the generation of ozone in aqueous solution at room temperature, irrespective of electrode area up to 4 cm × 6 cm, and using different electrochemical cells. The objectives of the work reported in this chapter were: (1) to assess if, and to what extent, Ti/Ni/Sb – SnO_2 anodes could be employed to decolourise water contaminated with dyes, (2) to compare the efficiency of the Ti/Ni/Sb – SnO_2 anodes with the literature and (3) to identify the optimum conditions for decolourisation.

The dyes studied in the work reported in this chapter were: Reactive Blue 50 (RB50, as a model for anthraquinone dyes); Congo Red (CR, as a model for azo dyes) and Naphthol Green B (NGB, as a model for nitrozo dyes). To date, RB50 has not been studied previously. The dyes were employed to investigate the activity of NATO anodes with respect to the removal of colour (decolourisation) and chemical oxygen demand (COD). The complex molecular structure and high molecular mass of those dyes render their remediation a challenging task.

As discussed in section 2.14.1, the UV – Vis spectra of the types of the dye under investigation (shown in fig. 2.13) show bands in the visible region (associated with colour) and in the UV region (associated with aromatic rings)[111, 123]. In the case of RB50 (see fig. 2.13 and table 2.6), bands at 625 nm and 586 nm have been attributed to the anthraquinone moiety of the dye, and the band at 254 nm to the benzene ring[111, 123, 147]. The UV – Vis spectrum of the CR (see fig. 2.13 and table 2.6) has a band at 500 nm, due to the presence of the diazo bonds[111, 123, 147], and of NGB (see fig. 2.13 and table 2.6) has a band at 715 nm, due to the nitroso chromophore.

As discussed in section 2.15, small (0.8 cm × 0.8 cm) NATO anodes were used in the quartz cuvette cell with (0.8 cm × 0.8 cm) Pt/Ti mesh cathodes. The anode used was NATO12J (see table 2.3 and Appendix II).

The sections below report a preliminary study of decolourisation of dye solutions, and an

investigation of the effect of various experimental parameters including: current density, electrolyte (type and concentration), pH, initial dye concentration and dye structure in order to obtain the optimum decolourisation conditions.

6.2 Preliminary Study

It is likely that ozone generated at NATO anodes will be involved in the dye molecular destruction in addition to direct and indirect electrochemical destruction. In order to focus on electrochemical destruction, it was decided to investigate dye remediation in alkaline solution, as it is well known that the ozone decomposes rapidly under such conditions according to scheme 5.1[175]. Hence, the preliminary study of dye decolourisation at NATO anodes was carried out in aqueous Na_2CO_3 (see section 6.4 for a detailed study of the effect of electrolyte)

As discussed in section 2.15.1, 3 cm^3 of 100 mg dm^{-3} RB50 in 3 g dm^{-3} aqueous Na_2CO_3 was electrolysed in the cuvette cell.

Figure 6.1 shows the UV – Vis spectra of the RB50 solution during the electrolysis; as was disused above in section 6.1, the spectrum of RB50 consists of three well – defined peaks at 254 nm, 586 nm and 625 nm. The figure is representative of all the electrochemical decolourisation experiments carried out using the RB50 solution and reported in this chapter. From the figure it may be seen that all three bands decreased with time. The loss of the UV band near 254 nm suggest that the dye is being oxidised into fragments[178], while the decrease in the intensities of the 625 nm and 586 nm bands may be attributed to the destruction of the anthraquinone moiety[122]. Figure 6.2 shows plots of the (A/A_0) of 254 nm, 586 nm and 625 nm bands as a function of time during the experiment in fig. 6.1 (calculated from the intensity change of the 254 nm, 586 nm and 625 nm bands in fig. 6.1). As can be seen from the figure the (A/A_0) of the 586 nm and 625 nm features track each other as would be expected as they are due to the anthraquinone chromophore destruction. Therefore, the decrease of the $(A/A_0)_{625}$ and $(A/A_0)_{254}$ of the 625 nm and 254 nm bands were taken as representative of the colour removal and benzene ring destruction of RB50, respectively, in all experiments reported in this chapter. As can be seen from fig. 6.2, both decolourisation and destruction of the benzene ring are complete after 60 min.

There are relatively few reports in the literature on ozone evolution at NATO anodes (see for example[42, 76, 77]). As discussed in section 1.1.1, based on literature precedent [8, 25, 64], the

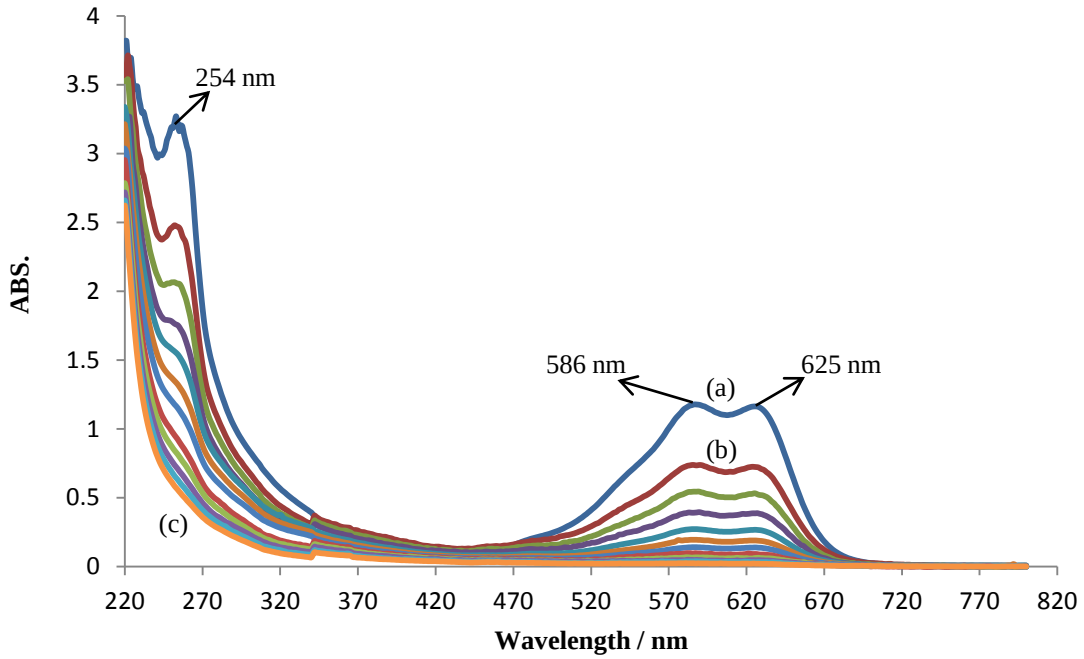

Figure 6. 1. UV – Vis spectra collected during the electrolysis of 100 mg dm^{-3} of RB50 in 3 g dm^{-3} aqueous Na_2CO_3 solution in the cuvette cell at 10 mA cm^{-2}, the NATO anode (NATO12J) was 0.64 cm^2 and the cathode was 0.64 cm^2 Ti/Pt mesh, at room temperature, the spectra collected (a) at the start of the electrolysis (t = 0), (b) after 10 min and then every 5 min up to (c) 60 min.

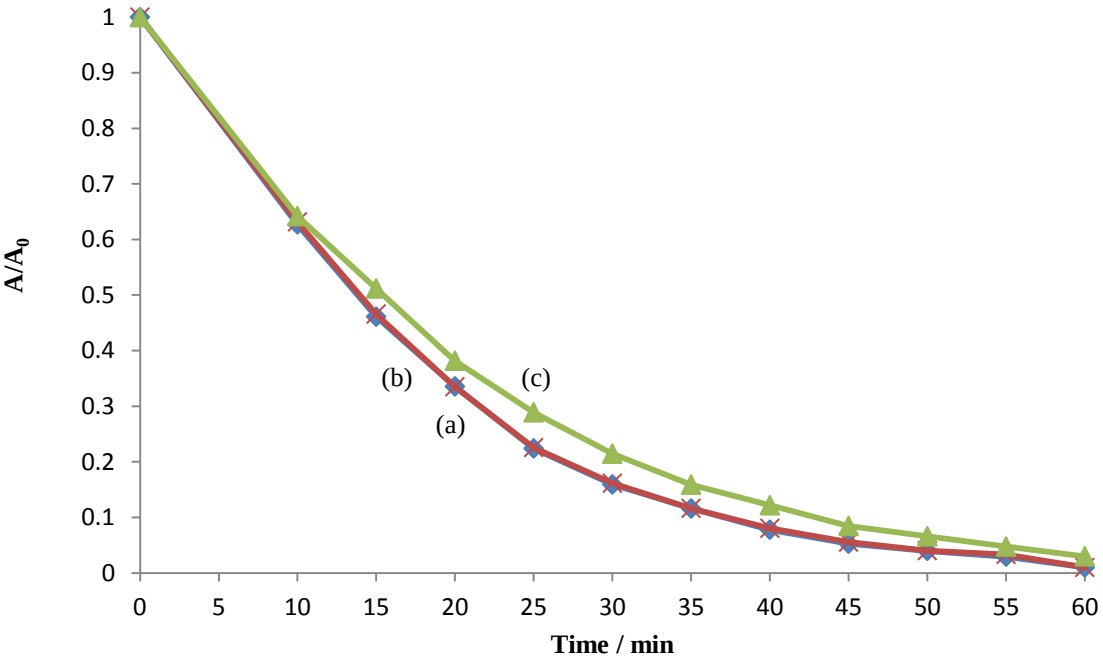

Figure 6. 2. Plots of: (a) $(A/A_0)_{625}$ for the 625 nm band, (b) $(A/A_0)_{586}$ for the 586 nm band and (c) $(A/A_0)_{254}$ for the 254 nm band of RB50 (100 mg dm^{-3}) vs. electrolysis time. The experimental conditions were as in fig. 6.1.

ozone generation at such anodes was postulated to include four main steps: (i) water discharge at the anode surface to give OH radicals adsorbed on active sites, (ii) decomposition of the OH_{ads} to give adsorbed atomic oxygen (O_{ads}), (iii) recombination of two O_{ads} to form adsorbed molecular oxygen ($O_{2\ ads}$) and (iv) the reaction of O_{ads} and $O_{2\ ads}$ to form $O_{3\ ads}$. Adsorbed ozone can then be released from the anode surface depending on its concentration in the bulk. In addition, adsorbed oxygen can be released from the anode surface.

In considering the ozone activity of NATO anodes, due to the lack of information regarding the role of Ni in the matrix of NATO anodes, it does not seem unreasonable to use the information available on Sb – SnO_2 (ATO) anodes as a starting point for discussion.

Comninellis[125] and Martinez – Huitle and Brillas[85] designated ATO anodes as "inactive" anodes (see section 1.3.2), capable of generating significant amounts of OH radicals from the discharge of water molecules, with the adsorption of these radicals on the anode surface being weak. The latter means that the OH radicals are readily available for reaction with solution species.

It is clear that nickel is crucial for ozone generation at NATO anodes (as ATO anodes generate no ozone under the same conditions [75, 164, 179]), and that ozone evolution must be a surface process. It has been reported that surface enrichment by Ni takes place[76, 77, 165], but, given the overall amount of Ni in the precursor solution, the surface concentration of Ni is still likely to be small compared to Sn and Sb. Again, the lack of detailed information on the electrochemistry of NATO anodes forces attention on the nearest possible models, in this case, bulk nickel. The electrochemistry of Ni is different to Sb – SnO_2 in terms of OH radical adsorption. Ni in alkaline solutions becomes passivated by a Ni(II) hydroxide thin film, and this Ni(II) can react with adsorbed OH radicals to generate higher oxides [179]:

$$Ni(OH)_2 \rightarrow NiO_x(OH^{\cdot}) + H^+ + e^- \qquad (6.1)$$

$$Ni(OH)_2 + OH^- \rightarrow NiO_x(OH^{\cdot}) + H_2O + e^- \qquad (6.2)$$

and the new oxide can oxidise an organic molecule (R) directly to products (P):

$$NiO_x(OH^{\cdot}) + R \rightarrow Ni(OH)_2 + P \qquad (6.3)$$

Alternatively, again, in the absence of detailed mechanistic studies on NATO anodes, it

doesn't seem unreasonable to draw on the electrochemistry of electrodes that contain Ni metal and/or Ni oxides as a starting point. According to Comninellis[125], Martinez – Huitle and Brillas[85] and Mendez-Martinez et al.[179], the water is first decomposed to generate OH radicals that are strongly adsorbed on the Ni, oxidising it to a higher oxidation state, that is able to oxidise organics, or itself undergoes decomposition to generate oxygen:

$$Ni^{2+} \rightarrow Ni^{2+}(OH^{\cdot}) + H^{+} + e^{-} \qquad (6.4)$$

$$Ni^{2+}(OH^{\cdot}) \rightarrow Ni^{3+} + H^{+} + e^{-} \qquad (6.5)$$

$$Ni^{3+} + R \rightarrow P + Ni^{2+} \qquad (6.6)$$

$$Ni^{3+} \rightarrow \tfrac{1}{2} O_2 + Ni^{2+} \qquad (6.7)$$

For Ni, the available oxidation states are Ni^{2+} and Ni^{3+}.[9]

From the discussion above, it can be seen that NATO anodes can support both the direct and indirect (mediated) electrochemical oxidation of organics, and can have active sites that weakly adsorb OH radicals (i.e. behaves as an inactive anode) and other active sites that strongly adsorb (react with) OH radicals (behaves as an active anode). Hence, it is possible that NATO anodes may exhibit the properties of both active and inactive anodes and both electrochemical incineration and conversion may be expected. However, and due to the very low amount of Ni on the surface of NATO anodes, the anodes will be more likely inactive and will facilitate electrochemical incineration.

6.2.1 Dye oxidation mechanism

As discussed above, when Faradic current is passed through the cuvette cell, water decomposition results initially in OH radicals [64, 85, 125], which can either be released from the electrode surface and react with dye molecules in the near – electrode region, or oxidise the Ni to generate Ni(III) which, in turn, oxidises the adsorbed dye molecules.

The OH radical reaction with organic molecules includes hydrogen abstraction and/or addition to unsaturated (- C = C -) carbon double bonds[180]. Therefore, the OH radicals (and probably, the Ni(III)) attack the dye molecule at the chromophore and the benzene ring, cleaving both. The cleavage of the anthraquinone and the benzene ring result in the formation of smaller molecules (mainly aliphatic acids[111]). These smaller molecules undergo decomposition because of the continuous attack of the OH radicals.

6.2.2 Rate constants

As discussed above, the dye molecule will react (most likely) with electrogenerated oxidising agents such as OH radicals. Other oxidants are available due to water discharge as discussed in section 1.1.1. In addition, dye oxidation is unlikely to take place in a single step. Therefore, and to simplify the discussion of the data, it does not seem unreasonable to postulate that the main oxidant is the OH radical and the overall decolourisation reaction may be represented simply as:

$$Dye + OH\cdot \rightarrow Products \qquad (6.8)$$

and the rate is given by[181]:

$$Rate = k_{obs}.\,[Dye]^{m}.\,[OH\cdot]^{n} \qquad (6.9)$$

Where k_{obs} is the observed rate constant ($k_{obs} = k_{m+n}$), and m+n is the overall reaction order. The reaction order can be zero, first or second. [Dye] is the dye concentration.

As will be discussed below, constant current electrolysis was employed, hence producing essentially constant oxidant concentration, and equation (6.9) can be rewritten as:

$$Rate = k'_{obs}.\,[Dye]^{m} \qquad (6.10)$$

$$\text{where } k'_{obs} = k_{obs}.\,[OH\cdot]^{n} \qquad (6.11)$$

Zero order kinetics will produce a linear plot of [Dye] vs. time, which will immediately be obvious. The integrated rate equations for first and second order kinetics are[181]:

$$\ln([C]/[C_0]) = -k_1.\,t \qquad (6.12)$$

$$1/[C] - 1/[C_0] = k_2.\,t \qquad (6.13)$$

respectively. Where C is the dye concentration.

To investigate the order of the reaction, it is important to collect the dye concentration [C] vs. time data, then plot [C] vs. t, ln[C] vs. t and 1/[C] vs. t for zero, first and second order, respectively, and check the linearity of those plots, the plot with R^2 closest to 1 may be taken as representative of the data and the rate constant may be determined from the slope of the plot.

The dye concentration during this chapter was estimated by measuring the absorbance at 625 nm; the absorbance at 254 nm was also monitored in order to estimate the destruction of the benzene ring.

As an example taken from the data presented in this chapter, fig. 6.3 shows plots of the dye concentration as absorbance at 625 nm (A), taken from the data described in fig. 6.1, ln(A) and 1/(A) vs. electrolysis time. It may be seen from the figure that the (A) and ln(A) plots varied linearly with electrolysis time, but 1/(A) did not. Therefore, the reaction order of the decolourisation process presented in fig. 6.1 cannot be second order, and it might be zero or first order. To investigate the latter, the R^2 for the two lines (see fig. 6.3 curves (a) and (b)) was calculated (using MS Excel 2007) and it was 0.85 and 0.996, respectively, suggesting that the reaction was first order.

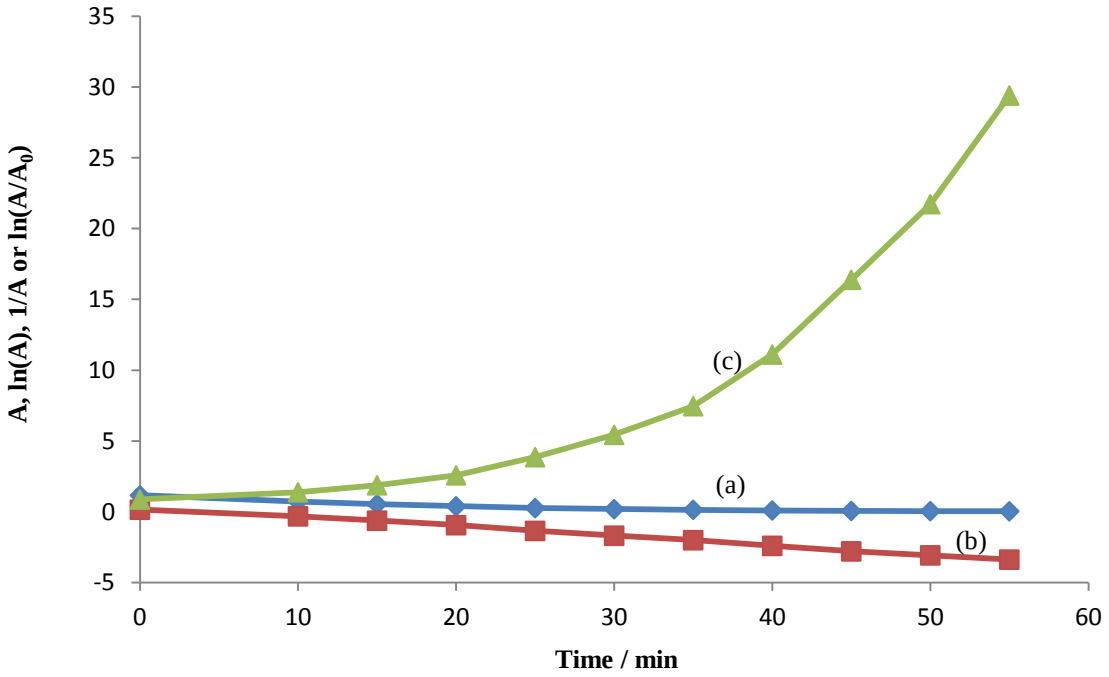

Figure 6. 3. Plots of (a) Absorbance at 625 nm (A), (b) ln(A) and (c) 1/(A) vs. electrolysis time for the data in fig. 6.1.

Figure 6.4 shows a plot of ln(A) vs. electrolysis time taken from the 625 nm and 254 nm bands in the spectra in fig. 6.1. The R^2 of the two lines were 0.99. From the slopes of the two plots, the rate constants for the degradation of the anthraquinone (decolourisation) and benzene rings are 0.064 min^{-1} and 0.053 min^{-1}, respectively, showing that the oxidation of the former moiety is somewhat faster than the later. In the analyses in the sections presented below, R^2 values were employed to decide on the most likely reaction order.

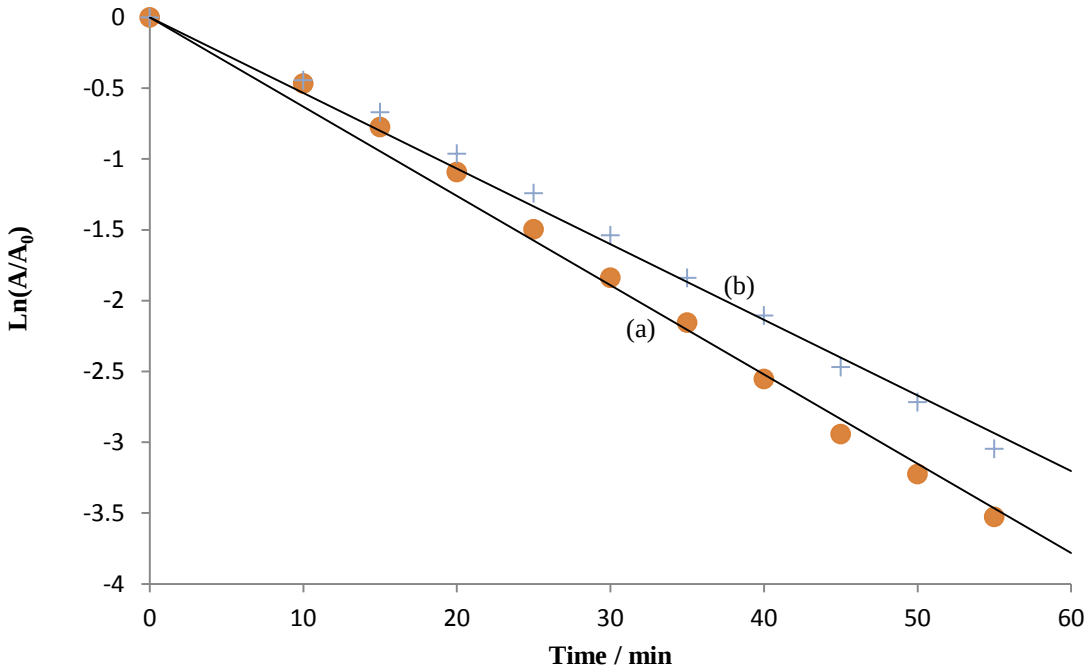

Figure 6. 4. Plots of ln(A) vs. electrolysis time for the (a) 625 nm (anthraquinone) and (b) 254 nm (benzene ring) in the spectra in fig. 6.1.

6.3 The Effect of Current Density

The performance of an electrochemical system can be affected by many parameters, one of the most important of which is current density[112, 124]. The effect of current density on the decolourisation of 100 mg dm^{-3} of RB50 was investigated over the range 10 mA cm^{-2} – 100 mA cm^{-2}, and plots of the variation in $(A/A_0)_{625}$ for the absorption at 625 nm are plotted as a function of electrolysis time for a range of current densities in fig. 6.5. It is clear from the figure that faster reduction of $(A/A_0)_{625}$ can be seen with increasing current density, probably due simply to the fact that more oxidising species (such as OH radicals) are produced at higher currents[115-117, 124]. At current densities more than 50 mA cm^{-2}, $(A/A_0)_{625}$ reached zero within 10 min. However, zero $(A/A_0)_{625}$ was achieved at all current densities after 60 minutes electrolysis. As may be seen from the figure, increasing the current density to 50 mA cm^{-2} resulted in a faster decrease in $(A/A_0)_{625}$; above this value, no further significant decrease in $(A/A_0)_{625}$ was observed.

In broad terms, the data in fig. 6.5 are in agreement with the work of Kariyajjanavar et al.[124], Montanaro and Petrucci[116], Yavuz et al.[112] and Tsantaki et al.[126]. Kariyajjanavar et al.[124] studied the electrochemical oxidation of 50 mg dm^{-3} of two reactive dyes, Novacron Deep Red & Novacron Orange, in 7 g dm^{-3} aqueous NaCl at pH = 3 in stirred, undivided cells containing graphite anode and cathode at current densities of 85 – 425 A m^{-2}.

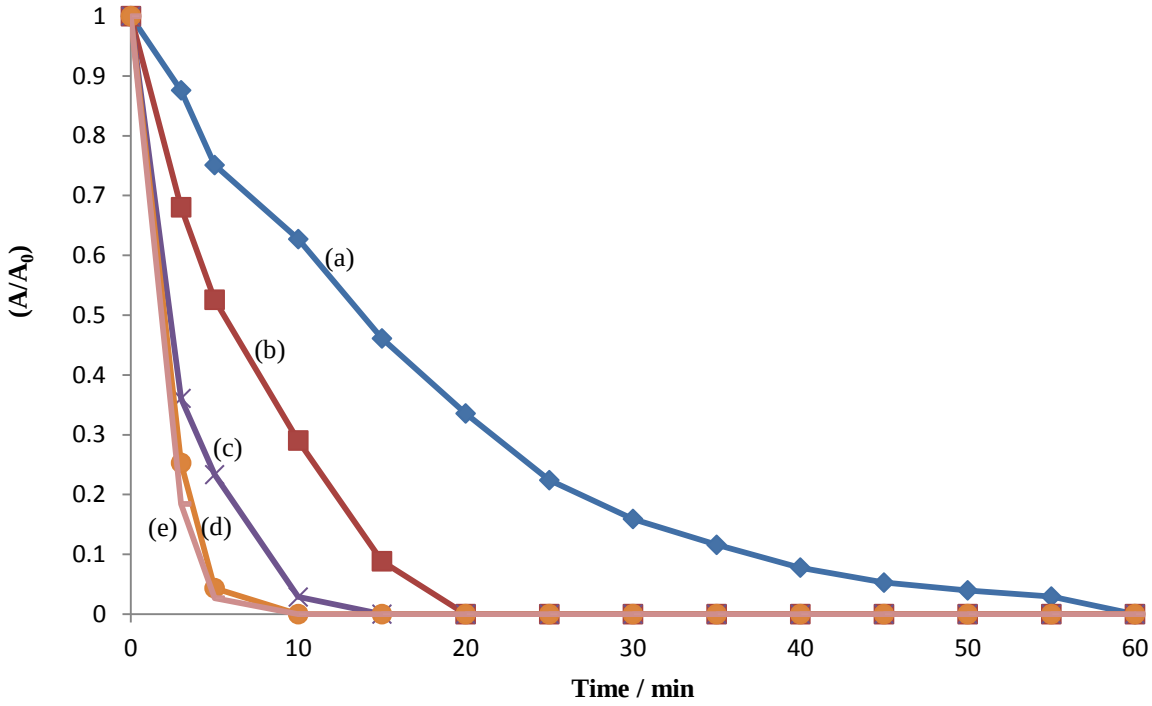

Figure 6. 5. Plots of $(A/A_0)_{625}$ for the 625 nm (anthraquinone) band of 100 mg dm^{-3} of RB50 vs. electrolysis time at: (a) 10 mA cm^{-2}, (b) 25 mA cm^{-2}, (c) 50 mA cm^{-2}, (d) 75 mA cm^{-2} and (e)100 mA cm^{-2}. The electrolyte was 3 g dm^{-3} of Na_2CO_3, and the experiment was carried out at room temperature using a 0.64 cm^2 NATO12J NATO anode and a 0.64 cm^2 Ti/Pt cathode in the cuvette cell, at room temperature.

Montanaro and Petrucci[116] investigated the electrolysis of 50 mg dm^{-3} of anthraquinone dye (Reactive Blue 19), in 0.05 M $NaSO_4$ together with 0.01 M NaCl at pH = 5.8 in a stirred, undivided cell containing platinum (Pt) cathode and boron doped diamond (BDD) anode, at current densities of 200 – 400 A m^{-2}. Yavuz et al.[112] electrolysed 20 mg dm^{-3} of Basic Blue 3, in 0.01 M Na_2SO_4 in a bipolar reactor with a BDD anode at 0.5 – 0.825 mA cm^{-2} . Finally, Tsantaki et al.[126] electrolysed a mixture of 17 dyes of total concentration of 361 mg dm^{-3}, in 0.5 M $HClO_4$ in a divided batch reactor using a BDD anode and a zirconium cathode enclosed in a porous porcelain pot, at current densities of 4 – 50 mA cm^{-2}. In all these experiments, operating at current densities above a limiting value gave negligible improvement in terms of both decolourisation and COD removal, and this was attributed to the fact that at higher current densities, side reactions (such as oxygen evolution) are taking place in parallel with the oxidation of the organic[112, 116, 119, 124, 126].

Figure 6.6 shows analogous plots to those in fig. 6.5 except for the 254 nm benzene band, taken from the same experiments. Absorbances at 625 nm and 254 nm taken from figs. 6.5 and 6.6 were used to calculate the rate constants as described in section 6.2.2., the

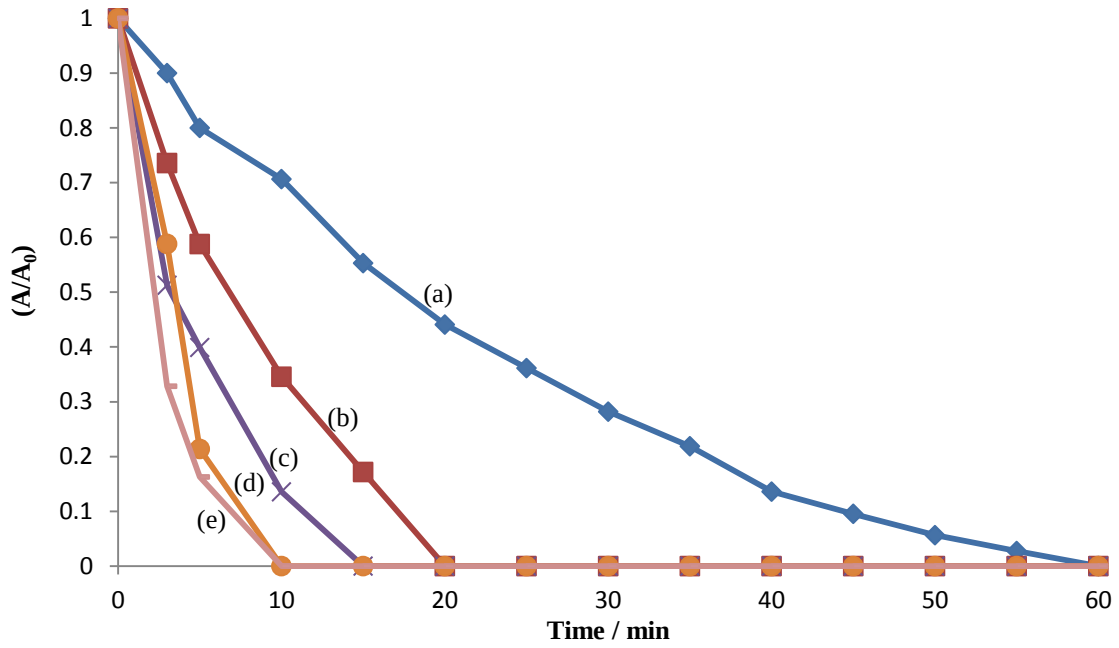

Figure 6. 6. Plots of (A/A_0) for the 254 nm (benzene ring) band of of RB50 (100 mg dm^{-3}) vs. electrolysis time at: (a) 10 mA cm^{-2}, (b) 25 mA cm^{-2}, (c) 50 mA cm^{-2}, (d) 75 mA cm^{-2} and (e)100 mA cm^{-2}. The data were collected as described in fig. 6.5.

decolourisation and benzene ring destruction kinetics were found to be first order. The rate constants for decolourisation (k_a) and benzene ring destruction (k_b) are presented in table 6.1. It may be seen from the table that colour removal is slightly faster than the destruction of benzene ring at all current densities studied.

Current density / mA cm^{-2}		**10**	**25**	**50**	**75**	**100**
Charge required for 100 % colour removal / C		23.0	28.8	28.8	28.8	38.4
Benzene ring Removal, (λ=254nm)	k_b / min^{-1}	0.05	0.11	0.20	0.25	0.37
	R^2	0.99	0.99	0.99	0.9	0.99
Anthraquinone Removal, (λ=625nm)	k_a / min^{-1}	0.06	0.15	0.34	0.55	0.68
	R^2	0.99	0.97	0.99	0.95	0.97
Cell Voltage / V		3.6	4.7	7.1	9	10

Table 6. 1. Summary of the rate constants for colour and benzene ring removal, the passed electrical charge at 100% decolourisation and the cell voltage after 60 min electrolysis vs. current density for the experiments depicted in fig. 6.5.

Table 6.1 also shows the electrical charge required for 100% colour removal at the various current densities. It may be seen that the same electrical charge was required to decolourise the dye solutions completely at current densities between 25 mA cm^{-2} and 75 mA cm^{-2}, with 33% more charge required for 100 mA cm^{-2}. Furthermore, only 5 C less charge was required for complete colour removal at 10 mA cm^{-2}. This is in general agreement with Fernandez et al.[182] who studied the electrochemical oxidation of 20 mg dm^{-3} of Acid

Organic 7 in 0.035 M Na_2SO_4 aqueous solution in a three-electrode cell with a BDD anode and copper cathode at current densities of 1.25 – 5 mA cm^{-2}. The authors found that more electrical charge was required to achieve the same colour removal using higher current densities. They interpreted this observation in terms of mass transport control (where the diffusion of the dye molecules to the electrode/electrolyte interface is the limiting step). This is in contrast to the work of Petrucci and Montanaro[117] who studied the electrochemical oxidation of 50 mg dm^{-3} of Reactive Blue 19 in a complex electrolyte comprising various sodium salts, at pH = 11.5 in an undivided cell using a Pt cathode and a BDD anode. They found that decolourisation took place under kinetic control and the current densities of 25 – 75 mA cm^{-2} requiring the same charge (Q) and the same energy consumption. The latter assertion cannot be correct as the charge may be the same (depending on current and time), but the energy consumption depends on the charge and cell voltage (Q × V), hence, if the energy consumption is constant the product (Q × V) must be constant, and it is unlikely that V remained the same when current density was increased.

The cell voltages observed during the experiments depicted in fig. 6.5 are also shown in table 6.1. As expected, the cell voltages increased with current density.

As was stated above, 50 mA cm^{-2} was sufficient to effect complete decolourisation within only 15 min, hence this current density was employed in the remaining experiments.

6.4 The Effect of Electrolyte

Electrochemical processes are well known to be affected by the electrolyte used; eg adding salt to the solution increases the conductivity, and hence increases the current density at constant cell voltage[111, 112, 119, 183], so decreasing the power wasted due to heat production[126]. In the work reported in this section, as discussed in section 2.15.2, 3 g dm^{-3} of Na_2CO_3, NaCl, $NaHCO_3$, Na_2SO_4 or $NaClO_4$ (separately) was added as electrolytes to 100 mg dm^{-3} RB50 solution. As an example, the effect of the various electrolytes on the decolourisation of RB50 after 5 min electrolysis in the cuvette cell at 50 mA cm^{-2} is presented in table 6.2. However, in all cases, 15 min electrolysis were sufficient to reduce $(A/A_0)_{625}$ to zero, see fig. 6.7. It is clear from fig. 6.7 that $(A/A_0)_{625}$ was dependent on the type of electrolyte used, but $(A/A_0)_{625}$ decreased exponentially irrespective of the nature of the electrolyte. Similar results were obtained for benzene ring removal (see fig. 6.8). The data in the two figures were best described by first order kinetics and the rate constants are presented in table 6.2.

Electrolyte /3 g dm^{-3}	Conc. / M	Ionic strength / M	Cell Voltage / V	Decolourisation after 5 min / %	k_a / min^{-1}	R^2	k_b / min^{-1}	R^2
Na_2SO_4	0.021	0.13	9.3	89.6	0.43	0.98	0.16	0.94
NaCl	0.051	0.1	7.8	100	1.62	1	1.14	1
$NaClO_4$	0.025	0.05	9.8	85.3	0.38	0.99	0.13	0.95
$NaHCO_3$	0.036	0.07	10.8	82.4	0.33	0.99	0.24	0.99
Na_2CO_3	0.028	0.17	6.6	76.7	0.34	0.99	0.20	0.99

Table 6. 2. Summary of the rate constants for colour and benzene ring removal, colour removal (after 5 min electrolysis) and cell voltage (at 60 min electrolysis) vs. the type of the electrolyte for the experiments depicted in fig. 6.7.

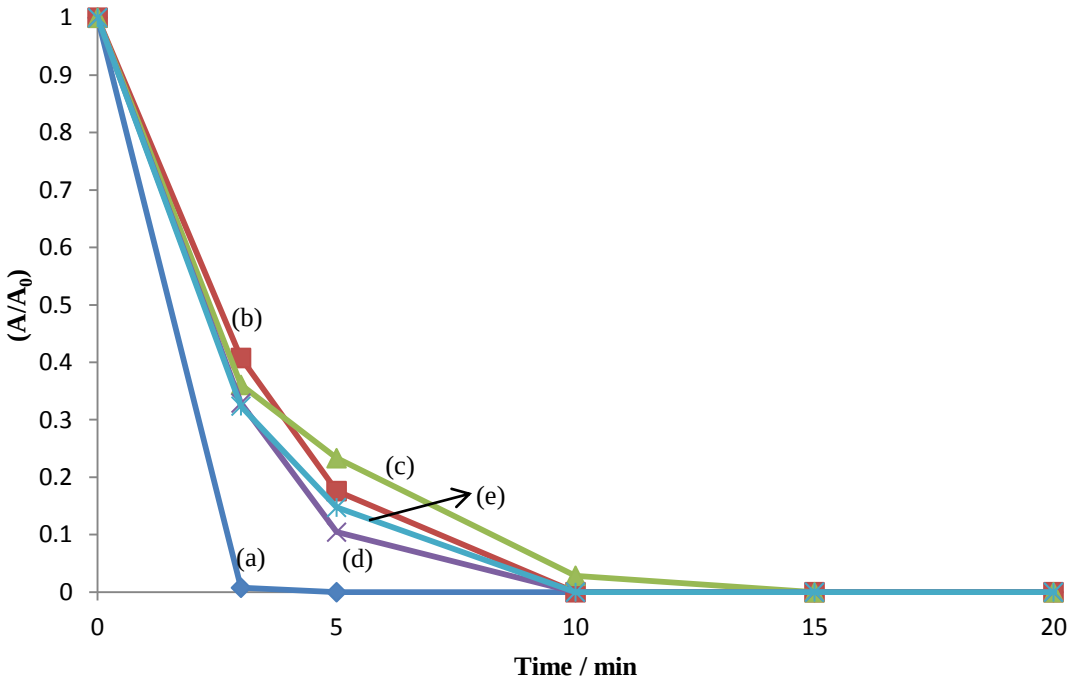

Figure 6. 7. Plots of $(A/A_0)_{625}$ vs. electrolysis time for the anthraquinone band of RB50 (100 mg dm^{-3}) at 50 mA cm^{-2}. The electrolytes were 3 g dm^{-3} of: (a) NaCl, (b) $NaHCO_3$, (c) Na_2CO_3, (d) Na_2SO_4 and (e) $NaClO_4$, the experiments were carried out at room temperature using a 0.64 cm^2 (NATO12J) NATO anode and a 0.64 cm^2 Ti/Pt cathode in the cuvette cell.

It is evident from table 6.2 that NaCl gave the fastest and most complete decolourisation after 5 min electrolysis (k_a = 1.62 min^{-1} and k_b = 1.14 min^{-1}; k_a was ca. 4 times greater than the corresponding values for the other electrolytes). Kariyajjanava et al.[124] have also reported that the addition of NaCl to dye solution resulted in fast decolourisation. Montanaro and Petrucci[116] also found that NaCl is significantly more effective than Na_2SO_4 as electrolyte; reporting only 2 min for complete decolourisation in aqueous NaCl electrolyte compared to 260 min in aqueous Na_2SO_4. Both groups considered the process as indirect electrochemical oxidation by active chlorine species, acting synergically with

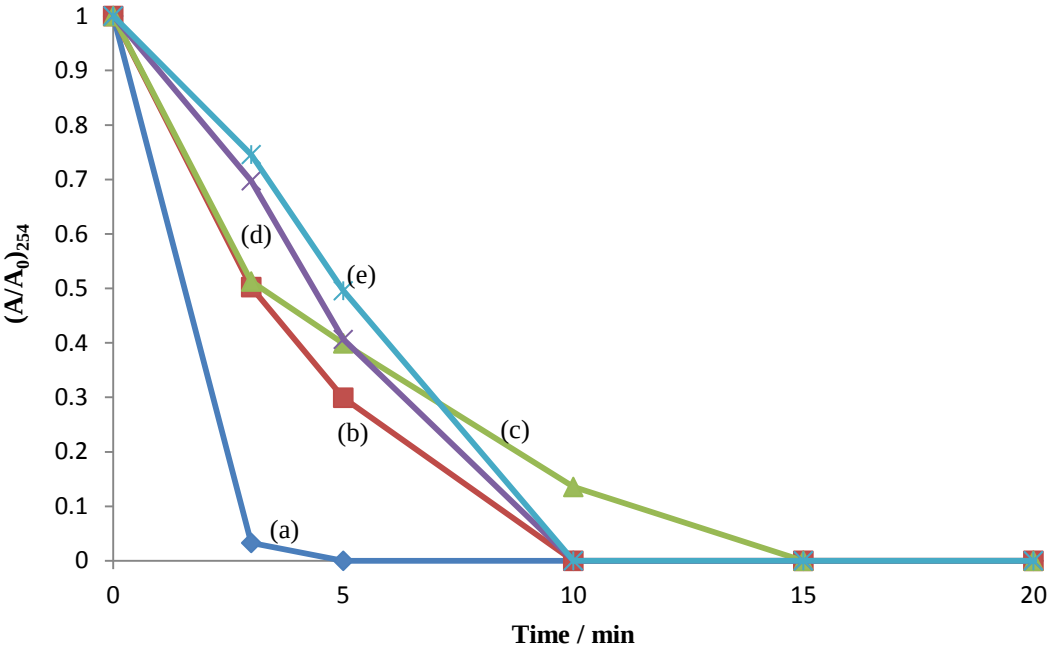

Figure 6. 8. Plots of $(A/A_0)_{254}$ vs. electrolysis time for the benzene ring band of RB50 (100 mg dm^{-3}) at 50 mA cm^{-2}. The electrolytes were 3 g dm^{-3} of: (a) NaCl, (b) $NaHCO_3$, (c) Na_2CO_3, (d) Na_2SO_4 and (e)$NaClO_4$, the experiments were carried out as in fig. 6.7.

the OH radicals produced at the anode surface[116, 124]. Chlorine species have a good selectivity for attacking and cleaving chromophore bonds, hence enhancing the rates of decolourisation[116].

It is well known that the oxidation of chloride ions in aqueous solution results in the formation of Cl_2, OCl^- and HClO, according to[122, 124, 184]:

$$2Cl^- \longrightarrow Cl_2 + 2e^- \qquad (6.14)$$

$$Cl_2 + 2H_2O \rightarrow 2HClO + 2H^+ + 2e^- \qquad (6.15)$$

$$HClO \rightarrow OCl^- + H^+ \qquad (6.16)$$

$$R + OCl^- \text{ or } Cl_2 \rightarrow PCl \qquad (6.17)$$

Where R is the organic dye molecule and P are decolourisation products.

Thus, the increased dye degradation in Cl^- – containing electrolyte may be attributed to the formation of active chlorine species. These species are known to be powerful oxidising agents that react with dye molecules in the bulk solution[122, 124]. However, their presence in the solution depends on the pH (in acidic media, Cl_2 is dominant, in neutral medium HClO

is dominant and in alkaline media OCl^- predominates)[117, 185].

The problem with the application of chloride – containing electrolyte is the generation of unwanted (typically chlorinated) side products[182, 186]. This may be seen in fig. 6.9 which shows plots of UV – Vis spectra of 100 mg dm^{-3} RB50 dye solution in 3 g dm^{-3} aqueous NaCl: (a) before electrolysis, (b) after 5 min electrolysis, and then every 5 min up to (c) 60 min. It may be seen from the figure that the intensity of the 292 nm band increased with electrolysis time reaching a steady state. The appearance of a band at 292 nm has been reported in the literature[182, 186] and attributed either to the formation of OCl^- [182] or to the formation of chloro-organic compounds[186], all of which exhibit a UV peak at this wavelength.

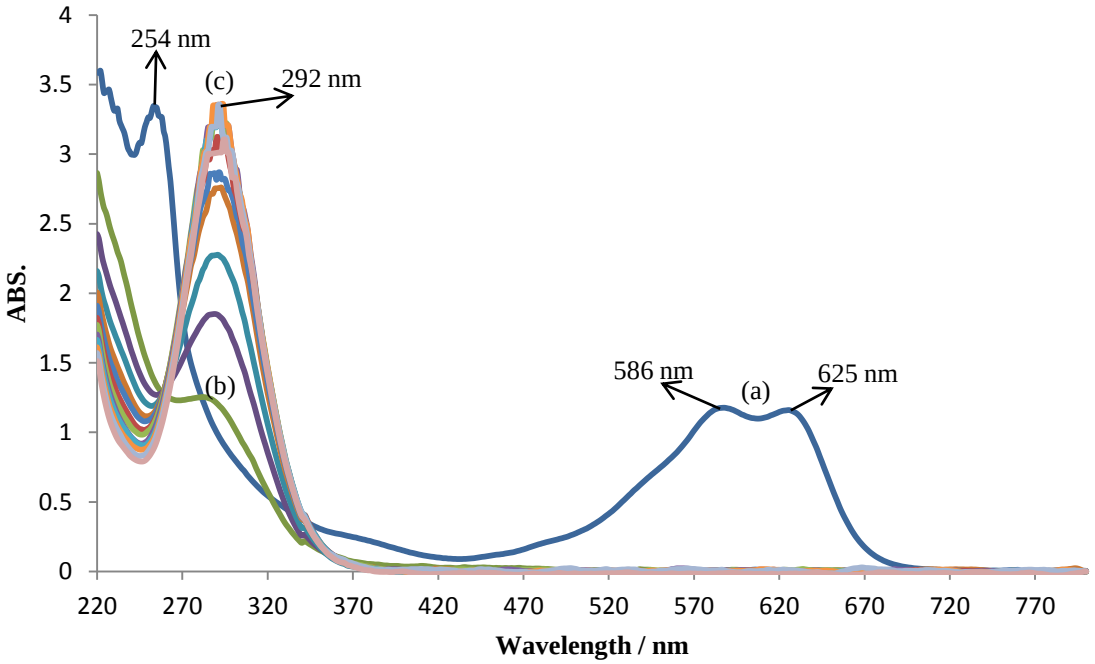

Figure 6. 9. UV – Vis spectra collected during the electrolysis of RB50 dye (100 mg dm^{-3}) in 3 g dm^{-3} aqueous NaCl solution in the cuvette cell at 50 mA cm^{-2}, the NATO anode (NATO12J) was 0.64 cm^2 and the cathode was 0.64 cm^2 Ti/Pt mesh, at room temperature, the spectra collected (a) at the start of the electrolysis (t = 0), (b) after 5 min and then every 5 min up to (c) 60 min.

Fernandes et al.[182] studied the electrolysis of KCl dissolved in deionised water, and reported that OCl^- exhibited a UV band at 292 nm. The authors reported that the Cl^- was oxidised during the electrolysis forming OCl^-. To investigate this possibility, electrolysis (under the same conditions but without dye) of a solution containing 3 g dm^{-3} of NaCl dissolved in Millipore water was performed at 50 mA cm^{-2} and monitored using UV – Vis spectra, and the results are shown in fig. 6.10. The electrolysis was carried out in the

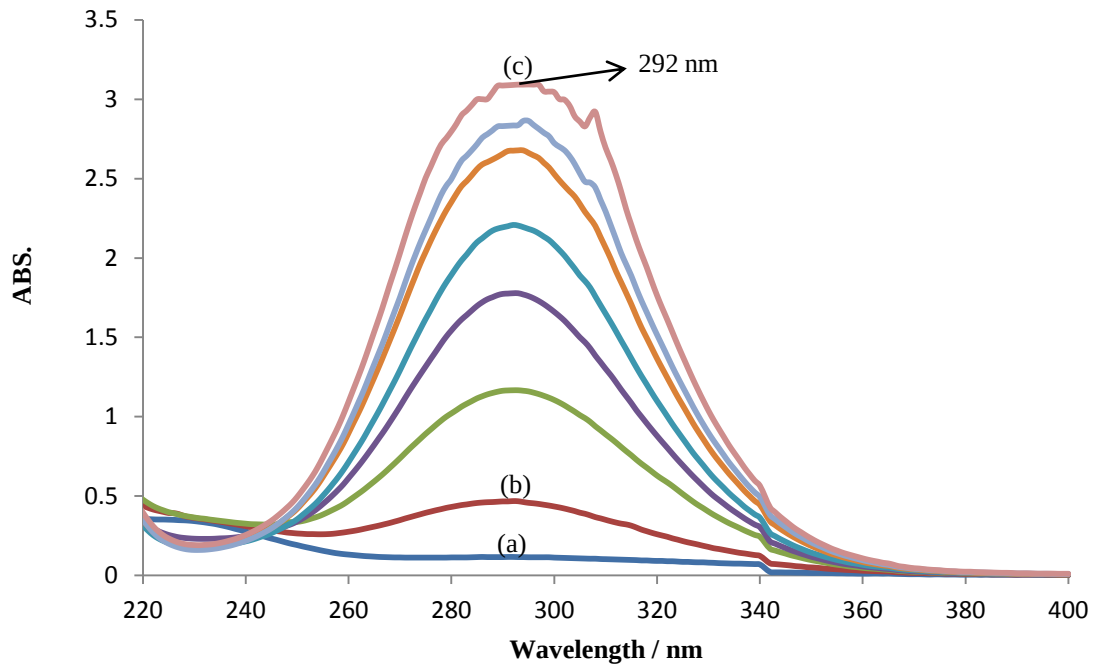

Figure 6. 10. UV – Vis spectra collected during the electrolysis of 3 g dm^{-3} aqueous NaCl solution in the cuvette cell at 50 mA cm^{-2}, the NATO anode (NATO12J) was 0.64 cm^2 and the cathode was 0.64 cm^2 Ti/Pt mesh, at room temperature, the spectra collected (a) at 1 min, (b) after 2 min and then every 1 min up to (c) 8 min.

cuvette cell. As may be seen from the figure, the intensity of the 292 nm band increased with electrolysis time and reached saturation after 8 min electrolysis.

Figure 6.11 shows UV – Vis spectra collected before and after the electrolysis of 100 mg dm^{-3} of RB50 dye solution: (a) before electrolysis commenced, and after 1hour of electrolysis in aqueous: (b) Na_2CO_3, (c) NaCl, (d) $NaHCO_3$, (e) Na_2SO_4 and (f) $NaClO_4$, as electrolytes. As may be seen from the spectrum (c), electrolysis of the RB50 in aqueous NaCl produced persistent side products, as evinced by the peak at 292 nm. 60 min electrolysis resulted in almost total removal of the absorbance in the UV region (see fig. 6.11); suggesting the removal of the organics in the dye solution due to the fact that organics with smaller molecular weight show less absorbance in UV region[123].

Figure 6.12 shows plots of the intensity at 292 nm (the data obtained from figs. 6.9 and 6.10) as a function of time. Comparing curve (c) of figs. 6.9 – 6 .11 shows that UV absorption peak at 292 nm in fig. 6.11 may be attributed to OCl^-. In addition, the absorption intensity at 292 nm reached saturation within only 8 min compared to about 40 min in the presence of the dye; which indicates that the oxidation of chloride during the electrolysis of the dye solution resulted in the formation of the OCl^-, some of this attacked the organics in the solution and some other remained free in the solution. The

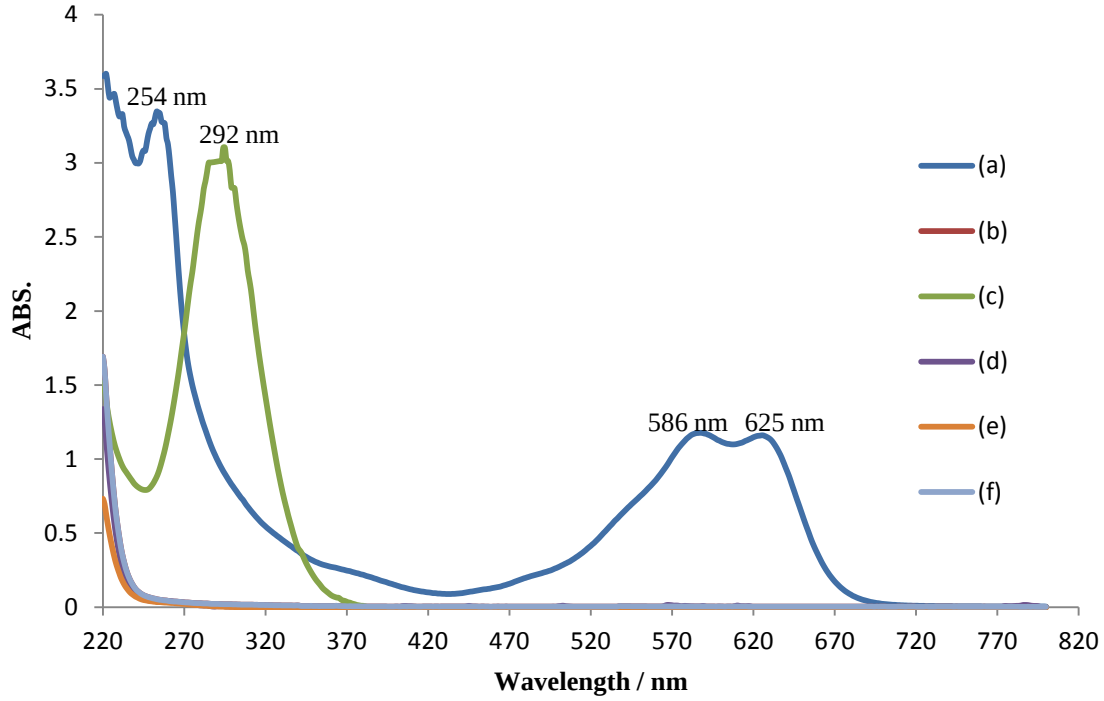

Figure 6. 11. UV – Vis spectra collected at: (a) before electrolysis of RB50 dye (100 mg dm^{-3}) and after 60 min electrolysis using 3 g dm^{-3} of aqueous (b) Na_2CO_3, (c) NaCl, (d) $NaHCO_3$, (e) Na_2SO_4 and (f) $NaClO_4$, in the cuvette cell at 50 mA cm^{-2}, the NATO anode (NATO12J) was 0.64 cm^2 and the cathode was 0.64 cm^2Ti/Pt mesh, at room temperature.

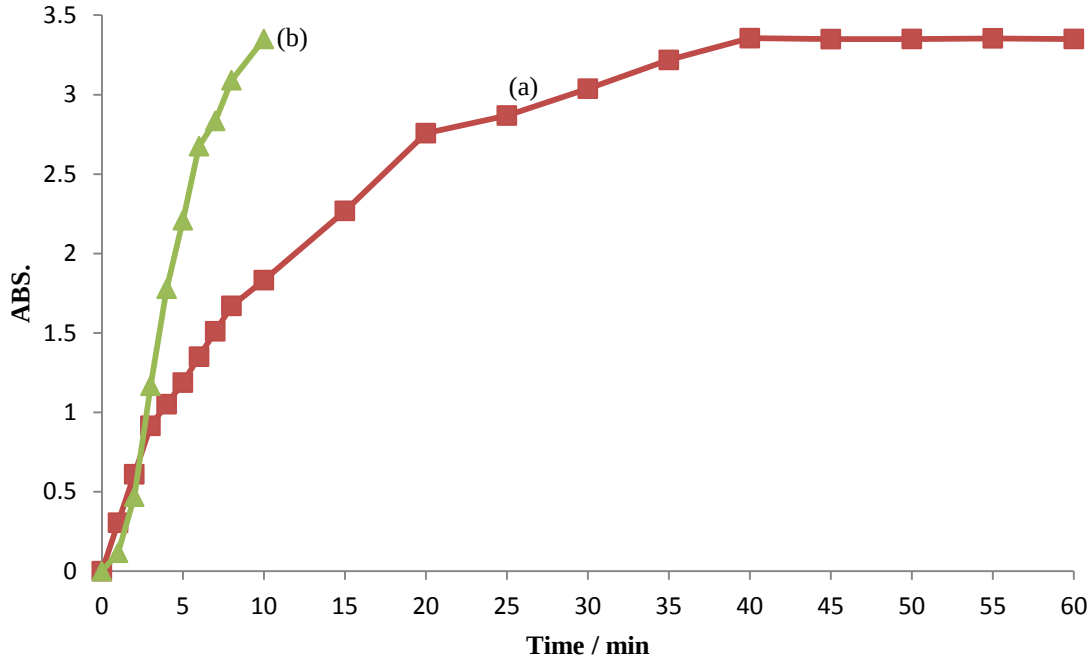

Figure 6. 12. Plots of the peak at 292 nm vs. time observed during the electrolysis of 3 g dm^{-3} of aqueous solution of NaCl: (a) with 100 mg dm^{-3}RB50 and (b) without the RB50, at 50 mA cm^{-2} in the cuvette cell. The anode was 0.64 cm^2 NATO (NATO12J), the cathodes was 0.64 cm^2 Ti/Pt, at room temperature.

concentration of the free OCl^- increased with the increasing electrolysis time of the dye solution due to the reduction in the concentration of the organics.

As the aim of this study was to investigate the efficiency of the NATO anodes with respect to the decolourisation of dyes, and due to the fact that the presence of chloride resulted in the generation of new oxidants (Cl_2, HClO and OCl^-), NaCl was not employed as an electrolyte any further.

Table 6.2 shows that electrolysis in aqueous $NaHCO_3$ and $NaClO_4$ resulted in high cell voltages compared to the other electrolytes studied; the cell voltages were 10.82 V and 9.83 V in $NaHCO_3$ and $NaClO_4$, respectively. This can be attributed to the fact that the lower ionic strength increased the solution resistance (see table 6.2). In contrast, electrolysis in Na_2SO_4 and Na_2CO_3 solutions was found to result in comparable cell voltages during the same electrolysis time for complete colour removal, and this may be due to the higher ionic strength (see table 6.2). The UV – Vis spectra of the dye solutions containing Na_2SO_4 or Na_2CO_3 as electrolytes showed almost no absorbance in both the visible and UV regions after 60 min of electrolysis (see fig. 6.11), indicating almost total organic removal as well as complete decolourisation, hence further investigation of Na_2CO_3 and Na_2SO_4 as electrolytes was carried out.

Solutions consisting of 3 cm^3 of 100 g dm^{-3} of RB50 dye in 1 g dm^{-3}, 3 g dm^{-3}, 5 g dm^{-3} and 7.5 g dm^{-3} Na_2SO_4 or Na_2CO_3 (separately) were electrolysed at 50 mA cm^{-2}. The decrease in $(A/A_0)_{625}$ and $(A/A_0)_{254}$ in all experiments followed first order kinetics, and the rate constants so obtained are shown in table 6.3 and fig. 6.13. Shown in the figure the rate constants variations vs. electrolyte concentration, where data from the table used to plot the figure.

As stated above, loss of the absorbance at 625 nm and 254 nm took place simultaneously at

Conc. g dm^{-3}	**Na_2CO_3**					**Na_2SO_4**				
	k_a	R^2	k_b	R^2	Cell Voltage/V	k_a	R^2	k_b	R^2	Cell Voltage/V
1	0.21	0.99	0.14	0.99	13.7	0.36	0.99	0.11	0.91	16.0
3	0.34	0.99	0.20	0.99	6.6	0.43	0.98	0.16	0.94	9.3
5	0.17	0.99	0.16	0.98	6.7	0.72	0.97	0.32	1	7.5
7.5	0.26	0.95	0.15	0.99	6.4	0.52	0.92	0.33	0.98	6.8

Table 6. 3. Summary of the rate constants for colour and benzene ring removal, and cell voltage vs. the concentration of the electrolyte for the experiments depicted in fig. 6.13.

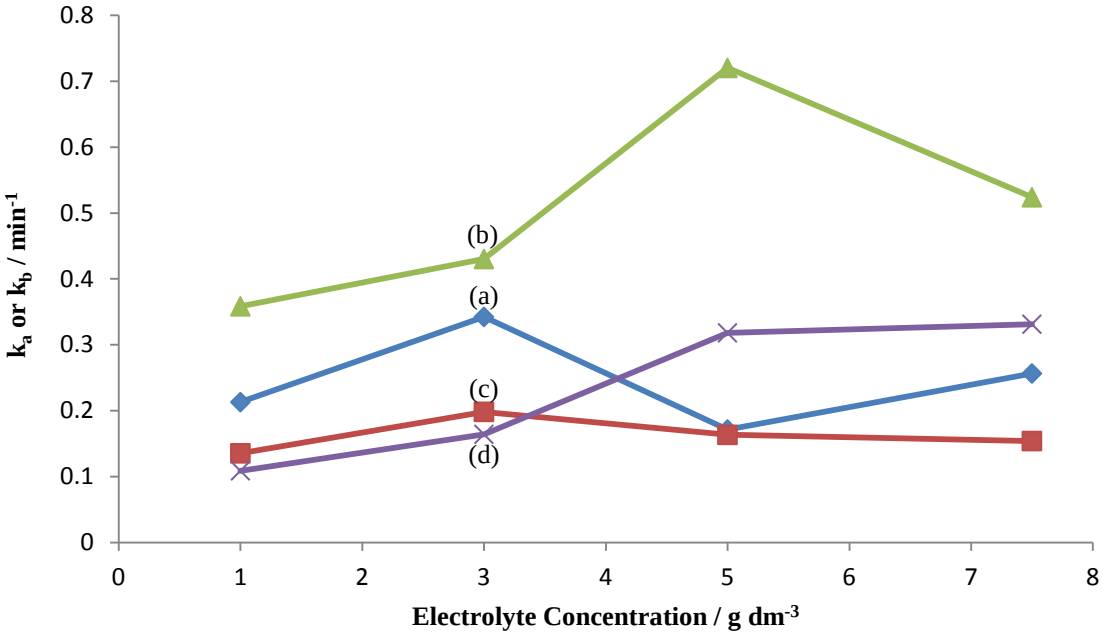

Figure 6. 13: Plots of the rate constants for: (a)&(b) anthraquinone removal and (c)&(d) benzene ring removal vs. electrolyte concentration. The electrolytes used were: (a)&(c) Na_2CO_3 and (b)&(d) Na_2SO_4, when decolourising 3 cm^3 of 100 mg dm^{-3} of RB50 dye at 50 mA cm^{-2} at room temperature in the cuvette, the anode was 0.64 cm^2 NATO12J anode, 0.64 cm^2 Pt/Ti cathode.

all concentrations. In the case of Na_2SO_4, electrolysis for only 10 min was enough to obtain zero $(A/A_0)_{625}$ & $(A/A_0)_{254}$, and the efficiency of the removal increased with increasing electrolyte concentration. In contrast, electrolysis for 20 min and 15 min was required for complete removal using Na_2CO_3 at concentrations of 1 g dm^{-3} & 7.5 g dm^{-3} and 3 g dm^{-3} & 5 g dm^{-3}, respectively.

It may be seen from the figure and the table that the decrease in $(A/A_0)_{625}$ using Na_2SO_4 was faster than that observed in Na_2CO_3, although the ionic strength of the latter solution was higher. This may be interpreted in terms of the fact that carbonate is a radical scavenger[117], (see the discussion below). The $(A/A_0)_{625}$ decay rate constant increased with increasing electrolyte (Na_2SO_4) concentration up to 5 g dm^{-3} after which it decreased, possible due to the fact, at higher sulphate concentrations, sulphate reaction with OH radicals generates peroxodisulphate (see discussion below). Similar behaviour was reported by Martinez – Huitle et al.[147] who studied the influence of Na_2SO_4 concentration on the degradation of actual textile effluent as a function of time at BDD anodes. They found that the degradation was poor at low electrolyte concentrations, but the removal rate increased when the concentration was increased up to 5 g dm^{-3}, after which little or no improvement was observed. However, the authors did not attempt to interpret this

behaviour. In addition, Fernandez et al.[182] found that Na_2SO_4 concentrations higher than 0.02 M (2.84 g dm^{-3}) had no effect on the decolourisation of Acid Orange 7 dye at BDD anodes at 5 mA cm^{-2}. In contrast to the behaviour observed in the case of Na_2SO_4, the rate constants for the decrease in $(A/A_0)_{625}$ in Na_2CO_3 increased to a maximum at 3 g dm^{-3} before decreasing. This is in general agreement with Petrucci and Montanaro[117] who studied the effects of different concentrations of carbonate on the colour removal of Reactive Blue 19 solutions at a BDD anode in 0.05 M NaCl, 0.023 M Na_2SO_4 and NaOH (to adjust the solution pH at 11). The authors found that the higher the carbonate concentration, the slower the colour removal; the authors interpreted their data in terms of a model in which the carbonate reacted with the active chlorine species, so removing them as primary oxidants. They claimed that the carbonate has a doubly negative effect: (i) involvement in competitive reactions with OH radicals, considered to be an important source of converting the chloride to active chlorine species (in addition to the direct reaction of the chloride on the anode surface), and (ii) increasing the pH; this results in the formation of OCl^- which is known to be the weakest oxidant of the active chlorine species[117].

For the decrease of $(A/A_0)_{254}$, the rate constants remained essentially constant with increasing electrolyte (Na_2CO_3) concentration, and increased with increasing the electrolyte (Na_2SO_4) concentration (see table 6.3 and fig. 6.13).

As can be seen from fig. 6.13 and table 6.3, electrolysis at concentrations of Na_2CO_3 > 3 g dm^{-3} gave less rapid decrease of $(A/A_0)_{625}$ and $(A/A_0)_{254}$ in all cases. This may be attributed to the fact that OH radicals react with carbonate to form reactive species whose oxidising power is less than that of OH radicals (for example the carbonate radical)[117,175, 180], so the carbonate ions act as a sink for OH radicals[180]:

$$OH^{\cdot} + CO_3^{2-} \rightarrow CO_3^{\cdot -} + OH^- \qquad (6.18)$$

Hence, it would be expected that the concentration of carbonate ions would be important, as increasing the concentration will clearly decrease the organic destruction efficiency due to the suppression of the oxidation process[117].

At an electrolyte concentration of 3 g dm^{-3}, the performance (in terms of the decrease of $(A/A_0)_{625}$) in both electrolytes (Na_2SO_4 and Na_2CO_3) was approximately similar; with Na_2SO_4 showing 3% higher decolourisation (after 10 min of electrolysis) as compared to

Na_2CO_3. At concentrations of Na_2CO_3 higher than 3 g dm^{-3}, the decolourisation time increased and rate constants decreased compared to those at 3 g dm^{-3}. This may be due to the scavenging effects of carbonate. In agreement with a behaviour reported by Petrucci and Montanaro[117].

At 5 and 7.5 g dm^{-3} Na_2SO_4, the decrease of $(A/A_0)_{625}$ was faster when compared to that of 3 g dm^{-3} Na_2SO_4. The higher rate of decrease of $(A/A_0)_{625}$ when using higher Na_2SO_4 concentrations could be due to the fact that more SO_4^{2-} is available for the electrochemical generation of the peroxodisulphate ($S_2O_8^{2-}$)[116, 119, 186]:

$$2SO_4^{2-} \rightarrow S_2O_8^{2-} + 2e^- \quad (6.19)[115, 187\text{-}189]$$

$$SO_4^{2-} + OH^{\cdot} \rightarrow SO_4^{-\cdot} + H_3O^+ \quad (6.20)[187]$$

$$SO_4^{-\cdot} + SO_4^{-\cdot} \rightarrow S_2O_8^{2-} \quad (6.21)[187]$$

that is well known to be an efficient oxidant (of standard oxidation potential of 2.01 V vs. NHE), its oxidising effects can be added to the effects of the other oxidising radicals (OH radicals)[190], a finding reported by Kariyajjanava et al.[124].

To investigate the possibility of the generation of peroxodisulphate ($S_2O_8^{2-}$), 3 g dm^{-3} of Na_2SO_4 and was electrolysed (under the same conditions but without RB50 dye) and UV – Vis spectra collected during the electrolysis; are shown in fig. 6.14. The generation of ozone was limited (the smell of ozone could be detected during electrolysis) as the ozone absorbance in solution at 258 nm was very small. To interpret the spectra in fig. 6.14, there may be two possibilities: peroxodisulphate or hydrogen peroxide electrogeneration as both show spectra similar to those shown in fig. 6.14. The electrogeneration of peroxodisulphate was discussed above. In terms of hydrogen peroxide, it can be generated as a result of ozone decomposition in neutral and alkaline media.

As long as the ozone is being generated (ozone smell could be detected), and due to the fact OH^- is known to be an initiator of the ozone decomposition chain reaction (see scheme 5.1)[175] as ozone does not react with carbonate or bicarbonate, hydrogen peroxide can be generated as follows[191]:

$$O_3 + OH^- \rightarrow HO_2^- + O_2 \quad (6.22)$$

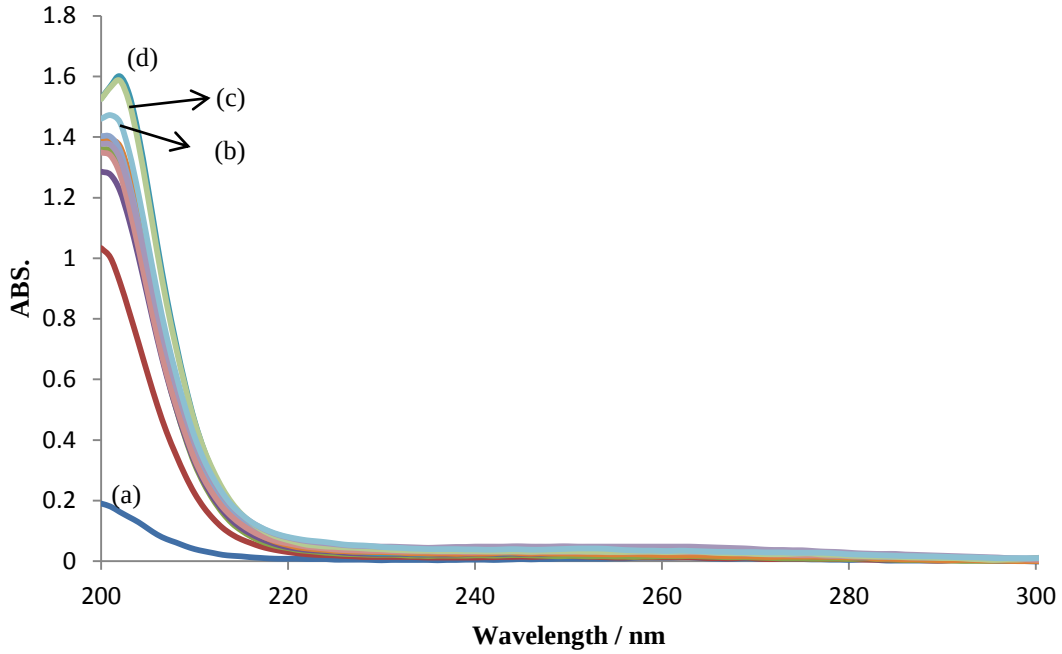

Figure 6. 14. UV spectra taken during the electrolysis of 3 g dm^{-3} aqueous Na_2SO_4 solution in the cuvette cell at 50 mA cm^{-2}, 0.64 cm^2 NATO12J anode and the cathode was 0.64 cm^{2}Ti/Pt mesh, at room temperature, the spectra collected at (a) 1 min and then every 1 min up to (b) 10 min, (c) 15 min and (d) 20 min, at room temperature.

$$HO_2^- + H^+ \leftrightarrow H_2O_2 \qquad (6.23)$$

or OH radicals can combine to form H_2O_2 as follows[191]:

$$2OH^{\cdot} \rightarrow H_2O_2 \qquad (6.24)$$

In addition, reaction between OH radicals and H_2O_2 is also possible[192]:

$$OH^{\cdot} + H_2O_2 \rightarrow H_2O + HO_2^{\cdot} \qquad (6.25)$$

It may be seen from equation (6.23) that H_2O_2 generation via ozone decomposition is not the primary product [191]. In addition, ozone is being generated from the OH radicals [64], therefore, it does not seem reasonable to postulate a mechanism in which ozone is generated from OH radicals and then ozone reacts with OH ions to decompose again to generate OH radicals that then combine to form H_2O_2. Furthermore, the presence of H_2O_2 in ozone – containing solution is well known to enhance ozone decomposition to OH radicals[191]. Hence, it seems unlikely that the UV absorbance in fig. 6.14 is due to the presence of H_2O_2. Therefore, and due to the lack of more special analysis details, it does not seem unreasonable to postulate that the presence of sulphate resulted in generating other oxidants, at least ozone and possibly peroxodisulphate and hydrogen peroxide, and

according to this fact, the use of sulphate was stopped.

As was carried out with sulphate, to investigate the possibility of the carbonate oxidation at NATO anodes, 3 g dm^{-3} of Na_2CO_3 was electrolysed (under the same conditions but without RB50) and the UV – Vis spectra during the electrolysis were collected and are shown in fig. 6.15. It is clear from the figure that there are little or no electrolysis products that show absorbance that may be due to the fact that the ozone that either was not allowed to form (carbonate ions reacted with OH radicals and stopped it from forming ozone) or it decomposed once it was generated (alkaline medium).

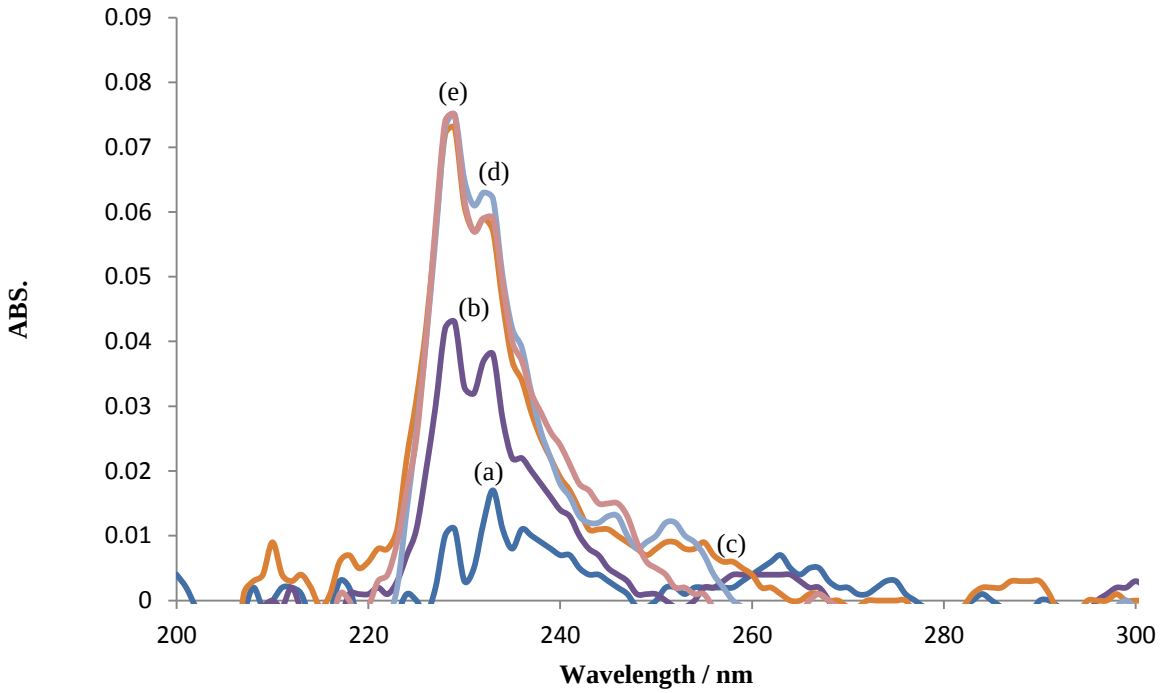

Figure 6. 15. UV spectra taken during the electrolysis of 3 g dm^{-3} aqueous Na_2CO_3 solution in the cuvette cell at 50 mA cm^{-2}, 0.64 cm^2 NATO12J anode and the cathode was 0.64 cm^2 Ti/Pt mesh, at room temperature, the spectra collected at (a) 1 min, (b) 5 min, (c) 10 min (d) 15 min and (e) 20 min, at room temperature.

Closer inspection of figs. 6.12, 6.14 and 6.15 shows clearly the fact that using any electrolyte other than carbonate (to a certain extent) results in the generation of other oxidants (Cl_2, OCl^-, HClO, O_3 and possibly $S_2O_8^{2-}$ and H_2O_2) that will work together with the NATO anode in degrading the dye molecules.

It may be seen from table 6.3 that the cell voltage for Na_2SO_4 is higher than that of Na_2CO_3 at all concentrations, especially at lower electrolyte concentrations, and this may simply be attributed to the higher ionic strength (greater electrolyte conductivity and less electrolyte

resistance) of the Na_2CO_3 and/or the fact that a number of SO_4^{-2} are converted to $S_2O_8^{-2}$ that is used in oxidation (the conductivity of the solution thus being reduced) . In addition, the cell voltages at 1g dm^{-3} electrolyte concentration for both Na_2CO_3 and Na_2SO_4 were too high, hence the use of these concentrations were ignored. However, at 3 g dm^{-3}, cell voltage of Na_2CO_3 is lower by almost 3 V as compared to Na_2SO_4 (see table 6.3). In addition, the rate constants (i.e. k_a and k_b) are comparable.

Due to the discussion above, 3 g dm^{-3} Na_2CO_3 was chosen as electrolyte concentration.

6.5 The Effect of pH

All tests with Na_2CO_3 so far were carried out without buffering, and hence the pH was allowed to vary from the starting value of ca. 11.1. Thus, as electrochemical processes are often affected by the solution pH[124], it was decided to investigate the effect of this parameter. Therefore, as was described in section 2.15.3, buffered 100 mg dm^{-3} RB50 solutions were prepared at pH 2, 7 and 11. The effect of pH on the variations of $(A/A_0)_{625}$ and $(A/A_0)_{254}$ are shown in fig. 6.16. As described in section 6.2.2, both decolourisation and benzene ring destruction best described by first order kinetics of which the rate constants so obtained, in addition to the cell voltages observed are presented in table 6.4.

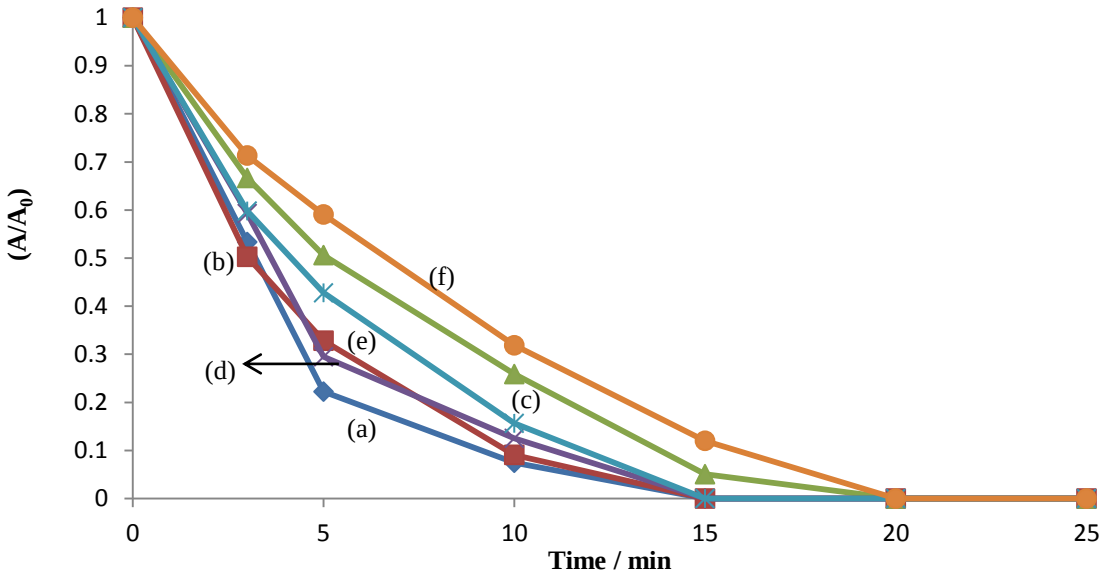

Figure 6. 16. Plots: (a), (b) and (c) of (A/A_0) for the 625 nm (anthraquinone) band and (d), (e) and (f) of (A/A_0) for the 254 nm (benzene ring) band of 100 mg dm^{-3} of RB50 vs. electrolysis time at 50 mA cm^{-2}. The electrolyte was 3 g dm^{-3} of Na_2CO_3, the experiment was carried out at room temperature using 0.64 cm^2 NATO12J anode and 0.64 cm^2 Ti/Pt cathode in the cuvette cell, at buffered pH of: (a)&(d) pH = 2, (b)&(e) pH = 7 and (c)&(f) pH = 11.

pH	Cell Voltage / V	k_a / min^{-1}	R^2	k_b / min^{-1}	R^2
2	6.8	0.26	0.98	0.21	0.98
7	7.0	0.24	0.99	0.18	0.99
11	7.6	0.13	0.97	0.13	0.97
Initial 11.1	6.6	0.34	0.99	0.2	0.99

Table 6. 4. Summary of the colour and benzene ring removal rate constants and cell voltage observed during the experiments in fig. 6.16.

The $(A/A_0)_{625}$ removal at 5 minutes was 80%, 68% and 48% in the pH 2, 7 and 11 buffers, respectively. In addition, it may be seen from fig. 6.16 that the acidic and neutral media favoured faster removal and achieved zero $(A/A_0)_{625}$ and $(A/A_0)_{254}$ within 15 min compared to 20 min for the alkaline electrolyte. Furthermore, the rate constants for both colour and benzene ring removal seem to decrease with increasing pH. The effect of pH may be interpreted as: (i) extensive oxidation and/or chemical modification of the electrode surface leading to a change in the anode surface properties[126] and/or (ii) OH radical scavenging by the buffer chemicals.

With respect to modification of the anode: (i) the anode used in this study was Ti mesh coated with Ni and Sb doped SnO_2, and as mentioned above, the Ni must be on the surface of the anode, (ii) it is well known that Ni is affected by pH (see fig. 4.10), for example, at pH 11 (at the potential applied in this study), Ni is in the form of NiO, whereas Ni is in the form of $Ni(OH)_3$ at pH 7 and 2. As discussed in section 6.2, the oxidation state of the Ni plays an important role in the decolourisation process.

With respect to possible radical scavenging: at pH = 2, KCl and HCl were added to the solution (as described in section 2.15.3), as discussed in section 6.4, the presence of chloride in the solution promotes the generation of active chlorine species (Cl_2, HClO and OCl^-). The dominant species will be Cl_2 (pH 2). The Cl_2 will be generated on the surface of the anode or as result of the reaction between OH radicals and chloride, and it will be involved in the dye oxidation reactions. In pH = 7, NaOH and KH_2PO_4 were added to the solution (as described in section 2.15.3). The dissociated ions may react with OH radicals acting as radical scavenger and reduce the amount available for dye oxidation. In pH = 11, $NaHCO_3$ and NaOH were added to the solution (as described in section 2.15.3). The bicarbonate is a well known scavenger of OH radicals, reacting more slowly with the radicals than that of CO_3^{2-} (1.5×10^7 M^{-1} s^{-1} compared to 4.2×10^8 M^{-1} s^{-1}, respectively)[175, 180]:

$HCO_3^- + OH^{\cdot} \rightarrow CO_3^{\cdot -} + H_2O$ (6.26)

However, when the rate constant of the unbuffered solutions are considered (see table 6.4) it is possible to postulate that the effects of the modification of the anode surface are limited because the pH of the solution without buffering is high due to the presence of carbonate (pH 11.1). In addition, it seems that the optimum conditions are when the solution is not buffered (see table 6.4). On the other hand, the decolourisation of the dye will result in accumulation of aliphatic acids (see discussion above) that will neutralise (and possibly acidify) the solution pH; making the effects of the modification of the anode surface more unpredicted. Therefore it is fair to postulate that OH radical scavenging by buffer chemicals is the likely reason as it is clear that addition of more salts to the solution results in depletion of the oxidising agents (OH radicals) due to the reaction of the anions of those salts with the OH radicals.

The effect of pH is in general agreement with Kariyajjanava et al.[124], Montanaro and Petrucci[116]. In addition, Mukimin et al.[193] studied the electrochemical oxidation of Reactive Blue 19 solution in 4 g dm^{-3} aqueous NaCl in undivided, stirred cell using PbO_2 anode and Ti cathode at cell voltage of 5 V for 60 min as function of initial pH, and Parsa and Abbasi[122] studied the initial pH effects when oxidising 10^{-3} M of Mordant Red 3 in 0.5 g dm^{-3} aqueous NaCl in undivided, stirred cell using Pt as anode and two stainless steel 304 as cathode at 16 V for 120 min). These workers studied the effects of the initial pH on the decolourisation of dyes in Cl^- - containing electrolytes and interpreted their findings in terms of the oxidation potential of the dominant chlorine species, as this depends on the pH with HClO (pH 7, 1.49 V vs. NHE) the most powerful oxidant, then Cl_2 (acid solution, 1 V vs. NHE) and OCl^- (alkaline solution, 0.94 V vs. NHE). In contrast, Yavuz and Shahbazi[119] studied the effect pH on the decolourisation of 40 mg dm^{-3} Reactive Black 5 in 0.02 M aqueous Na_2SO_4 in bipolar reactor using a BDD anode at a current density of 0.75 mA cm^{-2}. The authors found that initially acidic, neutral and alkaline pH had no significant effect on decolourisation rate. The authors postulated that this was due to the degradation of dye resulting in the neutralisation of the solution pH, whatever the initial value, and Petrucci and Montanaro[117] postulated similar conclusions . On the other hand, Miled et al.[185] who studied the electrochemical decolourisation of 177.5 mg dm^{-3} C.I. Vat Blue 1dye in 0.1 M aqueous NaCl in an undivided, stirred cell using graphite as anode and stainless steel as cathode, found that decolourisation was favoured under highly basic conditions (pH 13).

It may be seen from table 6.4 that the cell voltage of the buffered solutions increased with increasing pH, and the cell voltage using unbuffered solution was the lowest. This change in cell voltage may be due to the change in the anode surface properties as discussed above.

The results (see table 6.4) showed that decolourisation was slower (the exception being for buffered pH 2's electrolyte) and resulted in greater cell voltages, when the buffers were employed than when using the unbuffered solution. Therefore, it was decided to use unbuffered solution (pH 11.1).

6.6 The Effect of Initial Dye Concentration

The electrochemical decolourisation of different concentrations of 3 cm^3 RB50 solutions was investigated at 50 mA cm^{-2} in 3 g dm^{-3} of aqueous Na_2CO_3 in order to determine the effect of dye concentration in terms of decolourisation, benzene ring removal and COD removal. The variation in $(A/A_0)_{625}$ as a function of electrolysis time for different initial dye concentrations is shown in fig. 6.17. It is clear from the figure that complete decolourisation requires 5 min, 15 min, 20 min, 40 min and 45 min for the dye concentrations of 50 mg dm^{-3}, 100 mg dm^{-3}, 200 mg dm^{-3}, 300 mg dm^{-3} and 500 mg dm^{-3}, respectively. As described in section 6.2.2, the decolourisation and the benzene ring destruction were found to be first order and the rate constants are shown in table 6.5. Also shown in the table are the cell voltages and COD removal measured after 60 min electrolysis. Both the colour and benzene ring removal rate constants decreased with increasing dye concentration (see table 6.5). These findings may be interpreted by the fact that the process is kinetically controlled, especially at higher dye concentrations (i.e the electrochemical reaction rate is slower than the dye molecule diffusion rate to the anode/electrolyte interface and/or anode surface). In other words, the applied current density is higher than the limiting one. To determine the limiting current density, Fernandez et al.[182] used this formula ($j_{lim} = (1/8)k_m.F.COD$) where: k_m is the diffusion coefficient (m s^{-1}), and F is Faraday constant.

The effect of the initial dye concentration is in general agreement with the work of Yavuz et al.[112] who studied the electrochemical oxidation of 10 mg dm^{-3}, 20 mg dm^{-3} and 40 mg dm^{-3} Basic Blue 3 solution in aqueous Na_2SO_4 at 0.875 mA cm^{-2}. The authors concluded that the greater the initial dye concentration, the lower the decolourisation efficiency. The same conclusion was reached by the same group in another study[119]. In contrast, Montanaro and Petrucci[116] found that decolourisation of the dye over the concentration

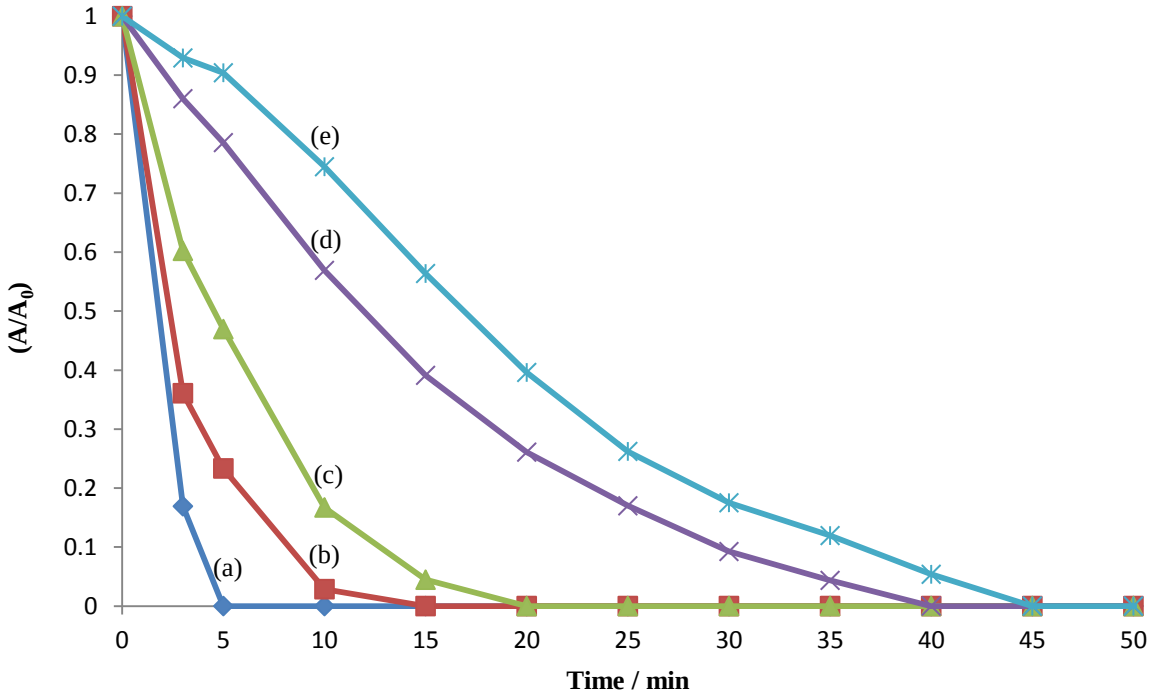

Figure 6. 17. Plots of $(A/A_0)_{625}$ for the 625 nm (anthraquinone) band of RB50 at: (a) 50 mg dm^{-3}, (b) 100 mg dm^{-3}, (c) 200 mg dm^{-3}, (d) 300 mg dm^{-3}, and (e) 500 mg dm^{-3} vs. electrolysis time at 50 mA cm^{-2}. The electrolyte was 3 g dm^{-3} aqueous Na_2CO_3, and the experiment was carried out at room temperature using 0.64 cm^2 NATO12J anode and 0.64 cm^2 Ti/Pt cathode in the cuvette cell.

Dye / mg dm^{-3}	k_a / min^{-1}	R^2	k_b / min^{-1}	R^2	Cell Voltage / V	COD Removal /%
50	0.60	1	0.45	1	6.6	100
100	0.34	0.99	0.2	0.99	6.6	97
200	0.19	0.98	0.10	0.92	6.65	90
300	0.08	0.96	0.07	0.93	6.5	85
500	0.06	0.93	0.06	0.93	6.7	82

Table 6. 5. The colour and benzene ring removal rate constants, cell voltage and COD removal vs. initial dye concentrations for the experiments in fig. 6.17.

range 50 -150 mg dm^{-3} followed zero order kinetics i.e. the decolourisation rate was independent of initial dye concentration.

The cell voltages observed (see table 6.5) in the experiments reported in this section were between 6.5 V – 6.7 V. In other words, the cell voltage was not affected by dye concentration, as expected, suggesting that no anode poisoning took place. To explain this, let us assume a direct electrochemical oxidation process is taking place on the anode surface, this means during the process, the dye should be adsorbed on the anode surface, and the oxidation product will be adsorbed on the anode surface as a consequence. The

latter would be expected to block the active sites of the anode surface causing an increase in cell voltage[194]. Since the NATO anodes have a high oxygen overpotential, any product of the direct electrochemical oxidation of the dye molecules on the anode surface will be oxidized by OH radicals[194] converting the former to CO_2 and H_2O as follows[194]:

$$H_2O \rightarrow OH^{\cdot} + H^{+} + e^{-} \qquad (6.27)$$

$$\text{Dye} \rightarrow \text{Adsorbed Product (AP)} \qquad (6.28)$$

$$AP + OH^{\cdot} \rightarrow CO_2 + H_2O + ze^{-} \qquad (6.29)$$

and keeping the cell voltage almost steady. The fact that the cell voltage was almost steady suggests that indirect electrochemical oxidation process was dominant on the NATO anode surface. In addition, as the current density is constant, the number of oxidants (OH radicals) that will be generated on the anode surface is expected to be the same. This supports the speculation that the dye destruction took place via indirect (mediated) electrochemical oxidation by OH radicals rather than direct electrochemical oxidation[124].

It is clear from table 6.5 that the COD removal after 60 min electrolysis decreased with increasing initial dye concentration, as expected. However, achieving more than 80% of COD removal reflects the high efficiency of the process, and the amount of generated OH radicals on the surface is enough to react with the dye molecules available[147]. As the initial dye concentration increased the time required for complete COD removal increased, a behaviour also reported by Montanaro and Petrucci[116].

On the basis of colour and COD removal and cell voltage, 200 mg dm^{-3} RB50 initial dye solution was selected for the remaining study using the 0.64 cm^2 NATO anodes.

6.7 COD Removal and Decolourisation Current Efficiency

The dye decolourisation current efficiency was calculated by employing the widely used formula shown as equation (2.32).

The electrolysis discussed in the previous sections was repeated under the same conditions (200 mg dm^{-3} RB50 solution in 3 g dm^{-3} aqueous Na_2CO_3, at 50 mA cm^{-2}, pH of 11.1) for a range of electrolysis times, replacing the solutions in the cuvette after each experiment (see section 2.15.5), and the results are shown in fig. 6.18. The figure shows plots of $(A/A_0)_{625}$, $(A/A_0)_{254}$, (COD/COD_0) and dye degradation current efficiency vs. electrolysis time. It is

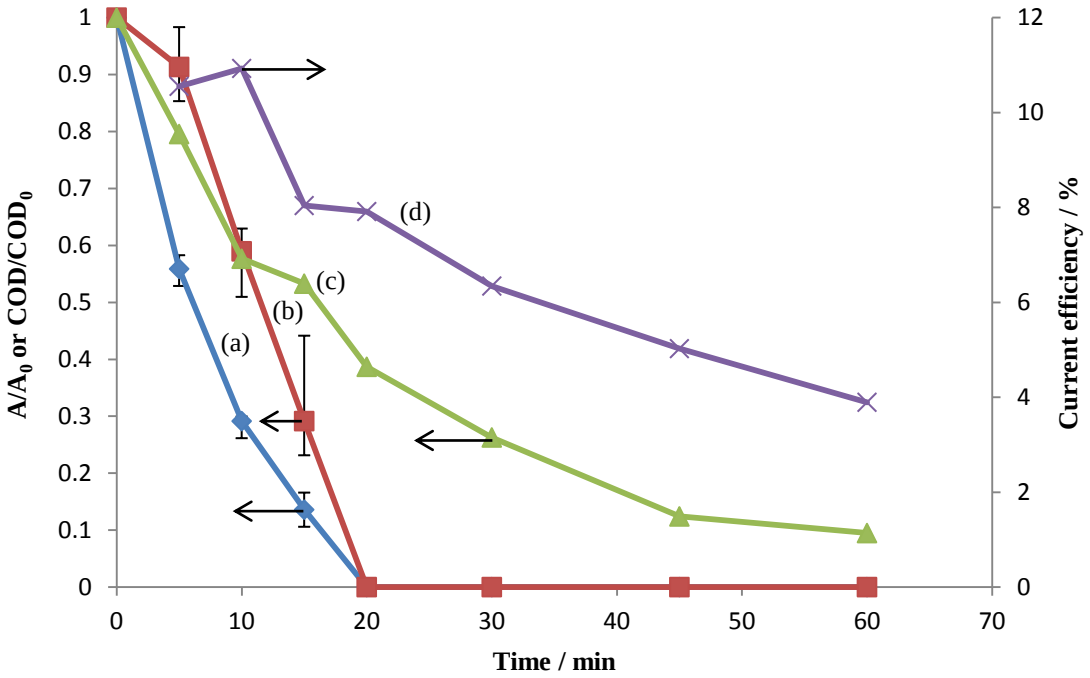

Figure 6. 18. Plots of: (a) $(A/A_0)_{625\ nm}$ for the 625 nm (anthraquinone) band , (b) $(A/A_0)_{254\ nm}$ for the 254 nm (benzene ring) band, (c) COD/COD_0 and (d) current efficiency vs. electrolysis time. 200 mg dm^{-3} initial concentrations of RB50, in 3 g dm^{-3} aqueous Na_2CO_3, electrolysed at 50 mA cm^{-2} in the cuvette using 0.64 cm^2 NATO12J anode and 0.64 cm^2 Ti/Pt cathode, at room temperature.

clear from fig. 6.18 that complete bleaching of the 625 nm and 254 nm bands was achieved after 20 min electrolysis. It may be seen from fig. 6.18 that COD decreased steadily with electrolysis time, but slower than that for the decolourisation and the benzene ring, as expected. Yavuz et al.[112] reported 86% COD decrease at the best operation condition after 60 min of electrolysis, and Parsa and Abbasi[122] reported 86 % COD removal of 400 cm^3 of 342 mg dm^{-3} Mordant Red 3 in 0.5 g dm^{-3} aqueous NaCl using platinum as an anode and stainless steel 304 as a cathode after 120 minutes electrolysis. The difference between the decolourisation rate and the COD removal rate indicates that the degradation of RB50 takes place in stages: the anthraquinone moiety is rapidly degraded (indicated by decolourisation), followed by the benzene ring. The side products/intermediates species (presumably smaller fragments) are only destroyed (indicated by COD removal) over significantly longer time scales[112, 119, 182].

The dye degradation current efficiencies are included in fig. 6.18. It is clear from the figure that the dye degradation current efficiency is higher at the beginning of the test than that at the end due to the decrease in dye concentration. This indicates that the process is mass – transport controlled and the destruction of the dye is mainly due to the OH radicals

generated on the anode surface (indirect electrochemical oxidation)[117, 195]. In addition, when less dye is available for degradation, side reactions will be favoured (such as O_2, O_3, H_2O_2, etc)[126]. Panizza and Cerisola[188] reported that current efficiencies less than 100% indicate that the process is under mass – transport control.

To summarise, the optimum conditions observed so far for the degradation of the RB50 dye in the cuvette cell at 0.64 cm^{-2} NATO anodes are: 50 mA cm^{-2}, 3 g dm^{-3} of Na_2CO_3, natural pH of 11.1, 200 mg dm^{-3} as initial dye concentration. This results in complete colour removal in 20 min and 90 % COD removal in 60 min.

6.8 The Effect of Dye Structure

Using the optimum conditions stated in the previous section, 200 mg dm^{-3} NGB and 200 mg dm^{-3} CR solutions were electrolysed in the cuvette cell (see figs. 6.19 and 6.20), in order to compare the colour and COD removal efficiencies. The figures show the UV – Vis spectra of the NGB and CR solutions taken before and during the electrolyses. It may be seen from the figures that the absorbance at 715 nm (NGB colour) and 500 nm (CR colour) decreased with electrolysis time, as did the absorbance in the UV region for both dyes indicating the degradation of the dye molecules. It may seen from fig. 6.20 that the concentration of the dye is high so that the intensity at 500 nm could not be trusted; therefore, the absorbances at 570 nm were used to evaluated the colour removal. Plots of (A/A_0) vs. time for the 715 nm band of NGB and the 570 nm band of CR, from the experiments in figs. 6.19 and 6.20 are presented in fig. 6.21 along with the RB50 data from fig. 6.18 for comparison.

The fastest decrease in (A/A_0) was observed for RB50 dye, where zero $(A/A_0)_{625}$ was achieved after 20 min electrolysis. However, only 85 % and 45 % decrease of $(A/A_0)_{715}$ and $(A/A_0)_{570}$ were observed for NGB and CR, respectively, over the same time. The complete removal of the 715 nm NGB band required 45 min electrolysis, whereas only 90% removal of the 570 nm CR band was achieved after 60 min electrolysis. This may be due to the dye structure and the nature of the chromophore group, where the anthraquinone chromophore is the easiest to degrade and the diazo is the most difficult[196]. This in general agreement with Rivera et al.[196] who studied the electrochemical oxidation of Trupocor Red (commercial acid dye), Reactive Black 5 (diazo dye), Lissamine Green B

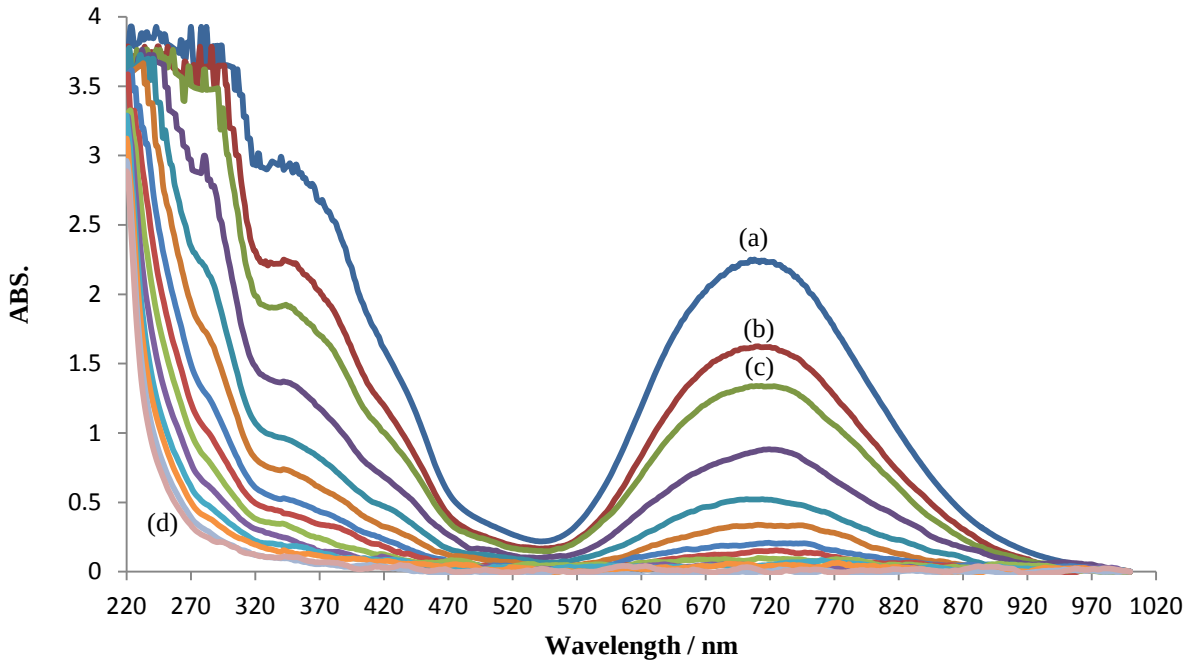

Figure 6. 19. UV – Vis spectra collected during the electrolysis of 200 mg dm^{-3} of NGB dye in 3 g dm^{-3}aqueous Na_2CO_3 electrolyte in the cuvette cell at 50 mA cm^{-2}, 0.64 cm^2 NATO12J anode and the cathode was 0.64 cm^2 Ti/Pt mesh, at room temperature, the spectra collected (a) at the start of the electrolysis (t = 0), (b) after 3 min (c) after 5 min and then every 5 min up to (d) 60 min.

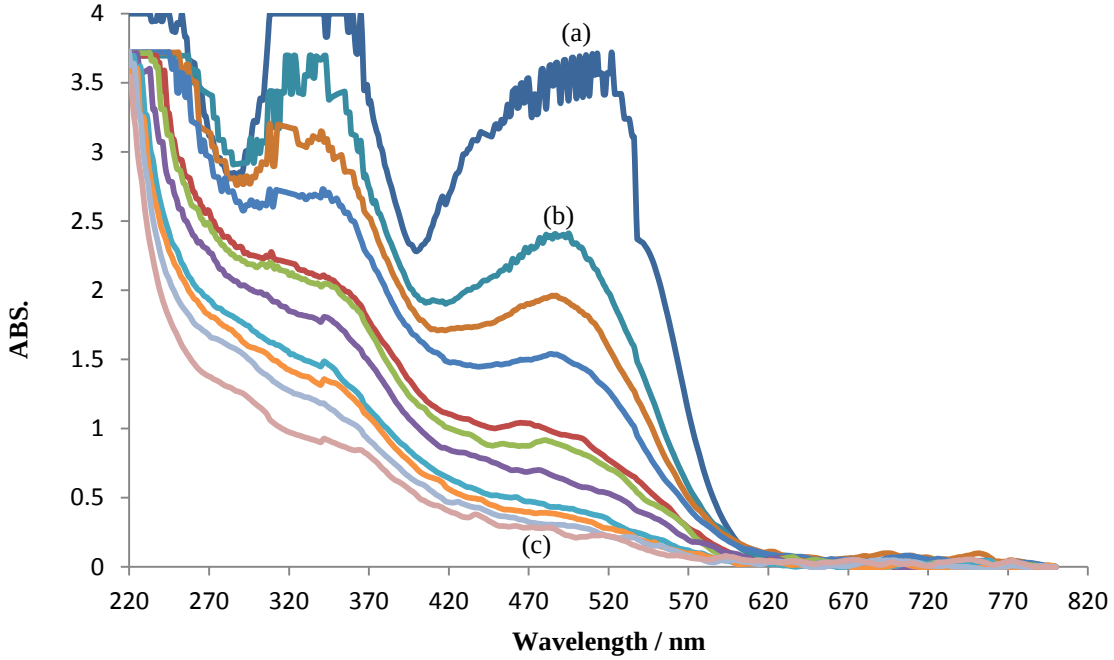

Figure 6. 20. UV – Vis spectra collected during the electrolysis of 200 mg dm^{-3} of CR dye in 3 g dm^{-3}aqueous Na_2CO_3 electrolyte in the cuvette cell at 50 mA cm^{-2}, 0.64 cm^2 NATO12J anode and the cathode was 0.64 cm^2 Ti/Pt mesh, at room temperature, the spectra collected (a) at the start of the electrolysis (t = 0), (b) after 15 min and then every 5 min up to (c) 60 min.

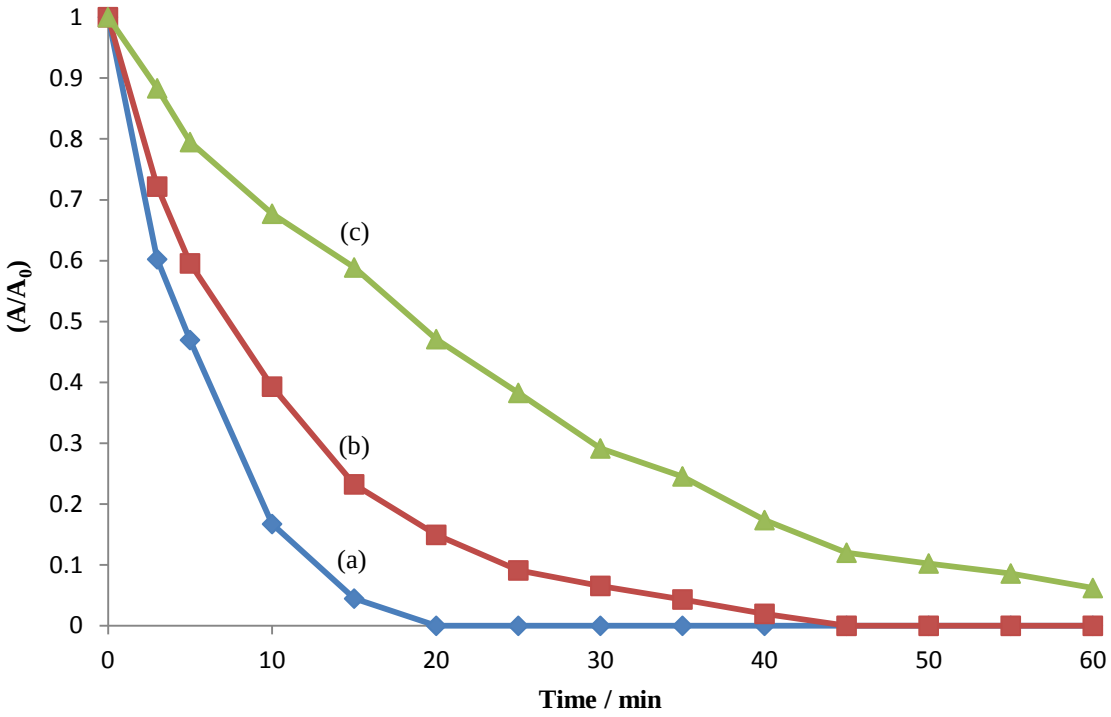

Figure 6. 21: Plots of: (a) $(A/A_0)_{625\ nm}$ for the 625 nm band of RB50, (b) $(A/A_0)_{715\ nm}$ for the 715 nm band of 200 mg dm^{-3} of NGB and (c) $(A/A_0)_{570\ nm}$ for the 570 nm band of 200 mg dm^{-3} of CR vs. electrolysis time at 50 mA cm^{-2}. The electrolyte was 3 g dm^{-3} of Na_2CO_3, and the experiment was carried out at room temperature using 0.64 cm^2 NATO12J anode and 0.64 cm^2 Ti/Pt cathode in the cuvette cell.

(diphenylnaphthyl-methane dye), Methyl Orange (mono-azo dye) and Acid Black 24 (diazo anionic dye) dye solutions in 0.01 M aqueous Na_2SO_4 in an undivided, stirred cell using graphite electrodes at 5 V. They reported that the decolourisation efficiency is related to the chemical structure of the dye studied and its substituents. The authors found that the colour removal rate was lower for diazo dyes than for mono-azo dyes and diphenylnaphthyl-methane dyes.

Rocha and co-workers[115] studied the electrochemical oxidation of Remazol Red B (RRB) and Novacron Blue C-D (NB) in 0.5 M aqueous Na_2SO_4 in an undivided, stirred cell using a BDD anode and Pt cathode at pH = 1 at different current densities. The authors reported that at low pH values (pH = 1), the influence of the dye molecule structure was evident. They found at pH = 1 that the electrochemical oxidation of RRB was independent of current density, whereas the electrochemical oxidation of NB was strongly dependent on the applied current density at the same pH (where faster decolourisation was observed at higher current density).

In terms of COD removal, the COD of the three dye solutions was measured at the end of

the experiment (i.e. after 60 min electrolysis), and it was found that 90 % of the COD was removed from the RB50 dye solution. In contrast, little or no COD removal was observed from the NGB and CR dye solutions, despite achieving promising colour removal. This low COD removal may be due to the complex chemical structure of these dyes; in addition, the diazo bond of CR poses an obstacle for colour and COD removal. This is in agreement with the work of Rivera et al.[115] who found that COD reduction was dependent on the dye structure, where the COD removal rate was less for diazo than mono-azo or diphenylnaphthalmethane dyes. In addition, Aquino et al.[186] studied the electrochemical oxidation of 100 mg dm^{-3} of an anthraquinone dye (Acid Blue 62) and three azo dyes (Reactive Red 141 (diazo), Direct Black 22 (4-azo), and Disperse Orange 29 (diazo)) in 0.1 M Na_2SO_4 with added NaCl at different concentrations in a single compartment filter-press reactor using a BDD anode and stainless steel cathode at neutral pH and 30 mA cm^{-2}. The authors reported that chloride – containing electrolyte promoted the rate of mineralisation of some dyes (Direct Black 22) but had no effect on others (Reactive Red 141 and Acid Blue 62); explaining that by the fact that some dye structures are susceptible to the oxidation by chlorine active species and other dye structures not. In contrast, Canizares et al.[195] found no difference in terms of COD removal during the electrolysis of Methyl Orange, and Eriochrome Black T (both mono-azo dyes) and Congo Red (diazo dye). The electrolysis carried out in 5 g dm^{-3} aqueous Na_2SO_4 in a single compartment electrochemical flow cell using a BDD anode and stainless steel cathode at neutral pH and 300 A m^{-2}. The authors found only that COD removal efficiency depended on the initial concentration of the dyes. Similarly, Kariaijanavar et al.[124] did not observe any significant difference between the mono-azo and diazo dyes they studied in terms of both COD and colour removal.

The rates and extent of colour removal for the three dyes studied (RB50, NGB and CR) is higher than COD removal, and this may be attributed to the fact that the chromophores are easier to remove and they can be degraded faster resulting in generation smaller and colourless organics[186, 196].

The cell voltages observed during the experiments were comparable: 6.7 V, 6.5 V and 6.6 V for RB50, NGB and CR, respectively, as expected.

6.9 Conclusions

In this chapter, the electrochemical decolourisation of RB50, NGB and CR solutions on

small (0.64 cm^2) NATO anodes was investigated. In addition, the destruction of parts of the RB50 dye was monitored (benzene ring destruction) as well as the COD removal from all solutions. The investigation was carried out mainly using the RB50 solution, where the optimum conditions for the complete decolourisation were investigated. These conditions were: 3 g dm^{-3} Na_2CO_3 as electrolyte, 50 mA cm^{-2}, pH without buffering and 200 mg dm^{-3} of initial dye concentration. The complete decolourisation (under the optimum conditions) was achieved within 20 min electrolysis with decolourisation current efficiency of ca. 8%, and 90% COD removal was obtained after 60 min electrolysis. The NGB and CR solutions were decolourised at the same optimum conditions, where 45 min electrolysis was sufficient to decolourise NGB completely, but after 60 min, only 90% of the CR colour was removed. No significant COD removals were obtained for both NGB and CR solutions.

The NATO anodes seemed to behave (most likely) as inactive electrode in terms of the decolourisation, where the main oxidation mechanism was the indirect (mediated) electrochemical process in which the anodes generated OH radicals from the water discharge on their surfaces and the OH radicals decolourised the dye solutions in the very near electrode/electrolyte interface. The direct electrochemical decolourisation cannot be ruled out completely; however, the current applied was sufficient to generate considerable amount of oxidants (mainly OH radicals) that destroyed any possible adsorbed byproducts of the direct electrochemical process.

In all cases, the decolourisation of RB50 solutions took place a bit faster than the benzene ring destruction, but the COD removal depended on the operation conditions.

Higher current densities resulted in greater amount of electrogenerated oxidants that achieved faster decolourisation and dye molecular oxidation (benzene ring destruction). However, increasing the current density above a limit resulted in no further improvement of the decolourisation process because of the domination of side reactions (oxygen and ozone).

The employment of some electrolytes can inhibit decolourisation. In contrast, the use of chloride containing electrolytes was superior due to the generation of additional oxidants (ClO, HClO and Cl_2). The presence of sulphate can result in the generation of peroxodesulphate, hydrogen peroxide and ozone that will improve the decolourisation process. The carbonate – containing electrolyte was chosen because of its alkaline nature

and the possibility of ozone decomposition to OH radicals.

The buffered pH was not helpful in the decolourisation of RB50 solution because either the pH changed the anode surface properties or the salts used to prepare the buffer contained radical scavengers.

In general, increasing the initial dye concentration resulted in increasing the time required for the complete decolourisation and decreased COD removal, as expected. However, the increase of the initial dye concentration rendered the electrochemical process to be current controlled rather than diffusion controlled (at low dye concentrations).

The decolourisation current efficiency was not very high and decreased with electrolysis time due to the fact that less dye was available for decolourisation. This suggested that oxidants electrogenerated at the anode surface underwent side reaction including ozone and oxygen evolution, the former was decomposed directly due to the alkaline conditions.

The dye structure played an important role in the electrochemical decolourisation process, where the presence of some chromophore bonds and some substitutes resulted in longer electrolysis time required to achieve complete decolourisation and COD removal.

To date the RB50 solution has not be decolourised previously in the literature and the NATO anode were not used in electrochemical decolourisation, and the results obtained so far were promising and encourage the employment of the NATO anodes in electrochemical applications for industrial wastewater treatment. This needs continuous research.

In the following chapter, the ozone will be generated using MEA – based ozone generation system and it will be applied in bubble column reactor to investigate the decolourisation of the RB50, NGB and CR solutions by ozonation. UV_{254} irritation and O_3/UV_{254} irradiation will be employed for the decolourisation if the same solutions and the results will be compared with the results of this chapter.

CHAPTER SEVEN

7 Dye Decolourisation by Ozone, UV irradiation and O_3/UV Combination

7.1 Introduction

In this chapter, data are presented about dye solution decolourisation by ozone, UV irradiation and O_3/UV combination. The decolourisation by ozone optimum conditions were investigated using RB50 solutions; including the ozone dose and pH. As discussed in sections 2.16 - 2.18, the dye solutions were decolourised by ozone in the bubble column reactor (BCR) where the ozone was generated electrochemically using the MEA – OGS. The optimum conditions were employed to decolourise NGB and CR solutions by ozone. UV irradiation using a UV lamp (λ_{max} =254nm) was used to decolourise the three dye solutions, then the solutions were exposed to ozone and UV simultaneously. At the end of this chapter, the efficiencies of the technologies (including the electrochemical method studied in chapter 6) employed to decolourise the RB50, NGB and CR solutions were compared.

7.2 Decolourisation by Ozonation

As discussed in section 1.2, the ozone in the gas phase can be generated either by the discharge of oxygen or the discharge of water because of a current passing through two electrodes. In the work reported in this chapter, the ozone was generated electrochemically by MEA – OGS (see section 2.16). Then the ozone was bubbled in a BCR to decolourise dye solutions, as described in section 2.16.1. In the following sections, a preliminary ozonation study on RB50 solutions, and effect of ozone dose, pH and dye structure on the decolourisation by ozone were studied.

7.2.1 Ozone generation

The ozone doses and the cell voltages of the MEA – OGS operated at different current densities (25 mA cm^{-2}, 50 mA cm^{-2}, 75 mA cm^{-2}, 80 mA cm^{-2} and 100 mA cm^{-2}) are shown in fig. 7.1. 1 M $HClO_4$ was used as catholyte and anolyte with anolyte recycle flow rate of 200 cm^3 min^{-1}, nitrogen flow rate to the gas separator was 1000 cm^3 min^{-1}. Higher ozone dose was obtained when higher current density was applied to the MEA – OGS, hence resulting in higher cell voltage as can be seen in fig. 7.1.

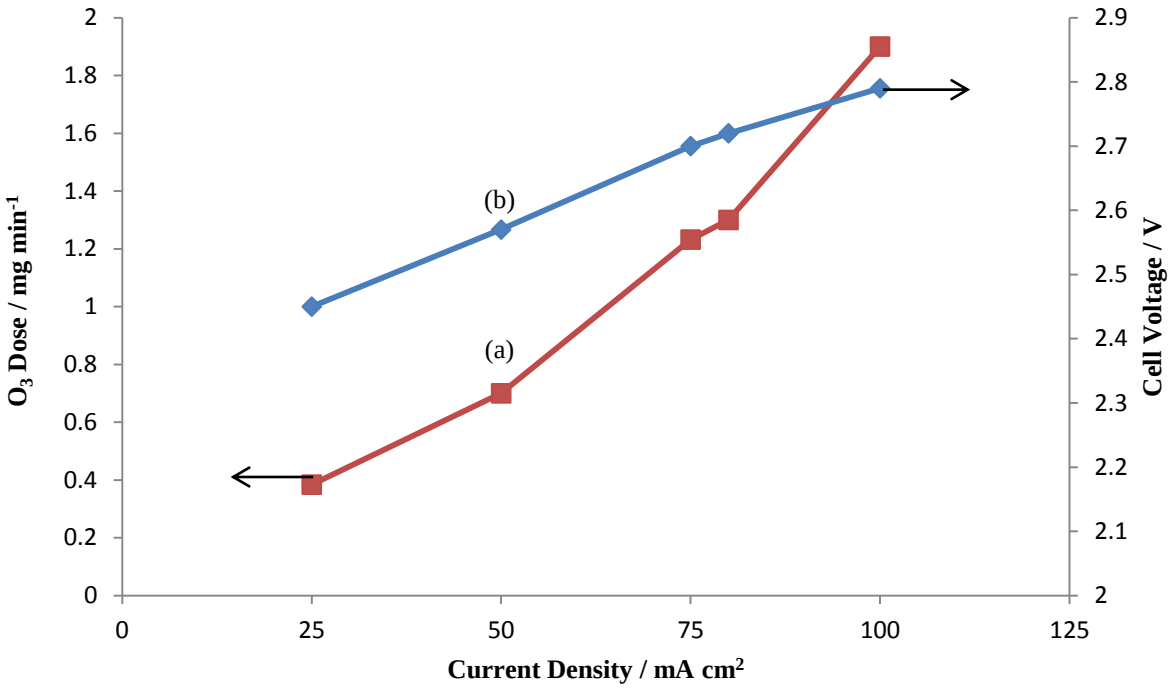

Figure 7. 1. Plot of: (a) ozone dose and (b) cell voltage vs. current density at the end of the ozone generation experiment using MEA – OGS. The anode of the MEA was 24 cm^4 NATO17I, the cathode was 24 cm^4 Pt/Ti mesh separated by Nafion 117 membrane. 1 M $HClO_4$ as catholyte and anolyte, at different current densities of 25 mA cm^{-2}, 50 mA cm^{-2}, 75 mA cm^{-2}, 80 mA cm^{-2} and 100 mA cm^{-2}, for 60 min, at room temperature

7.2.2 Preliminary study on ozonation of RB50 solution

Figure 7.2 shows the UV – Vis spectra collected during the ozonation of 500 cm^3 of 100 mg dm^{-3} RB50 solution. The gas phase ozone was bubbled at 0.7 mg min^{-1} dose and carried by N_2 at 1 dm^3 min^{-1} flow rate. The figure is representative of all the ozonation experiments carried out on the RB50 solution and reported in this chapter. As was discussed in section 2.14.1, the spectrum of RB50 consists of three well – defined peaks at 254 nm, 586 nm and 625 nm. It may be seen from the fig. 7.2 that the colour (at 625 nm and 586 nm) and benzene ring absorption (at 254 nm) were decreased with ozonation time. The loss of the UV band near 254 nm suggest that the dye is being oxidised into fragments[178], while the decrease in the intensities of the 625 nm and 586 nm bands may be attributed to the destruction of the anthraquinone moiety[122].

Plots of variation in $(A/A_0)_{625}$, $(A/A_0)_{586}$ and $(A/A_0)_{254}$ vs. ozonation time are shown in fig. 7.3. It may be seen from the figure that the plots of variation of $(A/A_0)_{625}$ and $(A/A_0)_{586}$ track each other as would be expected as they are due to the anthraquinone chromophore destruction. Therefore, the decrease of the $(A/A_0)_{625}$ was taken as representative of the decolourisation by ozonation of RB50 solutions in all experiments reported in this chapter.

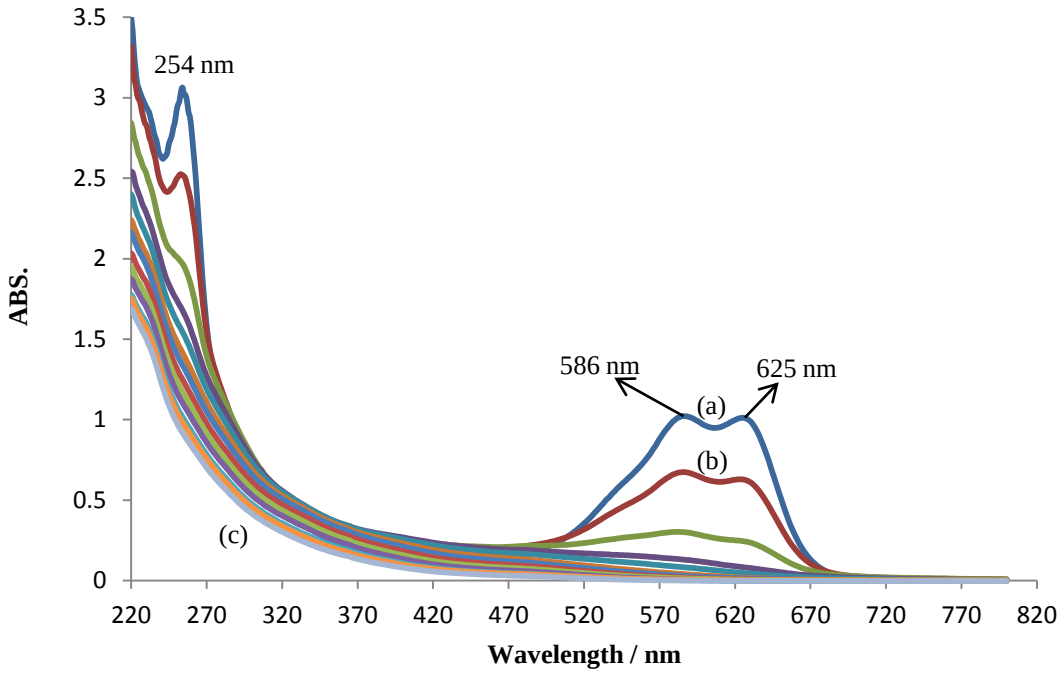

Figure 7. 2. UV – Vis spectra collected during the ozonation of 500 cm^3 of 100 mg dm^{-3} RB50 solution in Millipore water in the BCR at an ozone dose of 0.7 mg min^{-1}, the ozone was generated as described in fig. 7.1. The N_2 flow rate into the bubble reactor was 1 dm^3 min^{-1}, the spectra collected at room temperature: (a) before ozonation, (b) after 5 min ozonation, then every 5 min up to (c) 60 min.

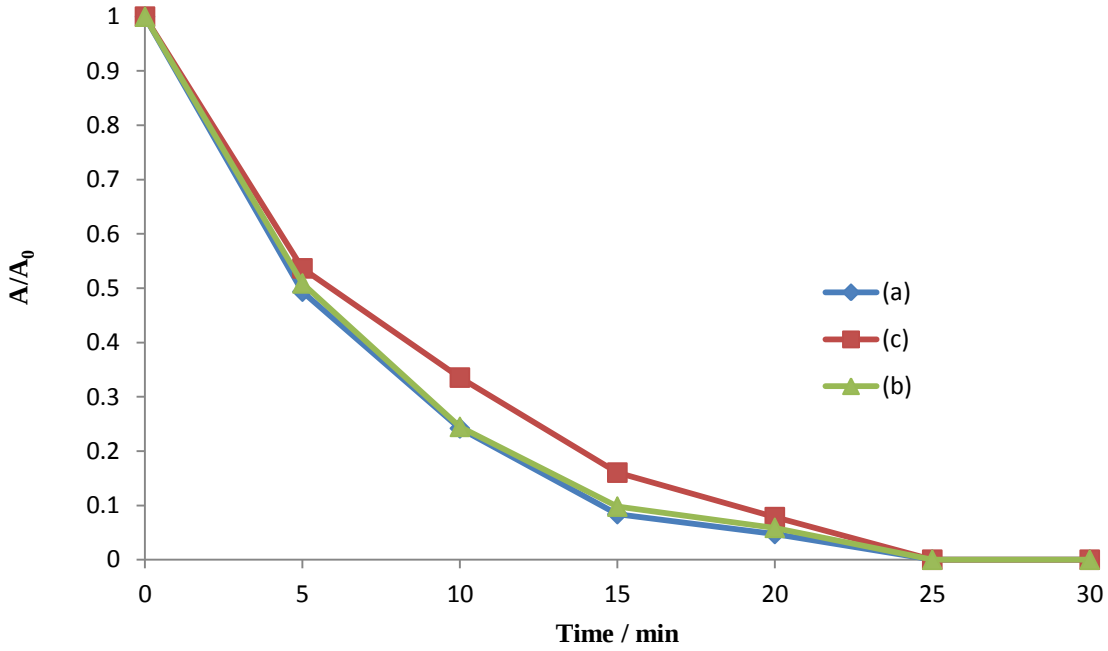

Figure 7. 3. Plots of: (a) $(A/A_0)_{625}$, (b) $(A/A_0)_{586}$ and (c) $(A/A_0)_{254}$ from the spectra in fig. 7.2.

Furthermore, the $(A/A_0)_{625}$, $(A/A_0)_{586}$ and $(A/A_0)_{254}$ all decreased to zero after 25 min treatment.

Dye ozonation mechanism

According to Poznyak et al.[114], it is likely that the first step of the decolourisation of many dyes by ozone involves the reaction of ozone with a single chromophore group or C = C bond connecting aromatic rings. Taking that as starting point, it does not seem unreasonable to postulate the following mechanism for the degradation of RB50 by ozone: (i) ozone attacks, simultaneously, the anthraquinone and benzene ring, (ii) the cleavage of anthraquinone will reduce the colour intensity of the solution, and the cleavage of the benzene ring will promote the dye molecule destruction to smaller organics and (iii) smaller organics will be generated as ozonation byproducts, these include aliphatic (organic) acids[114, 197] and inorganic acids[197, 198]. The former acids are refractory towards ozone attack[114].

Ozone has been known to oxidize organics by itself, as well as producing strong oxidative species such as hydroxyl radicals ($OH^{\cdot}$) and hydrogen peroxide (H_2O_2)[199] depending on the pH of the solution[114, 200, 201]. As was shown in scheme 5.1, ozone can decompose to generate OH radicals in alkaline solutions[175], and it may generate H_2O_2 as it decomposes[191]. Ozone, OH radicals and H_2O_2 are known to be strong oxidants. However, OH radicals are the strongest and the least selective with standard reduction potential of 2.8 V vs. NHE[134]. So, the dye destruction mechanism is then affected by the solution pH, where the mechanism may be direct ozonation (at acidic pH, where O_3 is the main oxidant) or indirect ozonation (at alkaline pH, OH radicals are the main oxidants). However, in neutral pH, both mechanisms may take place.

Decolourisation by ozonation rate constants

It is important to investigate the ozonation reaction order and rate constants of the ozone reaction with dyes in order to get more information about reaction mechanism[114]. It may be expected that ozonation depends on the dye and ozone concentrations[114], according to:

$$d[C]/dt = k[C].[O_3] \qquad (7.1)$$

where k is the second order rate constant, [C] is the dye concentration. However, the dye and ozone reaction is first order with respect to ozone and the dye[202].

As was discussed in section 6.2.2, to investigate the reaction order, it is important to collect the dye concentration (absorbance at 625 nm for RB50 solution) vs. ozonation time data, then plot (A), ln(A) and 1/(A) vs. time. The slope of which is the decolourisation rate constant. The R^2 of the so obtained relationships will be employed to decide reaction order.

Figure 7.4 shows the absorbance (A) at 625 nm, data taken from fig. 7.2, ln(A) and 1/(A) vs. time. It may be seen from the figure that 1/(A) variation was not linear with ozonation time. In contrast, both (A) and ln(A) seemed to decrease linearly with time. To decide the reaction order, R^2 was calculated using MS Excel 2007, and it was 0.87 and 0.99, respectively. Therefore, it is possible to say that the decolourisation by ozonation happened at first order kinetics. The same procedures have been performed for all the data presented in this chapter to know the decolourisation kinetics and the rate constants.

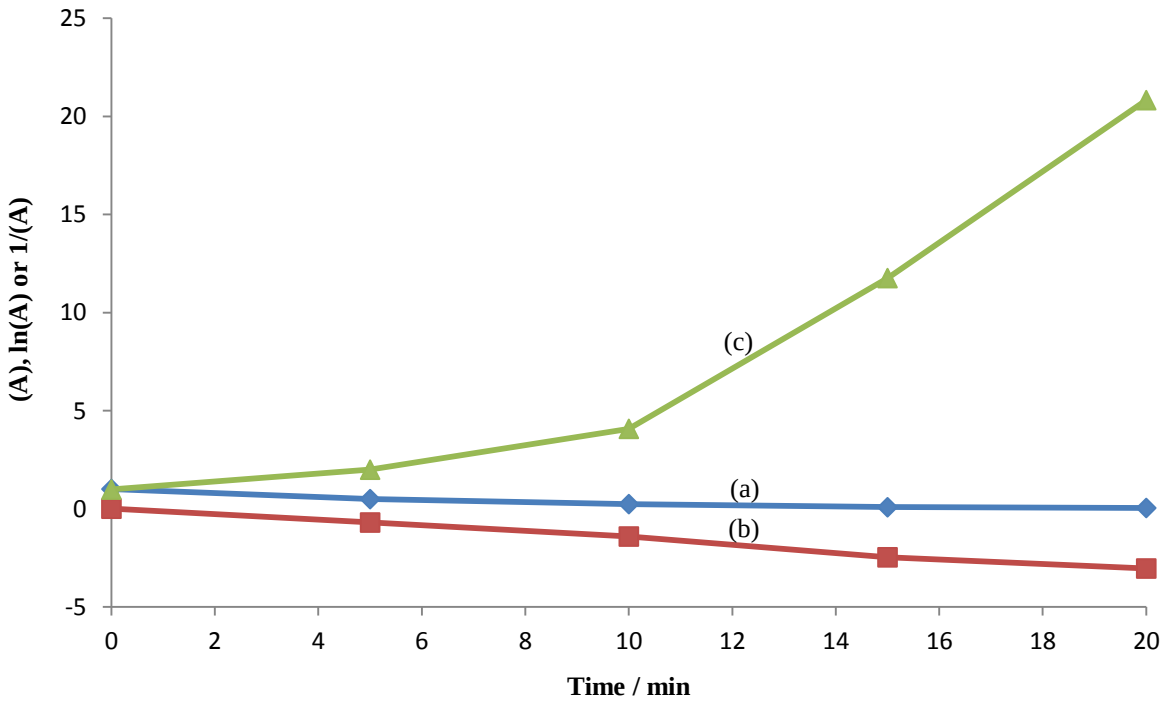

Figure 7. 4. Plots of (a) Absorbance at 625 nm (A), (b) ln(A) and (c) 1/(A) vs. ozonation time for the data in fig. 7.2.

Similarly, the benzene ring destruction (for RB50) and COD removal kinetics and rate constant can be achieved by the same way. Figure 7.5 shows a plot of ln(A) vs. ozonation time taken from the 625 nm and 254 nm bands in the spectra in fig. 7.2. The R^2 of the two lines were 0.99, and the rate constants for the decolourisation and benzene ring destruction were 0.15 min^{-1} and 0.12 min^{-1}, respectively, showing that the oxidation of the former moiety is somewhat faster than the latter.

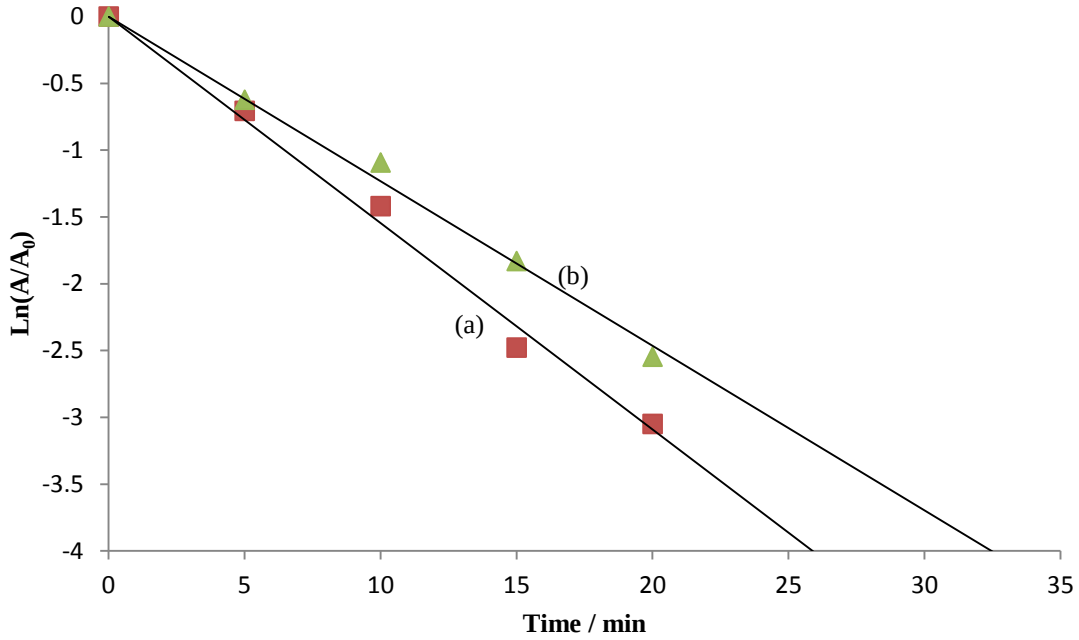

Figure 7. 5. Plots of ln(A) vs. ozonation time for the (a) 625 nm (anthraquinone) and (b) 254 nm (benzene ring) bands in the spectra in fig. 7.2.

7.2.3 The effect of ozone dose

Determining the required ozone dose is essential for the economical evaluation of the ozonation process[200]. To investigate the ozone dose effect, 500 cm^3 of 100 mg dm^{-3} RB50 in Millipore water was placed in the BCR and decolourised by ozone at an initial pH 4.72. The effect of ozone dose on the decolourisation of 100 mg dm^{-3} of RB50 was investigated over the range 0.4 mg min^{-1} – 1.9 mg min^{-1}, and plots of $(A/A_0)_{625}$ for the absorption at 625 nm are plotted as a function of ozonation time for a range of ozone dose in fig. 7.6. As may be seen from the figure, the rate of decrease of $(A/A_0)_{625}$ increased with ozone dose. However, less than 25 min was sufficient to completely decolourise the RB50 solution at all doses used except for the 0.4 mg min^{-1} dose, which required 40 min ozonation. These findings are consistent with the role of ozone mass transfer, where the driving force for the transfer of ozone to the dye solution increases due to the increase of ozone concentration in the bubbles, and this increases the ozone concentration in the solution and hence the rate of oxidation of the dye molecules[201].

In broad terms, the data in fig. 7.6 are in agreement with the work of Soares et al.[200] who studied the ozonation of 50 mg dm^{-3} of Acid Blue 116 in a continuous mode in a cylindrical column at pH 7 at 15 – 80 g O_3 m^{-3}, Turhan et al.[201] who studied the ozonation of 400 mg dm^{-3} of Basic Blue 9 (Methylene Blue) solutions in column reactor at pH 12 and ozone flow rate of 120 dm^3 h^{-1} by applying ozone doses between 4 – 24 g m^{-3} and

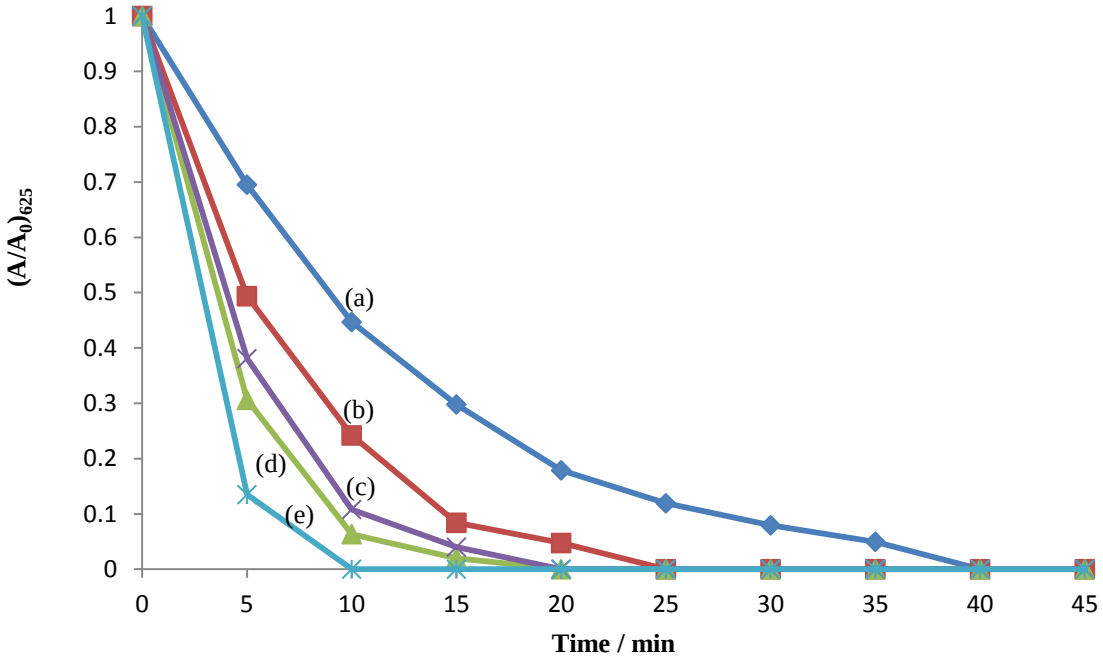

Figure 7. 6. Plots of $(A/A_0)_{625}$ vs. ozonation time obtained during the ozonolysis of 100 mg dm^{-3} RB50 in Millipore water in the BCR at an ozone dose of: (a) 0.4 mg min^{-1}, (b) 0.7 mg min^{-1}, (c) 1.2 mg min^{-1}, (d) 1.3 mg min^{-1} and (e) 1.9 mg min^{-1} injected into the bubble reactor by N_2 gas at flow rate of 1 dm^3 min^{-1}, the ozone was generated electrochemically at room temperature, see text for details.

Cuiping et al.[133] who studied the ozonation of 100 mg dm^{-3} of Rhodamine B solution in column reactor at ozone dose range of 50 – 200 mg dm^{-3} of flow rate of 30 cm^3 min^{-1} at initial pH 3. These groups reported that the decolourisation increased with increasing ozone dose due to the fact that the ozone per volume solution also increased and reduced the ozonation time.

Figure 7.7 shows analogous plots to those in fig. 7.6 except for the 254 nm benzene ring band, taken from the same experiments. The same observations can be made as for the plots in fig. 7.6. It may be seen from the figs. 7.6 and 7.7 that the decrease in $(A/A_0)_{625}$ and in $(A/A_0)_{254}$ was greater with higher ozone dose, probably due simply to the fact that more ozone was available.

Applying the methodology described above to determine the decolourisation reaction order on the data in figs. 7.6 and 7.7 suggested that decolourisation and benzene ring destruction can be described as first order of which the rate constants are presented in table 7.1. It may be seen from the table that the rate constants of decolourisation are slightly faster than those for the oxidation of benzene ring at all ozone doses studied.

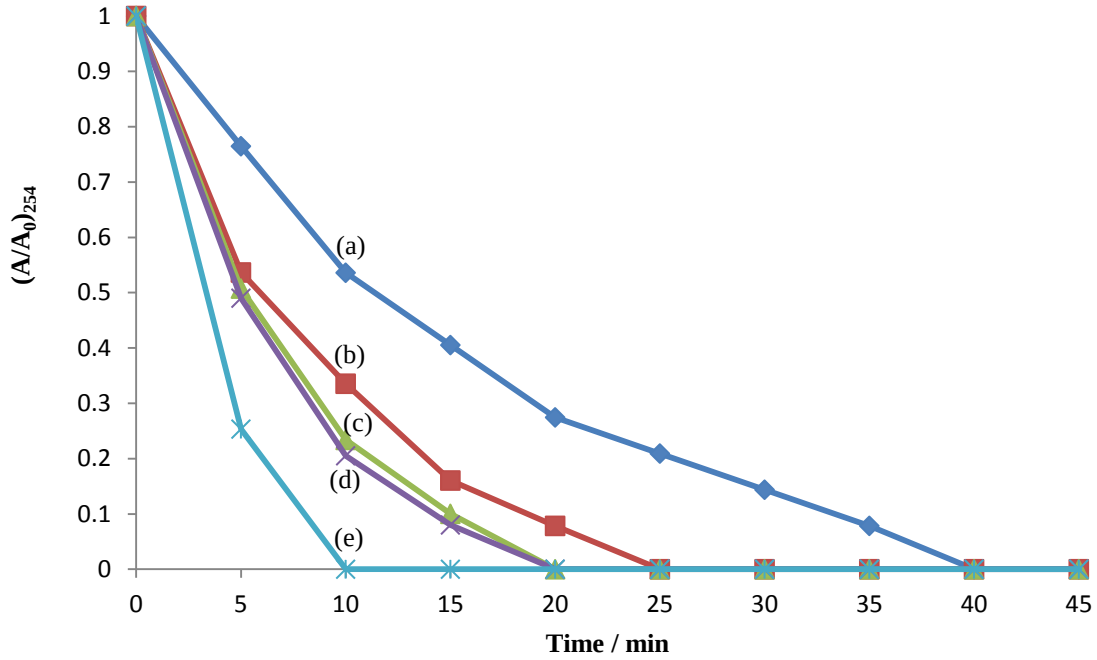

Figure 7. 7. Plots of $(A/A_0)_{254}$ vs. ozonation time obtained during the ozonolysis of 100 mg dm^{-3} RB50 in Millipore water in the BCR at an ozone dose of: (a) 0.4 mg min^{-1}, (b) 0.7 mg min^{-1}, (c) 1.2 mg min^{-1}, (d) 1.3 mg min^{-1} and (e) 1.9 mg min^{-1} injected into the bubble reactor by N_2 gas at flow rate of 1 dm^3 min^{-1}, the ozone was generated electrochemically at room temperature.

Ozone dose / mg min^{-1}		**0.4**	**0.7**	**1.2**	**1.3**	**1.9**
Anthraquinone removal (λ=625nm)	k_a / min^{-1}	0.09	0.15	0.22	0.26	0.4
	R^2	0.99	0.99	0.99	0.99	1
Benzene ring removal (λ=254 nm)	k_b / min^{-1}	0.07	0.12	0.15	0.16	0.27
	R^2	0.99	0.99	0.99	0.99	1
COD after 60 min ozonation		6.2	15	24.7	26.8	27.8
pH after 60 min ozonation		4.02	3.73	3.6	3.6	3.6

Table 7. 1. Summary of the rate constants for colour and benzene ring removal, COD and pH values after 60 min ozonation voltage vs. the applied ozone dose for the experiments depicted in fig. 7.6.

It may be seen from table 7.1 that COD removal increased with increasing ozone dose, as expected. The COD removal was low compared to that of the colour removal where the highest COD removal rate (28%) was observed at the highest ozone dose employed, and the lowest COD removal (6%) at the lowest. Ozone is well known as a selective oxidant that attacks a wide range of organics, but not all organics especially organic acids[200, 201], this might explain the lower COD removal rate of the RB50 solution compared to that of decolourisation (see table 7.1). The fact that COD removal was always less than that of colour may be explained by the fact that ozone can provide fast destruction of the chromophore groups responsible for the colour as well as to the aromatics to generate

smaller organics that are recalcitrant to ozone attack[200, 201].

The effect of ozone dose on the pH of the RB50 solution after one hour ozonation is shown in table 7.1. Ozonation at higher ozone dose caused little or no further decrease in the pH value of the solution at the end of the ozonation test. The decrease in the solution pH treated by ozone is expected due to the acidic byproducts, as discussed above in section 7.2.2.[114, 198]

The difference between the removal efficiencies using 1.3 and 1.9 mg min^{-1} for both colour and COD removal rate is less than 2 %. Therefore, ozone dose of 1.3 mg min^{-1} will be used for the remaining study.

7.2.4 The effect of pH

As stated above, dye solution pH is an important parameter affecting the ozonation process[200, 203]; however, some researchers have reported that ozonation is independent of solution pH over the range 4 – 9.[200]

All the experiments carried out so far were without buffering, and hence pH was allowed to vary from the starting value of about 4.72. However, as briefly discussed above in section 7.2.2, it is well known that ozone molecule will be the main oxidant in acidic conditions, whilst OH radicals will be the main oxidants in alkaline conditions. In neutral conditions, both direct and indirect ozonation can occur[200, 201, 204]. In contrast, Muthukumar and Selvakumar[204] reported that at pH > 6, the main oxidant is OH radicals. Therefore, it is important to investigate the best pH condition for colour removal from RB50 solution. Thus, as was described in section 2.16.1 , buffered 100 mg dm^{-3} RB50 solutions were prepared at pH 2, 7 and 11. The ozone dose of 1.3 mg min^{-1} was employed. The effect of pH on the variations of $(A/A_0)_{625}$ and $(A/A_0)_{254}$ variations are shown in fig. 7.8. The variations of $(A/A_0)_{625}$ and $(A/A_0)_{254}$ with time can be described by first order kinetics, as discussed in section 7.2.2, and the rate constants so obtained are presented in table 7.2.

It may be seen from fig. 7.8 that the variation in $(A/A_0)_{625}$ as a function of time for RB50 solutions buffered at pH 2, 7 and 11 were similar, and zero $(A/A_0)_{625}$ was achieved after 15 min ozonation for all three buffered dye solutions. The same observations can be observed for the benzene ring destruction from fig. 7.8. The observations may be explained in terms of either: (i) at pH 7, the ozone dissociation is less than that of acidic pH, but at alkaline

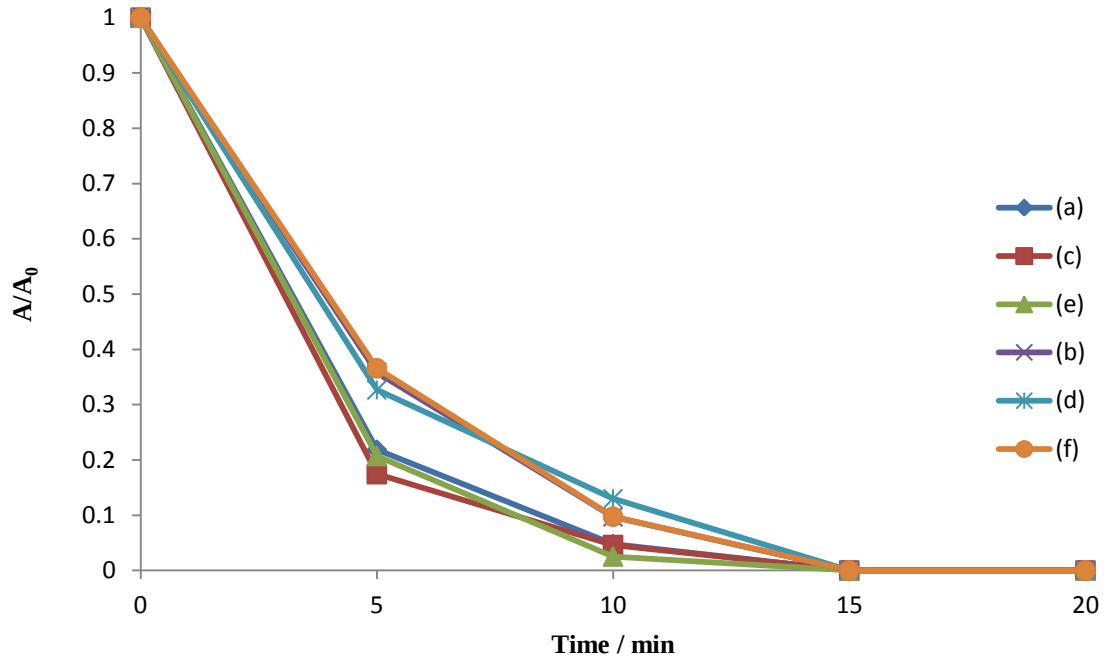

Figure 7. 8. Plots of: (a), (c) & (e) $(A/A_0)_{625}$ and (b), (d) & (f) $(A/A_0)_{254}$ of RB50 (100 mg dm^{-3}) vs. ozonation time, at ozone dose of 1.3 mg min^{-1} injected into bubble reactor by N_2 flow rate of 1 dm^3 min^{-1}. The solutions were buffered at pH of: (a)&(b) 2, (c)&(d) 7 and (e)&(f) 11, at room temperature.

Buffered pH		**2**	**7**	**11**	**unbuffered**
Anthraquinone removal (λ=625nm)	k_a / min^{-1}	0.3	0.32	0.36	0.26
	R^2	1	0.99	0.99	0.99
Benzene ring removal (λ=254 nm)	k_b / min^{-1}	0.23	0.21	0.23	0.16
	R^2	1	0.99	0.99	0.99
pH after 60 min ozonation		2	7	11	3.6
COD after 60 min ozonation %		13	18	0	27

Table 7. 2. Summary of the rate constants for colour and benzene ring removal of RB50 solution and pH values after 60 min ozonation vs. buffered pH for the experiments depicted in fig. 7.8.

pH (despite lower ozone dissociation) more OH radicals are formed[204], (ii) the ozone oxidising potential decrease with increasing the solution pH from 2.07 V (in acidic media) to 1.4 V (in alkaline media)[134], and ozone decomposes to produce OH radicals in alkaline solutions, and/or (iii) the expected reactions between the ozone and/or OH radicals with the added salts (for preparing the buffers); for example, buffered solution pH 11 contains the anion HCO_3^- well known for scavenging OH radicals[205]. This results in almost similar decolourisation times.

In terms of the time required for complete decolourisation, the data in fig. 7.8 are in broad agreement with the work of Balcioglu and Arslan[203] who studied the ozonation of 500 mg

dm^{-3} of Reactive Black 5 in a column reactor at an ozone flow rate of 2340 mg dm^{-3} h^{-1} at initial pH of 2, 5, 7, 9 and 11. The authors reported that the same ozonation time was required for complete decolourisation at all pH studied. In addition, Santana et al.[197] studied the effect of pH on the ozonation of 300 mg dm^{-3} of Reactive Orange 112 solutions in a column reactor at an ozone rate of 250 mg h^{-1} at initial pH of 4.5 and 12. The authors found that complete decolourisation was only slightly faster at pH 12. In contrast, Cuiping et al.[133] studied the effect of pH on ozonation at unspecified ozone dose at flow rate of 30 cm^3 min^{-1} and initial pH of 2, 3, 2, 5, 7 and 10. The authors found that complete colour removal was achieved faster at more acidic pH due to the dominance of radical scavengers (HCO_3^-, CO_3^{-2}, etc) at high pH. On the other hand, Muthukumar and Selvakumar[204] studied the ozonation of 0.5 mM of Acid Red 12, Acid Violet 12, Acid Brown 14 and Acid Blue 113, separately, in a column reactor at an ozone dose of 2 g h^{-1} and flow rate of 2 dm^3 min^{-1} in the absence and presence of different concentrations of NaCl and Na_2SO_4. The authors found that the ozonation time required for complete decolourisation increased at pH 7, was less for pH 3 than pH 11 and was the lowest with no salts. They explained their findings in terms of two different ozonation mechanisms; direct and indirect, and by the fact that at pH 7, ozone dissociation is lower than in acidic pH, leading to less OH radicals being produced.

Generally, most of research on the effect of pH on dye solution ozonation has been carried out by adjusting the initial pH of the solutions rather than employing buffers. However, Soares et al.[200] studied the effect of pH in the presence and absence of buffers including, eg: initial, unbuffered pH 3, 5, 7, 9 and 11, and buffered at pH 5, 7 and 9. The authors found that the rate of decolourisation in unbuffered solutions were greater than those in buffered ones. In addition, unbuffered solutions with initial pH between 5 and 9 did not show any significant difference in the amount of decolourisation. They explained these observations by the fact that, in buffered solutions, the final pH is close to the initial pH, and in unbuffered solutions with initial pH of 5, 7 and 9 the final pH is practically the same for all experiments (4–5). Under these conditions, the direct ozone molecular reactions prevail, leading to higher rates of decolourisation.

It may be seen from table 7.2 that the decolourisation rate constants did not change significantly with pH in buffered solutions, but they were greater than those observed in unbuffered experiment is in general agreement with the work of Balcioglu and Arslan[203]

who did not report any significant difference in the decolourisation rate constants over the pH range 2 – 9, but a remarkable enhancement in the rate constant was observed at pH 11. The authors interpreted their findings in terms of the fact that ozone decomposition to form OH radicals is enhanced at pH 11. In contrast, Cuiping et al.[133] found that the decolourisation rate constants decreased with increasing pH. On the other hand, Chu and Ma[129] studied the ozonation of 500 cm^3 of each of six dye solutions including: Reactive Blue 19, Disperse Violet 28, Reactive Black 5, Direct Green 26, Reactive Violet 5 and Direct Red 80 in a column reactor at ozone flow rate of 1 dm^3 min^{-1} and initial pHs of 4, 7 and 10. The authors found that the decolourisation rate constants generally increased with increasing pH except for the anthraquinone dyes (Reactive Blue 19, Disperse Violet 28) where their decolourisation rate constants slightly decreased. They explained their findings by two reasons: (i) the dye structures and (ii) changes in the dyes at acidic conditions.

It may be seen from table 7.2 that the COD removal at pH 2 and pH 7 was 13% and 18% respectively. However, no COD removal was observed at pH 11, and this may be due to the scavenging effect of the HCO_3^- and/or CO_3^{-2} employed in the buffer. The effect of the buffers on COD removal suggests that ozone is the dominant oxidant at pH 2. As COD removal increased at pH 7, both ozone and OH radicals (or may be OH radicals alone) are the main oxidant at this pH (there is little or no scavengers in the solution). However, at pH 11, OH radicals produced due to ozone decomposition may be used for decolourisation and/or were scavenged by CO_3^{2-} and/or HCO_3^-; resulting in no COD removal. This COD removal behaviour is in disagreement with the work of Balcioglu and Arslan[203] who reported that COD removal was almost similar for pH over the range 2 – 9, and increased significantly at pH 11. In addition, Turhan et al.[201] who studied the effect of initial pH on COD removal at pH over the range 2 – 12, reported that COD removal increased with increasing solution pH and it was remarkable at pH 12, in complete contrast to the findings reported in this section.

Although the decolourisation of buffered dye solutions was faster (see table 7.2) than that of the unbuffered ones, the COD removal was less. Therefore, it was decided to keep the solution at its original, unadjusted pH.

7.2.5 The effect of dye structure

To investigate the effect of dye structure on decolourisation and degradation (in terms of COD removal) of RB50, NGB and CR solutions, the ozonation of 500 cm^3 of 100 mg dm^{-3}

NGB and CR solutions in Millipore water at an ozone dose of 1.3 mg min^{-1} and N_2 flow rate of 1 dm^3 min^{-1} was carried out.

Figures 7.9 and 7.10 show the UV – Vis spectra collected during the ozonation of NGB and CR solutions in the BCR, respectively. As was discussed in section 6.1, the spectrum of NGB consists of two well – defined peaks at 715 nm and 280 nm, and the spectrum of CR consists of three well – defined peaks at 500 nm, 340 nm and 237 nm. It may be seen from the figs. 7.9 and 7.10 that the colour of both dyes decreased with ozonation time. The loss of the UV bands suggests that the dyes were oxidised into fragments[178], while the decrease in the intensities of the visible bands (715 nm and 500 nm) may be attributed to the destruction of the chromophore moiety of each dye[122]. Plots of $(A/A_0)_{625}$, $(A/A_0)_{715}$ and $(A/A_0)_{500}$ vs. time observed during the ozonation of the RB50, NGB and CR, respectively, are shown in fig. 7.11. It may be seen from the figure that zero $(A/A_0)_{625}$ and $(A/A_0)_{715}$ was achieved at 20 min and 45 min ozonation, respectively. However, zero $(A/A_0)_{500}$ was not achieved within the ozonation time studied (60 min): a value of 0.08 was observed for $(A/A_0)_{500}$ after 60 min ozonation. The ozonation reaction order, rate constants and R^2 for each dye solution decolourised are presented in table 7.3.

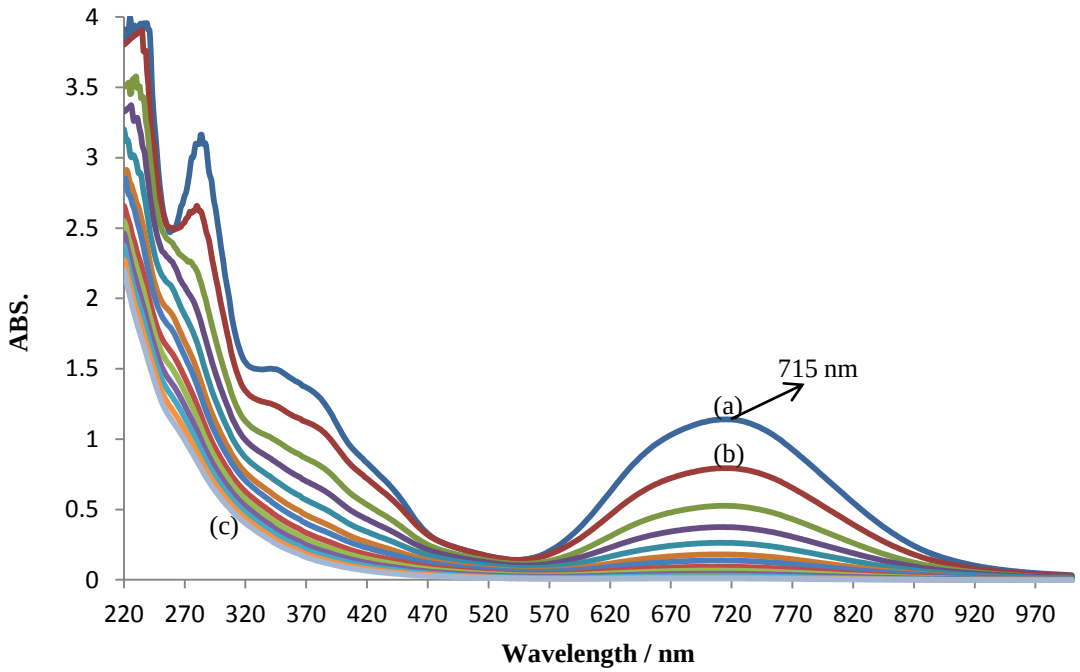

Figure 7. 9. UV spectra collected during the ozonation of 500 cm^3 of 100 mg dm^{-3} of NGB solution in Millipore water in the BCR at an ozone dose of 1.3 mg min^{-1}, the ozone generated as described in fig. 7.1. The ozone was injected in the column reactor by N_2 at flow rate of 1dm^3 min^{-1}, the spectra were collected at room temperature at: (a) before ozonation, (b) after 5 min ozonation, then every 5 min up to (c) 60 min.

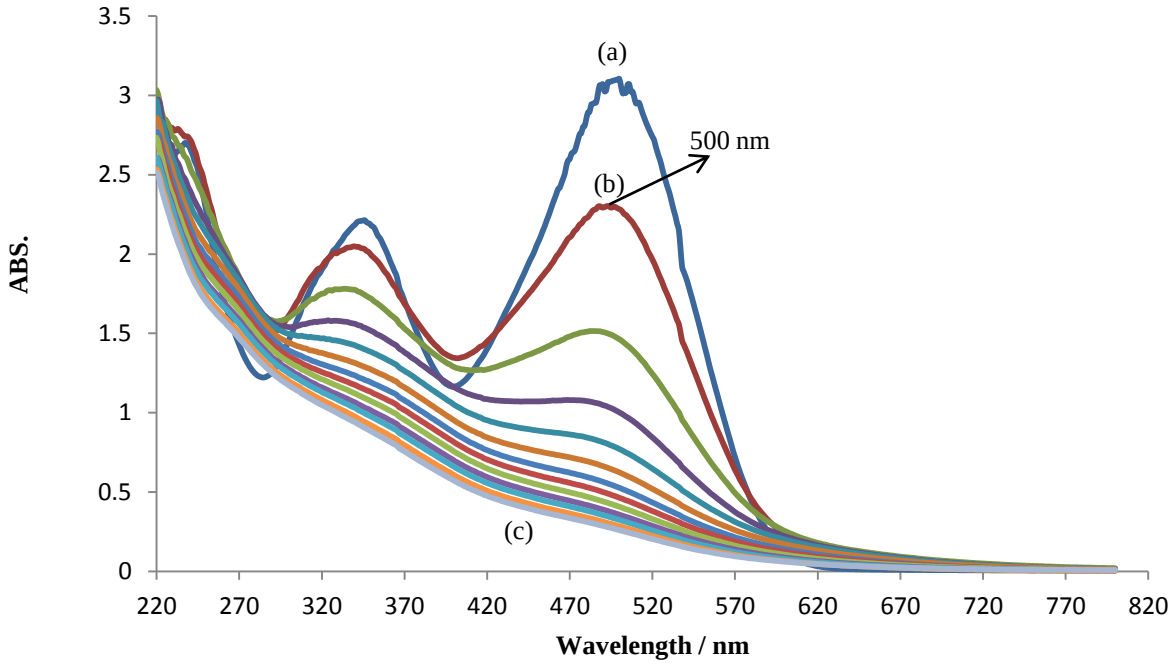

Figure 7. 10. UV spectra collected during the ozonation of 500 cm^3 of 100 mg dm^{-3} of CR solution in Millipore water in the BCR at an ozone dose of 1.3 mg min^{-1}, the ozone generated as described in fig. 7.1. The ozone was injected in the column reactor by N_2 at flow rate of 1dm^3 min^{-1}, the spectra were collected at room temperature at: (a) before ozonation, (b) after 5 min ozonation, then every 5 min up to (c) 60 min.

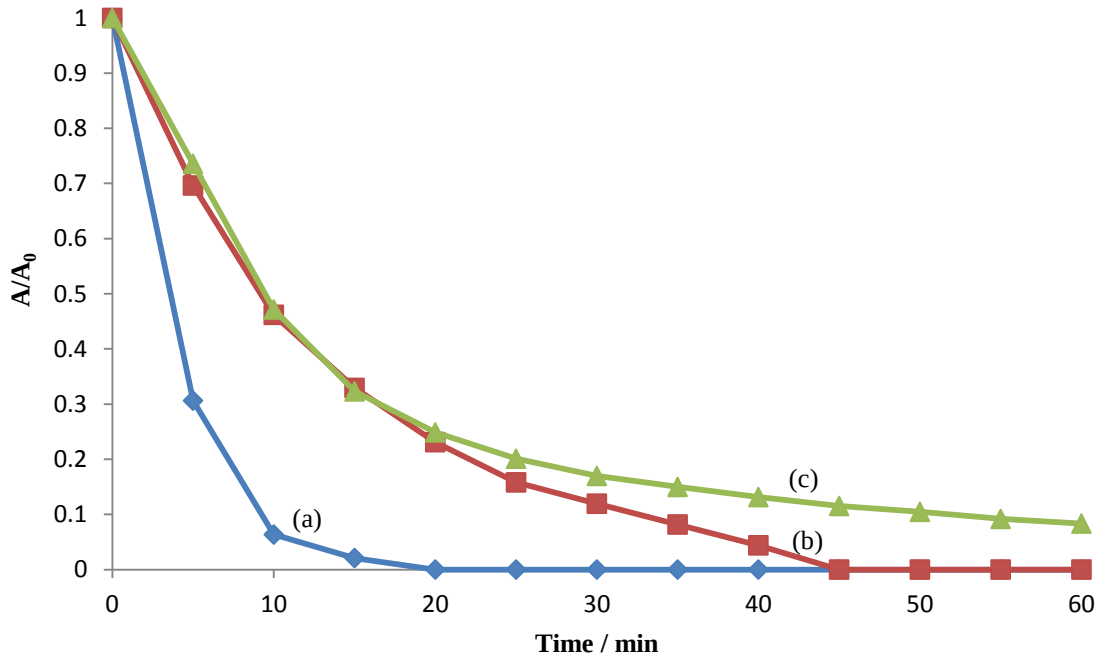

Figure 7. 11. Plots of: (a) $(A/A_0)_{625}$ of RB50, (b) $(A/A_0)_{715}$ of NGB and (c) $(A/A_0)_{500}$ of CR vs. ozonation time. 500 cm^3 of 100 mg dm^{-3} of the dye solutions was ozonised at 1.3 mg min^{-1} ozone dose that injected to the BCR by N_2 at flow rate of 1 dm^3 min^{-1}, at room temperature.

Dye		RB50	NGB	CR
Decolourisation rate constant	Type	1st Order	1st Order	2nd Order
	k_a / min $^{-1}$	0.26	0.07	0.19
	R^2	0.99	0.99	0.99
pH before		4.72	5.67	6.4
pH after		3.6	3.81	3.84
COD removal %		26.8	37	26.6

Table 7. 3. Summary of the first order decolourisation rate constants, pH values before and after 60 min ozonation and COD removal for RB50, NGB and CR vs. ozonation for the experiments depicted in fig. 711.

It may be seen from the table that the decolourisation of RB50 and NGB solutions were first order, but it was second order for CR solutions. The difference in the rates of decolourisation of the various dye solutions may be attributed to differences in the molecular structure of each dye. This is in broad agreement with the work of Arslan and Balcioglu[205] who studied the ozonation of 75 mg dm^{-3} of two diazo dyes, Reactive Yellow 84 and Reactive Black 5, in a column reactor for 1 h at an ozonation dose of 2340 mg and flow rate of 100 dm^3 h^{-1} at pH 12. The author reported a higher decolourisation for the black dye due to its less complicated molecular structure, and less (50%) molecular weight than that of the yellow dye. In addition, Muthukumar and Selvakumar[204] studied the ozonation of two mono-azo dyes, Acid Red 12, Acid Violet 12, and two diazo dyes, Acid Brown 14 and Acid Blue 113. The authors found that the time for complete decolourisation was always greater for diazo dyes than for mono-azo dyes, irrespective of the pH. In contrast, Poznyak et al.[114] studied the ozonation of Reactive Black 5, Direct Red 28 and Basic Green 4 in column reactor at ozone dose of 24 -31 mg dm^{-3} and flow rate of 500 cm^3 min^{-1} at initial pHs of 6.5, 6.9 and 3.7 respectively. The authors found that complete decolourisation for the three dyes was achieved after 2 min ozonation. In addition, Soares et al.[200] studied the ozonation of Acid Blue 113, Basic Red 14, Direct Blue 78, Disperse Violet 26, Reactive Blue 5, Reactive Yellow 3, Reactive Red 241 and Sulphur Black 1. The authors found that the ozonation is effective for decolourisation of almost all dyes with exception of Disperse Violet 26 and Sulphur Black 1 which presented much lower decolourisation. However, the decolourisation of Disperse Violet 26 was improved at higher ozone doses.

It may be seen from table 7.3 that the decolourisation rate constants of the dyes are different probably due to the different molecular structures and weights. The observed rate constants are in broad agreement with the work of Chu and Ma[129] who studied the

ozonation of two anthraquinone dyes: Reactive Blue 19 and Despise Violet 28, one diazo dye: Reactive Black 5, one tri-azo dye: Direct Green 26, one mono-azo dye: Reactive Violet 5 and one poly-azo dye: Direct Red 80. The authors found that at pH 4, decolourisation rate constant of the mono-azo dye was the greatest, and the lowest was for the poly-azo dye, reflecting the molecular structure effect on the decolourisation rate constants.

It may be seen from table 7.3 that COD removal after 60 min ozonation was about 27% for both the RB50 and CR solutions, and was about 37% for the NGB solution. The difference in the colour and COD removal indicates that the chromophore is first removed by the ozone, and the colour removal is not necessarily correlated with the COD removal as discussed in section 7.2.2. However, the chromophore of the RB50 molecule was the easiest to remove by ozone, then that of NGB and CR molecules, respectively (see fig. 7.11). The COD data are in general agreement with the work of Arslan and Balcioglu[205] who reported a higher COD removal rate for the black dye due to its less complicated molecular structure, and < 50 % of its molecular weight than that of the yellow dye. In addition, Poznyak et al.[114] found that the time required for COD removal was quite different; thus, the black dye decomposed within 10 min and the red one within only 1 min. Furthermore, Soares et al.[200] reported that for all dyes studied, the COD removal was low, with the reactive and direct dyes that showing the highest degradation rates. Comparing the reactive dyes, they found that Reactive Blue 5 presented the highest decolourisation and Reactive yellow the lowest. However, Reactive Red showed the highest COD removal.

The effect of ozonation on the pH of dye solutions after 60 min ozonation is shown in table 7.3. The pH after ozonation decreased for all of the dye solutions (see discussion above).

7.3 Decolourisation by Ultraviolet Irradiation

To investigate the possibility of the decolourisation of RB50, NGB and CR solutions by ultraviolet (UV) irradiation, 500 cm^3 of dye solution (100 mg dm^{-3}) was irradiated by UV lamp (λ_{max} = 254 nm) for one hour, the lamp placed in Pyrex tube that was surrounded by the dye solutions (as discussed in section 2.17). The variation in (A/A_0) was evaluated for the three dyes during the irradiation time and the results are shown in fig. 7.12. It may be seen from the figure that the only dye solution affected by the UV light was RB50 giving a value of $(A/A_0)_{625}$ = 0.72 after 60 min irradiation. In contrast, $(A/A_0)_{715}$ and $(A/A_0)_{500}$ of NGB and CR solution changed very little during the irradiation time; achieving only values

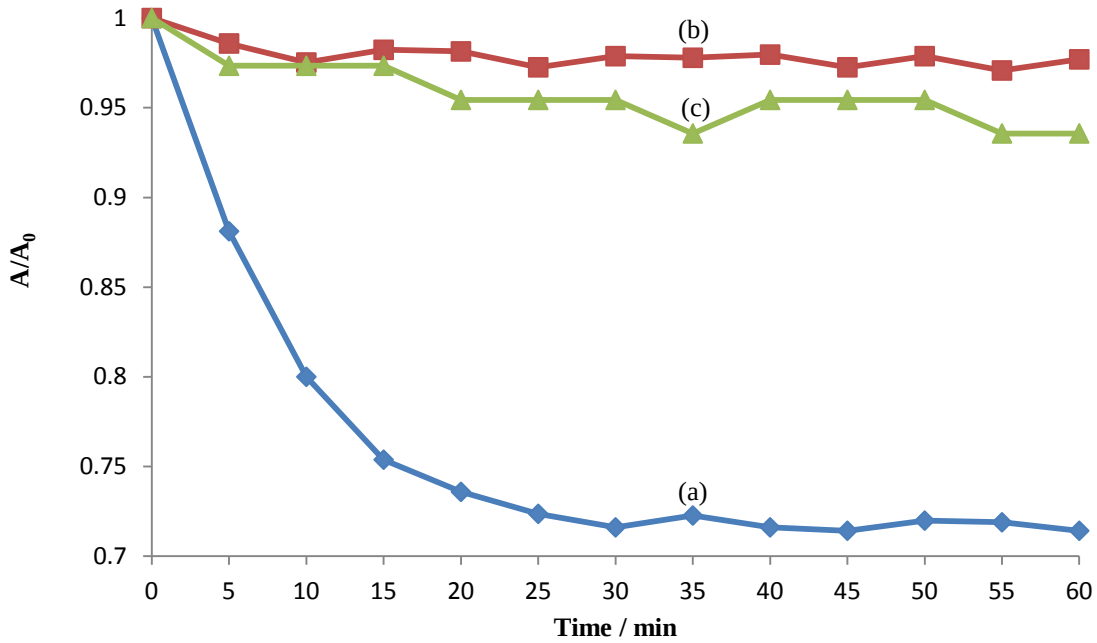

Figure 7. 12. Plots of: (a) $(A/A_0)_{625}$ of the 625 nm band of RB50 solution, (b) $(A/A_0)_{715}$ of the 715 nm band of NGB solution and (c) $(A/A_0)_{500}$ of the 500 nm band of CR solution vs. UV irradiation time. 500 cm^3 of 100 mg dm^{-3} of the dye solutions was irradiated along with N_2 injected to the bubble reactor at flow rate of 1 dm^3 min^{-1}.

of only 0.98 and 0.94 at the end of the experiments. The results of decolourisation of RB50 are in general agreement with the work of Haji et al.[192] who irradiated 7.8×10^{-5} M of Methyl Orange for 4 h using UV source (R-52 Mineralight® Lamp, 254 nm). The authors reported only 26% decolourisation after 4 hours irradiation, and they claimed that their results was due to the reaction between the dye and OH radicals that was generated due to water photolysis by UV. The results of the experiments on the decolourisation of the NGB and CR solutions are in general agreement with the work of Shu and Chang[198] who irradiated 20 mg dm^{-3} of Acid Orange 10 solution by UV light using low pressure mercury lamp and reported that the UV light alone was not able to decolourise the dye solution significantly.

No COD removal was obtained in the case of NGB and CR, and only 1.5 % of COD removal was achieved in the case of RB50. This suggest that removing the chromophore is the fastest part of dye molecule destruction, and it seems that the chromophore of the RB50 molecule is the easiest to remove by the UV light irradiation compared to NGB and CR molecules, and the dye molecule destruction remains harder by the irradiation.

7.4 Decolourisation by The O_3/UV_{254} Irradiation Combination

To investigate the effect of the combination of UV irradiation and ozonation (O_3/UV), as

discussed in section 2.18, 500 cm^3 of 100 mg dm^{-3} RB50, NGB and CR solutions was exposed to O_3 / UV simultaneously for 1 hour.

Figures 7.13 – 7.15 show the UV – Vis spectra of the RB50, NGB and CR solution, respectively taken during the O_3 / UV exposure at 1.3 mg min^{-1} ozone dose and 1 dm^3 min^{-1} flow rate at unadjusted pH, along with UV irradiation. As discussed in section 6.1, the spectra of these dye solutions have well defined bands in the UV and visible regions. It may be seen from the figures that intensities in the UV and visible regions decreased with O_3/UV exposure time, which suggests that degradation of the dye molecules and decolourisation occurred.

Figure 7.16 shows the $(A/A_0)_{625}$, $(A/A_0)_{715}$ and $(A/A_0)_{500}$ vs. O_3/UV exposure time for RB50, NGB and CR solutions, respectively, where the data were obtained from figs. 7.13 – 7.15. It may be seen from fig. 7.16 that the O_3/UV combination was effective in decolourising the three dye solutions. However, zero $(A/A_0)_{625}$ and $(A/A_0)_{715}$ could be achieved within 20 and 35 min, respectively, O_3/UV exposure time. In contrast, 60 min was not sufficient to reduce $(A/A_0)_{500}$ to less than 0.08. In case of RB50 and NGB, the decolourisation was 1st order, whereas it was second order for CR solutions from which the

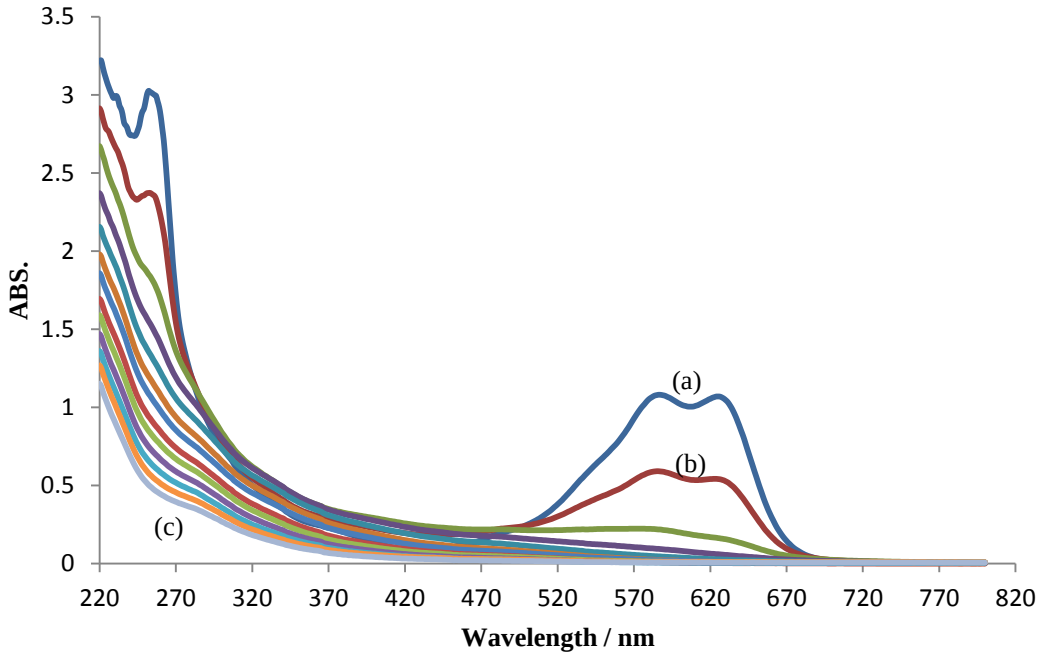

Figure 7. 13. UV – Vis spectra collected during the O_3/UV process of 500 cm^3 of RB50 solution (100 mg dm^{-3}) in bubble reactor at ozone dose of 1.3 mg min^{-1}, the ozone generated as described in fig. 7.1. The ozone flow rate into the bubble reactor was 1 dm^3 min^{-1}, the spectra collected at room temperature at: (a) before exposure, (b) after 5 min exposure, then every 5 min up to (c) 60 min.

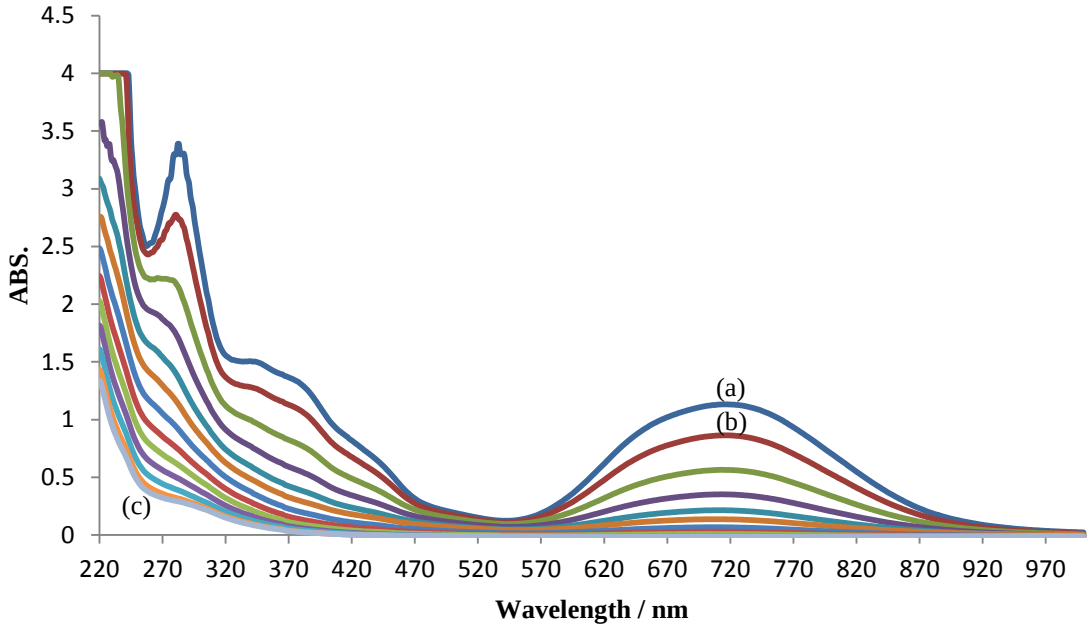

Figure 7. 14. UV – Vis spectra collected during the O_3/UV process of 500 cm^3 of NGB solution (100 mg dm^{-3}) in bubble reactor at ozone dose of 1.3 mg min^{-1}, the ozone generated as described in fig. 7.1. The ozone flow rate into the bubble reactor was 1 dm^3 min^{-1}, the spectra collected at room temperature at: (a) before exposure, (b) after 5 min exposure, then every 5 min up to (c) 60 min.

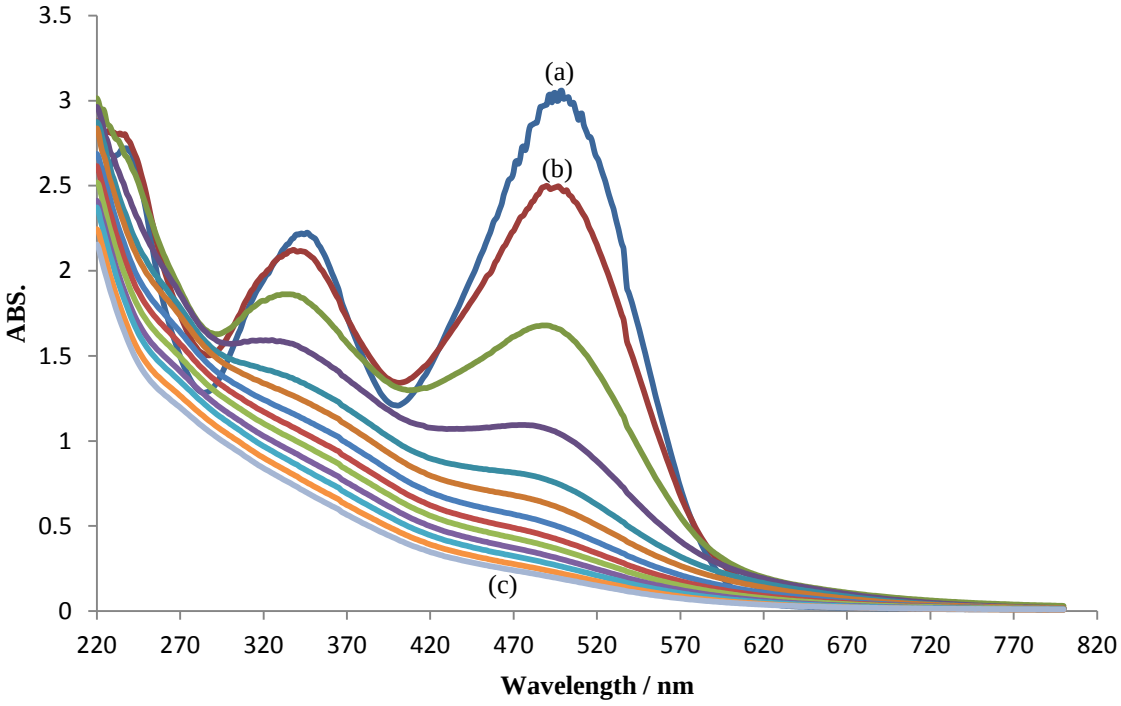

Figure 7. 15. UV – Vis spectra collected during the O_3/UV process of 500 cm^3 of CR solution (100 mg dm^{-3}) in bubble reactor at ozone dose of 1.3 mg min^{-1}, the ozone generated as described in fig. 7.1. The ozone flow rate into the bubble reactor was 1dm min^{-1}, the spectra collected at room temperature at: (a) before exposure, (b) after 5 min exposure, then every 5 min up to (c) 60 min.

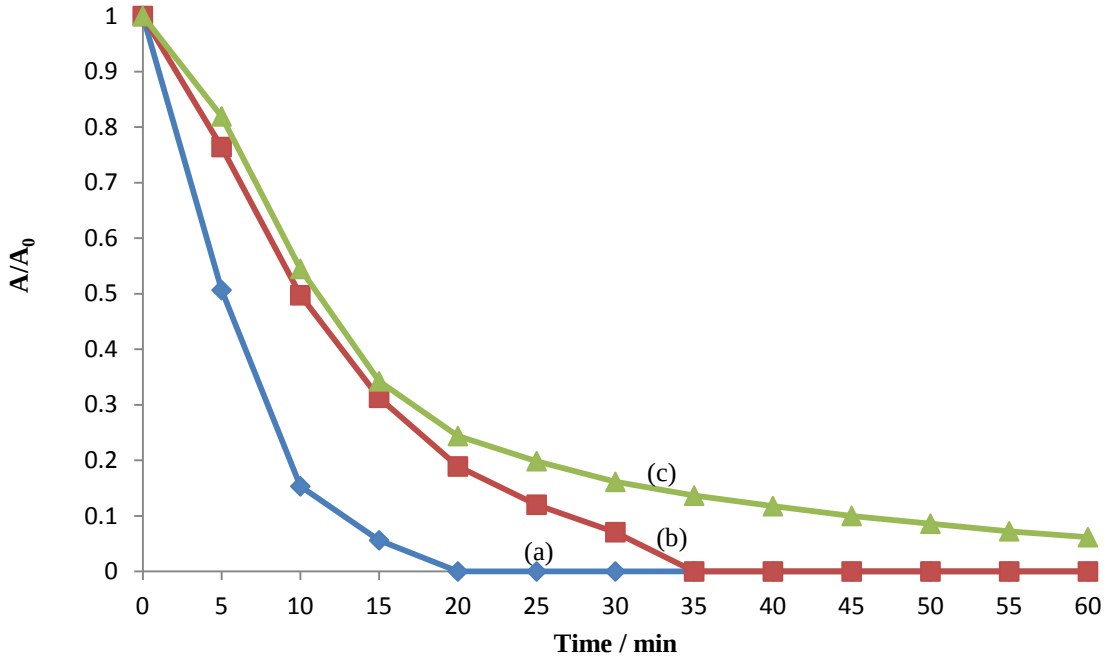

Figure 7. 16. Plots of: (a) $(A/A_0)_{625}$ of the 625 nm band of RB50 solution, (b) $(A/A_0)_{715}$ of the 715 nm band of NGB solution and (c) $(A/A_0)_{500}$ of the 500 nm band of CR solution vs. O_3/UV exposure time. 500 cm^3 of 100 mg $dm^{-3}$of the dye solutions was irradiated along with ozone dose of 1.3 mg min^{-1} injected to the bubble reactor by N_2 gas at flow rate of 1 dm^3 min^{-1}.

rate constants were calculated and are presented in table 7.4.

Dye		**RB50**	**NGB**	**CR**
Decolourisation rate constant	Type	1st Order	1st Order	2nd Order
	k_a / min^{-1}	0.19	0.08	0.12
	R^2	0.99	0.99	0.98
pH before		4.72	3.27	6.4
pH after		3.6	3.94	3.64
COD removal %		33	64	41

Table 7. 4. Summary of the first order decolourisation rate constants, pH values before and after 60 min and COD removal for RB50, NGB and CR, vs. O_3/UV process for the experiments depicted in fig. 7.16.

The use of UV light combined with O_3 reduced the time at which the zero $(A/A_0)_{715}$ was achieved of NGB solution, where 35 min was required instead of 45 min (see figs. 7.16 and 7.11). In addition, the reduction in $(A/A_0)_{500}$ after 60 min of O_3/UV process applied to the CR solution increased from 0.08 (O_3 only) to 0.06 (O_3/UV). This improvement in reducing the exposure time may be due to the formation of the OH radicals because of the decomposition of the O_3 molecule by the UV light or due to the effect of UV light on the dye molecular structure as discussed in section 1.3.4. [109, 133, 134] In contrast, little or no

improvement in the time required to decolourise the RB50 solution completely was achieved.

The findings in terms of RB50 solution decolourisation are in general agreement with the work of Shu and Chang[198] who studied the effect of ozonation and O_3/UV on the degradation of 22.4 mM of two diazo dyes (Direct Yellow 4 and Acidic Black 1), and four mono-azo dyes (Acid Yellow 17, Acid Red 14, Acid Red 18 and Acid Orange 10) in a column reactor with and without UV irradiation from a low pressure mercury lamp, at an ozonation flow rate of 6 $dm^3\,min^{-1}$. The authors reported that the presence of UV light hardly affected the decolourisation rates, and the two processes (with and without UV) resulted in exactly the same decolourisation (A/A_0) curves. In contrast, Muthukumar et al.[134] applied the O_3/UV on three mono-azo dyes: Acid Red 88, Acid Orange 7 and Acid Orange 10, and one diazo dye: Acid Red 73. The authors reported that the time required for complete decolourisation depended on the dye molecular structure where the diazo dye required the longest time for achieving the 100% decolourisation. However, the authors did not use ozone alone.

In terms of the COD removal, as presented in table 7.4, significant increase of the COD removal can be observed for the NGB solution from ca. 37% (O_3 only) to ca. 64% (O_3 / UV), and for RB50 and CR solutions from ca. 27% to ca. 33% and ca. 41%, respectively. The improvement in the COD removals is evident that other oxidising agents should be presented along with O_3 when using the O_3 / UV process. These oxidising agents probably are OH radicals (see discussion above). This improvement of COD removal because of the UV light combined with O_3 was also reported by Cuiping et al.[133] (see above for details), and Chen et al.[206] who studied the degradation of 2-naphthalenesulfonate by ozone and O_3/UV, using a low pressure mercury UV lamp, at an ozone dose of 44 $g\,m^{-3}$. The authors attributed the improvement to the formation of OH radicals due to ozone photolysis.

The effect of O_3/UV process on the pH of dye solutions after 60 min O_3/UV process is presented in table 7.4. It may be seen from the table that the pH value after treatment decreases for all of the dye solutions (see discussion in section 7.2.2). However, the use of UV light combined with O_3 caused little or no further decrease to the pH of the dye solutions studied compared to that of ozonation only (see tables 7.3 and 7.4), in contrast to the findings of Chen et al.[206], who reported that the O_3/UV resulted in more significant decrease of the pH than ozonation alone.

7.5 Comparison of the Efficiency of the Decolourising Methods Used

The comparison is carried out in terms of the decolourisation and the COD for the RB50, NGB and CR solutions. Therefore, the efficiency of the electrochemical (data from chapter 6), ozonation, UV irradiation and O_3/UV combination methods on decolourisation and COD removal was compared at the optimum conditions.

As discussed above in different section of this chapter and the previous chapter, the optimum conditions for decolourising dye solutions on 0.64 cm^2 NATO anodes were: 200 mg dm^{-3} dye concentration in 3 g dm^{-3} aqueous Na_2CO_3, at current density of 50 mA cm^{-2} and pH 11.1. For ozonation and O_3/UV combination: 100 mg dm^{-3} dye concentration, ozone dose of 1.3 mg min^{-1} and natural pH of 4.72.

7.5.1 RB50 solution

The reduction of $(A/A_0)_{625}$ of RB50 solutions by the decolourisation technologies employed, during the 60 min treatment time at the optimum conditions for each process is shown in fig. 7.17. It may be seen from the figure that all of the technologies used achieved zero $(A/A_0)_{625}$ after 20 minutes of treatment except for UV irradiation. In addition, ozonation showed the fastest and most efficient decolourisation in the first 15 min ozonation. Furthermore, ozonation, UV and O_3/UV decolourised 100 mg dm^{-3} of the RB50 solution, but 200 mg dm^{-3} was decolourised at the 0.64 cm^2 NATO anodes. This suggests the superior efficiency of NATO anodes on the other technologies studied.

In terms of the percentage of COD removal, only 27%, 1.5% and 33% COD removal using ozonation, UV irradiation and O_3/UV combination, respectively, was achieved in comparison to 97% COD removed using the 0.64 cm^2 NATO anodes (see table 6.5). Again, this reflects the superiority of the NATO anodes.

7.5.2 NGB solution

Figure 7.18 shows the variations of $(A/A_0)_{715}$ for NGB solutions under the optimum conditions using the decolourisation methods employed during the 60 min. It may be seen from the figure that all of the technologies used achieved zero $(A/A_0)_{625}$ at different operation times with the fastest achieved at 35 min using the O_3/UV combination, whereas 45 min of treatment was required for 0.64 cm^2 NATO anodes and ozonation. However, it seems that UV irradiation alone could not change the colour of NGB solutions. Taking into consideration the fact that the dye concentration decolourised using the 0.64 cm^2 NATO

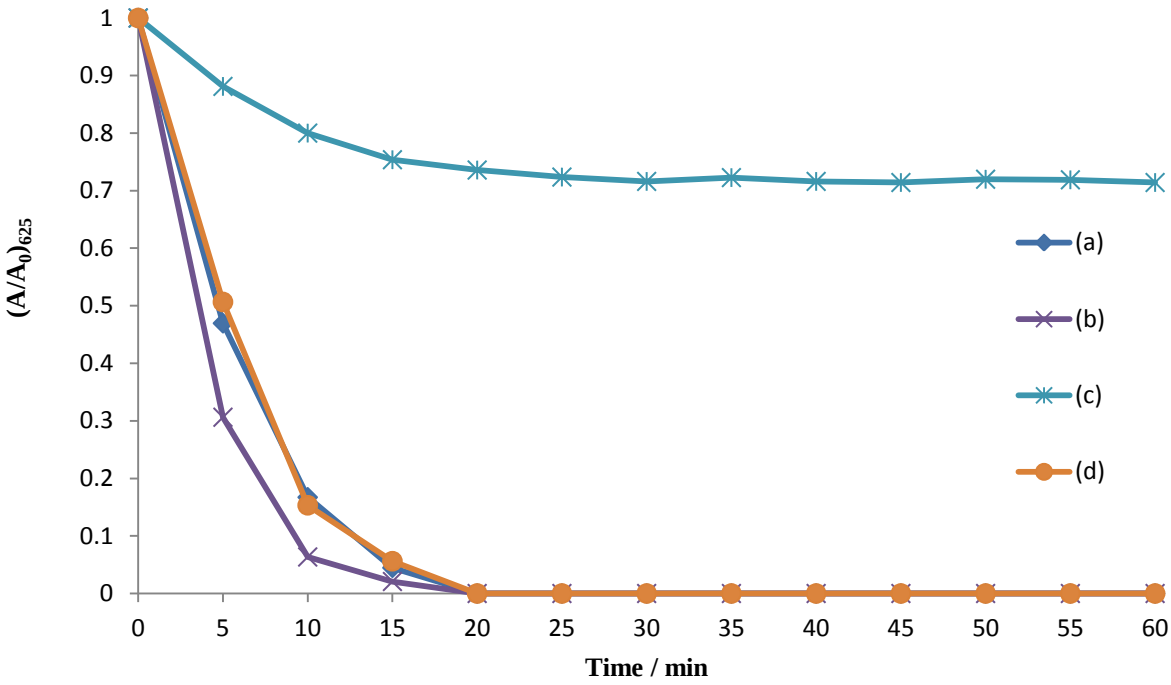

Figure 7. 17. Plots of $(A/A_0)_{625}$ of RB50 solutions vs. decolourisation time during the decolourisation at optimum conditions (see text) using: (a) 0.64 cm^2 NATO anodes, (b) ozonation, (c) UV irradiation, and (d) O_3/UV combination.

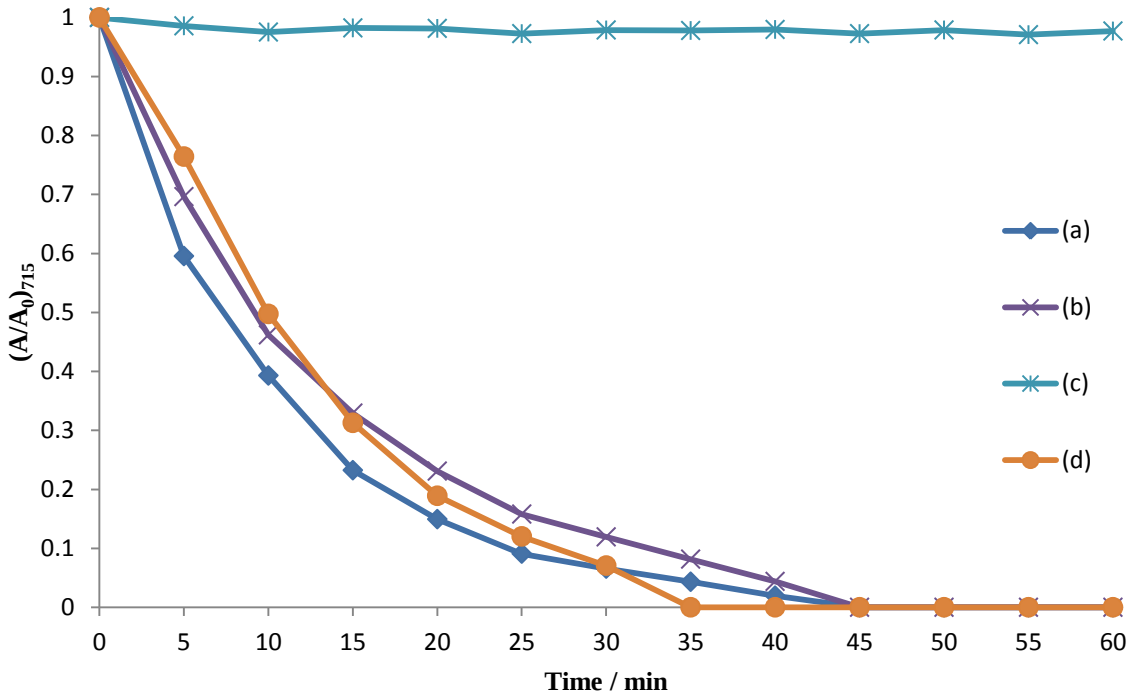

Figure 7. 18. Plots of $(A/A_0)_{715}$ of NGB solutions vs. decolourisation time during the decolourisation at optimum conditions (see text) using: (a) 0.64 cm^2 NATO anodes, (b) ozonation, (c) UV irradiation, and (d) O_3/UV combination.

anodes was twice as that used in the remaining decolourisation technologies may suggest the higher efficiency of the electrochemical decolourisation over the other decolourisation methods used.

The corresponding COD removal was not that good. The only methods that removed COD were ozonation and O_3/UV combination with 37 % and 64 %, respectively. However, little or no COD was removed using the remaining methods. The superiority of the O_3/UV combination in removing COD from NGB solution strongly suggests the effect of the dye structure and its susceptibility to a certain kind of decolourisation technology.

7.5.3 CR solution

Figure 7.19 shows the reduction of $(A/A_0)_{500}$ of CR solutions at the optimum conditions using the decolourisation technologies used. It may be seen from the figure that none of the technologies used could achieve the complete decolourisation of CR solutions (zero $(A/A_0)_{500}$). Nevertheless, all technologies except for UV irradiation when applied alone, could remove more than 90 % of the dye solution colour. Yet, the electrochemical decolourisation may be suggested as the superior technology (200 mg dm^{-3} dye concentration compared to 100 mg dm^{-3} used in the remaining methods).

The corresponding COD removal was not comparable to that of colour. The only methods

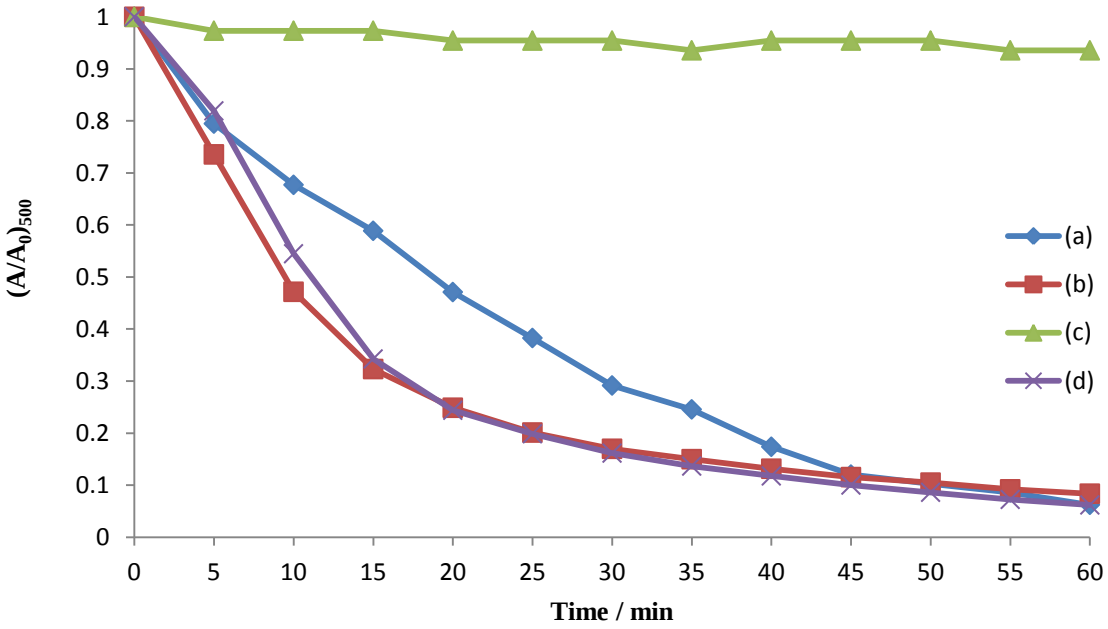

Figure 7. 19. Plots of $(A/A_0)_{500}$ of CR solutions vs. decolourisation time during the decolourisation at optimum conditions (see text) using: (a) 0.64 cm^2 NATO anodes, (b) ozonation, (c) UV irradiation, and (d) O_3/UV combination

that removed COD were ozonation and O_3/UV with 27 % and 41 %, respectively. Again, the effect of the dye molecular structure is clear.

7.5.4 pH at the end of the decolourisation

The pH values at the end of the experiments of different technologies are shown in table 7.5. It is clear from the table that the UV irradiation technology caused an increase of pH values for all dye solutions treated (may be due to the effect of the UV light on the dye structure). On the other hand, the remaining technologies have caused a decrease of the pH. This indicates that the byproducts of the technologies used, other than UV irradiation, were acidic, and might include organic and inorganic acids.

Dye Solution		***BR50***	***NGB***	***CR***
pH Before		*4.72*	*3.27*	*6.4*
pH After	*Ozonation*	*3.62*	*3.81*	*3.84*
	UV	*6.53*	*6.16*	*7.44*
	O_3/UV	*3.6*	*3.94*	*3.64*

Table 7. 5. pH values at the end of the decolourisation experiments by different technologies

7.6 Conclusions

In this chapter, the RB50, NGB and CR solutions were decolourised using ozone, UV irradiation and O_3/UV combination. The ozone was generated using MEA – based ozone generation system (MEA – OGS). The optimum conditions of the ozonation process were investigated, where: ozone dose of 1.3 mg min^{-1} carried by N_2 gas at flow rate of 1000 cm^3 min^{-1} and natural pH were obtained when decolourising the RB50 solutions by ozonation. The NGB and CR were decolourised by ozonation at those optimum conditions. The three dye solution then were irradiated by UV lamp (λ_{max} = 254 nm) for one hour and the RB50 solution was the only dye solution that was affected by the irradiation. A combination of the ozone (at optimum conditions) and the UV irradiation was used to decolourise the three dye solutions, where they were exposed to ozone and UV light simultaneously for 1 hour. This exposure resulted in clear improvement of the time required for the complete decolourisation of the NGB and CR solutions compared to that of ozonation alone or UV alone. In contrast, the same time was required for complete decolourisation for RB50 solution using ozone and O_3/UV combination. At the end of this chapter, a comparison between the decolourisation efficiencies of the ozone, UV, O_3/UV and electrochemical decolourisation using 0.64 cm^2 NATO anodes (data from chapter 6) was carried out.

In terms of the decolourisation and the benzene ring destruction of RB50 solution, the colour was removed faster than the benzene ring destructions in all cases.

The higher the current density at which the MEA – OGS was operated, the higher the ozone dose and the lower time required for complete decolourisation of RB50 solution. The effect of the buffered pH at 2, 7 and 11 on decolourising RB50 solutions was not significant, where the same time was required for the complete decolourisation. Although the decolourisation was faster when using buffered pH than non-buffered, the COD removal was much less especially at buffered pH 11. The dye structure effect was obvious when comparing the NGB and CR to RB50 decolourisation efficiency and COD removal by ozone.

UV irradiation alone failed to decolourise the dye solutions completely within one hour, and the only dye solution affected by the UV irradiation was RB50 where only ca. 28% and ca. 1.5% of the colour and COD was removed, respectively.

The ozone and UV irradiation combination was superior on the ozone alone or UV alone for decolourising the NGB and CR dye solutions, but it was not of significant effect on the decolourisation of the RB50 solution. In contrast, the COD removal was significantly improved when using the combination (O_3/UV) compared to ozone alone or UV alone.

Although the effect of the combination (O_3/UV) was significant on both the decolourisation and COD removal, still the electrochemical method was more efficient.

CHAPTER EIGHT

8 Conclusions

In terms of the 0.64 cm^2 anodes, replacing $SbCl_3$ and $NiCl_2$ by their oxides had little or no effect upon their electrochemical properties. The SNATO, AuSNATO and PbSNATO anodes were all porous with dimensionalities < 2, most probably due to electro inactive areas. The addition of Au to SNATO anodes reduced the ozone efficiency due to the relatively low oxygen overpotential of the metal. Lead had little or no effect. Current efficiencies of ca. 30% at cell voltages of ca. 2.7 V (ca. 85 mA cm^{-2}) could be routinely achieved with these anodes.

The scale up of the synthesis to 2.5 cm × 2.5 cm was achieved. Interestingly, replacing $SbCl_3$ and $NiCl_2$ with their respective oxides in the precursor solution and annealing the anodes at 550 ^oC in the furnace resulted in more durable anodes that were able to sustain significantly higher current densities (i.e. 100 mA cm^{-2}) cell voltages of ca. 3 V in acid electrolyte. These current densities are the highest reported to date as is the optimum lifetime of 200 h. Later work has increased this to 600 h. The highest current efficiency observed was 38%, with 25 -30% routinely achievable. The optimum Ni content (in the precursor solution) was found to be ca. 1.04 at % Ni, higher concentrations leading to increased resistance. The optimum furnace temperature was 460 ^oC.

Membrane Electrode Assemblies (MEA's) were successfully prepared for use with electrolyte – free water. The use of air breathing cathodes imposed a sever limitation on the current densities that could be sustained due to flooding of the cathode pores. The use of hydrogen – evolving cathodes overcome this problem as they do not suffer from flooding. Overall, with pure water as anolyte, the optimum current efficiency observed ca. 36% at a current density of ca. 40 mA cm^{-2} using air breathing cathode at cell voltage of 1.6 V; corresponding to a power consumption of 16.7 kWh kg^{-1} O_3, the lowest yet reported. The corresponding values observed using a H_2 cathode were 37% at ca. 50 mA cm^{-2}, corresponding to ca. 22 kWh kg^{-1} O_3.

The electrochemical decolourisation of solutions containing the dyes RB50, NGB and CR was investigated using the small (0.64 cm^2) anodes. Under optimum conditions of 3 g dm^{-3}

Na_2CO_3 as electrolyte, 50 mA cm^{-2} and 200 mg dm^{-3} dye in Millipore water. Complete decolourisation of RB50 solution was observed in 20 min, with 90% COD removal after 60 min, NGB and CR proved more recalcitrant. The NATO anodes degraded the dyes by indirect oxidation via OH radicals.

Decolourisation of dye – containing solutions was also investigated by ozone that was generated by MEA – based electrochemical cells. The ozonation took place in bubble column reactor on 500 cm^3 dye solution. The effect of UV irradiation alone and with ozone was also explored. The combination of ozone and UV proved the most effective, with complete decolourisation of RB50, NGB and CR requiring 20, 35 and more than 60 min, respectively, and 33%, 64% and 41% COD removal taking 60 min.

Although the effect of the combination (O_3/UV) was significant on both the decolourisation and COD removal, still the electrochemical method was more efficient.

CHAPTER NINE

9 Future Work

It is clear that a fundamental understanding of the structure of the NATO anodes is still lacking, with routine analytical techniques unable to detect the very small amounts of Ni present. Whilst it does not seem improbable that the active site for ozone involves Ni^{3+}, no definitive proof exists. Hence, there is an urgent need for a careful, methodical study of and Sb/SnO_2 powder prepared by the method developed in this thesis should be fully characterised using e.g. XRD, thermal analysis and XPS. The effect on this structure of adding various amounts of Ni should then be elucidated, along with the effect on current and ozone efficiency; eg a structure/activity relationship formulated. The latter will require new fabrication methods for MEA's based on powder anodes. A core aspect of this study will be to elucidate the oxidation state and environment of the Ni. Achieving the latter will be helpful in achieving the following:

- Ozone generation mechanisms on the $Ni/Sb – SnO_2$ anode surface,
- The role of all catalyst components and their effect on both ozone current efficiency and the generation mechanism,

It is important to investigating more parameters that affect the anode preparation, selectivity, activity and durability such as: using different EDIL, the type and purity of the ethanol used, furnace and oven temperatures, the composition of the precursor solution, …etc.

With respect to the MEA, achieving the following is crucial:

- Solving the flooding problem of the air breathing cathodes used in the MEA,
- Trying alternative membrane to Nafion 117 to get rid of the calcinations problem associated with Nafion to enable the use of salt – containing electrolytes such as tap water, this will open the door wide for unlimited applications.

In terms of the application side, investigating the following is important:

- Scaling up and investigating the ability to generate greater amount of ozone

required for large applications,

- Investigating the efficiency of the anodes to degrade different organics with small and large molecular weights,
- Trying different anode sizes and cell configurations to treat different types of industrial wastewater,
- Comparing the efficiency of the anodes with more advanced oxidation processes in treating different types of industrial wastewater.

10 References

1. C. F. Schönbein, *Bericht über die Verhandlungen der Naturforschenden Gesellschaft in Basel,* **4** (58), (1838-1840).
2. C. F. Schönbein, *Philos. Mag. (III),* **17** (*), 293 - 294 (1840).
3. C. F. Schönbein, *Seances Acad. Sci. Ser. C,* **10** (*), 706 - 710 (1840).
4. Y. H. Wang, S. Cheng, and K.-Y. Chan, *Green Chemistry,* **8** (6), 568-572 (2006).
5. M. B. Rubin, *Bull. Hist. Chem.,* **26** (1), 40 - 56 (2001).
6. T. Andrews and P. G. Tait, *Philosophical Transactions of the Royal Society of London,* **150** (*), 113 - 131 (1860).
7. L. M. Da Silva, D. V. Franco, J. C. Forti, W. F. Jardim, and J. F. C. Boodts, *Journal of Applied Electrochemistry,* **36** (5), 523-530 (2006).
8. L. M. Da Silva, L. A. De Faria, and J. F. C. Boodts, *Electrochimica Acta,* **48** 699 - 709 (2003).
9. A. J. Bard, R. Parsons, and J. Jordan, *Standard Potentials in Aqueous Solution,* p. 339, International Union of Pure and Applied Chemistry, New York and Basel (1985).
10. E. R. Kotz and S. Stucki, *J. Electroanal. Chem.,* **228** (1-2), 407-415 (1987).
11. J. R. Feng, D. C. Johnson, S. N. Lowery, and J. J. Carey, *J. Electrochem. Soc.,* **141** (10), 2708-2711 (1994).
12. K. Kaneda, M. Ikematsu, K. Kitsuka, M. Iseki, H. Matsuura, T. Higuchi, T. Hattori, T. Tsukamoto, and M. Yasuda, *Japanese Journal of Applied Physics Part 1-Regular Papers Brief Communications & Review Papers,* **45** (8A), 6417-6419 (2006).
13. A. Seidel, *Kirk-Othmer Encyclopedia of Chemical Technology*, p. 851, John Wiley & Sons, Inc, New Jersey (2006).
14. F. De Smedt, S. De Gendt, M. M. Heyns, and C. Vinckier, *J. Electrochem. Soc.,* **148** (9), G487-G493 (2001).
15. A. V. Levanov, I. V. Kuskov, E. E. Antipenko, and V. V. Lunin, *Russian Journal of Physical Chemistry A,* **82** (7), 1126-1131 (2008).
16. G. Gordon, G. E. Pacey, W. J. Cooper, and R. G. Rice, *Ozone-Science & Engineering,* **10** (4), 353-365 (1988).
17. S. Stucki, G. Theis, R. Kotz, H. Devantay, and H. J. Christen, *Journal of the Electrochemical Society,* **132** (2), 367-371 (1985).
18. A. Nemes, I. Fabian, and G. Gordon, *Ozone-Science & Engineering,* **22** (3), 287-304 (2000).
19. J. Hoigne and H. Bader, *Water Res.* , **10** 377 – 386 (1976).
20. M. L. Kilpatrick, C. C. Herrick, and M. Kilpatrick, *Journal of the American Chemical Society,* **78** (9), 1784 - 1789 (1956).
21. C. P. Meyer, C. M. Elsworth, and I. E. Galbally, *Rev. Sci. Instrum.,* **62** (1), 223-228 (1991).
22. K. Rakness, G. Gordon, B. Langlais, W. Masschelein, N. Matsumoto, Y. Richard, C. M. Robson, and I. Somiya, *Ozone-Science & Engineering,* **18** (3), 209-229 (1996).
23. D. Wabner and C. Grambow, *J. Electroanal. Chem.,* **195** (1), 95-108 (1985).
24. J. Kim and G. V. Korshin, *Ozone-Science & Engineering,* **30** (2), 113-119 (2008).

25. L. M. Da Silva, L. A. De Faria, and J. F. C. Boodts, *Pure Appl. Chem.*, **73** (12), 1871-1884 (2001).
26. D. V. Franco, W. F. Jardim, J. F. C. Boodts, and L. M. Da Silva, *Clean-Soil Air Water*, **36** (1), 34-44 (2008).
27. M. H. P. Santana, L. A. De Faria, and J. F. C. Boodts, *Journal of Applied Electrochemistry*, **35** (9), 915-924 (2005).
28. B. Eliasson and U. Kogelschatz, *Journal of Physics B-Atomic Molecular and Optical Physics*, **19** (8), 1241-1247 (1986).
29. P. C. Foller and C. W. Tobias, *J. Electrochem. Soc.*, **129** (3), 506-515 (1982).
30. Y. Beaufils, C. Comninellis, and P. Bowen, *5th European Symposium on Electrochemical Engineering*, **145** (*), 191-200 (1999).
31. S. Stucki, H. Baumann, H. J. Christen, and R. Kotz, *J. Appl. Electrochem.*, **17** (4), 773-778 (1987).
32. A. A. Babak, R. Amadelli, A. Debattisti, and V. N. Fateev, *Electrochimica Acta*, **39** (11-12), 1597-1602 (1994).
33. C. H. Hamann, A. Hamnett, and W. Vielstich, *Electrochemistry*, p. 531, Wiley-VCH, Weinheim (2007).
34. K. B. Oldham and J. C. Myland, *Fundamentals of Electrochemical Science*, p. 496, Academic Press Incorporated San Diego (1994).
35. J. O. M. Bockris and A. K. N. Reddy, *Modern Electrochemistry. 2*, p. 1432, Plenum, New York (1973).
36. L. M. Da Silva, M. H. P. Santana, and J. F. C. Boodts, *Quim. Nova*, **26** (6), 880-888 (2003).
37. M. H. P. Santana, L. A. De Faria, and J. F. C. Boodts, *Electrochim. Acta*, **49** (12), 1925-1935 (2004).
38. G. L. Putnam, R. W. Moulton, W. W. Fillmore, and L. H. Clark, *J. Electroanal. Chem.*, **93** (5), 211 - 221 (1948).
39. J. D. Seader and C. W. Tobias, *Industrial and Engineering Chemistry*, **44** (9), 2207 - 2211 (1952).
40. P. C. Foller and G. H. Kelsall, *Journal of Applied Electrochemistry*, **23** (10), 996-1010 (1993).
41. P. A. Michaud, M. Panizza, L. Ouattara, T. Diaco, G. Foti, and C. Comninellis, *Journal of Applied Electrochemistry*, **33** (2), 151-154 (2003).
42. P. A. Christensen, W. F. Lin, H. Christensen, A. Imkum, J. M. Jin, G. Li, and C. M. Dyson, *Ozone-Science & Engineering*, **31** (4), 287-293 (2009).
43. J. Larminie and A. Dicks, *Fuel cell systems explained*, p. 428, Wiley, Chichester (2003).
44. M. Katoh, Y. Nishiki, and S. Nakamatsu, *J. Appl. Electrochem.*, **24** (6), 489-494 (1994).
45. K. Arihara, C. Terashima, and A. Fujishima, *J. Electrochem. Soc.*, **154** (4), E71-E75 (2007).
46. L. M. Da Silva, D. V. Franco, L. G. Sousa, and I. C. Goncalves, *J. Appl. Electrochem.*, **40** (4), 855-864 (2010).
47. S. D. Han, J. D. Kim, K. S. Myung, R. K. Rana, and K. C. Singh, *Indian Journal of Chemical Technology*, **13** (2), 156 -161 (2006).
48. K. Onda, T. Ohba, H. Kusunoki, S. Takezawa, D. Sunakawa, and T. Araki, *J. Electrochem. Soc.*, **152** (10), D177-D183 (2005).
49. P. Tatapudi and J. M. Fenton, *Journal of the Electrochemical Society*, **140** (12), 3527-3530 (1993).

50. Y. Cui, Y. Wang, B. Wang, H. Zhou, K. Y. Chan, and Z. Y. Li, *J. Electrochem. Soc. ,* **156** (4), E75 - E80 (2009).
51. P. Tatapudi and J. M. Fenton, *Journal of the Electrochemical Society,* **141** (5), 1174-1178 (1994).
52. Y. Nishiki, N. Kitaori, and K. Nakamuro, *Ozone Sci. Eng.,* **33** (2), 114-120 (2011).
53. M. Katoh, Y. Nishiki, and S. Nakamatsu, *Meeting of the Journal Electrochemcial Society,* (1992).
54. F. Okada and K. Naya, *J. Electrochem. Soc.,* **156** (8), E125-E131 (2009).
55. H. Li, Y. Tang, Z. Wang, Z. Shi, S. Wu, D. Song, J. Zhang, K. Fatih, J. Zhang, H. Wang, Z. Liu, R. Abouatallah, and A. Mazza, *J. Power Sources,* **178** (1), 103-117 (2008).
56. T. Okada, S. Moller-Holst, O. Gorseth, and S. Kjelstrup, *Journal of Electroanalytical Chemistry,* **442** (1-2), 137-145 (1998).
57. T. I. Valdes and F. Moussy, *Biosensors & Bioelectronics,* **14** (6), 579-585 (1999).
58. C. N. Sawyer, P. L. McCarty, and G. F. Parkin, *Chemistry for environmental engineering and science*, p. 752, McGraw-Hill Science Engineering, Singapore (2002).
59. K. Kaneda, M. Ikematsu, Y. Koizumi, H. Minoshima, T. Rakuma, D. Takaoka, and M. Yasuda, *Electrochemical and Solid State Letters,* **8** (6), J13-J16 (2005).
60. M. I. Awad, S. Sata, K. Kaneda, M. Ikematsu, T. Okajima, and T. Ohsaka, *Electrochem. Commun.,* **8** (8), 1263-1269 (2006).
61. K. Arihara, C. Terashima, and A. Fujishima, *Electrochemical and Solid-State Letters,* **9** (8), D17 - D20 (2006).
62. A. Kraft, M. Stadelmann, M. Wunsche, and M. Blaschke, *Electrochemistry Communications,* **8** (5), 883-886 (2006).
63. K. Y. Chan and P. A. Christensen, (2011).
64. P. A. Christensen and A. Imkum, *Ozone-Science & Engineering,* **33** (5), 389-395 (2011).
65. E. I. Lash, R. D. Hornbeck, G. L. Putnam, and E. D. Boleter, *Journal of Electrochemical Society,* **98** (4), 134-137 (1951).
66. E. Briner, R. Haefeli and H. Paillard, *Helv. Chim. Acta,* **20** (1), 1510 - 1523 (1937).
67. E. Briner and A. Yalda, *Helvetica Chimica Acta,* **25** (6), 1188 - 1202 (1942).
68. R. Amadelli, A. De Battisti, D. V. Girenko, S. V. Kovalyov, and A. B. Velichenko, *Electrochimica Acta,* **46** (2-3), 341-347 (2000).
69. A. B. Velichenko, R. Amadelli, A. Benedetti, D. V. Girendko, S. V. Kovalyov, and F. I. Danilov, *J. Electrochem. Soc.,* **149** (9), C445-C449 (2002).
70. F. Fischer and K. Massenez, *Zeitschrift für anorganische Chemie,* **52** (1), 202 - 218 (1907).
71. B. Mazza, P. Pedeferri, and G. Re, *Electrochim. Acta,* **23** (2), 87-93 (1978).
72. F. Fischer and K. Bendixsohn, *Zeitschrift für anorganische Chemie,* **61** (1), 153 - 180 (1909).
73. J. Balej and M. Thumova, *Collect. Czech. Chem. Commun.,* **39** (12), 3409-3416 (1974).
74. M. I. Awad and M. M. Saleh, *Journal of Solid State Electrochemistry,* **14** (10), 1877-1883 (2010).
75. Y. H. Wang, S. A. Cheng, K. Y. Chan, and X. Y. Li, *Journal of the Electrochemical Society,* **152** (11), D197-D200 (2005).
76. P. A. Christensen, K. Zakaria, and T. P. Curtis, *Ozone-Science & Engineering,* **34** (1), 49 - 56 (2012).
77. P. A. Christensen, K. Zakaria, T. Yonar, and H. Christensen, *J. Electrochem. Soc.,*

160 (8), H405 - H413 (2013).
78. K. Kitsuka, K. Kaneda, M. Ikematsu, M. Iseki, K. Mushiake, and T. Ohsaka, *Electrochimica Acta,* **55** 31 - 36 (2009).
79. K. Kitsuka, K. Kaneda, M. Ikematsu, M. Iseki, K. Mushiake, and T. Ohsaka, *Journal of the Electrochemical Society,* **157** (2), F30-F34 (2010).
80. J. E. Graves, D. Pletcher, R. L. Clarke, and F. C. Walsh, *Journal of Applied Electrochemistry,* **22** (3), 200-203 (1992).
81. N. Katsuki, E. Takahashi, M. Toyoda, T. Kurosu, M. Iida, S. Wakita, Y. Nishiki, and T. Shimamune, *Journal of the Electrochemical Society,* **145** (7), 2358-2362 (1998).
82. M. Panizza and G. Cerisola, *Electrochimica Acta,* **51** (2), 191-199 (2005).
83. A. Kapalka, G. Foti, and C. Comninellis, *Electrochim. Acta,* **54** (7), 2018-2023 (2009).
84. B. Marselli, J. Garcia-Gomez, P. A. Michaud, M. A. Rodrigo, and C. Comninellis, *J. Electrochem. Soc.,* **150** (3), D79-D83 (2003).
85. C. A. Martinez-Huitle and E. Brillas, *Applied Catalysis B-Environmental,* **87** (3-4), 105-145 (2009).
86. P. A. Michaud, E. Mahe, W. Haenni, A. Perret, and C. Comninellis, *Electrochemical and Solid State Letters,* **3** (2), 77-79 (2000).
87. H. Bader and J. Hoigne, *Water Research,* **15** (4), 449-456 (1981).
88. S. Rau, *AirTree Europe GmbH,* (2009).
89. K. Sehested, H. Corfitzen, J. Holcman, and E. J. Hart, *J. Phys. Chem. A,* **102** 2667 – 2672 (1998).
90. J. B. Parsa and M. Abbasi, *J Solid State Electrochem,* **16** 1011 - 1018 (2012).
91. J. B. Parsa, M. Abbasi, and A. Cornell, *Journal of The Electrochemical Society,* **159** (5), D265 - D269 (2012).
92. H. Shekarchizade and K. M. Amini, *International Journal of Electrochemistry,* **2001** (1 - 13), 1 (2011).
93. S. A. Cheng and K. Y. Chan, *Electrochemical and Solid State Letters,* **7** (3), D4-D6 (2004).
94. M.-O. Buffle, J. Schumacher, E. Salhi, M. Jekel, and U. V. Gunten, *Water Res.,* **40** 1884 - 1894 (2006).
95. R. E. Buhler, J. Staehelin, and J. Hoigne´, *J. Phys. Chem.,* **99** 2560 – 2564 (1984).
96. M. K. Phibbs and P. A. Giguere, *Canadian journal of chemistry,* **29** (6), 490-493 (1951).
97. R. B. Holt, C. K. McLane, and O. Oldenberg, *The Journal of Chemical Physics,* **16** (3), 225 - 229 (1948).
98. H. Y. Ding, Y. J. Feng, and J. F. Liu, *Materials Letters,* **61** 4920 - 4923 (2007).
99. F. Montilla, E. Morallon, A. De Battisti, and J. L. Vazquez, *Journal of Physical Chemistry B,* **108** (16), 5036-5043 (2004).
100. L. Lipp and D. Pletcher, *electrochimica Acta,* **42** 1091 - 1099 (1997).
101. B. Correa-Lozano, C. Comninellis, and A. DeBattisti, *Journal of Applied Electrochemistry,* **27** (8), 970-974 (1997).
102. A. Chen and S. Nigro, *The Journal of Physical Chemistry B,* **107** 13341 - 13348 (2003).
103. X. Y. Li, Y. H. Cui, Y. J. Feng, Z. M. Xie, and J. D. Gu, *Water Research,* **39** 1972 - 1981 (2005).
104. D. V. Franco, L. M. Da Silva, W. F. Jardim, and J. F. C. Boodts, *Journal of the Brazilian Chemical Society,* **17** (4), 746-757 (2006).
105. W. El-Shall, H. Khordagui, O. El-Sebaie, F. El-Sharkawi, and G. H. Sedahmed,

Desalination, **99** 149 - 157 (1994).
106. A. Hickling and S. Hill, *Transactions of the Faraday Society,* **46** (0), 557 - 559 (1950).
107. R. Amadelli, L. Armelao, A. B. Velichenko, N. V. Nikolenko, D. V. Girenko, S. V. Kovalyov, and F. I. Danilov, *Electrochimica Acta,* **45** (4-5), 713-720 (1999).
108. W. Siemens, *Poggendorffs Ann. Phys. Chem.,* **102** 66 (1857).
109. J. R. Domınguez, J. Beltran, and O. Rodrıguez, *Catalysis Today,* **101** 389–395 (2005).
110. M. Karatas, Y. A. Argun, and M. E. Argun, *Journal of Industrial and Engineering Chemistry,* **18** 1058 - 1062 (2012).
111. M. Rivera, M. Pazos, and M. A. Sanromán, *Desalination,* **274** 39 - 43 (2011).
112. Y. Yavuz, A. S. Koparal, and U. B. Ogutveren, *J Chem Technol Biotechnol,* **86** 261 - 265 (2011).
113. E. Forgacs, T. Cserhati, and G. Oros, *Environment International,* **30** (7), 953 - 971 (2004).
114. T. Poznyak, P. Colindres, and I. Chairez, *J. Mex. Chem. Soc.,* **51** (2), 81-86 (2007).
115. J. H. B. Rocha, A. M. S. Solano, N. S. Fernandes, D. R. Da Silva, J. M. P. Hernandez, and C. A. Martınez-Huitle, *Electrocatal,* **3** (1 - 12), 1 (2012).
116. D. Montanaro and E. Petrucci, *Chemical Engineering Journal,* **153** 138 - 144 (2009).
117. E. Petrucci and D. Montanaro, *Chemical Engineering Journal,* **174** 612 - 618 (2011).
118. T. Robinson, G. McMullan, R. Marchant, and P. Nigam, *Bioresource Technology,* **77** (3), 247–255 (2001).
119. Y. Yavuz and R. Shahbazi, *Separation and Purification Technology,* **85** 130 - 136 (2012).
120. Y. M. Vera, R. J. de Carvalho, M. L. Torem, and B. A. Calfa, *Chemical Engineering Journal,* **155** 691 - 697 (2009).
121. G. Chen, *Separation and Purification Technology,* **38** 11 - 41 (2004).
122. J. B. Parsa and M. Abbasi, *Acta Chim. Slov.,* **54** 792 - 796 (2007).
123. E. Kusmierek, E. Chrzescijanska, M. Szadkowska-Nicze, and J. K. Czaplinska, *J Appl Electrochem,* **41** 51 - 62 (2011).
124. P. Kariyajjanavar, N. Jogttappa, and Y. A. Nayaka, *Journal of Hazardous Materials,* **190** 952 - 961 (2011).
125. C. Comninellis, *Electrochimica Acta,* **39** (11/12), 1857-1862 (1994).
126. E. Tsantaki, T. Velegraki, A. Katsaounis, and D. Mantzavinos, *Journal of Hazardous Materials,* **207 - 208** 91 - 96 (2012).
127. A. AL-Kdasi, A. IDRIS, K. SAED, and C. T. GUAN, *Global Nest: the Int. J.,* **6** (3), (2004).
128. S. Baig and P. A. Liechti, *Water Science and Technology,* **43** 197 - 204 (2001).
129. W. Chu and C.-W. Ma, *Wat. Res.,* **34** (12), 3153 - 3160 (2000).
130. H. Zhou and D. W. Smith, *Journal Environmental Engineering Science,* **1** 247 - 264 (2002).
131. K. R. Rajeswari, *in* "Department of Physics", Vol. Ph. D. University Malaysia, Kuala Lumpur, 2000.
132. N. Azbar, T. Yonar, and K. Kestioglu, *Chemosphere,* **55** 35 - 43 (2004).
133. B. Cuiping, X. Xianfeng, G. Wenqi, F. Dexin, X. Mo, G. Zhongxue, and X. Nian, *Desalination,* **278** 84 - 90 (2011).
134. M. Muthukumar, D. Sargunamani, and N. Selvakumar, *Dyes and Pigments,* **65** 151 - 158 (2005).

135. G. T. Guyer and N. H. Ince, *Ultrasonics,* **42** 603 - 609 (2004).
136. P. Trogadas, E. Pinot, and T. F. Fuller, *Electrochemical and Solid State Letters,* **15** (1), A5-A8 (2012).
137. T. C. Wen and C. C. Chang, *J. Electrochem. Soc.*, **140** (10), 2764-2770 (1993).
138. F. Vicent, F. Morallón, C. Quijada, J. L. Vázquez, and A. Aldaz, *Journal of Applied Electrochemistry,* **28** 607 - 612 (1998).
139. A. P. Christensen and A. Hamnett, *Techniques and Mechanisms in Electrochemistry*, p. 379, Chapman and Hall, Oxford (1994).
140. C. H. Hamann, A. Hamnett, and W. Vielstich, *Electrochemistry*, p. 423, Wiley - VCH, New York (1998).
141. W. G. Pell and B. E. Conway, *J. Electroanal. Chem.*, **500** 121 - 133 (2001).
142. N. L. Wu, *Materials Chemistry and Physics*, **75** 6 - 11 (2002).
143. M. Strømme, G. A. Niklasson, and C. G. Granqvist, *Solid State Communications,* **96** (3), 151 - 154 (1995).
144. J. Agrisuelas, J. J. García-Jareño, D. Gimenez-Romero, F. Negrete, and F. Vicente, *J Solid State Electrochem,* **13** 1599 - 1603 (2009).
145. C. P. Andrieux and P. Audebert, *J. Phys. Chem. B.*, **105** (2), 444 - 448 (2001).
146. L. Nyikos and T. Pajkossy, *Electrochimica Acta*, **31** (10), 1347 - 1350 (1986).
147. C. A. Martínez-Huitle, E. V. D. Santos, D. M. D. Araújo, and M. Panizza, *Journal of Electroanalytical Chemistry*, **674** 103 - 107 (2012).
148. A. D. Eaton, L. S. Clesceri, and A. E. Greenburg, *Standard Methods for the Examination of Water and Wastewater*, American Public Health Association (APHA), Washinton D.C (1998).
149. D. R. Lide, *CRC Handbook of Chemistry and Physics*, Chemical Rubber Publishing Company, U.S.A. (1991).
150. F. Montilla, E. Morallon, A. De Battisti, A. Benedetti, H. Yamashita, and J. L. Vazquez, *Journal of Physical Chemistry B,* **108** (16), 5044-5050 (2004).
151. F. Montilla, E. Morallon, A. De Battisti, S. Barison, S. Daolio, and J. L. Vazquez, *Journal of Physical Chemistry B,* **108** (41), 15976-15981 (2004).
152. J. O. M. Bockris and A. K. M. Shamshul Huq, *Proc. R. Soc. Lond. A,* **237** 277 - 296 (1956).
153. M. Strømme, G. A. Niklasson, and C. Q. Granqvist, *Phys. Rev. B,* **52** (19), 14192 - 14196 (1995).
154. J. Isidorsson, M. Stromme, R. Gahlin, G. A. Niklasson, and C. G. Granqvist, *Solid State Communications,* **99** (2), 109 - 111 (1996).
155. S. Shanthi, C. Subramanian, and P. Ramasamy, *Journal of Crystal Growth,* **197** (4), 858-864 (1999).
156. K. Y. Rajpure, M. N. Kusumade, M. N. Neumann-Spallart, and C. H. Bhosale, *Materials Chemistry and Physics*, **64** (3), 184-188 (2000).
157. R. Kotz, S. Stucki, and B. Carcer, *Journal of Applied Electrochemistry,* **21** (1), 14-20 (1991).
158. E. Shanthi, V. Dutta, A. Banerjee, and K. L. Chopra, *Journal of Applied Physics,* **51** (12), 6243-6251 (1980).
159. B. Correa-Lozano, C. Comninellis, and A. DeBattisti, *Journal of the Electrochemical Society*, **143** (1), 203-209 (1996).
160. H. W. Lehmann and R. Widmer, *Thin Solid Films,* **27** (2), 359-368 (1975).
161. K. L. Chopra, S. Major, and D. K. Pandya, *Thin Solid Films,* **102** (1), 1-46 (1983).
162. Y. Feng, Y. Cui, B. Logan, and Z. Liu, *Chemosphere* **70** 1629 – 1636 (2008).
163. Y. Cui, Y. Feng, J. Liu, and N. Ren, *Journal of Hazardous Materials,* **239 - 240** 225 - 232 (2012).

164. P. A. Christensen, T. Yoner, and K. Zakaria, *Ozone: Science & Engineering,* **35** 149 - 167 (2013).
165. Y. H. Wang, K. Y. Chan, X. Y. Li, and S. K. So, *Chemosphere* **65** 1087 – 1093 (2006).
166. J. F. Wang, H. C. Chen, W. X. Wang, W. B. Su, and G. Z. Zang, *Materials Science and Engineering B-Solid State Materials for Advanced Technology,* **99** (1-3), 465-469 (2003).
167. M. N. Rumyantseva, O. V. Safonova, M. N. Boulova, L. I. Ryabova, and A. M. Gas'kov, *Russian Chemical Bulletin,* **52** (6), 1217-1238 (2003).
168. F. H. Aragon, J. A. H. Coaquira, P. Hidalgo, S. W. da Silva, S. L. M. Brito, D. Gouvea, and P. C. Moraisa, *Journal of Raman Spectroscopy,* **42** (5), 1081-1086 (2010).
169. E. C. G. Rufino, M. H. P. Santana, L. A. De Faria, and L. M. Da Silva, *Chemical Papers,* **64** (6), 749 - 757 (2010).
170. P. C. Foller and C. W. Tobias, *Journal of the Electrochemical Society,* **129** (3), 567-570 (1982).
171. G. Kelsall and P. A. Christensen, 2011.
172. M. Pourbaix, *Atlas of Electrochemical Equilibria in Aqueous Solutions*, p. 342, National Association of Corrosion Engineering, Texas (1974).
173. D. D. Wagman, W. H. Evans, V. B. Parker, R. H. Schumm, I. Halow, S. M. Bailey, K. L. Churney, and R. L. Nuttall, *Journal of Physical and Chemical Reference Data,* **11** (2), 1807-1812 (1982).
174. F. A. Cotton, and G. Wilkinson, C. A. Murillo and M. Bochmann, *Advanced Inorganic Chemistry,* p. 854, Wiley - VCH, Toronto (1999).
175. D. Gardoni, A. Vailati, and R. Canziani, *Ozone: Science & Engineering,* **34** 233 - 242 (2012).
176. F. Onda and K. Naya, *Journal of The Electrochemical Society,* **156** (8), E125 - E131 (2009).
177. Y.-H. Wang, S. Cheng, and K.-Y. Chan, *Green Chemistry,* **8** (6), 568-572 (2006).
178. M. Faouzi, P. Canizares, A. Gadri, J. Lobato, B. Nasr, R. Paza, M. A. Rodrigo, and C. Saez, *Electrochimica Acta,* **52** 325 - 331 (2006).
179. A. J. Méndez-Martínez, M. M. Dávila-Jiménez, O. Ornelas-Dávila, M. P. Elizalde-González, U. Arroyo-Abad, I. Sirés, and E. Brillas, *electrochimica Acta,* **59** 140 - 149 (2012).
180. J. Grebel, J. J. Pignatello, and A. Mitch, *Environ. Sci. Technol.,* **44** 6822 - 6728 (2010).
181. C. E. Housecroft and E. C. Constable, *Chemisrty*, p. 1517, Pearson Education Limited, Essex (2010).
182. A. Fernandes, A. Morao, M. Magrinho, A. Lopes, and I. Goncalves, *Dyes and Pigments,* **61** 287 - 296 (2004).
183. Z. M. Shen, D. Wu, J. Yang, T. Yuan, W. H. Wang, and J. P. Jia, *journal of hazardous Materials B,* **131** 90 - 97 (2006).
184. M. Riera-Torres and C. Gutiérrez-Bouzán, *Separation and Purification Technology,* **98** 375 - 382 (2012).
185. W. Miled, A. Haj Said, and S. Roudesli, *JTATM,* **6** (3), 1 - 6 (2010).
186. J. M. Aquino, M. A. Rodrigo, R. C. Rocha-Filho, C. Sáez, and P. Canizares, *Chemical Engineering Journal,* **184** 221 - 227 (2012).
187. P. Canizares, C. Saez, J. Lobato, R. Paz, and M. A. Rodrigo, *J. Electroanal. Chem.,* **154** (3), E37 - E44 (2007).
188. M. Panizza and G. Cerisola, *Journal of Hazardous Materials,* **153** 83 - 88 (2008).

189. N. Bensalaha, M. A. Quiroz Alfarob, and C. A. Martínez-Huitle, *Chemical Engineering Journal,* **149** 348 - 352 (2009).
190. M. C. Gutiérrez, M. Pepió, M. Crespi, and N. Mayor, *Color. Technol.,* **117** 356 - 361 (2001).
191. P. J. Hauser, *Advances in Treating Textile Effluent*, p. 154, InTech, Rijeka (2011).
192. S. Haji, B. Benstaali, and N. Al-Bastaki, *Chemical Engineering Journal,* **168** 134 - 139 (2011).
193. A. Mukimin, K. Wijaya, and A. Kuncaka, *Separation and Purification Technology,* **95** 1 - 9 (2012).
194. M. Panizza and G. Cerisola, *Applied Catalysis B: Environmental,* **75** 95 - 101 (2007).
195. P. Canizares, A. Gadri, J. Lobato, B. Nasr, R. Paz, M. A. Rodrigo, and C. Saez, *Ind. Eng. Chem. Res.,* **45** 3468 - 3473 (2006).
196. M. Rivera, M. Pazos, and M. A. Sanroman, *J Chem Technol Biotechnol,* **84** 1118 - 1124 (2009).
197. M. H. P. Santana, L. M. Da Silva, A. C. Freitas, J. F. C. Boodts, K. C. Fernandes, and L. A. De Faria, *Journal of Hazardous Materials,* **164** 10 - 17 (2009).
198. H. Y. Shu and M. C. Chang, *Dyes and Pigments,* **65** 25 - 31 (2005).
199. F. Pan, Y. Luo, J. J. Fan, D. C. Liu, and J. Fu, *Clean Soil Air Water,* **40** 422 - 427 (2012).
200. O. S. G. P. Soares, J. J. M. Orfao, D. Portela, A. Vieira, and M. F. R. Pereira, *journal of hazardous Materials B,* **137** 1664 - 1673 (2006).
201. K. Turhan, I. Durukan, S. A. Ozturkcan, and Z. Turgut, *Dyes and Pigments,* **92** 897 - 901 (2012).
202. J. Wu and T. Wang, *wat. Res.*, **35** 1093 - 1099 (2001).
203. I. A. Balcioglu and I. Arslan, *Water Science and Technology,* **43** 221 - 228 (2001).
204. M. Muthukumar and N. Selvakumar, *Dyes and Pigments,* **62** 221 - 228 (2004).
205. I. Arslan and I. A. Balcioglu, *Desalination,* **130** 61 - 71 (2000).
206. Y. H. Chen, C. Y. Chang, S. F. Huang, C. Y. Chiu, D. Ji, N. C. Shang, Y. H. Yu, P. C. Chiang, Y. Ku, and J. N. Chen, *Wat. Res.,* **36** 4144 - 4154 (2002).

11 Appendices

11.1 Appendix I: An Overview of Electrode Kinetics

Consider aqueous Fe^{2+} and Fe^{3+} ions in equilibrium with an electrode at a potential E1; the oxidation of $Fe(H_2O)_6^{2+}$ and reduction of $Fe(H_2O)_6^{3+}$ may be represented by[33]:

$$Fe(H_2O)_6^{2+} \leftrightarrow Fe(H_2O)_6^{3+} + e^- \quad (a1)$$

The equilibrium in equation (a1) can be represented simplistically by fig. A.1. Electron transfer is postulated as taking place *via* an activated complex as shown. If the potential on the electrode is decreased from E_1 to E_2 ($E_2 < E_1$, *ie* ΔE is negative), only the Gibbs Free Energy of the electrons in the metal is affected, *so long as neither* $Fe(H_2O)_6^{3+}$ *nor* $Fe(H_2O)_6^{2+}$ *is adsorbed*, and this increases by $\Delta G = -zF\Delta E$, where z is the number of electrons transferred (z = 1 in this case) and F is Faraday's constant = 96480 C mol^{-1}. Not all of the increase in free energy is reflected in the change in the free energy of the activated complex, since there is no change in the free energy of the $Fe(H_2O)_6^{2+}$; the fractional change in ΔG is $(1 - \beta)$, see fig. A.2, where β is termed the asymmetry

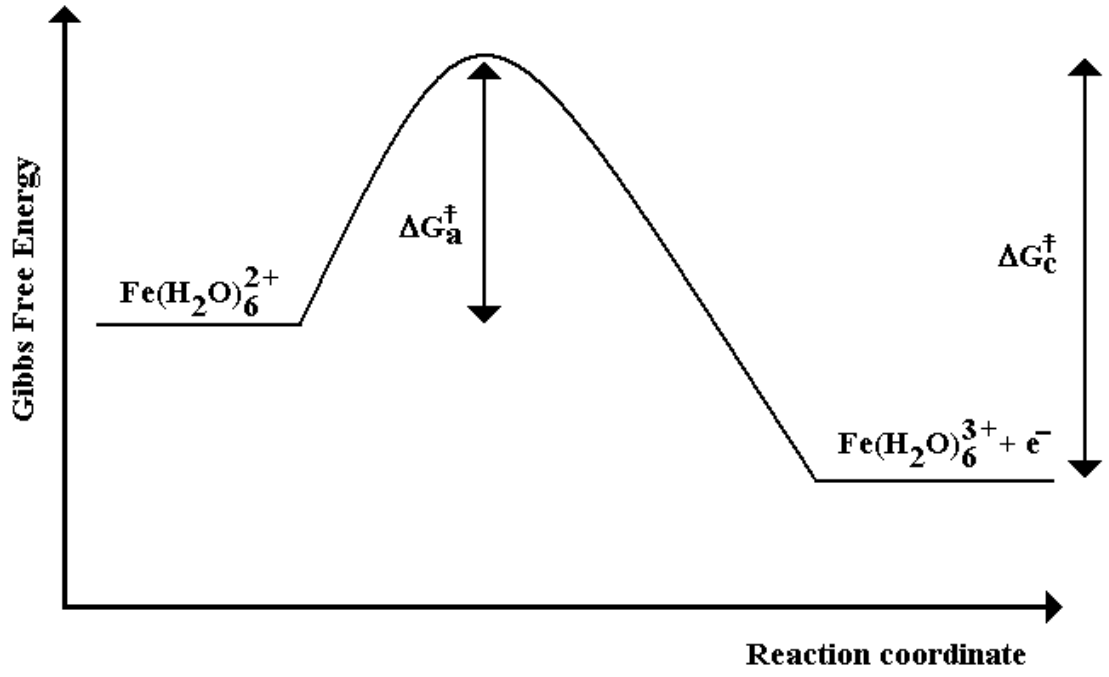

Figure A. 1. Schematic representation of the Gibbs Free Energy change during electron transfer between a metal electrode and the $Fe(H_2O)_6^{3+}/Fe(H_2O)_6^{2+}$ *redox couple.*

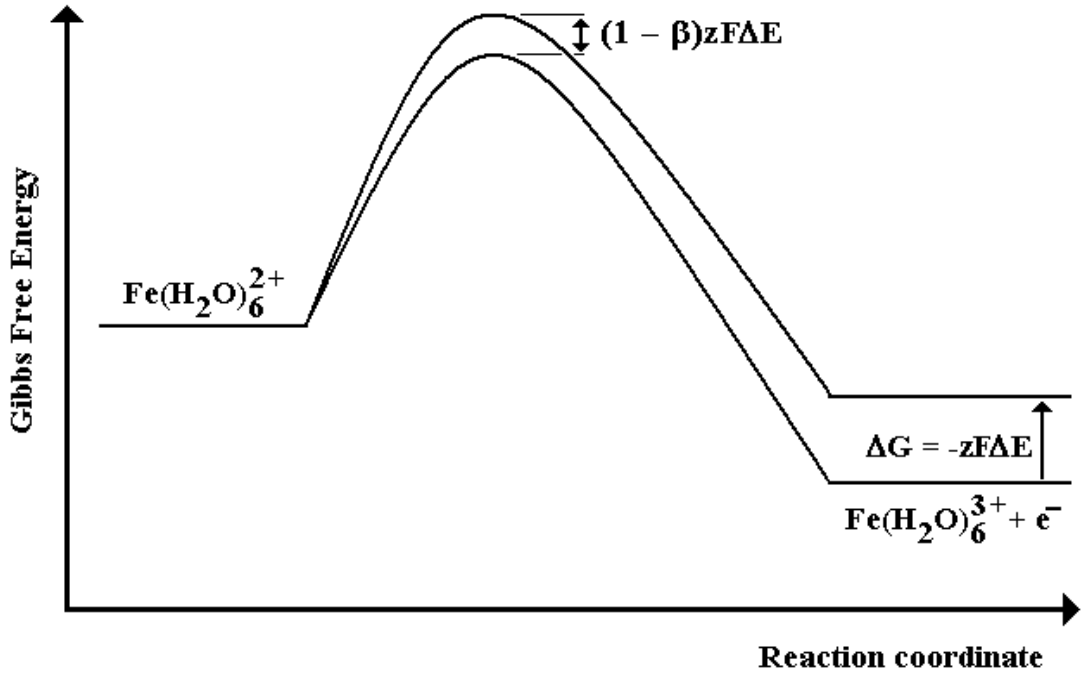

Figure A. 2. Schematic representation of the Gibbs Free Energy change during electron transfer between a metal electrode and the $Fe(H_2O)_6^{3+}/Fe(H_2O)_6^{2+}$ redox couple, showing the effect of decreasing the electrode potential from E_1 to E_2, $\Delta E = E_1 - E_2$.

parameter, which reflects the fact that asymmetry in the position of the activated complex will be reflected in the magnitude of β and hence in the fraction of ΔG by which the free energy of the activated complex changes. If the curve is symmetrical, β = 0.5, and this is very often assumed. The current density (A cm^{-2}) of the forward (anodic) reaction is:

$$J_a = k_a[Fe(H_2O)_6^{2+}]\exp(-\Delta G_a^{\ddagger}/RT) \qquad (a2)$$

and that of the cathodic process:

$$J_c = k_c[Fe(H_2O)_6^{3+}]\exp(-\Delta G_c^{\ddagger}/RT) \qquad (a3)$$

Straightforward development of the model represented by figs. A.1 and A.2 [33, 34] leads to an expression for the nett current density (*ie* anodic – cathodic), the Butler-Volmer equation:

$$j_{nett} = j_0[\exp\{(1 - \beta)f\eta\} - \exp\{-\beta f\eta\}] \qquad (a4)$$

where j_0 is a constant, the exchange current density, f = F/RT and η is the overpotential:

$$\eta = E - E_r \qquad (a5)$$

ie the difference between the potential on the electrode (E) and the potential where the nett current is zero (E_r). The overpotential reflects the energy required over and above that dictated by thermodynamics to drive an electrochemical process at the required rate (current). The exchange current density is a measure of the facile nature of the anodic and cathodic processes; the higher j_0, the more rapidly equilibrium will be established at low overpotential. At an anodic overpotential $|\eta| > RT/F$ (25.7 mV at 298 K), the second expression, the cathodic process, can be neglected in (a4), and j becomes:

$$j_{nett} = j_0[\exp\{(1 - \beta)f\eta\}] \qquad (a6)$$

Taking logs and re-arranging:

$$\eta = \{2.303/(1 - \beta)f\}.\log_{10}j_0 + \{2.303/(1 - \beta)f\}.\log_{10}j \qquad (a7)$$

or:

$$\eta = A + B\log_{10}j \qquad (a8)$$

which is the Tafel equation. The value of the asymmetry parameter is obtained from the slope of a Tafel plot, and j_0 from the intercept. If $\beta = 0.5$, the slope = 118 mV.

Oldham and Myland [34] take this (standard) Tafel analysis further to cover more complex, multistep electrochemical reactions having chemical as well as electrochemical steps, but involving, importantly, only solution species, whilst Hamann and co-workers[33] extend the approach still further to encompass adsorbed species. Taking the case of two sequential reactions involving solution species:

$$A \rightarrow B + e^- \qquad (a9)$$

$$B \rightarrow C + e^- \qquad (a10)$$

Overall:

$$A \rightarrow C + 2e^- \qquad (a11)$$

Equations (a9) – (a11) represent a general approach to multistep electrochemical reactions, in that the simultaneous transfer of two electrons is highly improbable, hence such multi-electron processes are regarded as combinations of one-electron transfers.

The kinetic treatment of (a9) and (a10) detailed below depends crucially upon the reactions achieving steady state, otherwise the derivation of simple kinetic rate laws such as Tafel equations would not be possible, as all the terms would be time-dependent. This means, in turn, that the mass transport of reactant to the electrode, and removal of products from the electrode, must be controlled through the use of, for example, rotating electrodes when acquiring data. Often, Tafel analyses are carried out on data obtained using static electrodes (see, for example, [7, 8, 10, 26, 27, 36]), in which case, the mechanistic models derived from such studies should be addressed with care.

If (a9) is the rate-determining step, it is found that the net current density is [33]:

$$J_{nett} = Fk_a'[A]\exp\{(2 - \beta_1)f\eta\} - k_c'[C]\exp\{-\beta_1 f\eta\} \qquad (a12)$$

Where k_a' and k_c' are the anodic and cathodic rate constants. At sufficiently high anodic overpotentials that the cathodic term in (a12) is negligible, and assuming $\beta = 0.5$, gives a Tafel slope of 118 mV for the anodic reaction.

If (a10) is the rate determining step:

$$J_{nett} = Fk_a'[A]\exp\{(2 - \beta_2)f\eta\} - k_c'[C]\exp\{-(1 + \beta_2)f\eta\} \qquad (a13)$$

and the anodic Tafel slope will be 39 mV. As the overpotential is increased in this case, the concentration of B builds up such that the rate of (a10) no longer becomes rate limiting and (a9) becomes rate limiting, indicated by a switch from low Tafel slope to high.

The model summarised above becomes significantly more complicated if adsorbed species are involved, *eg*. (a10) and (a11) above.

In summary, Tafel analysis cannot be used to derive unique mechanisms from experimental data; it may be possible to demonstrate that a certain mechanism is consistent with the current/voltage data, but it can never be demonstrated that this is the only mechanism. For this reason, a plethora of in-situ spectroscopic techniques were developed from the 1980's (eg. in-situ Infra Red spectroscopy) to provide essential molecular information about intermediates and products in electrochemical reactions and hence additional evidence to eliminate mechanisms that were otherwise consistent with the current/voltage data. Finally, there is a significant challenge in obtaining meaningful current/voltage data at high current densities involving vigorous gas evolution.

11.2 Appendix II: Anode Nomenclature

Series name	*Anode name*	*Composition: Sn:Sb:Ni:Au:Pb*	*Size cm × cm*	*EDIL / mg*	*N° of coats*	*Catalyst loading / mg*	*Furnace temp. °C*
KZ02	*SNATO02A*	*500:8:3:0:0*	*0.8 × 0.8*	*Broken*			
	AuSNATO02B	*500:8:3:2.25:0*	*0.8 × 0.8*	*1.2*	*20*	*4.9*	*460*
	AuSNATO02C	*500:8:3:2.25:0*	*0.8 × 0.8*	*0.2*	*20*	*4.5*	
	SNATO02D	*500:8:3:0:0*	*0.8 × 0.8*	*0.1*	*5*	*1.3*	
	AuSNATO02E	*500:8:3:2.25:0*	*0.8 × 0.8*	*0.1*	*20*	*4.6*	
	SNATO02F	*500:8:3:0:0*	*0.8 × 0.8*	*0.5*	*7*	*2.3*	
	SNATO02G	*500:8:3:0:0*	*0.8 × 0.8*	*0.2*	*10*	*2.6*	
	SNATO02H	*500:8:3:0:0*	*0.8 × 0.8*	*0.1*	*20*	*5.1*	
KZ03	*AuSNATO03A*	*500:8:3:0.1:0*	*0.8 × 0.8*	*0.7*	*20*	*4.6*	*460*
	AuSNATO03B	*500:8:3:0.1:0*	*0.8 × 0.8*	*2*	*20*	*4.7*	
	SNATO03C	*500:8:3:0:0*	*0.8 × 0.8*	*1.8*	*10*	*2.7*	
	SNATO03D	*500:8:3:0:0*	*0.8 × 0.8*	*1.8*	*10*	*2.3*	
	SNATO03E	*500:8:3:0:0*	*0.8 × 0.8*	*1.6*	*15*	*3.3*	
	SNATO03F	*500:8:3:0:0*	*0.8 × 0.8*	*1.7*	*15*	*3.8*	
	SNATO03G	*500:8:3:0:0*	*0.8 × 0.8*	*1.5*	*20*	*4.1*	
	SNATO03H	*500:8:3:0:0*	*0.8 × 0.8*	*2*	*20*	*3.9*	
	PbSNATO03I	*500:8:3:0:0.5*	*0.8 × 0.8*	*1.8*	*10*	*1.7*	
	PbSNATO03J	*500:8:3:0:0.5*	*0.8 × 0.8*	*2.2*	*10*	*2*	
	PbSNATO03K	*500:8:3:0:0.5*	*0.8 × 0.8*	*1.8*	*15*	*3.2*	
	PbSNATO03L	*500:8:3:0:0.5*	*0.8 × 0.8*	*1.8*	*15*	*3.2*	
	PbSNATO03M	*500:8:3:0:0.5*	*0.8 × 0.8*	*1.7*	*20*	*4.8*	
	PbSNATO03N	*500:8:3:0:0.5*	*0.8 × 0.8*	*1.7*	*20*	*4.7*	
	SNATO03O	*500:8:0:0:0*	*0.8 × 0.8*	*2.2*	*20*	*3.3*	
	SNATO03P	*500:8:0:0:0*	*0.8 × 0.8*	*2.6*	*20*	*3.3*	
	SNATO03Q	*500:8:3:0:0*	*0.8 × 0.8*	*1.8*	*20*	*0.5*	
	SNATO03R	*500:8:3:0:0*	*0.8 × 0.8*	*1.8*	*20*	*0.3*	
	SNATO03S	*500:8:3:0:0*	*5 × 7*	*5*	*20*	*18*	
	SNATO03T	*500:8:3:0:0*	*5 × 7*	*6*	*20*	*16.5*	
KZ04	*AuSNATO04A*	*500:8:3:0.1:0*	*0.8 × 0.8*	*0.3*	*20*	*2.9*	*460*
	AuSNATO04B	*500:8:3:0.1:0*	*0.8 × 0.8*	*0.2*	*20*	*2.9*	
	SNATO04C	*500:8:3:0:0*	*0.8 × 0.8*	*0*	*5*	*0.5*	
	SNATO04D	*500:8:3:0:0*	*0.8 × 0.8*	*0.2*	*10*	*1.1*	
	SNATO04E	*500:8:3:0:0*	*0.8 × 0.8*	*0.2*	*10*	*1.5*	
	SNATO04F	*500:8:3:0:0*	*0.8 × 0.8*	*0.1*	*15*	*2.1*	
	SNATO04G	*500:8:3:0:0*	*0.8 × 0.8*	*0.1*	*15*	*2.2*	
	SNATO04H	*500:8:3:0:0*	*0.8 × 0.8*	*0*	*20*	*3.5*	
	SNATO04I	*500:8:3:0:0*	*0.8 × 0.8*	*0*	*20*	*3.4*	
	SNATO04J	*500:8:3:0:0*	*0.8 × 0.8*	*0.1*	*5*	*0.5*	
	PbSNATO04K	*500:8:3:0:0.5*	*0.8 × 0.8*	*0*	*10*	*1.3*	
	PbSNATO04L	*500:8:3:0:0.5*	*0.8 × 0.8*	*0*	*10*	*1.2*	
	PbSNATO04M	*500:8:3:0:0.5*	*0.8 × 0.8*	*0*	*15*	*2*	
	PbSNATO04N	*500:8:3:0:0.5*	*0.8 × 0.8*	*0*	*15*	*2*	
	PbSNATO04O	*500:8:3:0:0.5*	*0.8 × 0.8*	*0*	*20*	*2.4*	
	PbSNATO04P	*500:8:3:0:0.5*	*0.8 × 0.8*	*0*	*20*	*2.9*	
	PbSNATO04Q	*500:8:3:0:0.5*	*0.8 × 0.8*	*0.3*	*20*	*2.9*	

KZ05	*SNATO05A*	*500:8:3:0:0*	*0.8 × 0.8*	*0*	*20*	*2.8*	*460*
	SNATO05B	*500:8:3:0:0*	*0.8 × 0.8*	*0*	*20*	*2.9*	
	SNATO05C	*500:8:3:0:0*	*0.8 × 0.8*	*1*	*20*	*2.6*	
	SNATO05D	*500:8:3:0:0*	*0.8 × 0.8*	*1.1*	*20*	*2.7*	
	SNATO05E	*500:8:3:0:0*	*0.8 × 0.8*	*0*	*20*	*3.5*	
	SNATO05F	*500:8:3:0:0*	*0.8 × 0.8*	*0*	*20*	*3.7*	
	AuSNATO05G	*500:8:3:0.1:0*	*0.8 × 0.8*	*0*	*20*	*2.9*	
	AuSNATO05H	*500:8:3:0.1:0*	*0.8 × 0.8*	*0*	*20*	*3.1*	
	AuSNATO05I	*500:8:3:0.1:0*	*0.8 × 0.8*	*1.3*	*20*	*3.1*	
	AuSNATO05J	*500:8:3:0.1:0*	*0.8 × 0.8*	*1.9*	*20*	*2.8*	
	AuSNATO05K	*500:8:3:0.1:0*	*0.8 × 0.8*	*0*	*20*	*3.8*	
	AuSNATO05L	*500:8:3:0.1:0*	*0.8 × 0.8*	*0*	*20*	*4*	
	AuSNATO05M	*500:8:3:0.3:0*	*0.8 × 0.8*	*0*	*20*	*2.9*	
	AuSNATO05N	*500:8:3:0.3:0*	*0.8 × 0.8*	*0*	*20*	*2.6*	
	PbSNATO05O	*500:8:3:0:0.5*	*0.8 × 0.8*	*0*	*20*	*2.9*	
	PbSNATO05P	*500:8:3:0:0.5*	*0.8 × 0.8*	*0*	*20*	*3.1*	
	PbSNATO05Q	*500:8:3:0:0.5*	*0.8 × 0.8*	*1.5*	*20*	*2.7*	
	PbSNATO05R	*500:8:3:0:0.5*	*0.8 × 0.8*	*1.9*	*20*	*2.3*	
	PbSNATO05S	*500:8:3:0:0.5*	*0.8 × 0.8*	*0*	*20*	*3.8*	
	PbSNATO05T	*500:8:3:0:0.5*	*0.8 × 0.8*	*0*	*20*	*3.8*	
	PbSNATO05U	*500:8:3:0:1.5*	*0.8 × 0.8*	*0*	*20*	*2.6*	
	PbSNATO05V	*500:8:3:0:1.5*	*0.8 × 0.8*	*0*	*20*	*3*	
	SATO05W	*500:8:0:0:0*	*0.8 × 0.8*	*0*	*20*	*2.8*	
	SATO05X	*500:8:0:0:0*	*0.8 × 0.8*	*0*	*20*	*3.1*	
	PbSATO05Y	*500:8::0:1.5*	*0.8 × 0.8*	*0*	*20*	*3.5*	
	PbSATO05Z	*500:8::0:1.5*	*0.8 × 0.8*	*0*	*20*	*2.8*	
KZ06	*NATO06A*	*67:4.3:1:0:0*	*0.8 × 0.8*	*-*	*8*	*1.3*	*550*
	NATO06B	*67:4.3:1:0:0*	*0.8 × 0.8*	*-*	*8*	*1.1*	
	PbNATO06C	*67:4.3:1:0:0*	*0.8 × 0.8*	*-*	*8*	*1.4*	
	PbNATO06D	*67:4.3:1:0:0*	*0.8 × 0.8*	*-*	*8*	*1.3*	
	NATO06E	*67:4.3:1:0:0*	*0.8 × 0.8*	*-*	*8*	*1.4*	*460*
	NATO06F	*67:4.3:1:0:0*	*0.8 × 0.8*	*-*	*8*	*1.1*	
	PbNATO06G	*67:4.3:1:0:0*	*0.8 × 0.8*	*-*	*8*	*1.6*	
	PbNATO06H	*67:4.3:1:0:0*	*0.8 × 0.8*	*-*	*8*	*1.2*	
	NATO06I	*67:4.3:1:0:0*	*0.8 × 0.8*	*-*	*8*	*0.7*	*390*
	NATO06J	*67:4.3:1:0:0*	*0.8 × 0.8*	*-*	*8*	*0.7*	
	PbNATO06K	*67:4.3:1:0:0*	*0.8 × 0.8*	*-*	*8*	*0.5*	
	PbNATO06L	*67:4.3:1:0:0*	*0.8 × 0.8*	*-*	*8*	*0.4*	
KZ07	*NATO07A*	*67:4.3:1:0:0*	*2.5 ×2.5*	*-*	*8*	*11.25*	*550*
	NATO07B	*67:4.3:1:0:0*	*2.5 ×2.5*	*-*	*8*	*10.7*	
	NATO07C	*67:4.3:1:0:0*	*2.5 ×2.5*	*-*	*8*	*Broken*	
	NATO07D	*67:4.3:5:0:0*	*2.5 ×2.5*	*-*	*8*	*13.8*	
	NATO07E	*67:4.3:5:0:0*	*2.5 ×2.5*	*-*	*8*	*11.25*	
	NATO07F	*67:4.3:5:0:0*	*2.5 ×2.5*	*-*	*8*	*Broken*	
	NATO07G	*67:4.3:0.5:0:0*	*2.5 ×2.5*	*-*	*8*	*10.7*	
	NATO07H	*67:4.3:0.5:0:0*	*2.5 ×2.5*	*-*	*8*	*10.7*	
	NATO07I	*67:4.3:0.5:0:0*	*2.5 ×2.5*	*-*	*8*	*Broken*	
	NATO07J	*67:4.3:1:0:0*	*2.5 ×2.5*	*-*	*8*	*10*	
	NATO07K	*67:4.3:1:0:0*	*2.5 ×2.5*	*-*	*8*	*8.1*	

KZ08	*NATO08A*	*67:4.3:0.1:0:0*	*2.5 ×2.5*	*-*	*8*	*5.6*	*550*
	NATO08B	*67:4.3:0.1:0:0*	*2.5 ×2.5*	*-*	*8*	*6.2*	
	NATO08C	*67:4.3:0.5:0:0*	*2.5 ×2.5*	*-*	*8*	*5.3*	
	NATO08D	*67:4.3:0.5:0:0*	*2.5 ×2.5*	*-*	*8*	*5*	
	NATO08E	*67:4.3:1:0:0*	*2.5 ×2.5*	*-*	*8*	*5.6*	
	NATO08F	*67:4.3:1:0:0*	*2.5 ×2.5*	*-*	*8*	*4.8*	
	NATO08G	*67:4.3:2:0:0*	*2.5 ×2.5*	*-*	*8*	*5.1*	
	NATO08H	*67:4.3:2:0:0*	*2.5 ×2.5*	*-*	*8*	*5.3*	
KZ09	*NATO09A*	*67:4.3:0.5:0:0*	*2.5 ×2.5*	*-*	*8*	*7.5*	*550*
	NATO09B	*67:4.3:0.5:0:0*	*2.5 ×2.5*	*-*	*8*	*7.5*	
	NATO09C	*67:4.3:0.5:0:0*	*2.5 ×2.5*	*-*	*8*	*6.9*	
	NATO09D	*67:4.3:0.5:0:0*	*2.5 ×2.5*	*-*	*8*	*6.9*	
	NATO09E	*67:4.3:1:0:0*	*2.5 ×2.5*	*-*	*8*	*4.4*	
	NATO09F	*67:4.3:1:0:0*	*2.5 ×2.5*	*-*	*8*	*5*	
	NATO09G	*67:4.3:1:0:0*	*2.5 ×2.5*	*-*	*8*	*5*	
	NATO09H	*67:4.3:1:0:0*	*2.5 ×2.5*	*-*	*8*	*5*	
KZ10	*NATO10A*	*67:4.3:0.5:0:0*	*2.5 ×2.5*	*-*	*15*	*1.7*	*550*
	NATO10A	*67:4.3:0.5:0:0*	*2.5 ×2.5*	*-*	*15*	*1.5*	
	NATO10A	*67:4.3:0.5:0:0*	*2.5 ×2.5*	*-*	*15*	*1.7*	
	NATO10A	*67:4.3:0.5:0:0*	*2.5 ×2.5*	*-*	*20*	*2.1*	
	NATO10A	*67:4.3:0.5:0:0*	*2.5 ×2.5*	*-*	*20*	*2.3*	
	NATO10A	*67:4.3:0.5:0:0*	*2.5 ×2.5*	*-*	*20*	*2.2*	
KZ11	*NATO11A*	*67:4.3:0.5:0:0*	*2.5 ×2.5*	*-*	*8*	*6.8*	*390*
	NATO11B	*67:4.3:0.5:0:0*	*2.5 ×2.5*	*-*	*8*	*7.4*	
	NATO11C	*67:4.3:0.5:0:0*	*2.5 ×2.5*	*-*	*8*	*7.2*	
	NATO11D	*67:4.3:0.5:0:0*	*0.8 ×0.8*	*-*	*8*	*1.4*	
	NATO11E	*67:4.3:0.5:0:0*	*0.8 ×0.8*	*-*	*8*	*1.5*	
	NATO11F	*67:4.3:0.5:0:0*	*0.8 ×0.8*	*-*	*8*	*1*	
	NATO11G	*67:4.3:1:0:0*	*2.5 ×2.5*	*-*	*8*	*7.6*	
	NATO11H	*67:4.3:1:0:0*	*2.5 ×2.5*	*-*	*8*	*7.8*	
	NATO11I	*67:4.3:1:0:0*	*2.5 ×2.5*	*-*	*8*	*7.9*	
	NATO11J	*67:4.3:1:0:0*	*0.8 ×0.8*	*-*	*8*	*2.7*	
	NATO11K	*67:4.3:1:0:0*	*0.8 ×0.8*	*-*	*8*	*2.5*	
	NATO11L	*67:4.3:1:0:0*	*0.8 ×0.8*	*-*	*8*	*2.2*	
	NATO11M	*67:4.3:1:0:0*	*2.5 ×2.5*	*-*	*8*	*8.7*	
	NATO11N	*67:4.3:1:0:0*	*2.5 ×2.5*	*-*	*8*	*8.3*	
	NATO11O	*67:4.3:1:0:0*	*0.8 ×0.8*	*-*	*8*	*1.2*	
	NATO11P	*67:4.3:1:0:0*	*0.8 ×0.8*	*-*	*8*	*1.5*	
KZ12	*NATO12A*	*67:4.3:0.5:0:0*	*2.5 ×2.5*	*-*	*8*	*6.8*	*550*
	NATO12B	*67:4.3:0.5:0:0*	*2.5 ×2.5*	*-*	*8*	*6.3*	
	NATO12C	*67:4.3:0.5:0:0*	*2.5 ×2.5*	*-*	*8*	*5.9*	
	NATO12D	*67:4.3:0.5:0:0*	*0.8 ×0.8*	*-*	*8*	*1.3*	
	NATO12E	*67:4.3:0.5:0:0*	*0.8 ×0.8*	*-*	*8*	*1.3*	
	NATO12F	*67:4.3:0.5:0:0*	*0.8 ×0.8*	*-*	*8*	*1.5*	
	NATO12G	*67:4.3:1:0:0*	*2.5 ×2.5*	*-*	*8*	*7*	
	NATO12H	*67:4.3:1:0:0*	*2.5 ×2.5*	*-*	*8*	*7*	
	NATO12I	*67:4.3:1:0:0*	*2.5 ×2.5*	*-*	*8*	*7.2*	
	NATO12J	*67:4.3:1:0:0*	*0.8 ×0.8*	*-*	*8*	*1.4*	

	NATO12K	*67:4.3:1:0:0*	*0.8 ×0.8*	*-*	*8*	*1.7*	
	NATO12L	*67:4.3:1:0:0*	*0.8 ×0.8*	*-*	*8*	*1.1*	
	NATO12M	*67:4.3:1:0:0*	*2.5 ×2.5*	*-*	*8*	*7.1*	
	NATO12N	*67:4.3:1:0:0*	*2.5 ×2.5*	*-*	*8*	*7.5*	
	NATO12O	*67:4.3:1:0:0*	*0.8 ×0.8*	*-*	*8*	*1.6*	
	NATO12P	*67:4.3:1:0:0*	*0.8 ×0.8*	*-*	*8*	*1.7*	
KZ13	*NATO13A*	*67:4.3:0.5:0:0*	*2.5 ×2.5*	*-*	*8*	*7.1*	*460*
	NATO13B	*67:4.3:0.5:0:0*	*2.5 ×2.5*	*-*	*8*	*6.4*	
	NATO13C	*67:4.3:0.5:0:0*	*2.5 ×2.5*	*-*	*8*	*6.9*	
	NATO13D	*67:4.3:0.5:0:0*	*0.8 ×0.8*	*-*	*8*	*1.3*	
	NATO13E	*67:4.3:0.5:0:0*	*0.8 ×0.8*	*-*	*8*	*1.2*	
	NATO13F	*67:4.3:0.5:0:0*	*0.8 ×0.8*	*-*	*8*	*0.8*	
	NATO13G	*67:4.3:1:0:0*	*2.5 ×2.5*	*-*	*8*	*7.2*	
	NATO13H	*67:4.3:1:0:0*	*2.5 ×2.5*	*-*	*8*	*6.9*	
	NATO13I	*67:4.3:1:0:0*	*2.5 ×2.5*	*-*	*8*	*6.9*	
	NATO13J	*67:4.3:1:0:0*	*0.8 ×0.8*	*-*	*8*	*1.3*	
	NATO13K	*67:4.3:1:0:0*	*0.8 ×0.8*	*-*	*8*	*1.5*	
	NATO13L	*67:4.3:1:0:0*	*0.8 ×0.8*	*-*	*8*	*1.7*	
	NATO13M	*67:4.3:1:0:0*	*2.5 ×2.5*	*-*	*8*	*11*	
	NATO13N	*67:4.3:1:0:0*	*2.5 ×2.5*	*-*	*8*	*8*	
	NATO13O	*67:4.3:1:0:0*	*0.8 ×0.8*	*-*	*8*	*1.4*	
	NATO13P	*67:4.3:1:0:0*	*0.8 ×0.8*	*-*	*8*	*1.7*	
KZ14	*NATO14A*	*67:4.3:0.5:0:0*	*2.5 ×2.5*	*-*	*2*	*1.6*	*550*
	NATO14B	*67:4.3:0.5:0:0*	*2.5 ×2.5*	*-*	*2*	*1.3*	
	NATO14C	*67:4.3:0.5:0:0*	*2.5 ×2.5*	*-*	*4*	*3.7*	
	NATO14D	*67:4.3:0.5:0:0*	*2.5 ×2.5*	*-*	*4*	*3.7*	
	NATO14E	*67:4.3:0.5:0:0*	*2.5 ×2.5*	*-*	*6*	*5.4*	
	NATO14F	*67:4.3:0.5:0:0*	*2.5 ×2.5*	*-*	*6*	*4.9*	
	NATO14G	*67:4.3:0.5:0:0*	*2.5 ×2.5*	*-*	*10*	*8.8*	
	NATO14H	*67:4.3:0.5:0:0*	*2.5 ×2.5*	*-*	*10*	*9*	
	NATO14I	*67:4.3:0.5:0:0*	*2.5 ×2.5*	*-*	*12*	*10.5*	
	NATO14J	*67:4.3:0.5:0:0*	*2.5 ×2.5*	*-*	*12*	*9.3*	
	NATO14K	*67:4.3:0.5:0:0*	*2.5 ×2.5*	*-*	*15*	*13.4*	
	NATO14L	*67:4.3:0.5:0:0*	*2.5 ×2.5*	*-*	*15*	*12.5*	
	NATO14M	*67:4.3:0.5:0:0*	*2.5 ×2.5*	*-*	*18*	*15.9*	
	NATO14N	*67:4.3:0.5:0:0*	*2.5 ×2.5*	*-*	*18*	*14.4*	
	NATO14O	*67:4.3:0.5:0:0*	*2.5 ×2.5*	*-*	*20*	*17.2*	
	NATO14P	*67:4.3:0.5:0:0*	*2.5 ×2.5*	*-*	*20*	*16.6*	
KZ15	*NATO15A*	*67:4.3:0.25:0:0*	*2.5 ×2.5*	*-*	*8*	*6.6*	*550*
	NATO15B	*67:4.3:0.25:0:0*	*2.5 ×2.5*	*-*	*8*	*6.9*	
	NATO15C	*67:4.3:0.75:0:0*	*2.5 ×2.5*	*-*	*8*	*6.4*	
	NATO15D	*67:4.3:0.75:0:0*	*2.5 ×2.5*	*-*	*8*	*6.1*	
	NATO15E	*67:4.3:1.25:0:0*	*2.5 ×2.5*	*-*	*8*	*6.2*	
	NATO15F	*67:4.3:1.25:0:0*	*2.5 ×2.5*	*-*	*8*	*6.6*	
KZ16	*NATO16A*	*67:4.3:0.75:0:0*	*2.5 ×2.5*	*-*	*20*	*22.5*	*460*
	NATO16B	*67:4.3:0.75:0:0*	*2.5 ×2.5*	*-*	*20*	*23*	
	NATO16C	*67:4.3:0.75:0:0*	*7 ×5*	*-*	*20*	*94.5*	

KZ17	*NATO17A*	*67:4.3:0.75:0:0*	*2.5 ×2.5*	*-*	*20*	*16.9*	*550*
	NATO17B	*67:4.3:0.75:0:0*	*2.5 ×2.5*	*-*	*20*	*16.3*	
	NATO17C	*67:4.3:0.75:0:0*	*7 ×5*	*-*	*20*	*80.5*	
	NATO17D	*67:4.3:0.75:0:0*	*7 ×5*	*-*	*20*	*84*	
	NATO17E	*67:4.3:0.75:0:0*	*7 ×5*	*-*	*20*	*84*	
	NATO17F	*67:4.3:0.75:0:0*	*7 ×5*	*-*	*20*	*84*	
	NATO17G	*67:4.3:0.75:0:0*	*7 ×5*	*-*	*20*	*80.5*	
	NATO17H	*67:4.3:0.75:0:0*	*7 ×5*	*-*	*20*	*77*	
	NATO17I	*67:4.3:0.75:0:0*	*7 ×5*	*-*	*20*	*84*	
	NATO17J	*67:4.3:0.75:0:0*	*7 ×5*	*-*	*20*	*77*	
KZ18	*NATO18A*	*67:4.3:0.5:0:0*	*2.5 ×2.5*	*-*	*2*	*0.1*	*550*
	NATO18B	*67:4.3:0.5:0:0*	*2.5 ×2.5*	*-*	*2*	*0.1*	
	NATO18C	*67:4.3:0.5:0:0*	*2.5 ×2.5*	*-*	*5*	*1.9*	
	NATO18D	*67:4.3:0.5:0:0*	*2.5 ×2.5*	*-*	*5*	*0.6*	
	NATO18E	*67:4.3:0.5:0:0*	*2.5 ×2.5*	*-*	*8*	*1.9*	
	NATO18F	*67:4.3:0.5:0:0*	*2.5 ×2.5*	*-*	*8*	*3.1*	
	NATO18G	*67:4.3:0.5:0:0*	*2.5 ×2.5*	*-*	*10*	*4.4*	
	NATO18H	*67:4.3:0.5:0:0*	*2.5 ×2.5*	*-*	*10*	*3.8*	
	NATO18I	*67:4.3:0.5:0:0*	*2.5 ×2.5*	*-*	*12*	*5*	
	NATO18J	*67:4.3:0.5:0:0*	*2.5 ×2.5*	*-*	*12*	*4.4*	
	NATO18K	*67:4.3:0.5:0:0*	*2.5 ×2.5*	*-*	*15*	*6.9*	
	NATO18L	*67:4.3:0.5:0:0*	*2.5 ×2.5*	*-*	*15*	*6.9*	
	NATO18M	*67:4.3:0.5:0:0*	*2.5 ×2.5*	*-*	*18*	*9.3*	
	NATO18N	*67:4.3:0.5:0:0*	*2.5 ×2.5*	*-*	*18*	*8.1*	
	NATO18O	*67:4.3:0.5:0:0*	*2.5 ×2.5*	*-*	*20*	*8.8*	
	NATO18P	*67:4.3:0.5:0:0*	*2.5 ×2.5*	*-*	*20*	*9.4*	
	NATO18Q	*67:4.3:1:0:0*	*2.5 ×2.5*	*-*	*20*	*15*	
	NATO18R	*67:4.3:1:0:0*	*2.5 ×2.5*	*-*	*20*	*15*	
	NATO18S	*67:4.3:0.75:0:0*	*2.5 ×2.5*	*-*	*20*	*12.5*	
	NATO18T	*67:4.3:0.75:0:0*	*2.5 ×2.5*	*-*	*20*	*13.1*	
	NATO18U	*67:4.3:0.25:0:0*	*2.5 ×2.5*	*-*	*20*	*17.5*	
	NATO18V	*67:4.3:0.25:0:0*	*2.5 ×2.5*	*-*	*20*	*15.6*	